Measurement of the Thrust Generated by a Hollow Cathode with Noble Gases

Thesis submitted for the degree of Doctor of Philosophy

Paolo Gessini, MSc

Supervisor: Prof. Stephen B. Gabriel

April 2006

Abstract

Hollow cathodes (HCs) have been used for decades in various electric propulsion applications. They have been extensively investigated and tested, demonstrating excellent performance and durability, with tens of thousands of hours of successful operation. In spite of this, understanding and modelling of the HC discharge physical mechanisms is still far from satisfactory. Further investigations are therefore necessary. In particular, the thrust generated by a HC has actually been measured only in one instance, with a device quite different from the one investigated in this thesis. A thrust measurement system has therefore been developed, in order to evaluate for what discharge conditions the highest values of specific impulse and in general the best performance are attained. The system consists of a Cantilever Beam Target (CBT) and of a Laser Optical Lever (LOL). Extensive thrust measurements with several noble gases as propellants are presented and discussed. They show that several mN of thrust can be produced, at values of specific impulse exceeding, in some cases, 500 s. Such values confirm that the device is not just heating the gas, like a resistojet, but is operating in a fashion more similar to that of an arcjet, with the heavy particle average temperature sensibly higher than the wall value. These encouraging results were obtained just by varying the discharge parameters, with very little attempt at optimising the electrode configuration. The use of different electrode configurations, like for instance an enclosed keeper, and the investigation of other propellants, could lead to the development of a viable HC microthruster, competitive with already existing devices.

Acknowledgements

I have met so many people in these years, that it would be impossible to remember them all... This would become ridiculously long, and I am also sure that I would forget someone... Which I will do, all the same! Therefore, I will limit myself only to people directly involved with my academic career! Friends and housemates... I am sorry: you know I will always remember you!

First and foremost, I wish to acknowledge my supervisor, Prof. Stephen B. Gabriel. His guidance, encouragement, support and, above, all, patience, have all been well above the call of duty. I am especially honoured to have been his fffrrrrieeeeeeennnnd, and not only his student, throughout these years, and I am sure this will go on... Thank you, Steve!

Dr. Graham T. Roberts has been a very effective and efficient, as well as friendly, internal examiner. All the other members of the faculty and staff (thank you, Sonya and Dawn!) in the Aerospace Engineering Department, and some in the ISVR as well, have been friendly and supportive. I could not have done what I have without the people at EDMC, in Materials, Chemistry, ORC and Physics: thank you all! Simon Klitz was always ready to help, work, machine things in a hurry, and I cannot bear to think how much I have bothered Rob Stansbridge and especially David Beckett...

David's Fearn unceasing support, encouragement and advice have been invaluable, and he has also been a friend, who let me bother him way too much. I am honoured to have my name associated with his! Neil Wallace and Mike Kelly, both at QinetiQ, have also been extremely helpful and friendly.

I would like to remember my office mates, all the various generations of them! Neil Williams, Gavin Gittins, Balaji Kumar, Duncan Goulty, Sabrina Pottinger, Ismat Rudwan, Christoph Schwingshackl and, later, Rodrigo Intini Marques, Robin Amy, Gabriel Bianchi, Nick Bevan, David Webb, Sam Roberts and Michele Coletti. In the case of Duncan, Sabrina and Ismat many more things that we shared could be

remembered... Ismat, thank you for all the help you gave me with my experiments and my thesis, for all the theoretical and practical knowledge... And for the football matches in the corridor at night! Rodrigo, meu amigo (my fffrrrrieeeeeeennnnd), I do not need to go into details: you know... Not my office mates, but next door, in no special order: Mark Paine, Frank Crawford, Keith Hutchison, George Michalareas, Steffen Dransfeld, Scott Walker (colour printing and... Thank you for the music!), Carl White, Gareth, David, Aim and... Mark, you too have shared more than others with me, and so have Keith, Frank, George and Steffen... From the Aero crowd, Jim McManus: thanks for your electrifying help!

Giorgio Paccani has introduced me to Electric Propulsion and has continued to support me throughout these years. He has also become a great friend of mine: thank you, Giorgio! Eddie Choueiri, Bob Jahn and Peter Turchi have taught me a lot, probably more than they think... Thomas York and Vish Subramaniam had kind and encouraging words when they were needed...

John Ziemer and Ted Cubbin: endless homework assignments and late nights and... Cooking! Dimitris Kyritsis: late nights, excellent coffee, socio-political and scientifico-philosophical discussions and... Other things! Tomokazu Umeki, who will never read this. My American Brother Chris Schmahl, Bunny Bob Leiweke, Hani Kamhawi and Yiangos and Pavlos Mikellides, who will... Carsten Scharlemann and Ron Corey: so many things and... Beers! Carsten, you are one of the nicest persons I have ever met, and one of my best friends... I am not sure I know any other individual that would have endured what you have and still talked to me!

Natalia Mazour, Tesoro Mio, you changed my life forever... Cynthia Niehoff, My Manatee, you probably saved it... You will always be in my heart!

Last but not least, I owe a huge debt of gratitude to my family, for the unflagging moral and material support they have given me in all these years. I only wish my Dad and my Grandma were here to see this, and I am happy my Mum is... To my brother Riccardo Reim I am especially indebted. Apart from all his love, it is mostly his doing my not being entirely ignorant of the humanities and of the fine arts!

Table of Contents

Chapter 0 Introduction 1
0.0 – The Advantages of Electric Propulsion 1
0.1 – Background and Basic Description of HC Characteristics 2
0.2 – The HC as an Electric Thruster Component and as a Stand-Alone Thruster ... 5
0.3 – Assessing HC Performance 7
Chapter 1 Literature Review 9
1.0 – Overview of HC Investigations 9
1.1 – HC Discharge Physics 9
1.2 – Thrust Measurements of a Mercury HC Discharge 20
1.3 – Ion Emission Measurements 21
1.4 – Analytical, Semi-Analytical and Numerical Models 38
Chapter 2 Theoretical Analysis, Modelling and Estimates 42
2.0 – Flow Dynamics and Thrust Generation 42
2.1 – Model of HC Orifice Conditions 46
2.2 – HC Preliminary Thrust Assessment 47
Chapter 3 The Thrust Measurement System: Theoretical Analysis and Calibration 55
3.0 – Direct and Indirect Thrust Measurement 55
3.1 – The Cantilever Beam Target 56
3.2 – Measurement of Small Angular Deflections: the Laser Optical Lever 63
3.3 – Initial Target Calibration and System Validation 66
3.3.1 – Calibration Set-Up 66
3.3.2 – Results: Relative Calibration 69
3.4 – Electrostatic Calibration 71
Chapter 4 Experimental Apparatus and Procedures 73
4.0 – Vacuum Rig 73
4.1 – Propellant Feed System 74
4.2 – The T6 Hollow Cathode / Anode Assembly 74
4.3 – The Target Assembly 76
4.4 – The Optical Set-Up 77
4.5 – The Electrical Set-Up 81
4.6 – The Thrust Measurement: Issues and Procedures 81
Chapter 5 Results and Discussion 96
5.0 - Results 96
5.0.1 – T6 HC Characterisation in Open-Diode Discharge Configuration 96
5.0.2 – Plume Current Measurements 101
5.0.3 – Thrust Measurements 106
5.0.3.1 – Cold and Heater Thrust (Discharge Off) 107
5.0.3.2 – Electric Thrust (Discharge On) 112
5.1 – Discussion 123

Chapter 6 Conclusions and Future Work 140
6.0 – Conclusions 140
6.1 – Future Work 142
References 144

Chapter 0

Introduction

0.0 – The Advantages of Electric Propulsion

In recent years, the trend towards increasingly smaller spacecraft has generated the need for micro-thrusters. Also on larger spacecraft it is necessary to provide low-thrust auxiliary propulsion over many years, if possible consuming less propellant than needed by conventional chemical thrusters. By using small electric thrusters, with a high specific impulse (I_{sp}), significant propellant-mass savings can be achieved, which in turn translate into a reduced launch cost, an extended spacecraft lifetime or extra payload.

In general, there is a significant benefit from employing high I_{sp} propulsion technology. This can be seen from the classical rocket equation [1], also known as Tsiolkovski (or, sometimes, Tsiolkovski-Oberth) formula,

$$\Delta v = u_e \, ln \frac{m_0}{m_0 - \Delta m} = g I_{sp} \, ln \frac{m_0}{m_f} \ , \qquad (0.1)$$

where Δv is the magnitude of velocity increment achieved by the ejection of Δm of the initial mass m_0 at an exhaust velocity u_e relative to the rocket, related to I_{sp} by

$$I_{sp} = \frac{F}{\dot{m} g} = \frac{u_e}{g} \ , \qquad (0.2)$$

with F the thrust, $\dot{m}$ the mass flow rate of propellant and g the acceleration of gravity at sea level. Since m_f, the final mass, includes payload and structure ($m_f = m_{pay} + m_s$), from Eq. (0.1), it is clear that, in order to achieve high values of payload mass fraction m_f/m_0 for a specific mission, u_e should be at least comparable to Δv.

Chemical rockets are essentially energy-limited, since the quantity of energy per unit mass is limited by the energy released by the chemical reactions between the propellant and the oxidizer. Nuclear and electric thermal rockets, which raise the temperature of a fluid and expand it through a nozzle, like chemical thrusters, are still limited by the material properties of the solid walls. For all these devices, the specific impulse is therefore limited to values of several hundred seconds. In the case of devices that rely essentially on direct electrostatic or electromagnetic acceleration of the propellant, for example ion thrusters, there is no necessary upper limit to the amount of energy that could be added to the propellant and thus to the specific impulse. However, the rate of conversion of solar or nuclear energy to electrical and thence to kinetic energy is limited by the mass of the conversion equipment required, which could become a significant portion of the total vehicle mass. As a rule of thumb, in fact, the mass of the power plant M_P (including structure) is directly proportional to its power output P:

$$M_P = \alpha P \,. \tag{0.3}$$

The coefficient α is known as the specific mass of the power plant. Therefore, electric rockets are essentially power-limited [2].

0.1 – Background and Basic Description of HC Characteristics

Hollow Cathodes (HCs) have been built and operated for many years, mainly in support of their role as efficient, long life electron emitters. Many efforts aiming at a better understanding of their physics have been ongoing in several countries, with the ultimate objectives of reducing power input for a given electron emission current and increasing lifetime. Numerous papers about HC behaviour, including both experimental results and theoretical analyses, have been published since the late 1960s [3-9]. In its simplest incarnation, a HC could consist of a bare high-melting point metallic (e.g., tungsten) tube [8] or cavity [10]. Such configurations have been employed in quasisteady magnetoplasmadynamic (MPD) thruster [11] applications.

On the other hand, the HCs developed for use in ion engines or HETs, typically operating in steady state and at much lower power levels, incorporate features such as

low-work function inserts and heaters in order to improve their performance. The discharge to such a HC is initiated, in most cases, by heating it to a temperature of about 1300 K, passing a flow of propellant gas through it. Then a potential, often much higher than the steady-state discharge potential, is applied to a keeper electrode, situated adjacent to the tip. It is usual to continue to draw a current to this electrode under steady-state operating conditions, although this is not always the case with HET applications. This is to ensure that the discharge and cathode emission process will continue even if the main current to the anode or to the ion beam is interrupted. Hence the name "keeper" electrode, or simply keeper [12], is used. Early on it was discovered [13], and later confirmed [12, 14], that an enclosed-keeper configuration, where the keeper electrode completely surrounds the HC, forming a cavity from which the plasma can escape only through the keeper orifice, can significantly aid discharge stability and reduce the amplitude of electrical noise. This type of configuration has been adopted in recent experimental work at the University of Southampton [15]. Although sometimes convenient, starting the discharge with a keeper electrode and then transferring to a main anode is by no means necessary. Under carefully selected operating conditions the high-voltage keeper power supply can therefore be dispensed with [15]. The keeper electrode itself can be eliminated, thus further simplifying the experimental arrangement and operating the HC with a single anode. This kind of set-up is known as an open-diode configuration [12] and has been adopted in the experiments described in this thesis. A typical HC/keeper assembly is shown schematically in Figure 0.1 (courtesy of QinetiQ).

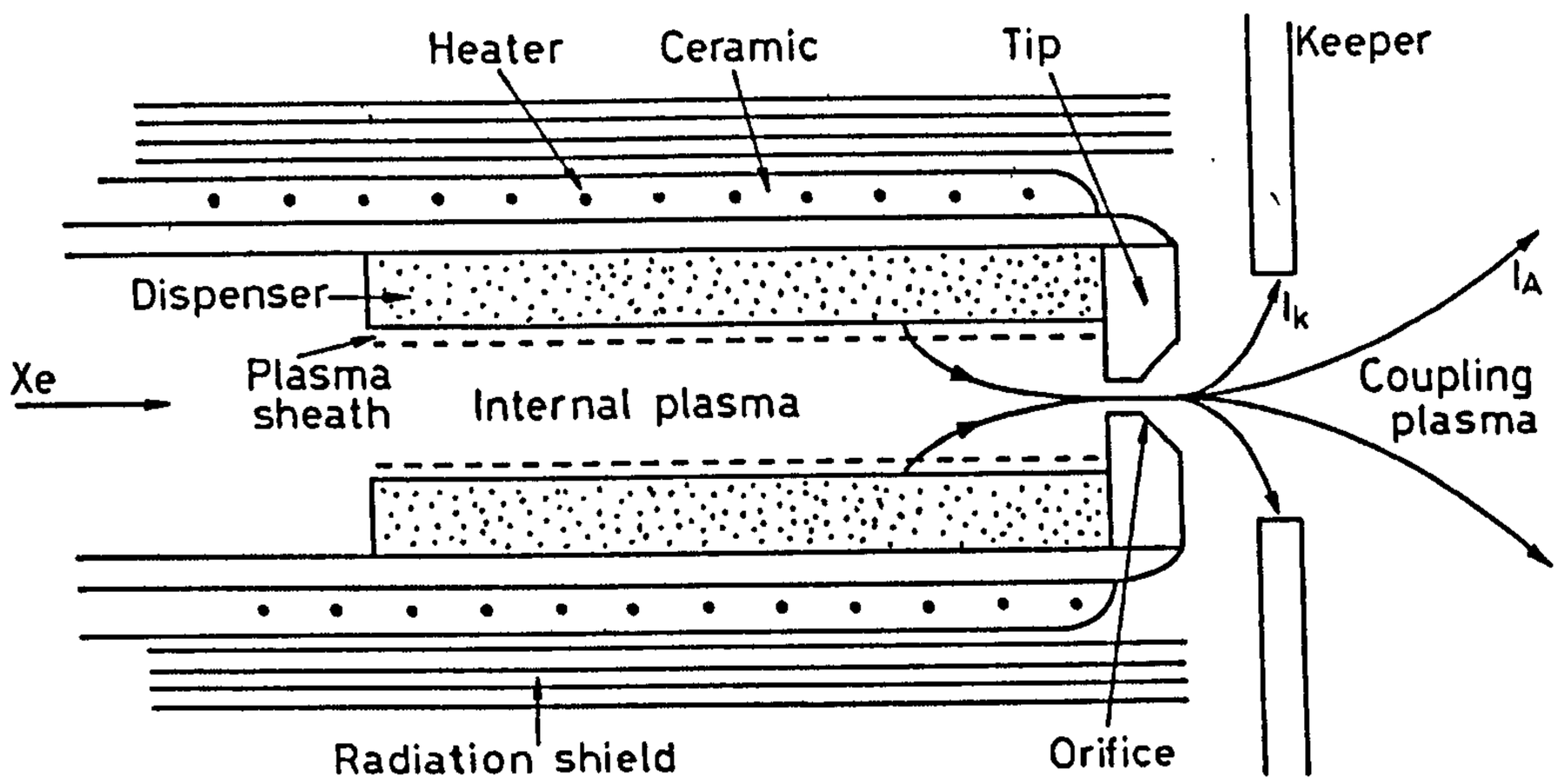

Figure 0.1 – HC/keeper assembly (QinetiQ).

Although many possible electron-emission mechanisms have been invoked to explain the high current densities, often of the order of 50 A/cm^2, obtained from the surface of the dispenser located within the cathode, the field-enhanced thermionic process would seem to dominate under many circumstances [6, 15, 16]. This occurs because a dense internal plasma is generated within the HC, as confirmed by both probe [6] and spectroscopic [17, 18] measurements. A very thin sheath then forms to separate this plasma from the wall, and the potential drop across this plasma sheath provides the high electric field at the surface needed to enhance the normal thermionic emission to the high current densities observed. The Richardson-Dushmann equation,

$$j_{th} = AT^2 e^{-\frac{e\varphi}{kT}}, \tag{0.4}$$

relating the thermionic current density j_{th} to the temperature of the emitting surface T and to its work function φ through the Richardson constant A ($\cong$ 60 A cm^{-2} K^{-2}), is therefore modified to include the Schottky effect. This is done by introducing an effective work function

$$\varphi_e = \varphi - \sqrt{\frac{eE}{4\pi\varepsilon_0}} \tag{0.5}$$

and rewriting the equation for field-enhanced thermionic emission as

$$j_S = AT^2 e^{-\frac{e\varphi_e}{kT}} = j_{th} e^{4.389\frac{\sqrt{E}}{T}} \tag{0.6}$$

where E is the electric field at the emitting surface in V/cm [19]. From the above equation it is clear how the emitted current density, already a strong function of T and φ (see Eq. 0.4), is greatly increased by the presence of an electric field at the emitting surface.

0.2 – The HC as an Electric Thruster Component and as a Stand-Alone Thruster

HCs are used as neutralizers in all gridded ion engines and also for the main discharge in electron-bombardment (Kaufman-type) ion thrusters. A schematic of a typical Kaufman-type thruster, with the various components clearly labelled, is shown in Fig. 0.2 [20]. Electrons from the main HC ionise the propellant atoms by collision. The ions are then extracted and accelerated with a system of grids to generate the thrust. A second HC (neutralizer) injects more electrons into the ion beam to prevent charge build-up and alleviate beam divergence. HCs are also used to provide the electrons in Hall-Effect Thrusters (HETs).

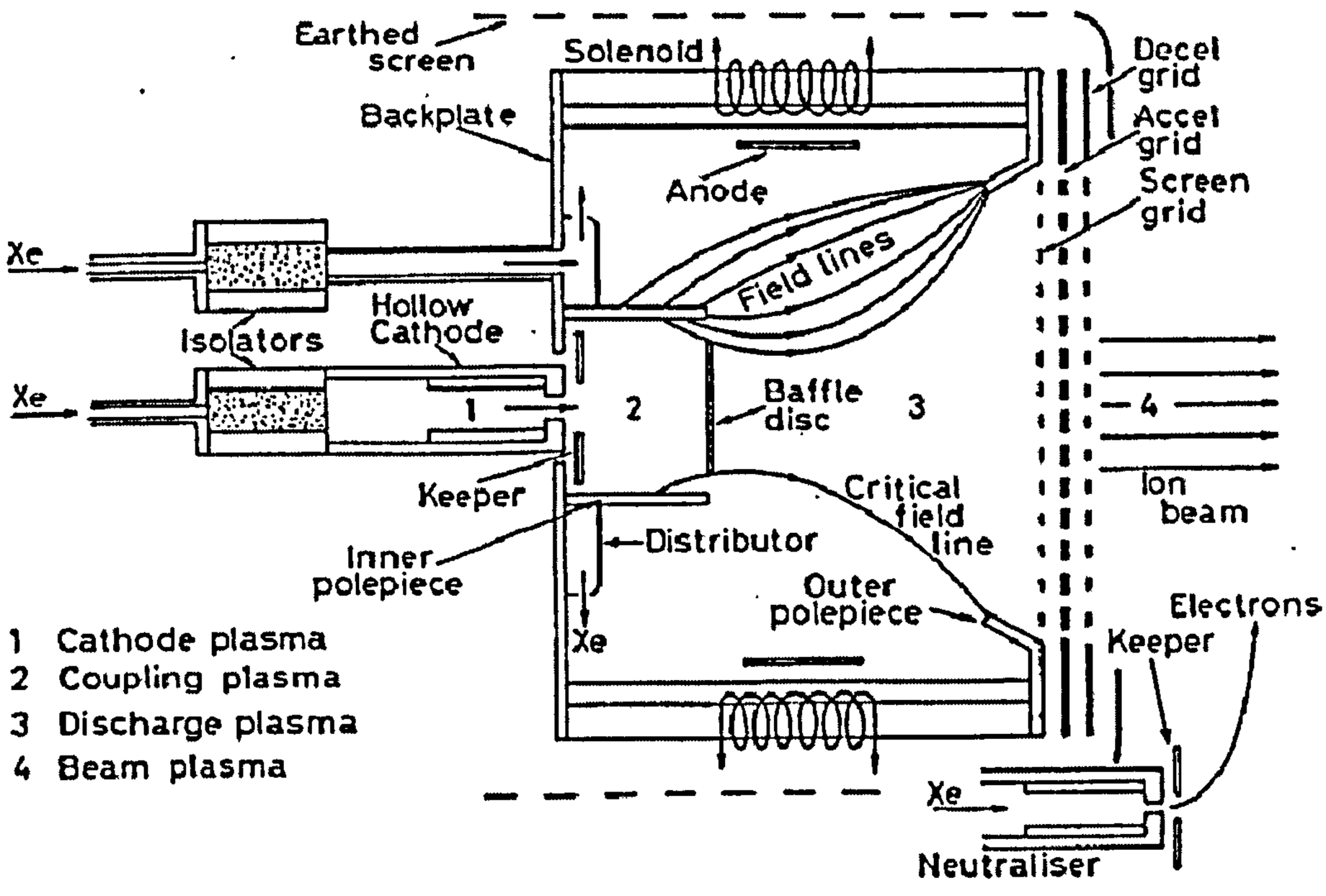

Figure 0.2 – Schematic of a Kaufman-type ion thruster [20].

Not all types of thruster can be scaled down easily. In gridded ion engines and HETs, magnetic fields are used to contain the electrons in the discharge volume, increasing their path length to a few ionisation mean free paths. This provides a high probability of ionisation before they are lost by contact with the interior surfaces.

Where magnetic fields are used, scaling down a thruster involves stronger and stronger fields, to ensure that the electrons are adequately contained within the available volume. This is because the electrons spiral around and progress along the magnetic field lines (see Fig. 0.2) with a radius of gyration (also known as cyclotron or Larmor radius) r_L inversely proportional to the magnitude of the field B, according to the equation [1, 21]

$$r_L = \frac{mv_\perp}{qB} \ , \tag{0.7}$$

where m and q are, respectively, the electron mass and charge and $v_\perp$ is the velocity component normal to B. Therefore, from Eq. (0.7), scaling down a 10 cm beam diameter ion thruster to a millimeter diameter, for example, would require increasing the magnetic field strength from 0.1 to 10 Tesla, in order to maintain efficient electron containment [22, 23]. Magnet weight and power requirements could easily become prohibitive.

In addition, efficiency falls dramatically with size, partly due to decreasing volume-to-area ratio. This is because ionisation is a volume phenomenon, whereas losses are proportional to area, so as the volume-to-area ratio falls as thrusters become smaller, so does the efficiency, which is proportional to it. In particular, for the cylindrical geometry generally adopted in ion thrusters, decreasing both radius and length by a certain factor will decrease the volume-to-area ratio by the same factor.

Thus the prospects of designing successfully a very small ion thruster of traditional design to operate at high efficiency are not very good, even if progress has been recently made. For this reason, there has recently been some interest in the possibility of developing non-magnetic micro-ion thrusters [22, 24-27].

However, it has been found by several research groups that HCs can produce significant amounts of relatively high energy ions, with energies often well above keeper or discharge plasma potential [25, 26, 28-42]. These results, while at the beginning mainly raising concerns about baffle and grid erosion, have later suggested

to some investigators that a HC, by itself, might be capable of producing an appreciable thrust at a relatively high value of I_{sp}.

This observation might not be particularly significant if the degree of ionisation within the plasma plume emerging from a HC were very low, as has often been assumed in the past, as any thrust produced by ions would then be very small, and might not be of practical interest. However, recent studies by Crofton [25, 26, 31, 34, 39, 40] suggest that this earlier assumption may not be correct. From the high level of Xe^{2+} observed in the plume emitted by the cathode of a T5 thruster, he concludes that the plasma emanating from a HC is almost completely ionised near the orifice, at least for certain flow rate and orifice current density conditions [25, 34, 39].

If HCs can be used as thrusters, as suggested in the present work, it should be noted that they are a well-established, flight-qualified technology. They have a very long proven life, with up to 2.8×10^4 hours having been demonstrated at the NASA Lewis Research Center (LeRC) with xenon [43]. This life test was terminated due to an ignition failure, when the cathode tip temperature exceeded 1600 K. Estimates of lifetime for the UK-25 HC yield more than 10^4 hours with a tip temperature of the order of 1400 K [44, 45] and more than $3x10^4$ hours (projected) for the HC employed in the experiments described in this thesis, which was developed for the T6 ion thuster [46, 47]. This is entirely consistent with many missions of interest.

It is concluded that it is worth investigating the possibility of developing HCs into simple and effective microthrusters. In order to do this, we first measured the thrust they produce and then investigated possible ways in which it might be enhanced. This allowed us to assess the I_{sp} that can be obtained, in order to establish the range of appropriate missions for these devices.

0.3 – Assessing HC Performance

A preliminary assessment of the thrust levels that could be obtained from a HC, performed at the beginning of this study, gave encouraging results [48]. The thrust

produced by a HC has been actually measured only once with a mercury HC and for a limited set of conditions [49].

A target system has been developed, calibrated and tested by the author at the University of Southampton to measure the thrust and to evaluate the discharge conditions under which the highest values of specific impulse are attained. The system consists essentially of three separate parts. The HC plume impinges upon a Cantilever Beam Target (CBT). As this deflects, due to momentum transfer, its rotation is amplified by a Laser Optical Lever (LOL). The resulting laser beam displacement is measured through a Position Sensitive Detector (PSD) [50].

This thesis describes the design, calibration and successive improvements of the CBT-LOL system [48, 51-53], together with an extensive set of thrust measurement data obtained with various noble gas propellants (argon, krypton and xenon) at different discharge current and $\dot{m}$ conditions [54-57]. The HC was tested in an open-diode configuration, with a single anode, circular in shape with a central orifice, mounted in front of it. The influence of HC and anode orifice diameter was explored as well. Thrust levels in the mN range, at values of specific impulse of several hundred seconds, make the HC microthruster an interesting candidate for many possible small-to-medium satellite missions.

The target, working as a Faraday plate, was also used to collect plume currents. The interpretation of these measurements is not completely clear [52]. However, they are also reported in this thesis.

Chapter 1

Literature Review

1.0 – Overview of HC Investigations

As generally pointed out [25, 58], the behaviour of HCs is complex and remains poorly understood, with no widely accepted theory explaining their high performance. While at the beginning experimental investigations aimed mainly at a broad understanding of the HC discharge characteristics [3, 4, 6, 8, 59-61], later on they tended to focus on some more specific aspects. Modelling efforts by different investigators have analysed the intricacies of the different physical mechanisms operating in the insert and orifice regions of a HC [5, 7, 9, 26, 39, 40, 58, 62-79]. Starting in the 1990s [73], numerical simulations have been undertaken. However, HCs have reached the present, rather advanced stage of development mainly through an extensive parametric experimental analysis, which has been ongoing since the late 1960s [3]. Since the body of literature existing on HCs in all their various incarnations and different applications is quite vast, while, on the other hand, no information is available on actual measurements of the thrust they can generate, with one notable exception [49], this review will focus on works that the author felt could be useful for an assessment of the HC capabilities as a stand-alone thruster. In particular, models and measurements of the HC interior conditions will be analysed, together with investigations of their high-energy ion emissions and, of course, estimates and measurements of the thrust they may be capable to produce.

1.1 – HC Discharge Physics

Most of the models discussed in Section 1.4 require for their application certain information concerning the physical conditions within and immediately outside the cathode. As well as propellant flow rates, voltages, currents, external wall and tip temperatures, which are relatively easy to measure accurately, other parameters of interest concern the plasma regions on both sides of and within the orifice. Owing to

the very small dimensions of these regions, very little experimental information is available and, as pointed out above, estimates are often necessary from sparse data.

Csiky was one of the first authors to describe the presence of different discharge modes during HC operation, and to use the terms spot and plume mode [3, 80, 81]. In later years, these terms have become synonymous with low-voltage, smooth HC operation, where only an intense luminous spot at the orifice was visible (hence the name, spot mode) and with higher-voltage, often noisy and oscillatory operation, where larger parts of the HC plume became luminous (hence the name, plume mode). Measurements performed by Csiky in a mercury HC plume did not show sharp plasma potential gradients either in the region between the HC tip and the anode. As he used very thin Langmuir probes, the reason in this case is probably the small number of experimental points and therefore the low resolution of his measurements along the symmetry axis.

Particular attention has been given by Fearn *et al.* to the characterization of the HC operation in various discharge conditions. Different discharge modes have been identified and mapped [12, 33, 45, 82-84]. Together with the "classic" spot and plume modes, a beam mode, where a luminous plume extends from the cathode, has been observed by Patterson and Fearn [33, 85] in open-diode configuration. The existence of these different modes has been clearly related to operation in diode configuration. Also, discharge oscillations, dominant in some regions, have been attributed to power supply operation [12, 83]. A general conclusion from years of investigations is that the presence of a keeper electrode, especially of an enclosed one, extends the regions of favourable operation, with little discharge noise and low, near-constant voltages, usually associated with spot-mode operation [12].

As summarized in Fig. 1.1, from Pottinger [86], spot mode generally occurs at high mass flow rates, high discharge currents and small HC to anode separations, and is associated with a low-voltage discharge. Conversely, plume mode generally occurs at low mass flow rates, low discharge currents and large HC to anode separations, and is associated with a high-voltage discharge. The transition between the two modes occurs rapidly if operating parameters such as mass flow rate and discharge current are varied and is accompanied by hysteresis, as shown in Fig. 1.1.

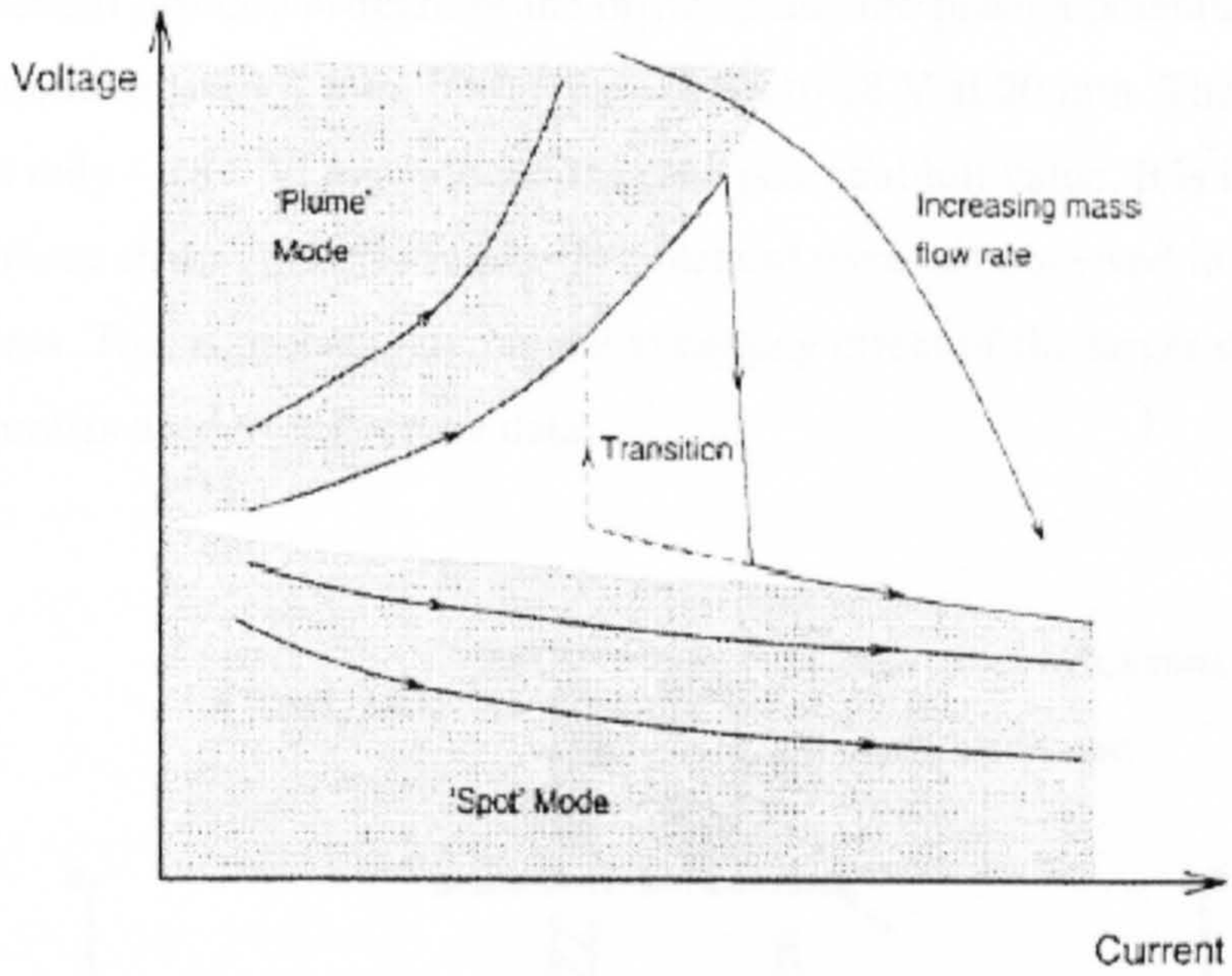

Figure 1.1 – Spot and plume modes, from [86].

Siegfried and Wilbur [60] used a vast array of instruments in an extensive investigation of mercury HC discharge phenomena. Of particular interest are their Langmuir probe measurements of the cathode internal plasma. Two probes were mounted upstream and downstream of the orifice, on the centreline of the assembly. These could be moved axially over a 0 to 25 mm distance from the orifice plate during HC operation. The electron temperature is essentially constant inside the cathode, varying between 0.5 and 0.8 eV, both in plume and spot mode. The electron density, instead, presents a very steep gradient in the direction of the orifice, increasing by more than three orders of magnitude from 15 mm to 5 mm upstream. Moreover, while the slope of the density vs. distance curves is approximately the same, the density is higher almost by an order of magnitude in spot mode than it is in plume mode. All this suggests that the plasma column does not extend far into the interior of the HC. The most striking difference in properties between the two discharge modes appears, however, when we examine the plasma potential profiles downstream of the HC orifice. While in spot mode the potential increases only from 11 to 12 V over a 20 mm distance, the potential profile in plume mode is completely different, as shown in Fig.1.2, where the electron temperature is also plotted. Here we notice very steep gradients in the potential, with the presence of a peak (the potential hill, or hump) just downstream of the keeper electrode. From a value of 12 V above

cathode potential just downstream of the orifice plate, the plasma potential climbs up to 30 V at approximately 7 mm, falling then down to 18 V at 20 mm. The discharge voltage was only ~ 18.5 V, much lower than the potential hill value. It is interesting to notice that these sharp gradients in plasma potential were not observed in other sets of measurements. This is probably due to the averaging effect of the larger diameter Langmuir probes used to collect the data.

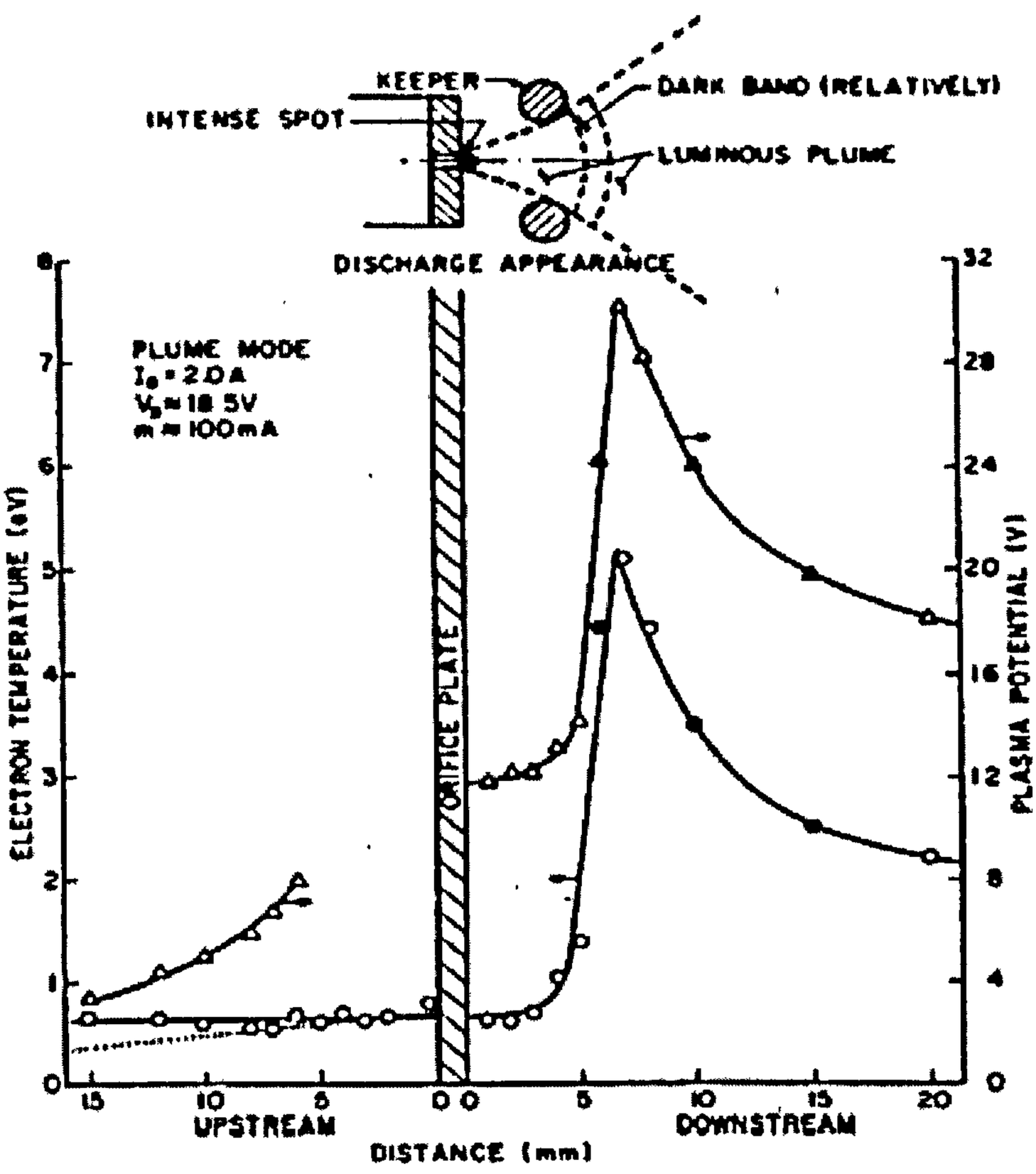

Figure 1.2 – The potential hill, or hump (plume mode), from [60].

The potential-hill (or hump) model was originally proposed by Friedly and Wilbur [29] to describe the generation of high-energy ions. It postulates the creation, in the plasma near the HC orifice, of a region at a positive potential in excess of keeper potential. This would arise due to positive space-charge build-up resulting from substantial ion production via collisional ionization by high-energy electrons. Presuming that the electrons gain kinetic energies significantly in excess of the ionisation energy of the gas atoms, then the secondary electrons produced by the

ionisation event would also tend to have substantial kinetic energies. These electrons would, therefore, tend to quickly escape from the region, leaving behind the less mobile ions that were a product of the ionisation. The height of the resulting potential hill would be limited by the net positive space-charge accumulation, eventually becoming sufficient to repel ions from the hill region as rapidly as they are created. If we assume that the ions suffer few collisions on leaving this region of higher potential and all have this same potential, then their energies will depend on their charge state. Thus, the potential hill model predicts that the ion velocities should increase with increasing charge $q = Ze$.

It was argued that this model was deficient because it predicts ions are created only near the crest of the hill and will, therefore, all have the same energy if they have the same charge. For singly-charged ions, for instance, this will be roughly equal to the difference between the peak and the downstream potentials. These deficiencies can be addressed, however, by introducing the effect of charge-exchange collisions between the high-energy ions created on the hill and the adjacent neutrals [87]. Such effect should be significant, because charge-exchange mean free paths are expected to be in the order of millimetres near the orifice, extremely small compared with the characteristic length (several centimetres) of the ambient plasma. The ions created at the crest of the potential hill undergo both acceleration and charge exchange as they fall through the potential gradient on the downstream side of the hill. The ions resulting from this process gain kinetic energy only as they fall down the rest of the potential hill, so they are detected with lower energies. Charge-exchange collision rates will increase with increasing neutral density, therefore producing more of these lower-energy ions and, also, a corresponding number of energetic neutrals. Scattering collisions occurring in the ambient plasma can also be significant. It is important to notice that this effect would not be observed in any model, like the MHD one, not involving the existence of a potential hill. In any such model, all low-energy ions created by charge-exchange collisions in the vicinity of the orifice would be drawn upstream into the HC by the adverse electric field. Low-energy secondary electrons, resulting from inelastic ionisation collisions, might have insufficient energy to escape the from the potential hill region. They could thus neutralize the positive ion space charge, unless they were removed as quickly as they are produced. Williams and

Wilbur suggested that their removal must be induced by elastic collisions with the streaming primary electrons [88].

In experiments with a cesium ion thruster a potential hump of 24 V was actually measured for an applied voltage of 20 V at a discharge current of 1.5 A [89]. This hump above anode potential followed closely the distribution of electron temperatures, which peaked at 4 eV. This was consistent with the fact that, to create a potential hump, electrons would need to be energetic enough to leave the region. Williams and Wilbur detected potential hill structures just downstream of the orifice in their investigations of HC-based plasma contactors [88, 90]. These structures did not present peak potential values in excess of applied voltages. However, the data were obtained using a floating emissive Langmuir probe. Such probes indicate potentials that fall progressively further below true plasma potential as they are moved into higher-density plasma regions [91]. As the plasma density is greatest at the orifice, the emissive probe probably indicates potentials that fall below actual values as the HC is approached. Hence, it is possible that the crest of the potential hill is actually higher, maybe even above discharge voltage.

The mechanism by which the high-energy ions arise has not been established, but two principal hypotheses have been previously put forward. One mechanism invokes the formation of a potential hill (or hump) a few mm downstream from the orifice [29], as described above in this Section. Although consistent with some of the data, no clear understanding had emerged of the means by which a hill of sufficient height could be formed. An alternative mechanism has been postulated whereby the current density at the orifice results in ion acceleration via a MHD effect [28, 33]. This mechanism is described below in this Section.

A third hypothesis concerning the formation of high-energy ions has been proposed for vacuum arc plasmas, where acceleration of ions also occurs in the direction away from the cathode and E/q can be much greater than the applied voltage. In this case a gas dynamic model is invoked that describes ion acceleration as driven by pressure gradients, through plasma expansion, and electron-ion friction, through collisions with the higher velocity electron flux [92, 93]. According to this approach, a small potential hump may exist as a consequence of plasma acceleration rather than as its

cause. In the gas dynamic model the ion energy distribution is independent of charge state: all the ions have the same velocity. A uniform flow of ions is established.

An extensive literature exists on the subject of emitted ion energies from vacuum arcs. The peak plasma densities are an order of magnitude or more higher than applies to HCs. A second distinguishing characteristic is that the gas supporting the discharge is driven out of the electrodes themselves.

Spatially-resolved experimental measurements of electric potential and ion velocities near a HC orifice have previously been performed [35]. A prominent potential hill was not found in either the Langmuir probe or LIF measurements. The measured velocity distribution near the HC test articles depended strongly on the cathode type and/or operating point, including plume-mode vs. spot-mode operation.

In the potential hill model, energy distributions will depend strongly on charge state ($E \sim qV$) and largely coincide when plotted vs. V_r ($V_r = E/q$). In contrast, the gas dynamic model predicts the kinetic energy distributions will be similar for all ions [92-94]. Available T5 and T6 cathode data imply that the kinetic energy distributions for Xe^+ and Xe^{2+} are similar. The potential hill model gives primary importance to plasma potential and electron temperature, whereas in the gas dynamic model the electron-ion friction term and ion-electron collision rates are critical. The simulation suggests that all of these parameters may contribute, however T_e dominates in the regime investigated.

Foster and Patterson presented a simple model providing a potential mechanism for the production of both energetic ions and neutrals [41]. This can happen through resonant collisions taking place inside the orifice channel. An ion, accelerated through the cathode sheath, will rebound from the surface as a low-energy neutral directed to the opposite cathode surface. Before reaching the sheath, it undergoes either a charge-exchange collision or an electron-impact ionisation event, becoming a low-energy ion still directed to the opposite surface. The particle is then accelerated again, only to rebound from the surface as a neutral once again. However, the resulting neutral is now slightly more energetic, as the incident neutral was more energetic because of its additional energy from the first impact. Repeated impacts of this nature, each time

with opposite sides of the channel wall, give rise to an energy accumulation process in which the particle can exit the cathode at considerable energies. This process will produce either an energetic neutral or an energetic ion, depending on whether the particle escapes out of the orifice before or after a charge-exchange collision can take place.

This energy-gain process depends on a number of length scales. If these do not satisfy certain conditions, the process will not be resonant and thus the fraction of energetic particles generated will not be appreciable. In particular, the cathode sheath thickness should be smaller than both electron-neutral ionisation and ion-neutral resonant charge-exchange mean free paths. These in turn should both be smaller than the HC orifice channel diameter, which should itself be smaller than the neutral-neutral collision mean free path. While the above conditions can be expected to be satisfied in the orifice at least for certain discharge conditions, this model still awaits experimental validation. Various data on charge-exchange cross sections for gases and operating regimes of interest are available in the literature [95].

Two possible mechanisms, the potential hill, described in this Section, and the orifice pinch, were suggested by Latham *et al.* for the production of the high-energy ions observed [28]. Together with the interaction between multiply and singly ionized species and the gas dynamic model, also described this Section, they remain, up to the present, the most valid, even if only qualitative, ideas suggested.

The orifice-pinch model, proposed by Latham *et al.* [28], postulates a MHD effect associated with current densities, in the orifice region, high enough to produce a pinching effect. The plasma would then be accelerated according to the equation

$$\rho \frac{D\vec{v}}{Dt} = \vec{j} \times \vec{B} - \nabla p , \qquad \textbf{(1.1)}$$

where ρ is the plasma mass density, v the flow velocity, j the current density, B the magnetic induction and p the plasma pressure. The plot of erosion against current density squared also suggests that a MHD effect might play some part in the acceleration process [28].

Jack, Patterson and Fearn [12] took measurements of the external plasma characteristics with a cylindrical Langmuir probe located 10 mm downstream of the keeper orifice in a HC-keeper-anode configuration essentially identical to that described above [33]. For a T5 HC, with anode currents below 1 A, the electron temperature T_e went above 4 eV and the electron number density n_e was of the order of 10^{11} cm^{-3}. For a T6 HC, T_e decreased with mass flow rate and increased with discharge current, reaching 5 eV for currents above 15 A, while n_e was of the order of 10^{12} cm^{-3}. The electrons were shown to have, to a good approximation, a Maxwellian distribution.

Rudwan at the University of Southampton investigated a T6 HC at discharge currents up to 5 A in diode configuration [15]. This particular cathode, designed for HET applications, had an enclosed keeper. Both breakdown and steady-state operation were investigated, and the operating characteristics were accurately related to discharge conditions and electrode geometry. Spectroscopic measurements, taken by looking into the orifice with an optical probe, give values for the plasma parameters in good agreement with those by Pottinger [57, 86, 96], when allowing for the differences in experimental configurations. An alternative anode current collection mechanism, based on the fact that the current collection capabilities of an electrode are dependent on its surface area, has been described by Rudwan [15]. An electrode that is positively charged with respect to the surrounding plasma will collect electrons in its vicinity that form a sheath. This electron sheath will act as a shield, therefore the field of the electrode will have no effect on the plasma beyond the outer edge of the sheath. As a consequence, the current collected by the anode depends on the rate of arrival of electrons to the outer edge of the sheath. If sufficient discharge current cannot be collected the anode potential increases to a point where ionisation may occur in the sheath by accelerating electrons interacting with the gas. This results in the breakdown of the sheath and the development of a luminous region characterised by a positive inner space of high ionisation surrounded by a layer of negative charge, referred to as a “double layer”. The outer edge of the double layer becomes the new collection area for electrons. This region of positive charge enveloped by electrons is known as the "virtual anode". When operating the HC with low discharge currents and mass flow rates, current collection is limited, the sheath breaks down and a virtual anode is formed with a larger area that is capable of collecting a greater current. The

discharge is then in plume mode. The spot mode occurs for passive current collection. This theory is in agreement with plasma potential and electron number density profiles obtained from Langmuir probe experiments [64]. The presence of anode noise is said to be due to the impingement of the double layer into the keeper/HC space causing perturbations and interfering with electron emission. To date Rudwan's is the most complete explanation of mode change characteristics and the associated physical phenomena. However, as pointed out by Pottinger [86] and others, this theory only provides a qualitative analysis. Mode change may be influenced by factors other than external electrode geometry. The orifice geometry, i.e., aspect ratio and contouring, has been shown to affect changes from spot to plume mode and these factors must be incorporated into the theory of mode change characteristics.

Edwards at the University of Southampton investigated a UK-25 HC in full ion thruster discharge configuration, although without any beam extraction [97, 98]. Voltage-current characteristics and Langmuir probe measurements were obtained in the various discharge regions, operating on propellants other than xenon and at points away from optimal.

Monterde, *et al.*, took measurements of the external plasma of a HC of the type designed for the UK-25 ion thruster, operating in a diode configuration, with an open keeper and an anode plate [99]. The plasma region between the keeper and the anode electrodes was investigated with a single Langmuir probe. Again, it was shown that the electrons have a Maxwellian distribution. Detailed scans gave a T_e between 0.3 and 0.4 eV, while n_e was of the order of 10^{11} cm^{-3}. These order-of-magnitude differences with respect to the results reported above [12] can be explained by the much higher mass flow rate employed. For example, at 10 A anode discharge current, ~4.5 mg/s [17] versus ~1 mg/s [12].

Using a monochromator and a photomultiplier, emission spectroscopic methods allowed Malik, Monterde and Haines [17, 18] to obtain measurements of the electron temperature and density of the internal plasma of a HC. The cathode type and discharge configuration were the same as above [99]. For a discharge current of 5-10 A and a mass flow rate of 2-5 mg/s, the estimated values of T_e and n_e are ~1 eV and of the order of 10^{14} cm^{-3} respectively. Therefore, the HC internal plasma does not satisfy

either the conditions (McWhirter) for local thermodynamic equilibrium (LTE) or for the coronal model (Bates) and the coronal-radiative model appears to be a more realistic representation [17]. Numerous discrete emission lines associated with Xe, Xe^+ and Xe^{2+} were observed in the recorded emission spectra. However, Xe^+ dominates. This is consistent with computer simulations performed by the same authors, for $T_e \sim 1$ eV. The results mentioned above are substantially confirmed by the analysis described in [18]. Here, the electron temperature is assessed using the intensity ratio in the bremsstrahlung continuum. This gives an average value of T_e = 1.1 eV, which can be used in conjunction with the Saha equation for the different ionisation stages to obtain a value for the electron density $n_e \sim 10^{14}$ cm^{-3}. This is only an approximation, as the Saha equation is strictly valid for LTE model, and this is not satisfied in the present case [18].

A modified T6 HC, originally designed by Rudwan [15] and built at QinetiQ, was used by Pottinger at the University of Southampton to take optical measurements of the cathode internal plasma. This cathode had the redundant heater coil removed, in order to allow for the drilling of holes along the axis of the HC body. In conjunction with special optical probes, developed by Rudwan [15], consisting of a sapphire fibre surrounded by a tantalum tube, these holes allow axially-resolved measurements of the HC internal plasma emissions. From these, the variation of plasma density and temperature, as well as the HC insert temperature, along the axis can be calculated. Values of interior plasma parameters and insert temperature were obtained in good agreement with previous results, demonstrating, among other things, that the insert temperature is strongly dependent on discharge current [57, 86, 96]. By recording plasma emission spectra at two different positions along the HC axis, it was noticed that intensities seem to drop sharply within a few diameter distance from the cathode tip [100]. This would confirm that, as is generally believed, the plasma does not penetrate deeply into the cathode cavity, and explain the good success of models, like Siegfried and Wilbur's one [15, 62, 64], based on the concept of an idealized "active zone" or "ion production region".

1.2 – Thrust Measurements of a Mercury HC Discharge

Snyder and Banks at NASA Lewis Research Center (now NASA Glenn) performed the only actual thrust measurements of a HC discharge previously reported in the literature, using a synthetic mica target on a torsion pendulum [49]. The cathode they used, operating with mercury, was a device quite different from our T6 HC. It consisted of a 3.2-mm diameter tantalum tube with a barium carbonate coated insert and had a 0.25-mm diameter orifice in the thoriated tungsten tip. The tantalum ring keeper was enclosed inside a ceramic tube. An additional electrode was placed downstream of the keeper to investigate the effects of accelerating ions and/or electrons on the measured thrust. This accelerator electrode consisted of a tantalum ribbon and could be biased positive or negative with respect to the cathode tip. The mercury flow rate was controlled by a porous tungsten vaporizer. Cathode tip temperature was measured with an optical pyrometer by looking through the plasma and assuming the surface of the tip to be a black body.

The measured thrust decreased with target angle and increased with tip temperature, flow rate, keeper discharge power and accelerator potential. For a tip temperature of 1110 K, an Aeq flow rate of 47 mA and a target angle of 10°, the measured thrust was between 26 μN (corrected for specular reflection from the target) and 52 μN (uncorrected value) for no keeper discharge. These values were in approximate agreement with theoretical values based on the thrust generated from only the neutral gas flow. In particular, the thrust was assumed to be proportional to the mass flow rate multiplied by the mean thermal speed, calculated with the tip temperature value. Using the coldest tip temperature as a starting point for comparison, the theoretically expected square-root variation was verified to within ~4%. The uncorrected measured values overestimate theoretical predictions, but the specular correction reflection (1/2) appears excessive. Values closer to the theoretically expected ones are obtained by applying a diffuse reflection correction (2/3). When the keeper discharge was turned on, the thrust increased at a decreasing rate with increasing discharge power, for a fixed mass flow rate. With the same tip temperature, flow rate and target angle, but with a keeper discharge current of 0.75 A at 19 V, the thrust increased by 28%. Additional thrust was obtained when positive accelerator voltages were applied (~5%

increase with +60 V), but not when the accelerator voltages were negative. As the positive accelerator voltages resulted in additional discharge power, while the negative ones did not (accelerator current was negligible for negative voltages), these measurements are consistent with the interpretation that the thrust is the result of a thermal acceleration/expansion of the gas, with additional power resulting in added heating of the gas.

1.3 – Ion Emission Measurements

Since the end of the 1980s [101] some investigators have observed that, under certain conditions, significant high-energy ion emissions may occur from a HC. Reasonably high fluxes of ions have been measured, even at energies greater than any applied voltage [25, 26, 28-42]. Such energies are sufficient to induce substantial sputter erosion rates, especially of the baffle disc in the Kaufman-type gridded ion thrusters [28, 29, 101]. This was the main initial concern fostering this kind of investigation. Various experimental results [25, 26, 28-34, 36-42] have shown that relatively high directed ion energies can be generated in the plasma emerging from the orifice of a HC, and several authors have suggested [25, 26, 67, 102] that it should be possible to obtain significant ion fluxes from HCs, especially if the efficiency of ion extraction is improved. These experiments were undertaken under widely different conditions, in particular with respect to measurement techniques employed and discharge configurations adopted, so a direct comparison of the results obtained is not necessarily valid.

Experiments carried out at Colorado State University have consistently employed a cylindrical-anode configuration. This was chosen in order to simulate typical HC operation within the main discharge chambers used in gridded ion propulsion systems. The keeper was a toroidal ring constructed from tantalum wire, positioned 1.0 mm downstream of the HC orifice in an open configuration. The HCs were constructed from tantalum tubes, with thoriated tungsten orifice plates. Various orifice diameters were used. By checking the bore before and after experimental sessions, it was observed that significant orifice enlargement by erosion occurred only for discharge currents in excess of 20 A. As regards instrumentation, Friedly and Wilbur [29] used a

retarding potential analyzer (RPA) for their experiments, whereas Kameyama and Wilbur [30, 36] employed an electrostatic energy analyzer (ESA).

In all the experiments mentioned above, ion energies were measured well above the potential differences available between electrode surfaces for their acceleration. Ion currents and mean energies both increased with increasing discharge current. Friedly and Wilbur observed also an increase in ion energies with decreasing $\dot{m}$ and an increase in their energy spread with increasing discharge current [29].

Farnell, Williams and Wilbur [42] performed experiments operating a HC in a simulated discharge chamber environment. The HC orifice had a 0.55 mm diameter. The enclosed keeper had a 2.54 mm diameter orifice positioned about 0.5 mm downstream of the cathode orifice plate. Ion energy distributions were recorded with an ESA. In agreement with previous studies of freestanding HC experiments, ion energies were found to increase as flow rate was decreased and discharge current was increased. In conflict with previous measurements [36, 39], though, no high-energy ion signals were recorded at small zenith angles, when the ESA was pointed at the cathode orifice. Instead, substantial high-energy ion currents were observed at large zenith angles under all operating conditions, except those where no high-energy ion signal was measured at any zenith angle. Farnell *et al.* believe that high-energy ions were not seen because the tests were conducted within a simulated discharge chamber environment [42], as opposed to a keeper-only or diode configuration, with no magnetic fields applied, as in previous experiments [36, 39].

A number of HCs have been developed at NASA GRC for a variety of electric propulsion applications, with emission current requirements ranging from 100 mA to 100 A [103]. Recent efforts have included testing [37, 38, 41] and modelling [70].

A laboratory model hollow cathode micro-thruster (HCMT) was fabricated and tested by Patterson and Foster [27]. It was based on one of the small (3.2 mm diameter) HCs developed at NASA GRC [103, 104]. Two Faraday probes of different diameters (1.5 mm and 3.2 mm), biased –25 V with respect to facility ground to repel plasma electrons, were used in the investigation. The ion beam current was calculated through integration of the profiles acquired by sweeping the probes across the beam.

The discharge was operated initially without the ion optics. The total ion current was found to increase with increasing $\dot{m}$, at a given discharge current, and with increasing discharge current, at a given $\dot{m}$. The maximum ionisation fraction (~ 0.5), though, occurred at the combination of highest discharge current (2 A) and lowest xenon $\dot{m}$ (~ 0.05 mg/s). The ionisation fraction is defined here as the ratio of collected ion current to the equivalent current of fully singly-ionized xenon. This latter is

$$J_{eq} = \frac{\dot{m}}{m_{Xe}} e, \tag{1.2}$$

where $\dot{m}$ is the mass flow rate, m_{Xe} the atomic mass of xenon and e the electron charge. The HCMT was then operated with a screen grid and an accelerator grid, biased at voltages ranging from about –150 V to –180 V. With beam extraction, the magnitude of the ion beam current was considerably lower, with the ionisation fraction never exceeding 0.14. This reduction in ion current is probably associated with ion recombination losses and direct impingement on the ion optics assembly. This would need modifications in order to improve the ion transparency.

Williams and Kovaleski [37] measured the electron number densities downstream of the orifice of a HC using laser deflection interferometry (LDI). The calculated electron density profiles appear to correlate with previous measurements of near-field HC phenomena, namely ion velocities and cathode erosion, which detected doubly-charged xenon ions and energetic back-flowing ions in the plume of ion thrusters. In these full-thruster configurations, however, large amounts of ions were generated by the interaction of the HC with the main xenon flow [105, 106].

Foster and Patterson investigated the ion energy distributions from a high-current HC in an NSTAR-type ring cusp discharge chamber [38, 41]. They used a combination of Langmuir probes, ESA and emission spectroscopy to characterize the plasma downstream of the HC. While the majority of the ions have energies close to the discharge voltage, the distribution functions are quite broad, presenting tails with energies in excess of such voltage. These high-energy tails tend to grow with increasing discharge current. Additionally, evidence provided by the Langmuir probes

suggests the existence of a double layer essentially separating the HC plasma column from the main discharge.

Williams *et al.* at the University of Michigan [32, 35] also employed a cylindrical anode, in order to approximate the conditions around the discharge HC of an ion thruster. They took their measurements with laser induced fluorescence (LIF) techniques and a Langmuir probe. The "AR3" HC [104] was tested with a keeper plate located 4.0 mm downstream of the HC orifice. This open-keeper configuration permitted very fine spatial resolution to be achieved using LIF in the cathode-to-keeper gap. A prototype space station contactor with an enclosed keeper was also used. The keeper-to-cathode gap was 2 mm. Experiments were also performed in a keeper-only discharge configuration.

The HCs used in the experiments at the University of Michigan were provided by the NASA GRC. Under an agreement with GRC the dimensions of the cathode orifices and details of their chamfering were not published [32, 35]. This makes it difficult to compare their results with those obtained using different devices.

High-energy xenon ions were detected, which were consistent with the potential-hill model of high-energy ion production [29]. This was especially true for plume-mode operation, even though no peaks were detected with the Langmuir probe [35].

LIF measurements were also taken in a full ion thruster configuration. Back-flowing ions were identified with energies potentially sufficient to generate the levels of observed HC erosion [105].

Crofton at The Aerospace Corporation took measurements with an RPA and a quadrupole mass spectrometer (QMS) using a keeper electrode just downstream of the HC in an enclosed configuration. A Langmuir probe was also used in some instances to measure plasma potential and electron temperature [39].

Experiments were performed with a T5 HC and a 3.0-mm-diameter aperture keeper [25, 26, 31, 34, 39] and, more recently, with a T6 HC and a 5.0-mm-diameter aperture keeper [40]. These experiments are extremely relevant to the present discussion,

because they were performed with a single anode (actually, a keeper electrode), therefore in a configuration similar to the open-diode one adopted in the present experiments.

The data acquired from this work suggested that the degree of ionisation in the plasma plume emitted by a HC might be very much higher than previously assumed by many investigators. Actually, results obtained as far back as the 1970s had indicated that plasmas in HCs utilizing an alkali metal to lower the insert work function could approach full ionization, at least in the orifice region [60, 107].

The first HC used by Crofton was originally designed for use with xenon as the main cathode in the UK-10 ion engine. An engineering model of this thruster, designated T5, has been well characterized by the same author [108]. Measurements with the RPA and the QMS were taken at different angular positions with respect to the cathode axis ($\phi = 0°$) and at different operating points. An interesting observation that can be made, especially relevant to the evaluation of the obtainable thrust, concerns the divergence of the ion beam. The angular dependence of the ion current at three operating points (OPs) is shown in Figure 1.3 [26, 39].

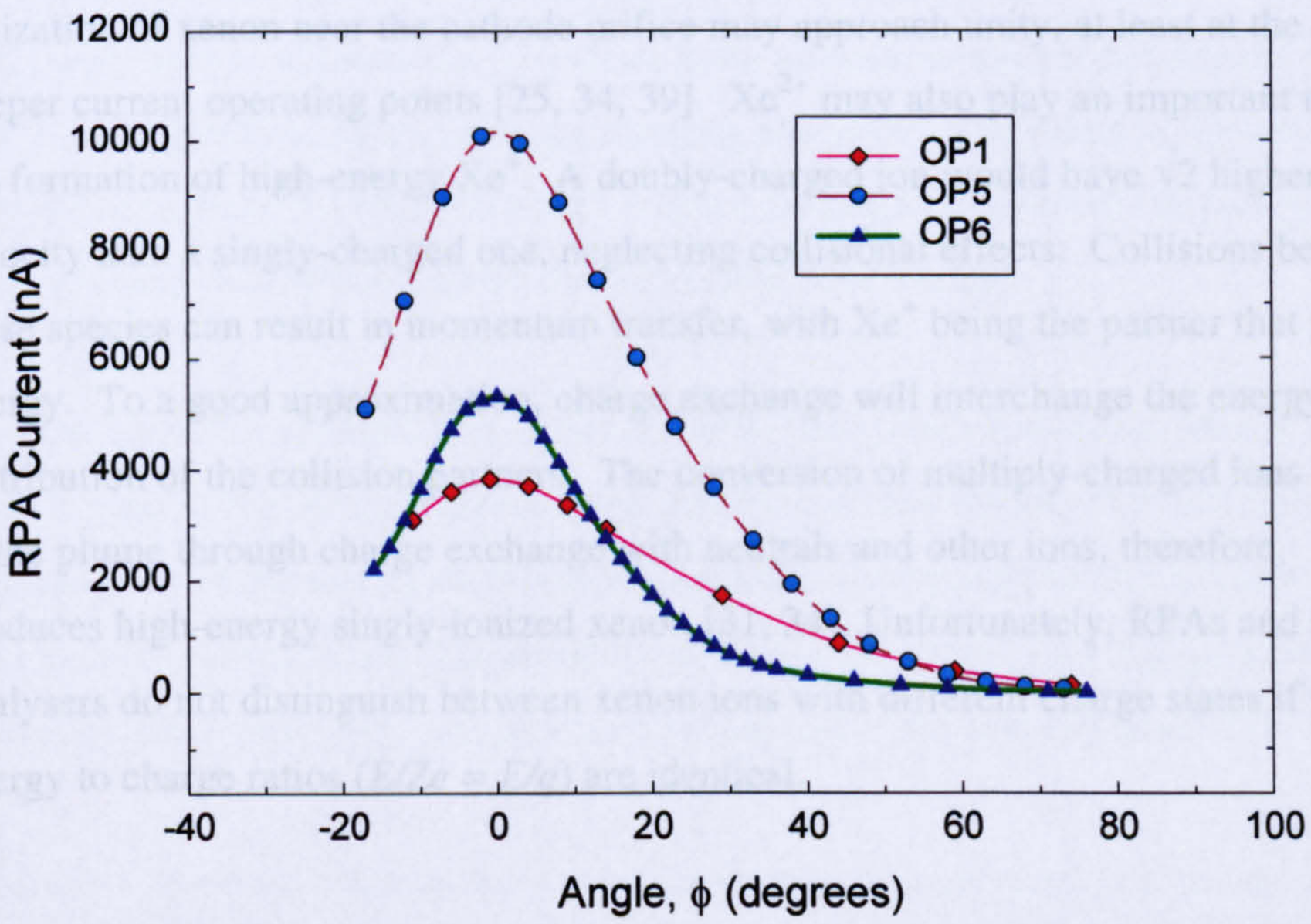

Figure 1.3 – Angular distribution of ion efflux (Aerospace Corp. data) [26, 39].

OP 5, at a low mass flow rate ($\dot{m}$ = 0.045 mg/s) corresponds to a higher peak and a lower full-width-half-maximum (FWHM) than those measured at OP 1, with a $\dot{m}$ of 0.1 mg/s.

Visual observation indicated a more extended plume, about 3 cm long, at OP 5. Penetration and divergence of the jet are therefore pressure dependent. It would be interesting to perform similar experiments in a facility with a pumping system capable of handling different propellant $\dot{m}$ values while keeping the background pressure sensibly constant. In Crofton's experiments, an increase in $\dot{m}$ from 0.045 mg/s (OP 5) to 0.1 mg/s (OP 1) caused an increase in test chamber pressure from 6.8×10^{-6} Torr to 1.4×10^{-5} Torr. The influence of the background pressure might therefore conceal any possible effect of the varying $\dot{m}$ on the plume structure, as well as any effect of the keeper potential and current (34 V, 1.30 A and 26 V, 1.12 A respectively at OPs 5 and 1). Also shown is data for a medium-flow (0.054 mg/s) case, with a higher keeper current of 1.77 A (OP 6). Here the divergence is lowest despite a keeper potential of just 28 V, consistent with the possible operation of a $\vec{j} \times \vec{B}$ pinch effect.

RPA measurements show relatively large amounts of ions with energies higher than the keeper voltage. Such ions are more energetic at small ϕ [25]. QMS measurements indicate the presence of a high level of plume Xe^{2+}. This suggests that the fractional ionization of xenon near the cathode orifice may approach unity, at least at the higher keeper current operating points [25, 34, 39]. Xe^{2+} may also play an important role in the formation of high-energy Xe^{+}. A doubly-charged ion would have $\sqrt{2}$ higher velocity than a singly-charged one, neglecting collisional effects. Collisions between these species can result in momentum transfer, with Xe^{+} being the partner that gains energy. To a good approximation, charge exchange will interchange the energy distribution of the collision partners. The conversion of multiply-charged ions to Xe^{+} in the plume through charge exchange with neutrals and other ions, therefore, produces high-energy singly-ionized xenon [31, 34]. Unfortunately, RPAs and energy analysers do not distinguish between xenon ions with different charge states if their energy to charge ratios ($E/Ze = E/q$) are identical.

As an example of these processes, King and Gallimore [109-112] and Gulczinski and Gallimore [113] suggest that these two mechanisms, momentum-exchange and charge-exchange collisions, may be acting in the plume of HETs (SPT-100 and P5, respectively). Even at modest density levels and Xe^{2+} : Xe^{+} ratios (~12% in the SPT-100 [109]) a high energy "tail" in the ion energy distribution function is produced, due to ions having energies greater than the potential applied to the thruster discharge. Even if the T5 HC approaches full ionization at the higher levels of orifice current density [25, 34, 39], the propellant mass utilization does not, in general, exceed 10% [25]. This latter parameter is defined as the ratio of extracted ion current over the equivalent current of 100% singly-ionized xenon. Such a discrepancy is probably caused by the fact that most ions are neutralized before they can escape through the keeper orifice [25]. Inside the cathode, and even more so in the expanding plume, the electron temperature T_e is much lower than the first ionization potential for xenon (12.13 eV). Recombination is thus bound to be significant [114].

The characterization data support the hypothesis of full ionization near the orifice at operating points involving high keeper current and low flow rate. On the other hand, the propellant mass utilization is far from 100%. Substantial current levels were observed without an attempt to improve the efficiency of ion extraction. The preliminary use of a biased extraction electrode produced a modest enhancement of the emitted ion flux on centreline [26]. In previous experiments Semenov and Batuev [102] were able to improve the propellant mass utilization, even if not beyond 10% still, in an argon flow by using an accelerating electrode. Their device, however, was very different from the HCs intended for space propulsion, especially in presenting a very wide aperture through which the ions could be extracted.

Simulations with combined particle-in-cell (PIC) and direct simulation Monte Carlo (DSMC) methods produced encouraging results, reproducing the experimental ion flux and peak of the energy distribution. The main discrepancy relates to the width of the ion energy distribution. The model predicts the existence of a small potential hill in the cathode-keeper gap, and plasma potential above the keeper voltage [26, 39].

Previously proposed mechanisms for the production of high velocity ions, like z-pinch and potential hill models, may be unable in themselves to explain the emitted ion

energy distribution in detail. All of these models predict the existence of a potential hill, established by some means, but its height is insufficient to account for the ions of highest energy. Other mechanisms, particularly charge transfer, ion-neutral scattering, and electron recombination of multiply charged ions need to be closely examined for their applicability to the problem [26]. More recent results [39] provide support for a potential-hill model of ion acceleration, but the presence of multiple peaks implies a level of complexity not previously anticipated. The operation of other proposed mechanisms, involving magnetohydrodynamic (MHD), gas dynamic and rapid charge-conversion effects was not apparent.

Recent measurements by Crofton [40] are even more interesting, because they were performed with a T6 HC, essentially identical to the one used in the experiments described in this thesis, but for the fact of having an enclosed keeper. From the results shown in Figure 1.4 it is evident that the collected current increases with increasing discharge current and decreasing mass flow rate. OP 2 ($\dot{m}$ = 0.125 mg/s, keeper current I_{ck} = 4.0 A and keeper voltage V_{ck} = 26.3 V) shows an RPA profile with the highest collected current at retarding potential (or repeller voltage) V_r = 0 and a much longer tail than in other cases.

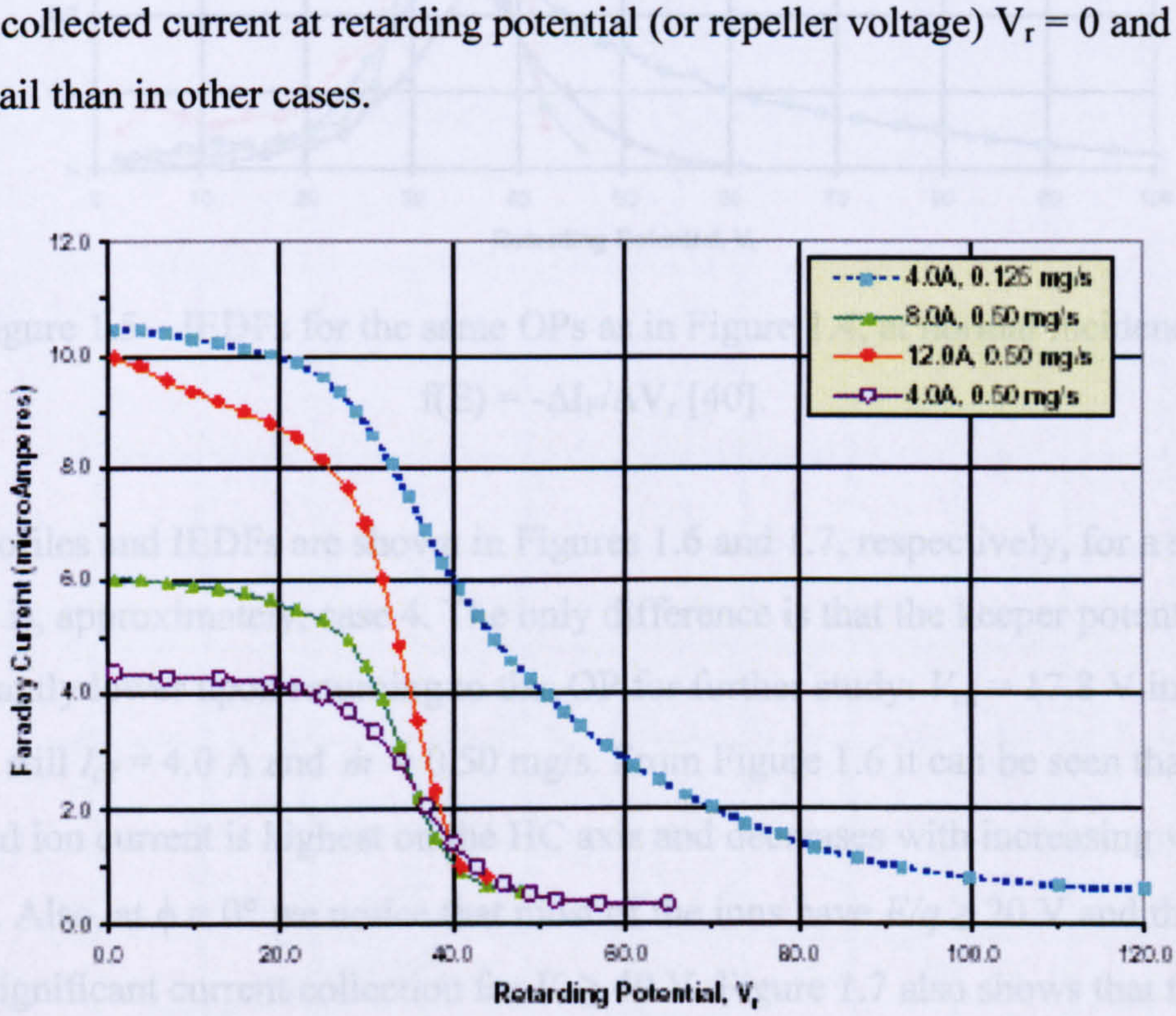

Figure 1.4 – RPA current as a function of repeller voltage at various OPs, at normal incidence [40].

This means that at OP 2 a greater number of positive ions are collected, and also that a substantial amount of these have high energies. While at the other OPs virtually no ions are present with *E/q* higher than 50 V, at OP 2 a significant number with *E/q* exceeding 100 V are seen. This is confirmed by inspection of the Ion Energy Distribution Functions (IEDFs) shown in Figure 1.5 for the same OPs as in Figure 1.4. We can see that, while for all OPs the IEDFs peak at $V_r \sim 35$ V, the curve for OP 2 is considerably broader than the others, with a higher FWHM and a long tail, showing the presence of high-energy ions still at $V_r = 100$ V.

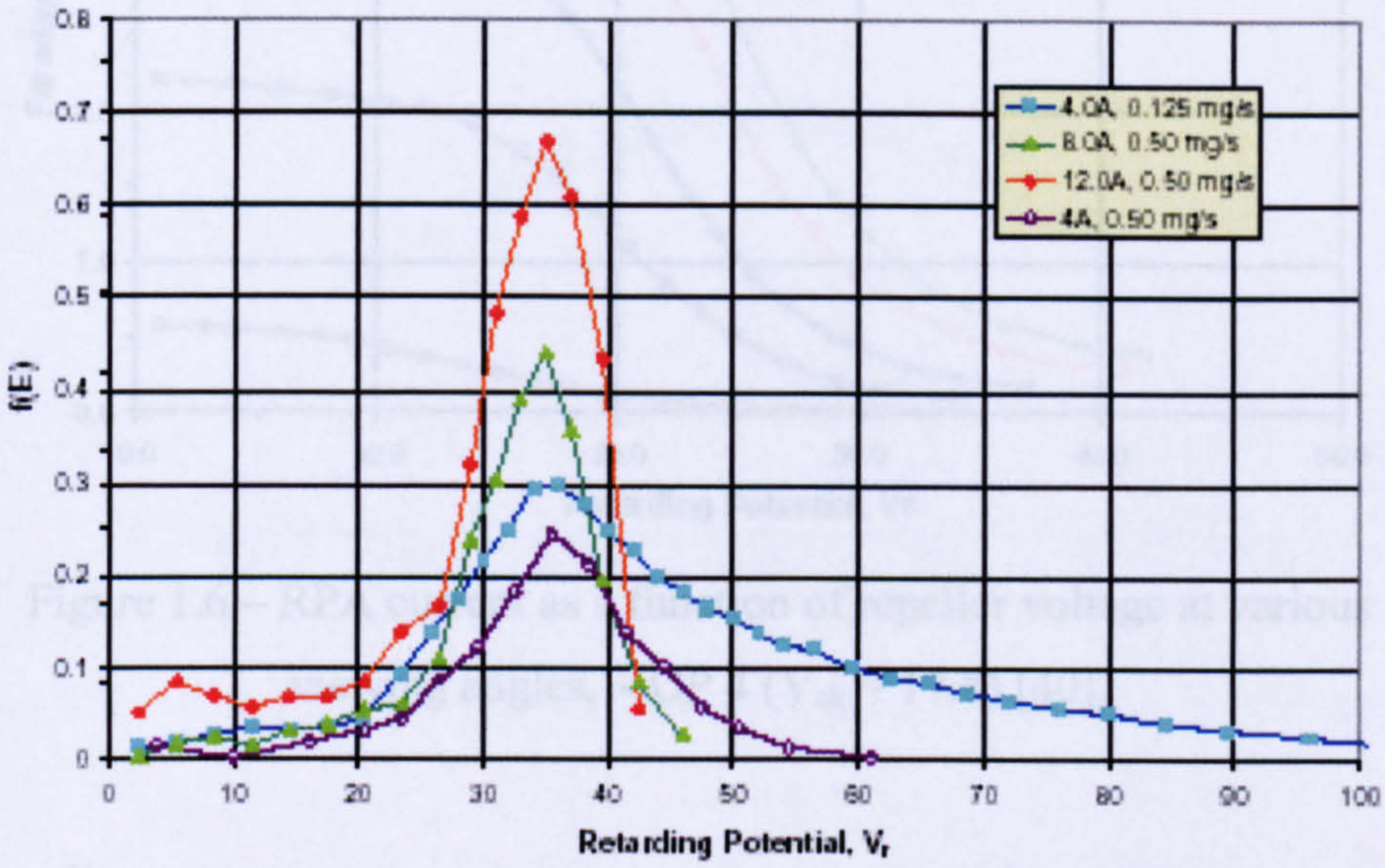

Figure 1.5 – IEDFs for the same OPs as in Figure 1.4, at normal incidence; $f(E) = -\Delta I_F/\Delta V_r$ [40].

RPA profiles and IEDFs are shown in Figures 1.6 and 1.7, respectively, for a single OP that is, approximately, case 4. The only difference is that the keeper potential was significantly lower upon returning to this OP for further study: $V_{ck} = 17.8$ V instead of 20.4 V, still $I_{ck} = 4.0$ A and $\dot{m} = 0.50$ mg/s. From Figure 1.6 it can be seen that the collected ion current is highest on the HC axis and decreases with increasing viewing angle ϕ. Also, at $\phi = 0°$ we notice that most of the ions have $E/q \geq 20$ V and that there is still significant current collection for $V_r \geq 40$ V. Figure 1.7 also shows that the on-axis ions are the most energetic, with an IEDF peaking at the highest value of V_r and extending beyond $V_r = 40$ V. We notice not only the presence of high-energy ion tails

in the RPA traces and IEDFs but also, and especially, that most of the ions have *E/q* values above the keeper potential, at least for $\phi \leq 45°$.

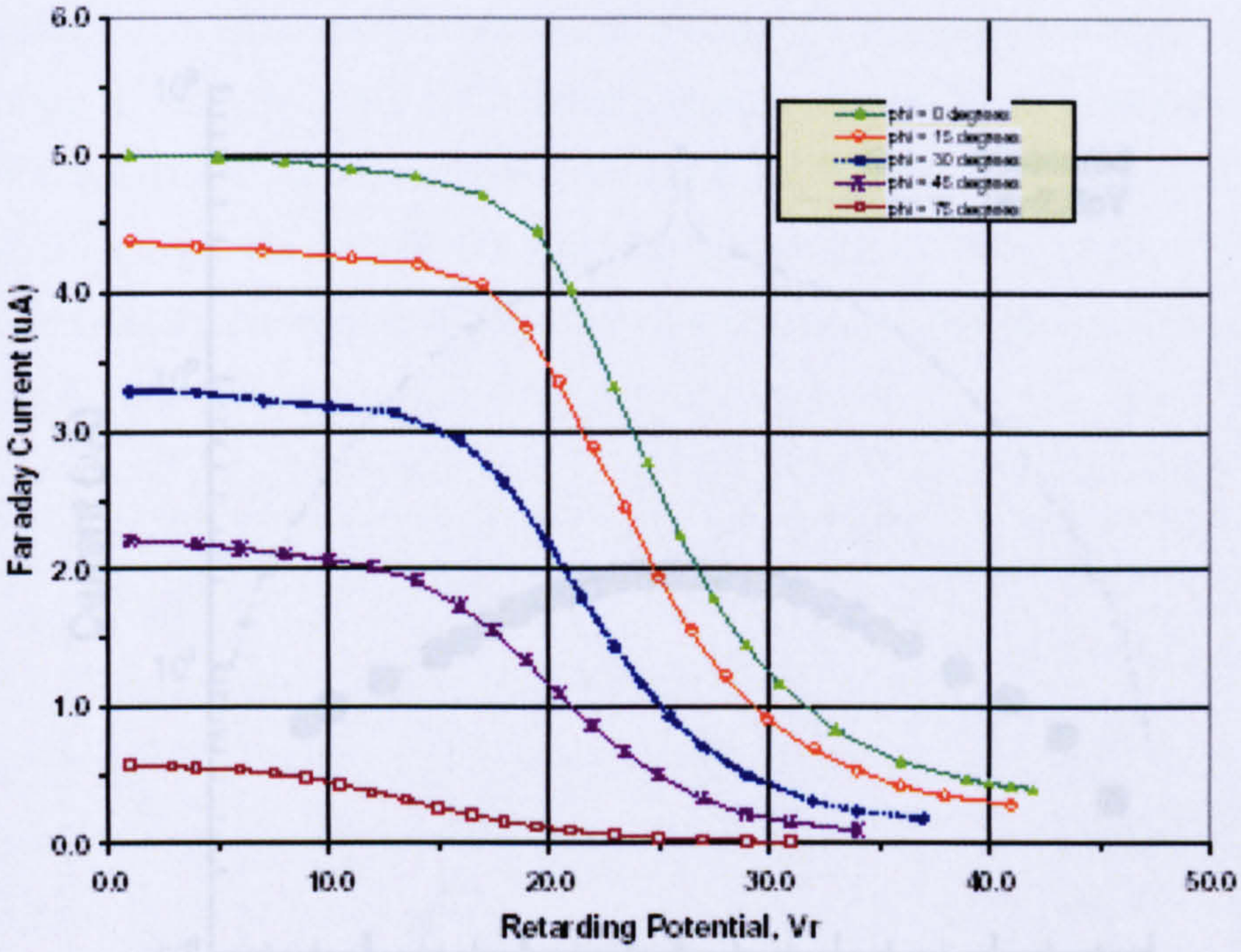

Figure 1.6 – RPA current as a function of repeller voltage at various viewing angles, ~ OP 4 (V_{ck} = 17.8) [40].

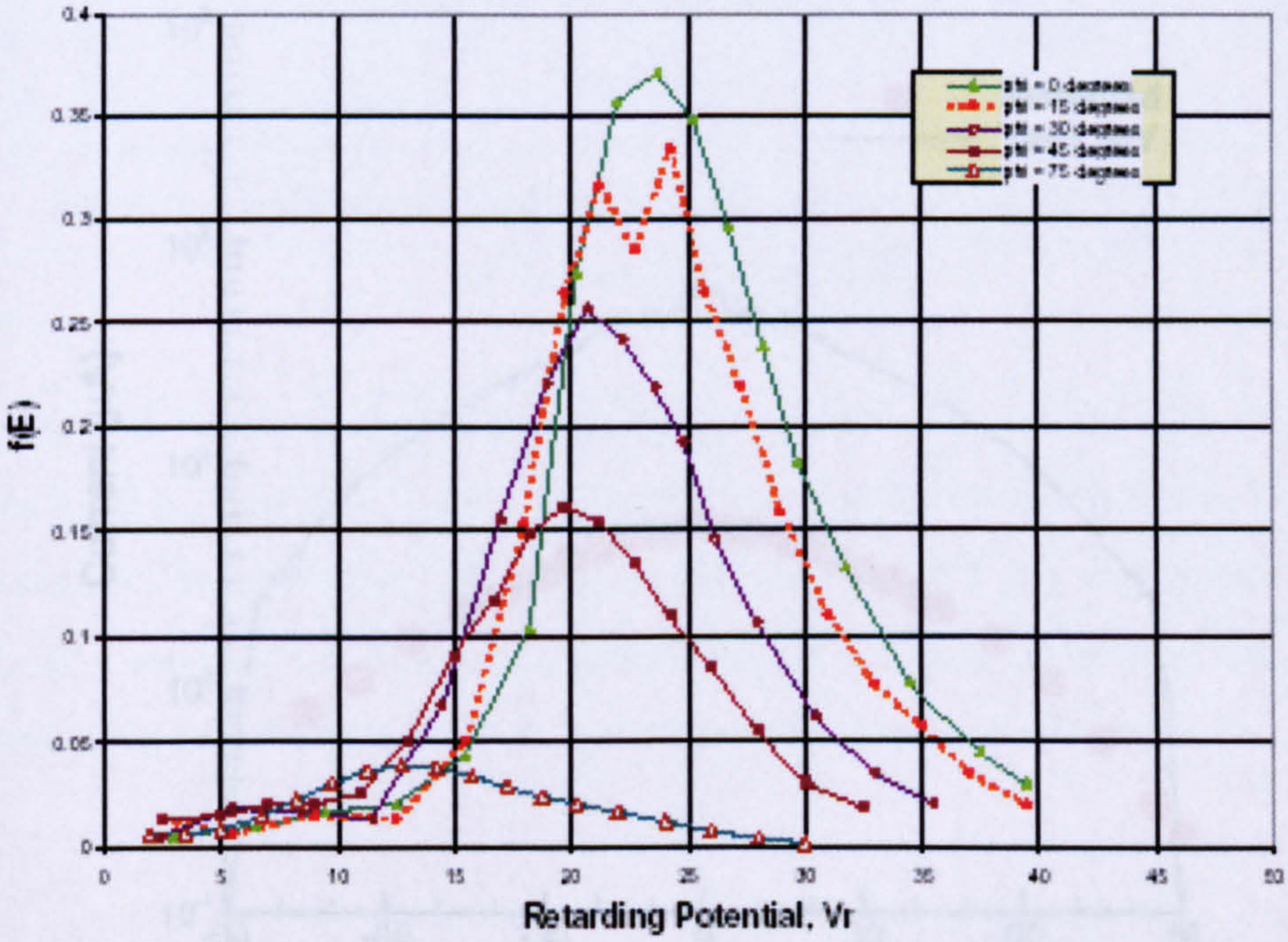

Figure 1.7 – IEDFs at various RPA viewing angles, ~ OP 4 (V_{ck} = 17.8); $f(E) = -\Delta I_F/\Delta V_r$ [40].

Finally, comparisons of measured angular emission profiles with PIC-DSMC simulation results, shown in Figures 1.8 and 1.9, reveal order of magnitude discrepancies, with the simulations over-predicting the emission flux.

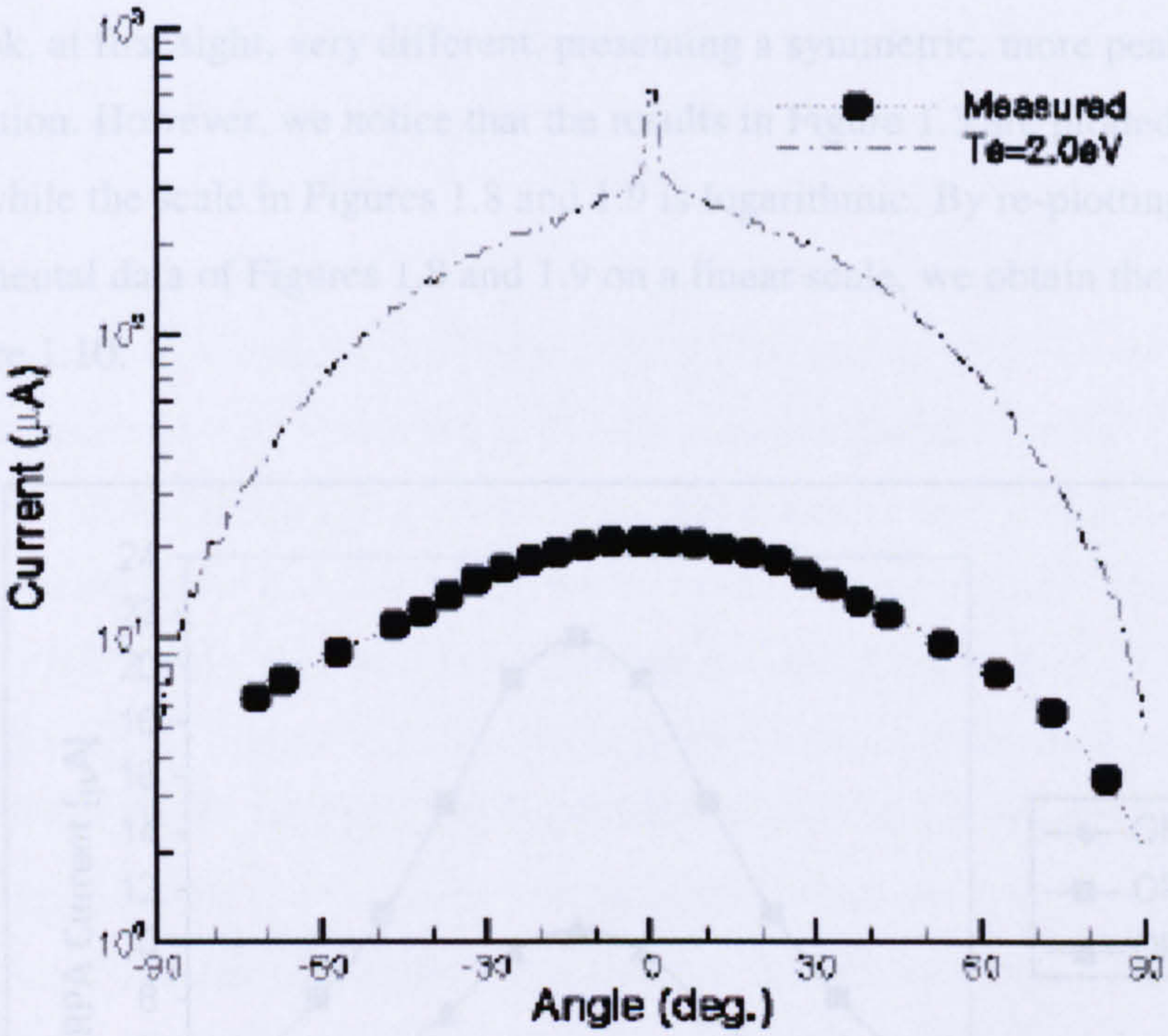

Figure 1.8 – Angular ion emission profiles at the RPA position for OP 10 [40].

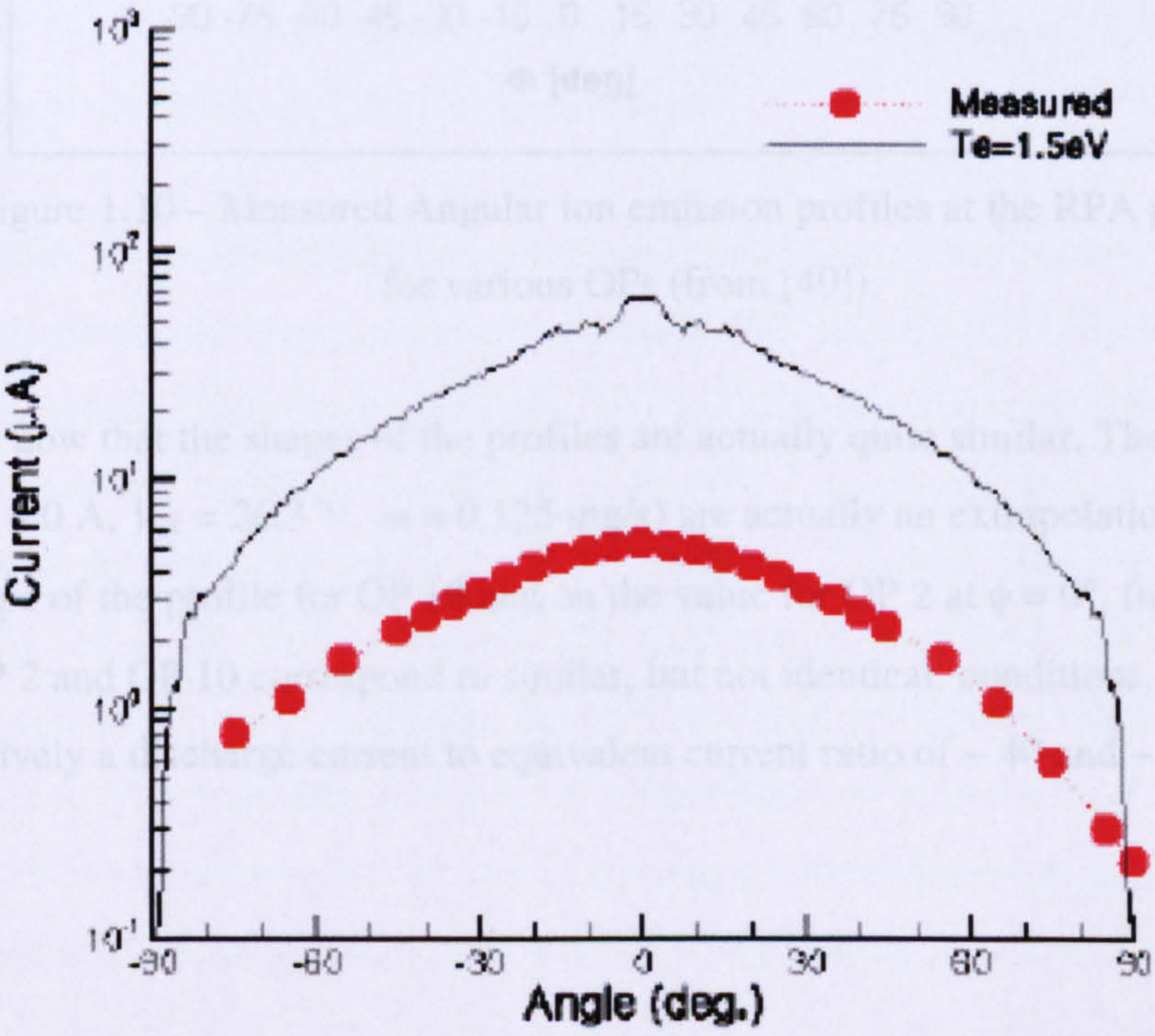

Figure 1.9 – Angular ion emission profiles at the RPA position for OP 4 [40].

The experimental profile for OP 10 (I_{ck} = 20.0 A, V_{ck} = 14.0 V, $\dot{m}$ = 1.08 mg/s) is obviously flatter than its theoretical counterpart (Figure 1.8). The shapes of the profiles compare better for OP 4 (Figure 1.9), where a lower value of electron temperature T_e was assumed as a parameter in the simulations (1.5 eV instead of 2.0 eV). The shapes of the profiles measured with the T5 HC, shown in Figure 1.3 [26, 39], look, at first sight, very different, presenting a symmetric, more peaked distribution. However, we notice that the results in Figure 1.3 are plotted on a linear scale, while the scale in Figures 1.8 and 1.9 is logarithmic. By re-plotting the experimental data of Figures 1.8 and 1.9 on a linear scale, we obtain the graph shown in Figure 1.10.

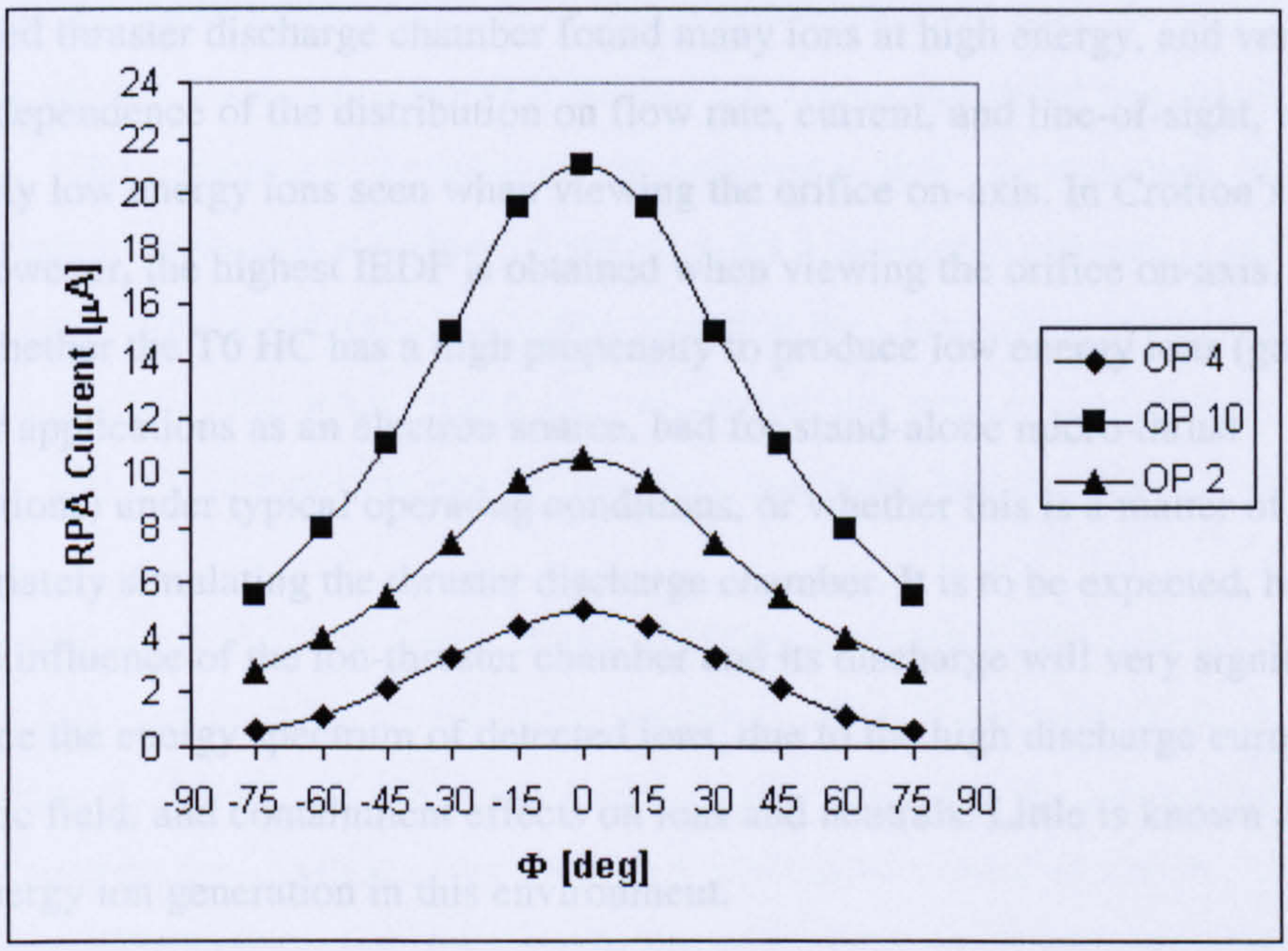

Figure 1.10 – Measured Angular ion emission profiles at the RPA position for various OPs (from [40]).

We see now that the shapes of the profiles are actually quite similar. The data for OP 2 (I_{ck} = 4.0 A, V_{ck} = 26.3 V, $\dot{m}$ = 0.125 mg/s) are actually an extrapolation, based on the shape of the profile for OP 10 and on the value for OP 2 at $\phi = 0°$, from Figure 1.4. OP 2 and OP 10 correspond to similar, but not identical, conditions, having respectively a discharge current to equivalent current ratio of ~ 40 and ~ 25.

The only parameter adjusted in the T6 simulations was T_e. The T5 simulations also showed that T_e was one of the parameters that exerted the most influence on the results. The simulation is also sensitive to assumptions concerning plasma potential distribution near the keeper aperture. While further parameter adjustments may improve the agreement between simulation and experiment, additional probe data in the orifice-keeper region is clearly needed to determine the correct parameters in this critical region and to establish definitive boundary conditions.

The IEDF peaks appeared at quite low energy in this study, similar to a previous result obtained by Patterson and Fearn with the T6 cathode [33]. Recent electrostatic analyzer measurements by Farnell *et al.* [42] with a different cathode in a well-simulated thruster discharge chamber found many ions at high energy, and very strong dependence of the distribution on flow rate, current, and line-of-sight, with relatively low energy ions seen when viewing the orifice on-axis. In Crofton's study [40], however, the highest IEDF is obtained when viewing the orifice on-axis. It is not clear whether the T6 HC has a high propensity to produce low energy ions (good for thruster applications as an electron source, bad for stand-alone micro-thrust applications) under typical operating conditions, or whether this is a matter of appropriately simulating the thruster discharge chamber. It is to be expected, however, that the influence of the ion-thruster chamber and its discharge will very significantly influence the energy spectrum of detected ions, due to the high discharge current, magnetic field, and containment effects on ions and neutrals. Little is known about high-energy ion generation in this environment.

IEDFs were generally simpler and less energetic than those observed in other cathodes previously. Simulation with combined PIC and DSMC methods has produced results in excellent agreement with the measured ion energy distribution functions under a variety of conditions, using only T_e as an adjustable parameter. Significant discrepancies appear in the comparisons of angular distributions of ion emission, and in the potential and electron temperature gradients in the restricted plume region that was investigated. Because retarding potential profiles exhibit little dependence on charge state and electron temperature has been the most important parameter in reproducing the T5 and T6 ion energy distribution functions, it is likely that a potential hill acceleration mechanism predominantly causes ion acceleration.

The influence of other parameters, particularly the ion-electron collision frequency in T5 simulations, may indicate that the mechanism is not purely potential hill.

The experiments conducted by Latham, Pearce and Bond at AEA Technology, Culham Laboratory [28] are particularly relevant here, because they employed during most of their work a cathode essentially identical to the T6 HC, which is the cathode used in our experiments. They took measurements with an RPA in a UK-25 ion thruster configuration and also in the case of a keeper-only discharge. Their HC had an orifice diameter of 0.6 mm chamfered to 0.8 mm. This relatively small orifice size limited discharge currents to 10 A, to avoid erosion. Orifice erosion and the need to reduce operating temperature was the reason that prompted the further increase of the T6 HC orifice diameter, originally 0.75 mm countersunk at an angle of 45° to a depth of 1 mm, up to 1.3 mm, previous experience [16] having suggested that this would be effective. The reduction in tip temperature achieved in this way was about 80 K [82]. The thruster experiments at Culham went up to 40 A discharge currents [115]. They used several different cathodes, including ones that they manufactured themselves to their own designs. The RAE/DERA HC, which was the cathode used during most of the work, had a 0.75-mm-diameter orifice, not chamfered, and its tip was 1 mm thick.

The measurements at Culham were made by fitting a compact RPA into a 6-mm-diameter hole drilled in the centre of the tantalum baffle, 55 mm downstream of the HC. Figures 1.11 and 1.12 [28] show a typical RPA trace and the corresponding ion energy spectrum for a cathode flow of 0.86 A equivalent current of xenon. This was obtained by differentiation of the curve in Figure 1.11. Keeper voltage and current are, respectively, 22 V and 1.0 A.

The ion energy peak is below keeper potential, but there are ions at least up to this potential. On lowering the cathode mass flow rate at fixed keeper current, the "tails" of ions with energies in excess of keeper potential become increasingly significant, even if the peaks of their energy distribution functions remain below keeper potential. This is shown in Figure 1.13 [28], for a keeper current again of 1.0 A, a keeper voltage of 42 V and a flow rate of 0.07 A equivalent current.

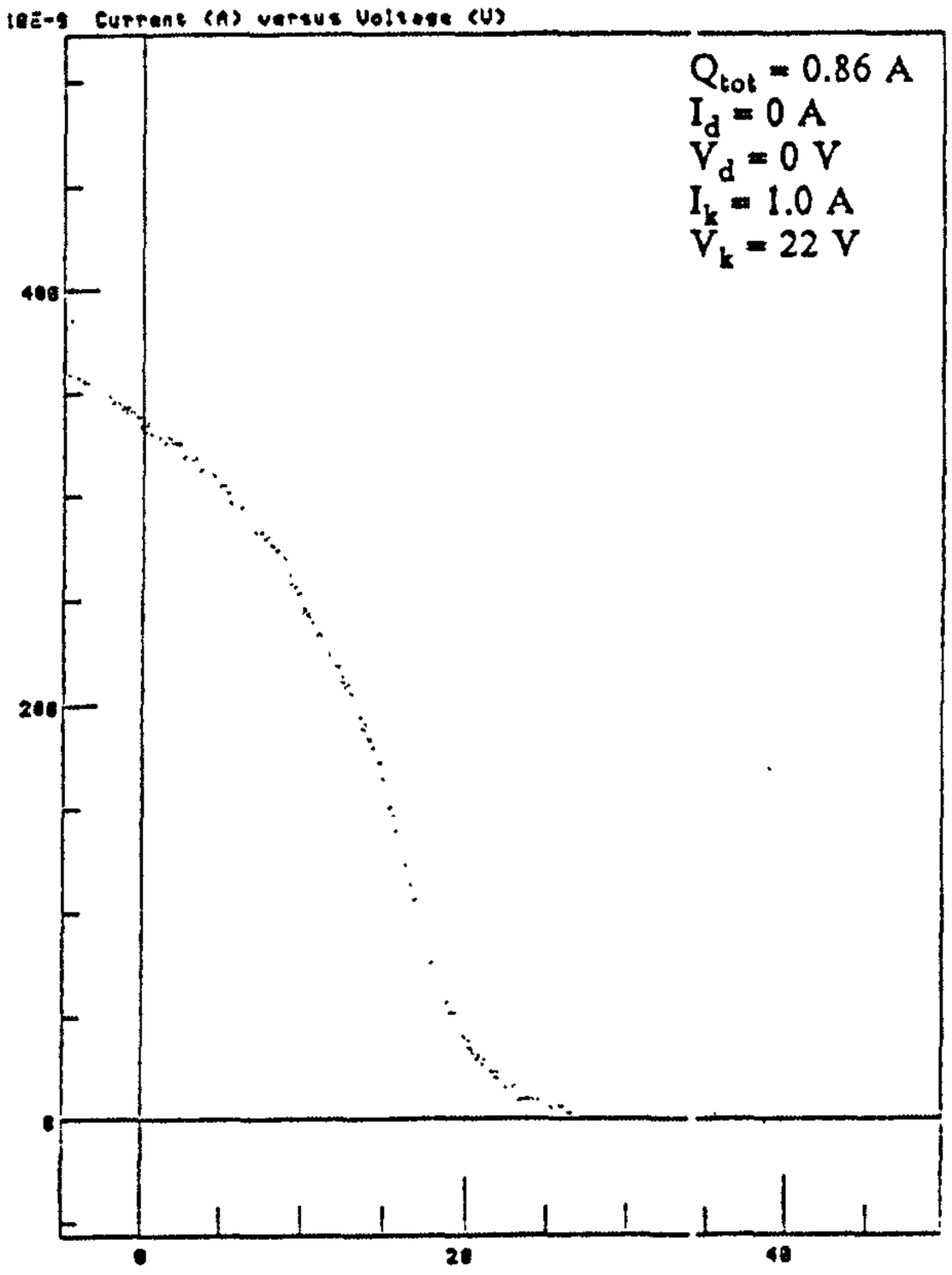

Figure 1.11 – RPA trace at 0.86 A equivalent current (Culham data) [28].

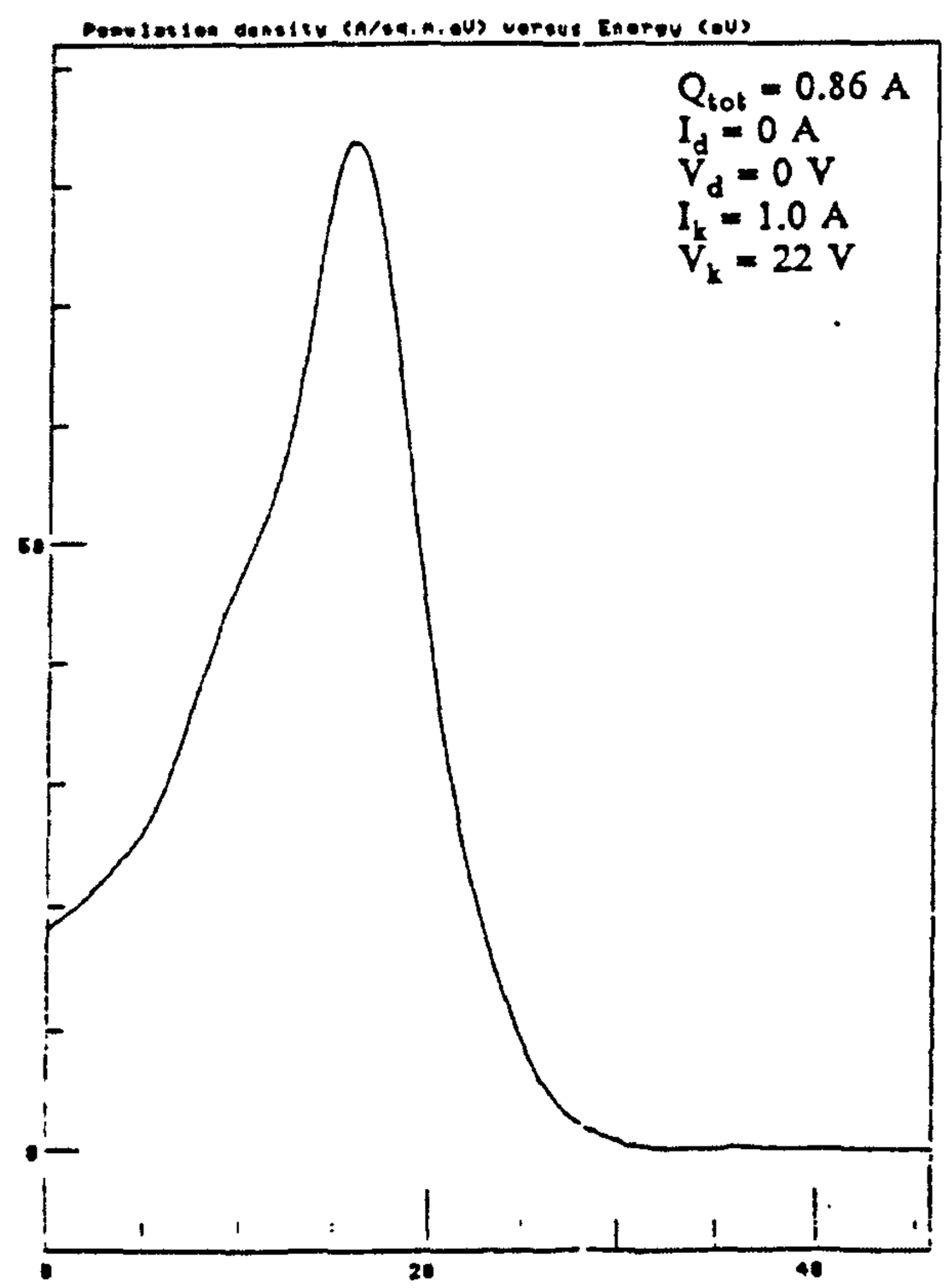

Figure 1.12 – Ion energy spectrum from Figure 1.10 (Culham data) [28].

It is also interesting to examine the behaviour when the discharge supply was operated, because the total current is what is relevant to the phenomena inside the HC and, as we said above, currents higher than those reported here for the keeper-only configuration are possible in a T6 discharge employing a larger anode in an open-diode configuration. The total propellant flow was split in the ratio 70:30 between main and HC propellant feeds. As the discharge current was increased and the flow rate lowered, the increase in the high-energy component, well above discharge voltage, was dramatic. This is shown in the ion energy spectrum in Figure 1.14 [28], for a discharge current of 10 A, a discharge voltage of 32 V and a flow rate of 1 A equivalent current.

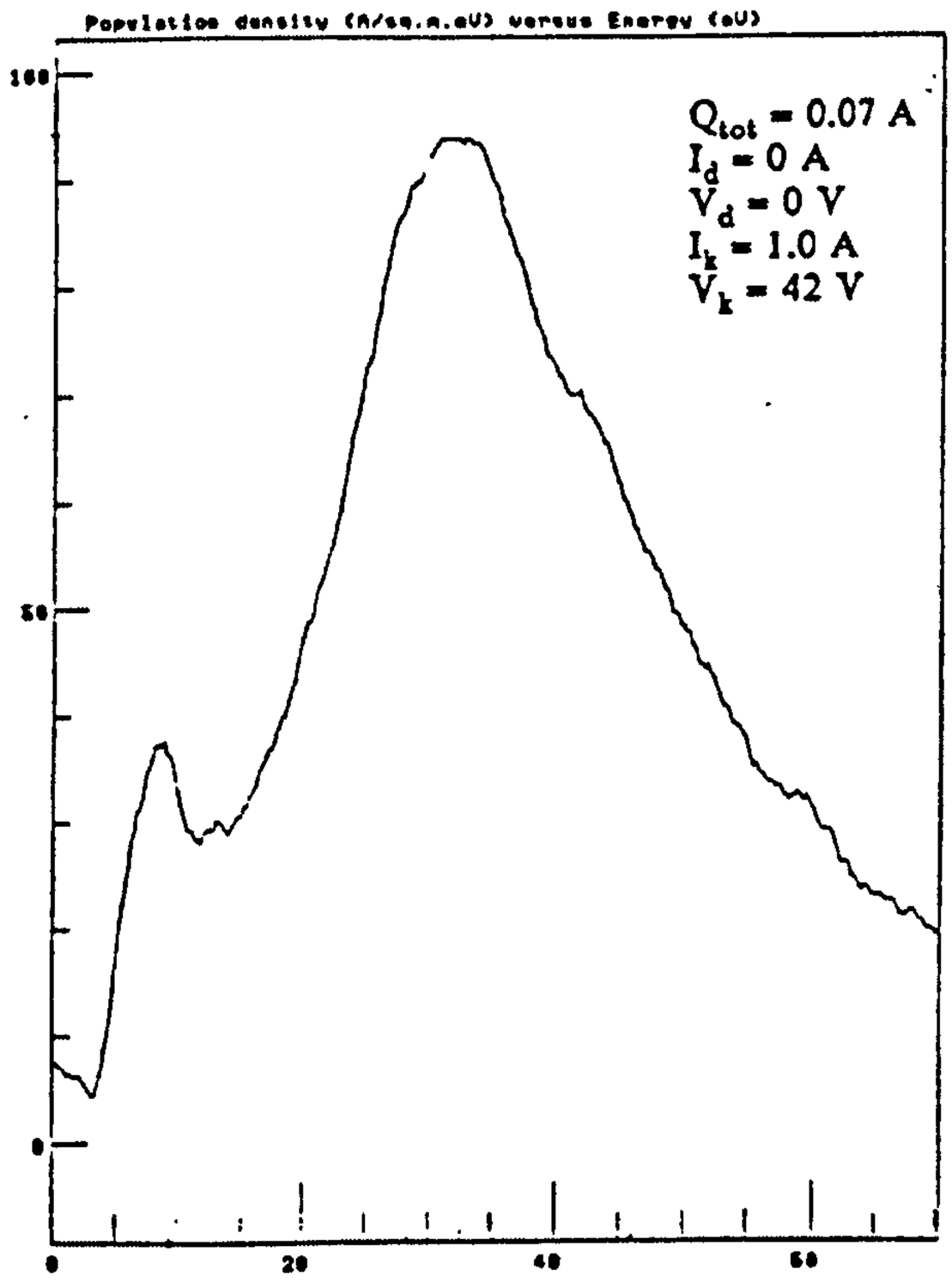

Figure 1.13 – Ion energy spectrum at 0.07 A equivalent current and 1.0 A keeper current (Culham data) [28].

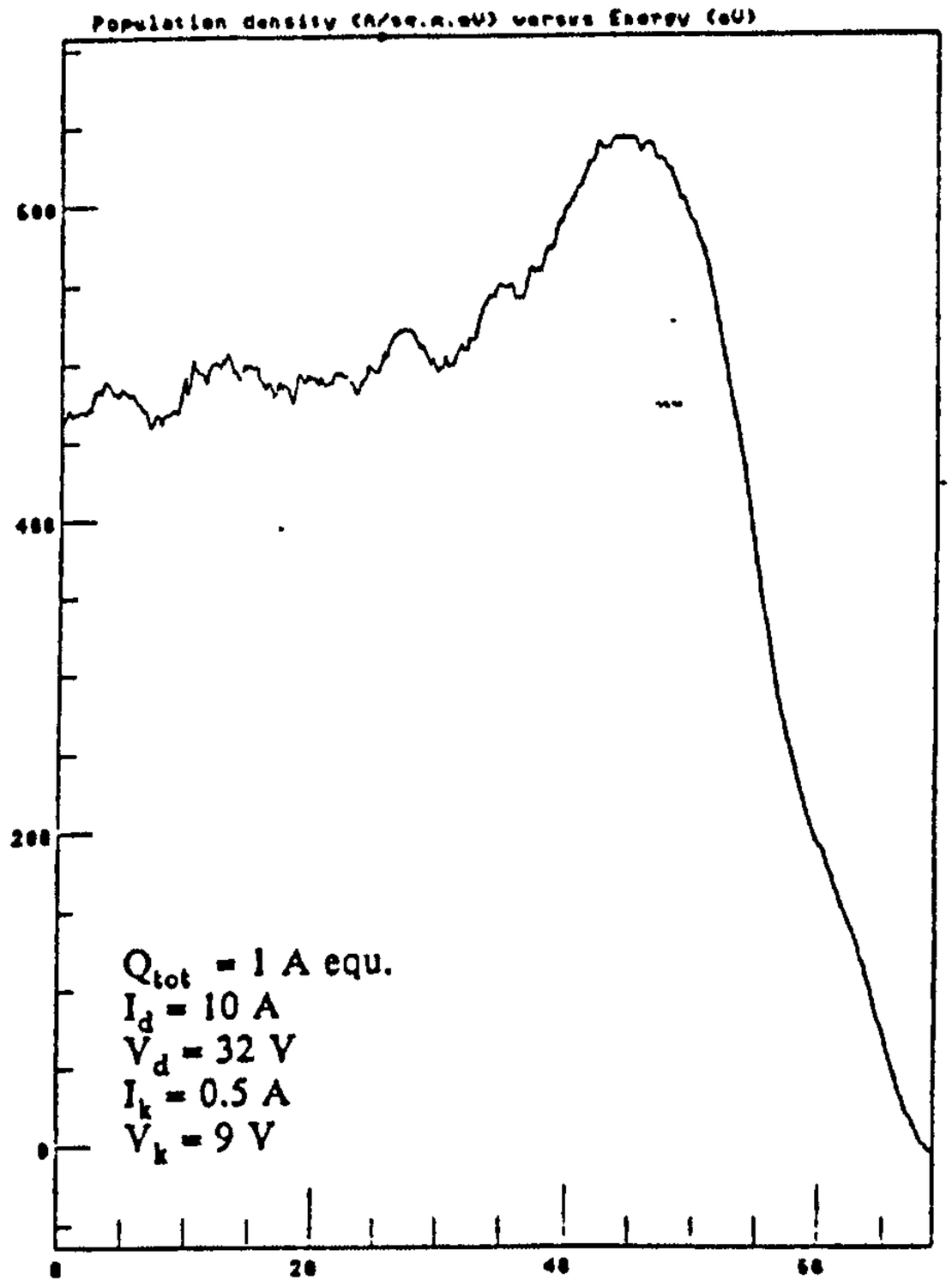

Figure 1.14 – Ion energy spectrum at 1 A equivalent current and 10 A discharge current (Culham data) [28].

Patterson and Fearn at DERA (now QinetiQ) adopted an anode-plate and open-keeper configuration for their investigation of a T6 HC [33, 85]. The keeper was a circular plate with a central orifice of 5 mm diameter. A central hole of 10 mm diameter in the anode allowed for optical-pyrometer measurements of the HC tip temperature, or for ion-energy measurements, to be made. The HC position could be varied at will with respect to the keeper by means of an externally actuated micromanipulator. A T5 thruster body acted as a convenient discharge vessel. In order to simulate within this the gas pressure in the coupling plasma region of the T6 thruster, the total exit area from the vessel was made equal to the area of the annular gap between the inner polepiece and the baffle disc in the thruster. Other studies were undertaken using an open-diode configuration, with a 13.5 mm thick anode placed just 6 mm from the HC tip. This is, to the author's knowledge, the only other example of a T6 HC investigated in a configuration somehow similar to the one adopted in the experiments described in this thesis. Measurements were performed with an RPA, confirming the presence of ion energy peaks in excess of anode and keeper voltages for several

discharge conditions [33, 85]. Theoretical work undertaken to explain these experimental observations invoked a combination of potential hill and $\vec{j} \times \vec{B}$ contributions [33, 85].

1.4 – Analytical, Semi-Analytical and Numerical Models

Various models of HC operation have been proposed in the last twenty years, ranging in complexity from simple analytical and semi-analytical models, which may involve the numerical solution of some equations, to more complex integro-differential models, leading to fully computational numerical simulations. In this thesis we will focus mainly on the analytical and semi-analytical models, which lend themselves more immediately to a simple assessment of HC performance.

In general, a successful model must include all relevant processes within a cathode, together with their dependence upon parameters such as propellant flow rate and the potentials of external electrodes. These processes include the formation of the internal plasma, the emission of the electrons, which pass eventually to the keeper electrode and anode, and the conduction of those electrons through the orifice. At the more detailed level, the model should be able to explain the generation of high-energy ions and of the observed significant levels of discharge noise and oscillations over a wide range of frequencies [12, 84]. Clearly, no model has yet accomplished all of these objectives, but good progress has been made.

One of the earliest models of HC operation is the one developed by Siegfried and Wilbur in the 1980s [62-64] based on numerous experimental results [59, 60]. The analytical formulation is based on the concept of an idealized "ion production region," defined as the volume circumscribed by the emitting portion of the insert, within which most of the processes are concentrated. The plasma properties are assumed to be constant in this region, the extent of which into the insert is only of the order of its inner diameter. The heavy particle temperature is assumed to be equal to the insert temperature. This model was originally developed for mercury HCs, but is easily adapted to noble gases as propellants, as shown by calculations recently performed by Rudwan for argon and xenon with a slightly modified version of it, closely matching

experimental results [15]. One of the limitations of this model is that the electron temperature cannot be calculated, so that an assumption has to be made from experimental data.

Another model, developed by Katz *et al.* [68, 72], focused at first on the tiny orifice region and has later been developed to include the insert region as well [78, 79], eliminating the need to make an assumption about the temperature of the electrons entering the orifice from the insert region. This can now be calculated with this model and agrees well with measurements by Malik, Monterde and Haines [17, 18]. In the insert region, we have a weakly-ionised, quasi-neutral plasma with relatively slow, diffusion-limited ion transport. The orifice is treated as a cylinder containing a homogeneous neutral plasma with a thin wall sheath. Such an assumption is justified by the fact that, although many times larger than the Debye length, the orifice extends for only a few mean free paths for electrons, ions or neutrals. In the orifice, multiple charge-exchange collisions between neutrals and ions act to heat the neutral gas far beyond the orifice plate temperature. The time to thermalize the energetic neutrals produced by charge exchange collisions is assumed to be short compared to the time between charge exchange collisions [78, 116, 117]. Katz *et al.* suggest that this heating increases the gas viscosity, accounting for the pressure rise observed when a HC discharge is started [78]. The original model was used to estimate the performances of a HC [118] and of a gridded, HC-based ion microthruster [67]. The fundamental information is that the HC plasma production is controlled by the ion current. Most of the ions generated in the orifice cannot escape through the keeper aperture without recombining on cathode surfaces [118]. An analysis, performed with the extended model, suggests that the Space Station HC plasma contactor was operating at a temperature far in excess of the minimum necessary to support the emission current density [79]. This is an important result, as a reduction in operating temperature would greatly extend the HC lifetime, already tested at 28,000 hours [43].

Domonkos, drawing on the models by Wilbur *et al.* and by Katz *et al.* and on work by several other authors, has developed a model of the orificed HC based on particle and energy balances [70], which includes the plasma in both the insert and orifice regions. Here the neutral temperature in the orifice is, however, assumed to be equal to the orifice plate temperature, estimated based on experimental data. The insert region

current emission is constrained by the calculated current required by the orifice region. When combined with experimental data [104], this model suggests the presence of double layers at the entrance and exit of the orifice.

The model developed by Salhi and Turchi [65] is the only one based on a purely analytical formulation founded on first principles. Its predictions are in good agreement with the experimental results obtained by Siegfried and Wilbur [62, 64]. This model was later expanded to incorporate some differential equations solved numerically, introducing new physical aspects. In particular, the assumption of thermal equilibrium between cathode wall and heavy particles was removed. The heavy particle temperature distribution is estimated by balancing electron collisional heating [21] of ions with heavy particle heat conduction in the radial direction [66]. A simplified version of this model was also presented by Turchi and Salhi [119] and is discussed in Section 2.2.

A HC model involving the numerical solution of a system of differential and integral equations has been developed in a collaboration between Centrospazio and RIAME MAI (Moscow Aviation Istitute) [75]. More recently a different model, involving the solution of a system of analytical and differential equations with the shooting technique, has been developed at Centrospazio by Rossetti *et al.* [74]. The two models are in good qualitative agreement with each other. However, the second model shows a better agreement with experimental data.

A HC model for the case of a low-pressure arc was developed by Kennedy [58]. It consists of a set of analytical, integral and differential equations, which need to be solved, in general, in an iterative way.

A viscous compressible code with a reacting gas capability was used in a simplified model of the flow in a HC at the University of Southampton by Murray, Tutty and Gabriel [73].

Crawford at the University of Southampton has developed a numerical code for the simulation of the HC plasma [76, 77, 120]. The DSMC method is used to model the neutral flow through the cathode. A plasma model is implemented upon this by

modelling the ions as DSMC species and adding electrostatic dynamics via the PIC plasma physics method.

Jugroot and Harvey at Imperial College performed numerical simulations of the flow in the interior and in the plume region of a HC, using a 3D Navier-Stokes continuum code and a DSMC program [71].

Boyd at the University of Michigan has developed a code and validated it by comparing the simulations with experimental results obtained by Crofton (The Aerospace Corporation) [26, 39, 40]. The plume expansion was modelled by explicitly including both electrons and heavy particles in a combined PIC-DSMC approach. The simulations were in good agreement with measured ion energy distributions. Comparisons of ion emission and plasma potential profiles were relatively poor.

Chapter 2

Theoretical Analysis, Modelling and Estimates

2.0 – Flow Dynamics and Thrust Generation

The specific impulse obtainable depends on how good a conversion of flow enthalpy into directed kinetic energy can be achieved. If the enthalpy of the flow is fully converted into directed kinetic energy, neglecting the plume divergence and other losses, we can write:

$$\frac{5}{2}\frac{\dot{m}}{m}kT = \frac{1}{2}\dot{m}v_e^2 \tag{2.1}$$

where k is the Boltzmann's constant, T the heavy-particle temperature, m the atomic mass and v_e the exhaust velocity. This yields for the exhaust velocity:

$$v_e = \sqrt{\frac{5kT}{m}} \tag{2.2}$$

The thrust and specific impulse are then:

$$F = \dot{m}v_e \quad ; \quad I_{sp} = \frac{F}{\dot{m}g} = \frac{v_e}{g} \tag{2.3}$$

This analysis yields a maximum specific impulse, unattainable in practice:

$$I_{sp} = \frac{1}{g}\left(5\frac{kT}{m}\right)^{\frac{1}{2}}, \tag{2.4}$$

where g is the acceleration of gravity at sea level.

In the orifice we have $Kn \sim 10^{-2}$, where $Kn = \lambda / d$ is the Knudsen number, for a large range of operating conditions [76, 77, 120]. λ is the mean free path and d the orifice diameter. This means that we should be in a regime of continuum flow, or better slip flow, at least inside the HC. Due to the low values of pressure in the vacuum chamber (10^{-2}-10^{-3} mbar even with HC discharging at high mass flow rates), sonic conditions consistently obtain at the orifice.

The orifice aspect ratio (length/diameter) varies from a value of 2 for the original 0.5 mm diameter, 1.0 mm length orifice, to a value ~1 for the 1.0 mm diameter orifice and a heavily eroded HC tip face. The orifice discharge coefficient is generally sensitive to pressure ratio and Reynolds number, but for aspect ratios between 1 and 7 it varies little, assuming values between 0.81 and 0.86. Our orifice is near the lower boundary of this range of values, close to a thin plate orifice but, as the pressure ratios are high (propellant feed lines at ~1.5 bar), the discharge coefficient will, if anything, be higher. The vena contracta, in fact, is bounded by a zone of recirculating gas immediately downstream of the orifice. Once sonic velocity has been achieved, further reduction of the downstream pressure cannot further increase the velocity through the vena contracta, but if the orifice plate is thin, it can increase the vena contracta's size. This is because the recirculating gas zone extends upstream of the vena contracta, and the shape of that zone can be affected even though the flow is sonic. Further reductions in downstream pressure cause the vena contracta to move upstream and to consequently increase in area. Ultimately, at high pressure ratios, the vena contracta can reach the upstream edge of the orifice. Then its area will equal that of the orifice and the discharge coefficient will be unity [121]. In our case, therefore, the discharge coefficient will have a value between 0.8 and 1. For the purpose of our analysis, which is mainly to establish proportionality trends and bracket magnitudes, we can assume it to be unity and neglect it from this point on.

Continuum-flow theory predicts, for a choked, sonic orifice, a specific impulse [2]

$$I_{sp} = \frac{1}{g}\left(2\frac{\gamma+1}{\gamma}\frac{kT}{m}\right)^{\frac{1}{2}}, \tag{2.5}$$

which is only 80% of that yielded by full conversion. Above, γ is the ratio of specific heats. Free-molecular, non-continuum flow theory yields a lower value [122]

$$I_{sp} = \frac{1}{g}\left(\frac{\pi}{2}\frac{kT}{m}\right)^{\frac{1}{2}}, \tag{2.6}$$

which is only ~ 70% of that predicted by continuum theory. This is to be expected, as the continuum flow conditions persist at least until the plume expansion begins, downstream of the orifice. Continuum flow theory is much more "efficient" at bulk displacement and acceleration of mass. By using free-molecular theory we are thus bound to obtain lower I_{sp} values, even while neglecting the drop in temperature due to the expansion from stagnation to orifice sonic conditions.

Our original analysis [52] can be taken a step further by assuming a continuum expansion upstream of the orifice and then a free-molecular process downstream of it. This corresponds, in practice, to halving the pressure term that accounts for the external expansion and can be seen, also, as a way for introducing some divergence losses in the plume, neglected by a simple quasi-1D gasdynamics analysis. We obtain the expression

$$I_{sp} = \frac{1}{g}(2\gamma+1)\left(\frac{1}{2\gamma(\gamma+1)}\frac{kT}{m}\right)^{\frac{1}{2}}, \tag{2.7}$$

which will be referred to as "Hybrid". The free-molecular isotropic expansion, in turn, probably overestimates such losses. Eq. (2.7) should therefore still produce an underestimate of I_{sp}.

Since the flow inside the HC is neither a simple adiabatic nozzle/orifice flow or a constant-area flow with heat addition (Rayleigh flow) [123], but a combination of the two, a simple analytical solution is not immediately available. On the other hand, even if heat is added all along the insert and at the orifice plate, choking conditions should still persist at the orifice. We may therefore say that the exhaust velocity is simply the sonic speed [2] at the tip temperature and therefore the specific impulse will be

$$I_{sp} = \frac{1}{g}\left(\gamma \frac{kT}{m}\right)^{\frac{1}{2}}. \tag{2.8}$$

Following the analysis in [49], we could also say that the specific impulse is

$$I_{sp} = \frac{1}{g}\left(\frac{8}{\pi}\frac{kT}{m}\right)^{\frac{1}{2}}, \tag{2.9}$$

by assuming that the particles are exhausted from the orifice at the mean, or average, thermal speed [124, 125], calculated with the tip temperature.

Eq. (2.4) definitely overestimates the specific impulse. The assumption of continuum flow breaks down just downstream of the orifice, therefore Eq. (2.5) is not completely appropriate either, also because T in it should be the stagnation value and not the tip/insert temperature. Eq. (2.7) gives a value for I_{sp} that is intermediate between those of Eq. (2.9) and Eqs. (2.6) and (2.8), which are very close to each other. A tentative value for the specific impulse could therefore be, remembering that $\gamma = 5/3$ for a monatomic gas,

$$I_{sp} = \frac{1}{g}\left(2\frac{kT}{m}\right)^{\frac{1}{2}}, \tag{2.10}$$

with an uncertainty of ±20%. All of the above formulas agree qualitatively on a square-root dependence of thrust on temperature, for a given mass flow rate, as a consequence of assuming the thermal acceleration/expansion of a gas as the mechanism for thrust generation.

In order to corroborate the continuum flow analysis that predicts choking at the orifice for a large range of flow conditions, numerical simulations were performed using a DSMC code developed at the University of Southampton [76, 77, 120] to simulate the experimental configuration used in these experiments. They confirm, at $\dot{m} = 0.414$

mg/s = 1 Aeq of Ar, T = 300 K, the presence of a sonic line at the orifice. Slip at the wall has been actually "seen" in some simulations [76, 77, 120].

2.1 – Model of HC Orifice Conditions

In order to be able to calculate the flow characteristics at the exhaust section and to use them for an assessment of the thrust generated, a modelling effort of the orifice plasma parameters was started. This was based on work by Katz *et al.* [67, 68] and by Salhi and Turchi [65]. For simplicity, only the orifice region was considered, without attempting to include the insert region in the model, as was done by Katz *et al.* in more recent work [78, 79]. The temperature of the electrons entering the orifice from the insert region is therefore treated as an input of the model. Based on results by Salhi *et al.* [65, 66, 126], values of T_e = 1.0 eV for xenon and T_e =1.1 eV for argon are used.

The orifice is so small that, although many times larger than a Debye plasma length, it extends for only a few mean free paths for electrons, ions and neutrals. Therefore, it is reasonable to treat the orifice as a cylinder containing homogeneous neutral plasma with a thin wall sheath [67, 68].

The model consists of a system of four non-linear equations in the four unknown quantities N, the neutral density, n, the electron and ion density, T, the heavy-particle temperature and T_e, the electron temperature. A fifth equation, decoupled from the others, allows calculation of the plasma pressure p.

Three equations can be written following the modelling in [67, 68], with some modifications, and are:

- A balance between the flux of neutrals and ions (moving at speeds between the local mean thermal and sonic value) through the orifice cross-sectional area and the input neutral gas mass flow rate
- A balance between ion production rate and ion loss rate

- A balance between the power dissipated in the orifice by ohmic heating and the power lost by the sum of ionisation, radiation and convection.

The fourth equation is a two-temperature Saha equation. Together with the more classic version adopted by Salhi and Turchi [65] and Kannappan and Bose [127], a different one, after Chen and Han [128], was considered.

The fifth, decoupled, equation (from Salhi and Turchi [65]), calculates the plasma pressure p by assuming that all particles behave like a perfect, dilute gas and by applying the equation of state.

Electron-temperature dependent cross-sections, scattering rates, plasma conductivity and other parameters are treated following Katz *et al.* [67, 68] and references therein [129] and various other references [1, 124, 125, 130].

Solution of this system of equations for different input conditions and parameters (mass flow rate, discharge current, orifice geometry, propellant gases) would allow the calculation of the plasma parameters in the flow exiting the orifice. The heavy-particle temperature T, in particular, could be immediately used to estimate the specific impulse. Unfortunately, due to time constraints, the numerical solution of the system, with C and MATLAB programming, has fallen beyond the scope of the present thesis and will constitute the subject of future work.

2.2 – HC Preliminary Thrust Assessment

Towards the beginning of our investigations, we tried to assess the thrust obtainable from a HC, making use of a critical review of relevant experimental results and theoretical models [48]. In this, we needed to concentrate on ion extraction and acceleration mechanisms, rather than electron emission, which is the usual area of concern for HC theories. Our early estimates are reported below, followed by subsequent calculations performed on T6 HC data by Crofton available in the literature at a later time [40].

A simplified model proposed by Turchi and Salhi [119] shows that, even if ionisation is excluded, HCs could make good electrothermal micro-thrusters. Of course, this will entail the use of low atomic weight propellants if higher specific impulse is needed. On the contrary, in ion thrusters high-atomic weight propellants, mainly xenon, are preferred, in order to increase the thrust density. Cathodes have therefore been extensively operated with "heavy" noble gases, usually Xe, but also including Kr and Ar, since the 1970s [61, 131].

The lighter noble gases, Ne and He, have also been studied [16], but to a lesser extent, in connection with fundamental physics investigations together with this possible application. Unpublished work by Davis, Charlton and Newson of Mullard Ltd [16] investigated the use of most of the rare gases in a T5 thruster HC and concluded that the cathode worked reasonably well on all gases, but the operating potential increased with ionisation potential, as might be expected. Edwards and Gabriel also examined the possible use of alternative propellants [97]. However, HCs reportedly also work successfully with hydrogen (H_2) and ammonia (NH_3), which are the "light" propellants used in quasisteady MPD thrusters [10].

Numerical computations performed by Jugroot with a continuum Navier Stokes 3D solver [71] show that the neutral xenon flow, heated by a HC insert at a temperature of 1000 K, reaches a Mach number M=0.9 in the orifice. The flow leaving the cathode expands but does not keep on accelerating to form a supersonic jet. Instead, it decelerates and disperses. This is due to the viscous mixing occurring in the coupling plasma volume, and would not happen without sufficient background pressure to form shear layers and retard the flow.

Indeed, computations by Crawford with a PIC-DSMC code developed by him at the University of Southampton [76, 77] show the presence of sonic lines both at the HC and at the keeper, or anode, orifices. These were performed for HC neutral flow expanding into a vacuum for two different geometries: enclosed keeper and anode, adopted by Rudwan [15] and open diode, adopted by Gessini [52]. The flow is therefore choked for a wide range of operating conditions and expands into the vacuum chamber as a supersonic plume [77].

Notwithstanding all the differences in experimental set-up and conditions, some interesting common features can be observed by comparing various results.

Even though the experiments by Latham *et al.* [28] were performed with a T6-type HC and those by Crofton [25] with a T5 HC, a comparison of the results is nevertheless possible. We assume, as is reasonable due to the high current densities [67], that the processes taking place in the orifice region govern the amount of plasma flowing from a HC. We can therefore expect that different cathodes at similar discharge currents and equivalent flow rates, having similar ratios between current densities and charge carrier densities in the orifice, will behave in a similar way. It is important to notice, though, that a smaller orifice diameter will give rise to a higher orifice impedance and, consequently, higher temperatures [45]. In this light, we can compare OP 1 from Crofton [25] with the data from Figure 1.5 (Culham) [28], as they both have a discharge current to equivalent current ratio (and therefore a current density to equivalent current density ratio in the orifice) ~15. We see that in both cases the ion energy spectrum presents a peak at ~35 eV and an appreciable amount of ions with energies above keeper voltage. The keeper voltage is, however, 26 V in the first case [25] and 42 V in the second [28].

It is important to note that the scaling used in this work is only tentative, and the author is aware of its inadequacy. Other possible ways of correlating the operation of different HCs are being considered. Taking into account the energy available to ionize a particle flowing through the orifice per unit time, even neglecting the dependency of dissipation in the orifice on temperature through the resistivity, leads to more complicated scaling expressions. It is felt that accurate comparisons between HCs with widely varying geometries and operating conditions would be beyond the scope of the present analysis.

In order to gain an idea of the actual thrust performance we can expect from a HC, we can analyze in more depth the experiments by Crofton [25] and Latham *et al.* [28].

OP 5 shows a relatively high ion current extracted. From Figure 1.2, taking into account the RPA area (1.0 cm^2) and integrating the ion flux over the angular distribution, we obtain 3.7 mA of ion current being exhausted. For a $\dot{m}$ of 33 mA

equivalent current of 100% singly ionized xenon, this corresponds to a mass utilization ~11% and is consistent with Crofton's estimate of ~10% for OP 2. The two points correspond to similar, but not identical, conditions, having respectively a discharge current to equivalent current ratio of ~ 40 and ~ 50.

The high level of Xe^{2+} observed in the plume suggests that full ionization is approached near the cathode orifice for orifice current densities ≥ 5000 A/cm^2 at $\dot{m}$ = 0.03 g/cm^{2}s of xenon. This corresponds to an electron efflux to atomic particle efflux ratio of ≥ 20 [25, 34]. OPs 5 and 2 amply satisfy this condition.

From Figure 1.2 we see that the contribution to the thrust of the ions at $\phi > 60°$ will be negligible, especially considering that the ions at small ϕ are more energetic [25]. From Crofton, let us assume that the ion kinetic energy varies linearly from 50 eV for $\phi = 0°$ to 20 eV for $\phi = 60°$. This is a crude approximation, but it is consistent with the data reported in Figures 1.14 and 1.15 [25]. Energies of the same order of magnitude were also measured at Culham for similar operating conditions and even for much higher currents, as shown respectively in Figures 1.12 and 1.13 [28], but only on the HC axis.

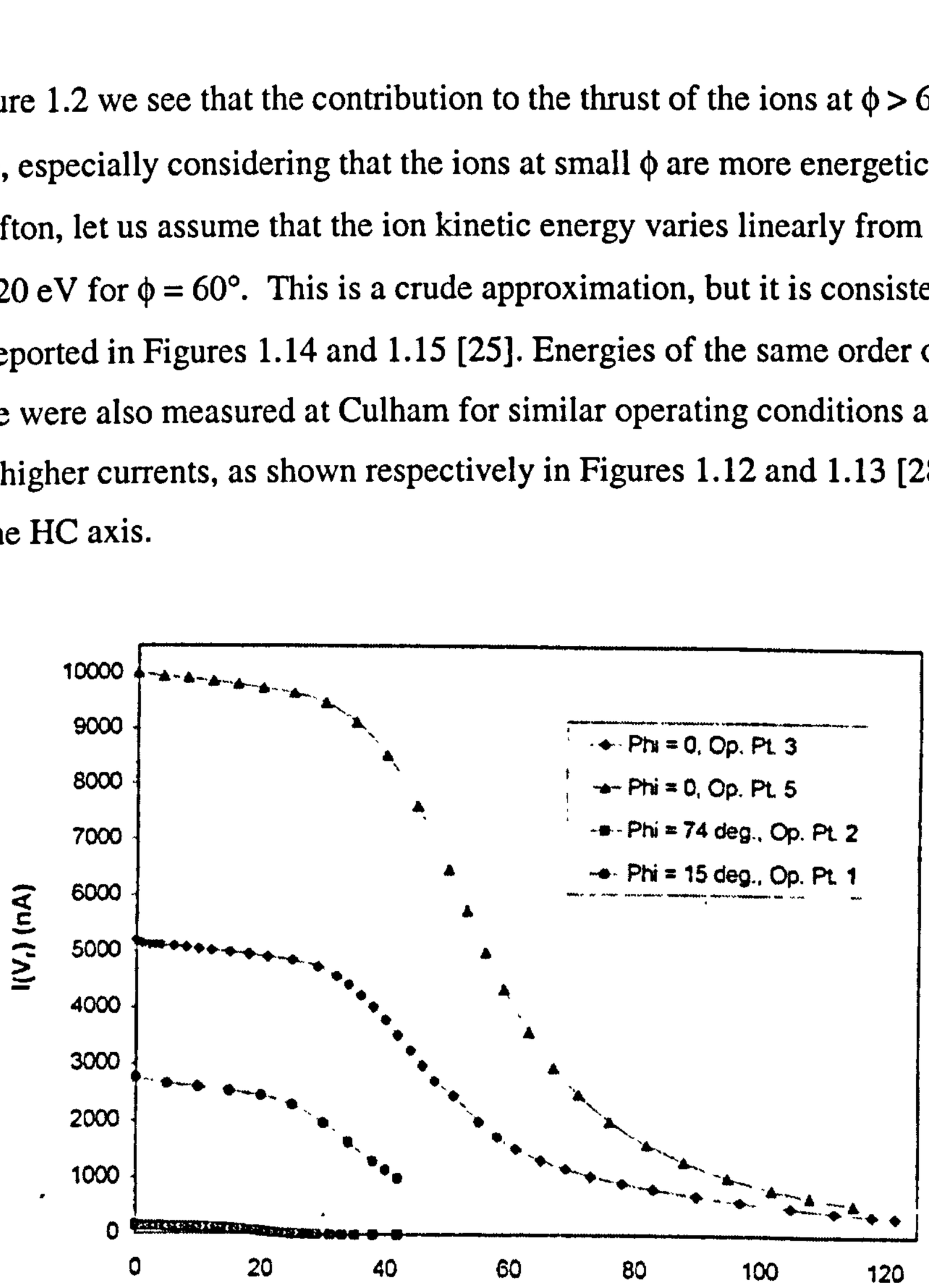

Figure 1.14 – RPA current vs. retarding potential (Aerospace Corp. data) [25].

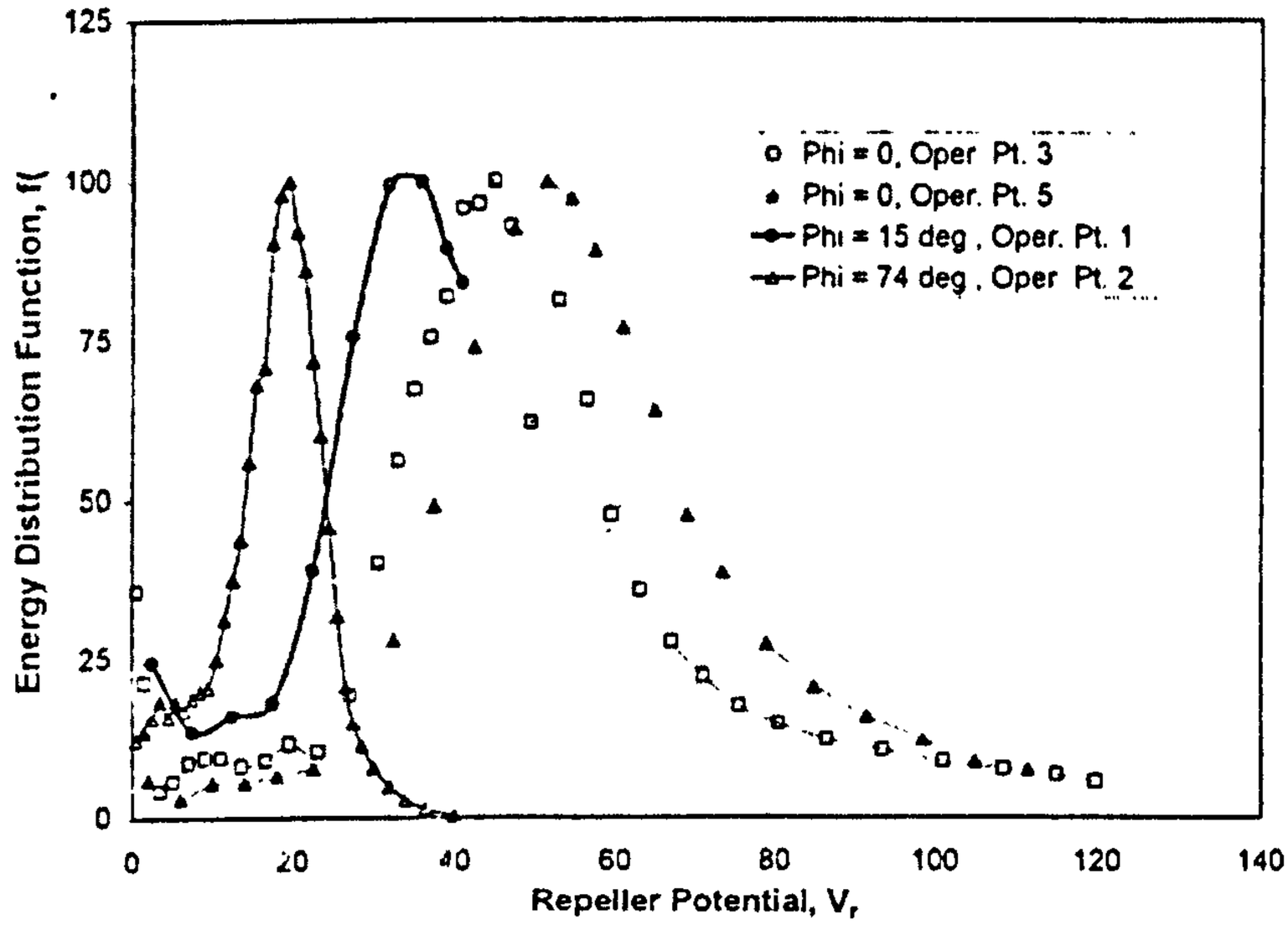

Figure 1.15 – Ion energy distribution function (Aerospace Corp. data) [25].

Knowing the angular distribution of ion flux, from Figure 1.2 [25], by performing again a discrete integration we can calculate the axial kinetic energy and thrust. For OP 5 we obtain a thrust of ~32 μN. The thrust density on the centerline is ~0.12 μN/ cm^2.

By operating a T6 HC with the same ratios mentioned above, but at a current 5 times higher than in OP 5, i.e., 6.5 A discharge current and 145 mA equivalent current, we should be able to obtain ~160 μN of thrust from the ions, according to our tentative scaling.

If a different approach is adopted and the curves resulting from the experiments performed at Culham (e.g., Figure 1.13) are integrated with respect to ion energy, the total ion current density is obtained as a function of energy. Dividing by the electron charge and multiplying by the ion mass gives the mass flow rate of ions per unit area as a function of energy. If this is then multiplied by the ion velocity (from the knowledge of ion energy and mass), the thrust of ions at that energy, per unit area, can be derived. Further integration would then yield the thrust.

This approximate calculation has been carried out for several sets of data acquired by the Culham Laboratory. The results are much higher than those discussed above,

perhaps indicating that this cathode was more effective as a thruster. Typical thrust densities were a few mN/cm^2 at the lowest flow rates (~3.6 mN/cm^2 for the 1 A keeper, 0.07 A equivalent current case of Figure 1.12) to a few tens of mN/cm^2 at the highest flows (~27 mN/cm^2 for the 10 A discharge, 1 A equivalent current case of Figure 1.13). The actual thrust, of course, will depend on the angular distribution of the ion flux, which is not known here. Measurements at Culham, in fact, were taken only on the centerline, with a compact RPA, as opposed to those by Crofton, who explored practically all angular positions. Highly localized sputtering damage on the baffle, however, seems to suggest, even if only qualitatively, a pretty collimated ion beam, with a tight energy distribution.

Unfortunately, it has not been possible to check the accuracy of the actual numbers on the energy spectra. They seem high compared to the RPA trace reported on the paper. The actual acceptance area of the particular RPA used is unknown, the only information being that it was fitted in a 6-mm diameter hole, but it should be, in all likelihood, not much less than 0.5 mm^2. All this casts a doubt over the validity of the above assessment, leading us to suspect that we might be grossly overestimating the obtainable thrust, even by orders of magnitude.

To the ion thrust derived in this way from the T5 data we have to add the electrothermal contribution given by assuming that the remaining ~87% of the flow is exhausted as neutrals. Using Turchi and Salhi's [119] simplified model, which considers the heavy particle flux not substantially ionized, we can have a first crude estimate. If just the enthalpy of the flow is fully converted into directed kinetic energy, neglecting the plume divergence and other losses, we can use Eq. (2.4). The temperature of the outer HC walls is generally around 1400 K. If we assume, quite conservatively, that the inner wall is only ~100 K hotter and that the heavy particles inside the HC are in thermal equilibrium with the walls, which is not an uncommon assumption [64], we can take T_h = 1500 K. We thus obtain, for xenon, v_e = 689 m/s. At a $\dot{m}$ of 0.2 mg/s, this generates thrust of 138 μN and a specific impulse of 70 s. From these numbers it is evident that a "heavy" propellant like xenon is not a good choice for an electrothermal thruster, as expected. According to more recent studies, the heavy-particle temperature might be much higher than the wall temperature [78]. This would make the electrothermal component of the thrust even more significant.

In the vacuum of space we can expect a good expansion of the plume, yet we will not actually have a full conversion of the enthalpy into useful kinetic energy, if only for the fact that the plume diverges. We can correct the result we have just obtained by assuming that the shape of the whole plume resembles the ion flux angular distribution. This is also quite a simplistic assumption. In this way we obtain an electrothermal contribution to the thrust of ~100 μN, with a 72% thrust efficiency and a specific impulse of just ~50 s.

Our HC could then give a total thrust of ~260 μN at 6.5 A. At a $\dot{m}$ of 0.2 mg/s, this corresponds to a I_{sp} of ~130 s. This would not make a very efficient thruster. In order to improve the performance, we could attempt to increase the extraction of ion flux, if we want to build a micro-ion thruster, or utilize propellants with lower atomic weight, if we instead want to realize an electrothermal thruster.

Of the other noble gases, only helium and neon are "light" enough to actually make a difference in the performance, but their ionisation potentials are much higher: 24.6 and 21.6 eV, respectively, versus 12.1 eV for xenon. Hydrogen has been used as a HC propellant, even if in different devices [10]. Its performance was investigated by Turchi and Salhi [119] for an application like the one we are discussing here. They assumed T_h = 2500 K, but even maintaining our conservative figure of 1500 K for hydrogen as well, we obtain a specific impulse of ~800 s. By applying the thrust correction calculated above, say a ~70% efficiency, we still have I_{sp} ~ 560 s, which is in the low range of arcjet performance. The use of hydrogen could cause chemistry-related problems that would probably reduce lifetime. With helium we might obtain a lifetime comparable to that resulting from the use of other noble gases, even if at a higher operating potential. In this case we would of course halve the specific impulse to a value of ~ 280 s, still comparable to that of some chemical thrusters.

Assuming that, even for a hydrogen HC, we have the same type of operation as with xenon, we might still achieve a ~10% mass utilization, while ~90% of our $\dot{m}$ is exhausted as neutrals. In order to estimate the ionic thrust, we now make another extremely crude assumption, that is we use the same energy and mass flow distribution as for xenon. With a propellant as light as hydrogen, we now have a

much higher ion velocity (and therefore I_{sp}), by a factor equal to the square root of the ratio of atomic weights. The ion momentum, though, will be lower by the same factor and thus the thrust will be reduced.

As already mentioned, such a simplistic scaling was felt, even originally, to be incorrect. It is now possible to check, at least partially, our previous estimates by analysing, in the same vein as for the T5, Crofton's more recent T6 data [40].

OP 2 for the T6 has a discharge current to equivalent current ratio of ~ 40 and should therefore, according to our tentative scaling, be in operating conditions very similar to those of OP 5 for the T5. By comparing the data in Figures 1.2 and 1.5, though, we see that the RPA ion current is more or less the same, only slightly larger for the T6. At a much higher value of $\dot{m}$ (0.125 mg/s = 92 mA equivalent current for the T6, 0.045 mg/s = 33 mA equivalent current for the T5) this corresponds to a mass utilization of only ~ 4%. If we further compare the data in Figures 1.3, 1.4, 1.5 and 1.6 to those in Figures 1.14 and 1.15, we see that the ions emitted by the T6 HC are much less energetic. Thus, their contribution to the thrust will be smaller. At a much higher $\dot{m}$, this means that the I_{sp} will be dominated by the gas dynamic contribution and will essentially be the electrothermal one.

We conclude that our initial tentative scaling relation [48] was grossly underestimating the complexity of HC operation, especially regarding the mechanisms governing the generation of high-energy ions. These are still, in large part, not understood, even if numerous models have been proposed. Even a simple, semi-empirical scaling relation aspiring to capture the essential features of these phenomena should probably incorporate more parameters than discharge current and mass flow rate. The orifice area might be involved in a more complex way than previously thought and it has been suggested [40] that the discharge voltage should play an important role.

Chapter 3

The Thrust Measurement System: Theoretical Analysis and Calibration

3.0 – Direct and Indirect Thrust Measurement

The various methods for the measurement of thrust fall into two general categories. Direct methods, where the thruster is suspended on a thrust balance, the displacement of which is measured by a sensor, and indirect methods, where the thruster is fixed and the displacement of a target balance, which is impacted by the thruster exhaust, is measured.

These latter techniques present several advantages over direct methods. The sensitivity of the balance is inversely proportional to the weight of the moving part and, if the thruster is mounted on it, this may be quite heavy, which also causes frictional losses due to the suspension. Unless the whole propulsion system is mounted on the balance, as could be the case with an ablative pulsed plasma thruster (APPT), electric power cables, propellant feed lines and, possibly, cooling flow lines will cause a high motion resistance [132, 133]. Target systems are currently being used by other investigators for the measurement of momentum and heat fluxes in plasma environments [134].

In general, an indirect system is independent of the specific thruster configuration and allows the measurement of the performance of different propulsion systems without changes to the balance and consequent recalibration [133]. A potential interpretation problem is caused by the imperfect knowledge of the interaction processes between the target and the plasma/ion beam. Problems concern the degree to which momentum is transferred to the target and the angular reflection processes. Impacts, in general, will neither be completely elastic nor inelastic. Another possible problem is ion sputtering, although this might not be too significant at the energy levels considered here, well below 100 eV, for which some information is available.

Common metals like iron, copper and aluminium have comparable yield factors, while refractory metals, like molybdenum, have considerably lower (roughly 50%) ion-induced sputtering yields [135-137]. A way to assess and reduce these errors will be to use different surface roughnesses and maybe materials. Experiments can be also devised to estimate particle reflection from the target.

At the very least, this system should be good for comparative tests, if we can assume the surface accommodation coefficients to have an approximately constant, though not exactly known, value. Accommodation coefficients are, in general, a function of the surface roughness, cleanliness, temperature and of the impinging particle molecular weight and kinetic energy [138]. Therefore, our assumption might not be rigorously verified throughout an experimental campaign, causing an error even in the relative measurement. A more detailed discussion of these issues is presented in Section 5.2.2.4.

3.1 – The Cantilever Beam Target

Three distinct targets were used during the development of the thrust measurement system described in this thesis. The preliminary two, referred to as First-Generation Target (1GT) and Second-Generation Target (2GT), are shown in Figure 3.1. The 1GT was described in papers [48, 51]. The 2GT, described in [52] has identical geometry: a square target with $D = 100$ mm connected to a thin beam with $b = 4$ mm and $L = 150$ mm, manufactured as a single piece from Al 3003 sheet with $h = 0.8$ mm. The only difference is that the free end of the beam, beyond the target, has been eliminated. It had been included in the original design in order to increase the displacement of the end of the beam, thus increasing the measurement resolution. As it was later decided to measure the angular deflection instead, and this is constant beyond the position where the load is applied, the end part of the beam became unnecessary.

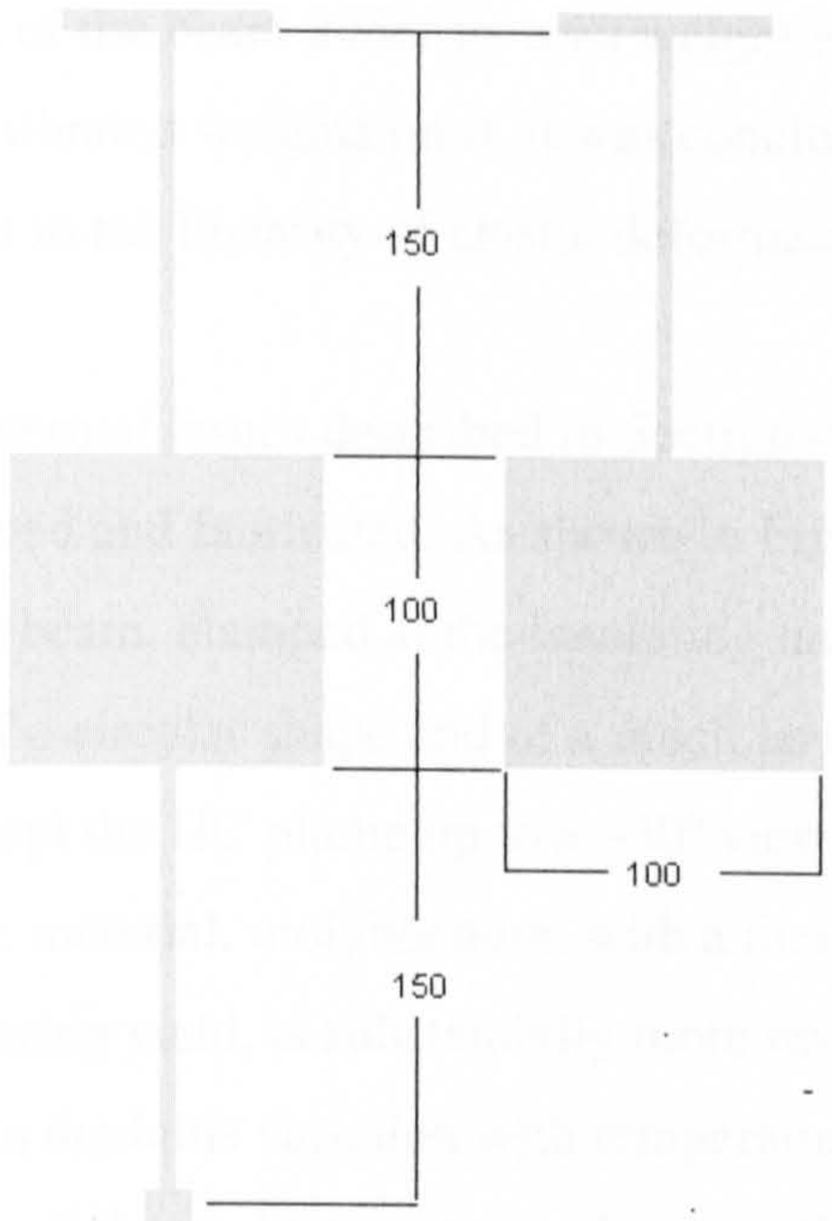

Figure 3.1 – First (left) and Second-Generation Targets (1GT and 2GT).

A more important difference is that in the 1GT the reflection of the laser beam from the backside of the target was obtained by attaching a thin mirror to it with a special, temperature-resistant cement. This method proved to be unreliable, though, as in one instance the mirror actually detached and fell off the target. Even if this was probably due to an imperfect curing of the cement, the investigators feared that small movements of the mirror with respect to the target, while not so dramatic, would introduce an additional source of error into the measurement. It was therefore decided to polish the backside of the target to a mirror quality. This gave satisfactory results, as the reflection from this Al mirror did not seem to alter the beam divergence and intensity to an extent excessively affecting the measurement. 1GTs and 2GTs, used in the initial experiments, were mounted at ~6 cm from the anode.

A static analysis, following the theory of slender beams, was performed. The analytical calculations were double-checked by running simulations in ANSYS®, a finite element analysis program. We obtained an expression for the sensitivity (angular deflection per unit force), which was confirmed, to a high degree of accuracy, by a direct calibration [51]. This was performed with accurate weights and our laser optical lever (LOL) in a horizontal position. By measuring deflections from

the equilibrium position of the beam under its own weight and the new positions obtained after adding calibrated weights on it, it was concluded that we could neglect the effect of gravity, due to the linearity of elastic deformations.

In order to address the thermal issues described in Section 4.6, a Third-Generation Target (3GT) was designed and fabricated. As shown in Figure 3.2, it is still made up of a T-shaped cantilever beam, clamped at the insulating mount, and of the target itself. This, though, is of a circular shape and of a much larger size than in the 1GT and 2GT, so as to intercept the HC plume up to a ~30º viewing angle when positioned further downstream. The material, molybdenum, with a melting point of 2896 K and a lower ion-induced sputtering yield, is substantially more resilient than aluminium. Its less pronounced Young's modulus variation with temperature, in our range of interest, and a ratio of coefficient of thermal linear expansion over thermal conductivity only one third of that of aluminium, together with a smaller length of the beam, definitely reduced the thermal deformation problems, according to the analysis presented in Section 4.6.

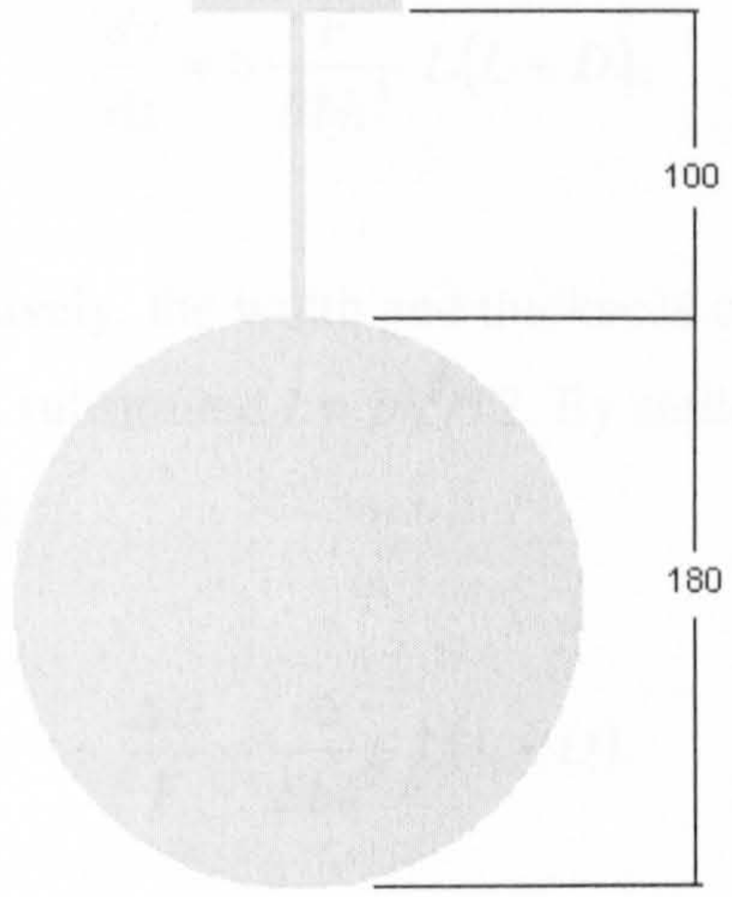

Figure 3.2 – Third-Generation Target (3GT).

Once the CBT is mounted vertically inside the vacuum chamber (1GT and 2GT), during the actual HC thrust measurement, the effect of gravity becomes important. The equilibrium configuration to which the device will tend, after a transient, is

determined by the HC thrust and by the target weight, producing bending moments of opposite sign. Therefore, gravity will effectively decrease the deflection caused by a certain force and thus the target sensitivity as any deflection will give rise to a bending moment countering the deflection itself.

The differential equation describing the behaviour of a cantilever beam subjected to a concentrated load F, perpendicular to the beam axis at $z = L+D/2$ is [139]

$$\frac{d^2y}{dz^2} = \frac{F}{EI}\left(L + \frac{D}{2} - z\right), \tag{3.1}$$

where z is the distance along the beam axis and $y(z)$ the displacement perpendicular to it. D is the target diameter, or its side in the case of a square target, like the one used in these initial experiments. E is the Young's modulus of the material used and I the moment of inertia of a beam cross-section about the neutral axis [139]. This equation can be immediately integrated with the boundary condition $dy/dz = 0$ for $z = 0$. The angular deflection at $z = L$ is

$$\frac{dy}{dz} = 6\frac{F}{Ebh^3}L(L+D), \tag{3.2}$$

where b and h are, respectively, the width and thickness of a beam with rectangular cross-section and we have substituted $I = bh^3/12$. By setting $dy/dz = \Delta\theta$ for $z = L$, we can write the sensitivity as:

$$\frac{\Delta\theta}{F} = \frac{6}{Ebh^3}L(L+D). \tag{3.3}$$

This is the equation used throughout our direct calibration [51]. It describes the behaviour of our CBT quite appropriately, as the target itself, for $z > L$, having a much greater width, can be considered rigid compared to the beam ($z \leq L$). The angular deflection $\Delta\theta$ is then constant for $z \geq L$ and the actual distribution of the applied load is irrelevant, as long as we can assume it is symmetric with respect to the target. We can then use the equivalent concentrated load F applied at the target centre.

The load on the beam, with a small frontal area and far away from the HC axis, will be negligible, as very few particles will impinge on it.

If we now consider the cantilever beam mounted vertically, as shown in Figure 3.3, and include the effect of the weight as a distributed load, the differential equation describing its behaviour changes substantially.

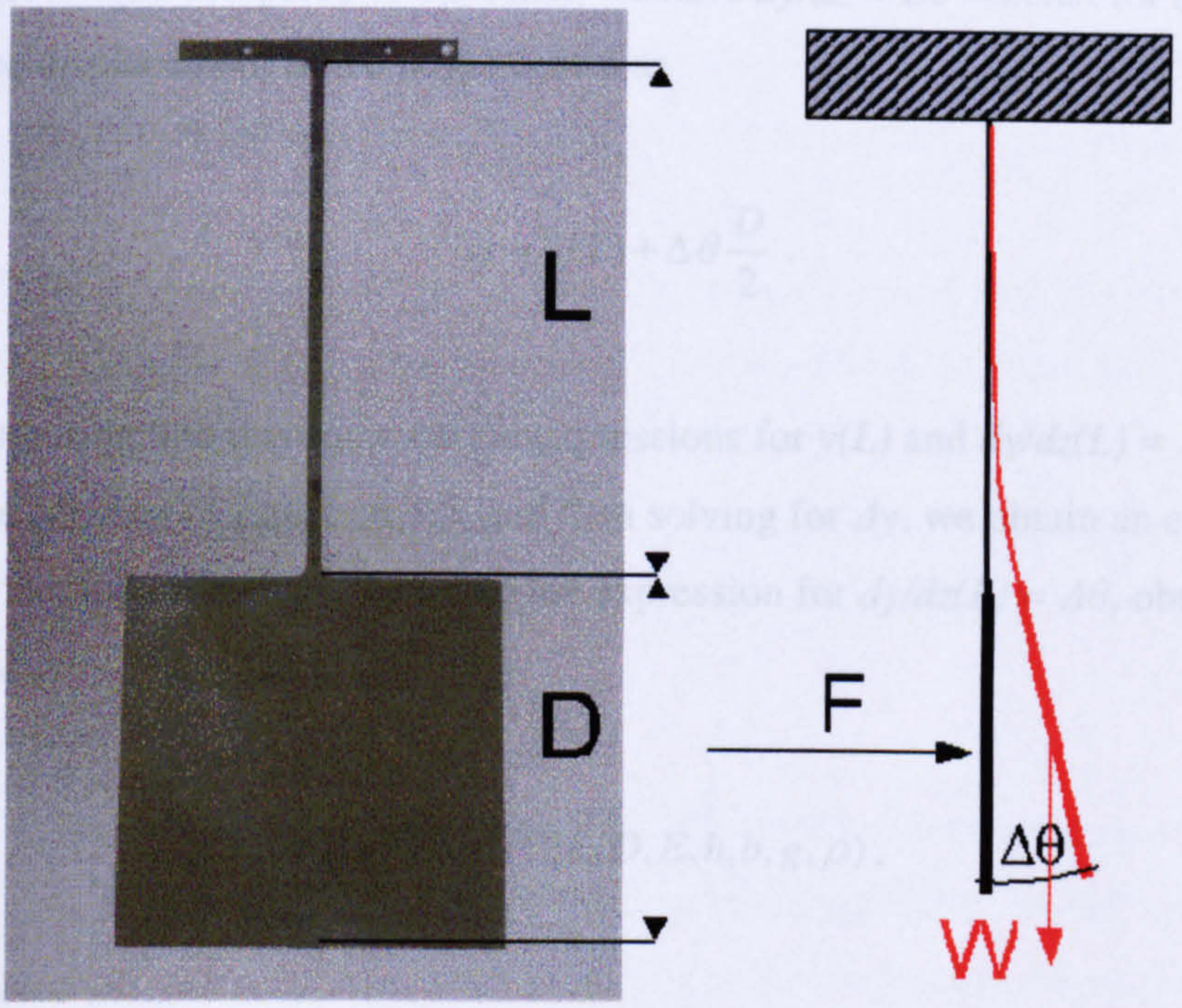

Figure 3.3 – Photo of the target (2GT) mounted vertically, with force diagram.

Assuming instead the weight of the beam to be negligible compared to the weight of the target itself, which is reasonable for our geometries, we can model it simply as a load $W = \rho g h D^2$ concentrated at the centre of the rigid target. Here, ρ is the density of the material and g the acceleration of gravity at sea level. As the beam deflects, the target experiences a rotation $\Delta\theta$ and its centre a displacement $y(L+D/2) = \Delta y$. For small values of the angle $\Delta\theta$, the load F will still be perpendicular to the target *(F cos* $\Delta\theta \sim F$*)*. Thus it can be shown that Equation 3.1 is modified by the addition of a bending moment term, yielding

$$\frac{d^2y}{dz^2} = \frac{1}{EI}\left[F\left(L+\frac{D}{2}-z\right)-W(\Delta y - y)\right], \qquad \textbf{(3.4)}$$

which can be rewritten as

$$\frac{d^2y}{dz^2}-\frac{W}{EI}y=\frac{1}{EI}\left[F\left(L+\frac{D}{2}-z\right)-W\Delta y\right]. \qquad \textbf{(3.5)}$$

This equation can still be solved analytically by treating Δy as an unknown parameter, yielding $y(z)$ as a function of Δy. Then, remembering that, under the assumption that the target is rigid compared to the beam, we have $dy/dz = \Delta\theta = const$ for $z \geq L$, we can write the displacement of the target centre as

$$\Delta y = y(L)+\Delta\theta\frac{D}{2}\,. \qquad \textbf{(3.6)}$$

By substituting into this equation the expressions for $y(L)$ and $dy/dz(L) = \Delta\theta$, obtained from the solution of Equation 3.5, and then solving for Δy, we obtain an expression that we can then substitute back into the expression for $dy/dz(L) = \Delta\theta$, obtaining, for the sensitivity of our CBT:

$$\frac{\Delta\theta}{F}=\frac{1}{W}\Psi(L,D,E,h,b,g,\rho), \qquad \textbf{(3.7)}$$

where Ψ is a function of the CBT geometry and material properties. From this expression it can be immediately seen that, for $F >> W$, the effect of the weight can be neglected. As W increases, gravity will contrast the moment produced by F, decreasing the bending of the beam. For our CBT geometry and material (Al 3003), Equation 3.3, appropriate during the calibration, yields for the sensitivity a value $\Delta\theta/F = 1.60\ \mu rad/\mu N$. Equation 3.7, appropriate during the actual thrust measurements, yields $\Delta\theta/F = 1.23\ \mu rad/\mu N$. If we used the uncorrected value from the simple Equation 2.3, we would be underestimating our thrust by 23%.

The introduction of this correction is only necessary when the CBT is mounted in a vertical position, as it was during our initial experiments (1GT and 2GT). In order to decouple the effect of the target weight and of the HC thrust, in the actual thrust measurements reported in this thesis, performed with the 3GT, a different

configuration was adopted, with the CBT rotated by 90° with respect to the present set-up (beam axis horizontal). In this way, the moments produced by F and W act perpendicularly to each other. With a beam with b substantially greater than h, the bending caused by the weight becomes negligible, as the moment of inertia around the neutral axis is $I = bh^3/12$ for F but $I' = hb^3/12$ for W. For the CBT used in the actual thrust measurements (3GT with h = 1.0 mm), for example, the sensitivity to bending by the weight, calculated using the simple beam equation 3.3, would be 16 times as small as the one by the thrust. This ratio could be easily varied with slight changes in the beam geometry but, as the two deflections are now decoupled, the thing is hardly necessary, as the weight no longer causes an error in the thrust measurement.

The CBT-LOL measurement system was originally designed with the purpose of measuring the static response of a beam to an applied load. In order to address the issues detailed in the chapter on hot thrust and alleviate the problems related to thermal deformation, it was decided to take thrust measurements at HC switch-off. In this way, the oscillations of the CBT do not have time to actually converge to the static solution due to damping.

The time necessary for the oscillations to be effectively damped depends essentially on the beam geometry and material properties, namely density, Young's modulus and a damping coefficient. Several models have been developed to address this phenomenon. For low levels of damping and within the linear region of the viscoelastic material, these models are quite equivalent and can be easily related to each other. Thus, the hysteretic loss factor η (energy dissipated during one cycle per radian/maximum strain energy in the cycle) is twice the viscoelastic damping ratio. The oscillations of the system will decrease exponentially in amplitude according to these coefficients. Aluminium, with $\eta = 0.0001 - 0.0006$, is one of the metals with the lowest damping. This produced very persistent oscillations during our first experiments. Dynamic transient simulations have been run in ANSYS®. These showed that the transient oscillations actually converge to a steady-state solution that can be determined with a static analysis. Unfortunately, due to the difficulties involved in accurately modelling the damping, it has not been possible to progress beyond qualitative indications.

Simulations in ANSYS® have confirmed to a high degree of accuracy the values of sensitivity obtained from analytical calculations for both 2GT and 3GT. A sample calculation of the static deflection of a 3GT under a force of 1 mN applied at the centre of the target is shown in Fig. 3.4.

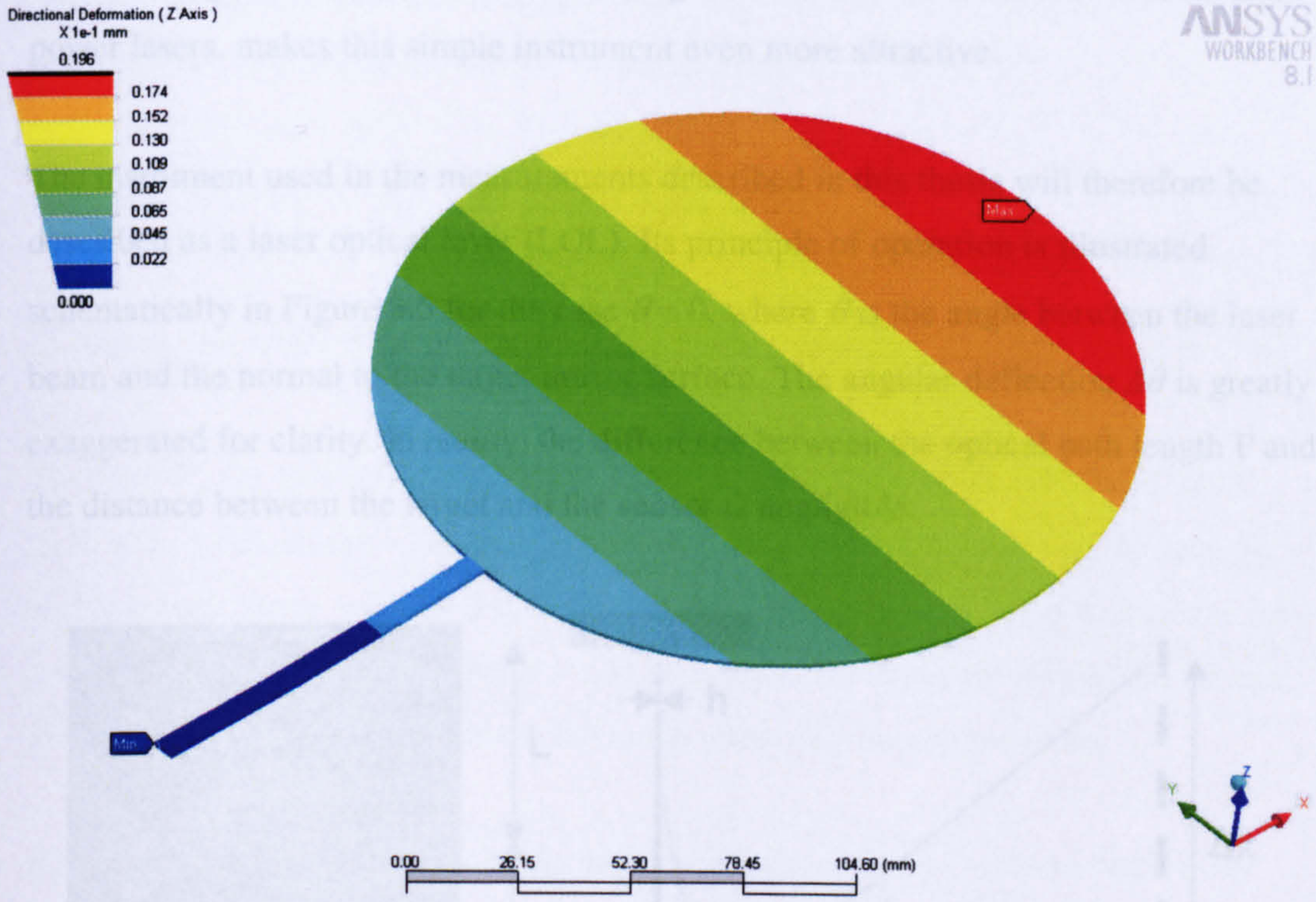

Figure 3.4 – 3GT static deflection, $F = 1$ mN.

3.2 – Measurement of Small Angular Deflections: the Laser Optical Lever

The accuracy of our thrust measurement is essentially dependent on the resolution with which we can measure the displacement of the free end of our beam or its angular deflection. We have decided to measure the angular deflection with an optical lever. This has the twofold advantage of making the measurement independent of the exact position along the beam where it is taken and of being non-intrusive and immune from any kind of interference from the plasma environment.

Optical levers have been long used in many applications. The first light beam deflection galvanometer appeared in 1826. In that year, Poggendorff invented a

system to read with great sensitivity the new type of galvanometer just built by Nobili. In these old instruments, a collimated beam of light was reflected off a flat mirror attached to the surface of which the angular deflection was to be measured. By employing long optical paths, of the order of several meters, the deflection could be easily read as a movement of the end of the beam on a scale. The modern availability of narrow light beams, collimated over long distances, in the form of low-to-medium power lasers, makes this simple instrument even more attractive.

The instrument used in the measurements described in this thesis will therefore be described as a laser optical lever (LOL). Its principle of operation is illustrated schematically in Figure 3.5 for the case $\theta = 0$, where θ is the angle between the laser beam and the normal to the target mirror surface. The angular deflection $\Delta\theta$ is greatly exaggerated for clarity. In reality, the difference between the optical path length P and the distance between the target and the sensor is negligible.

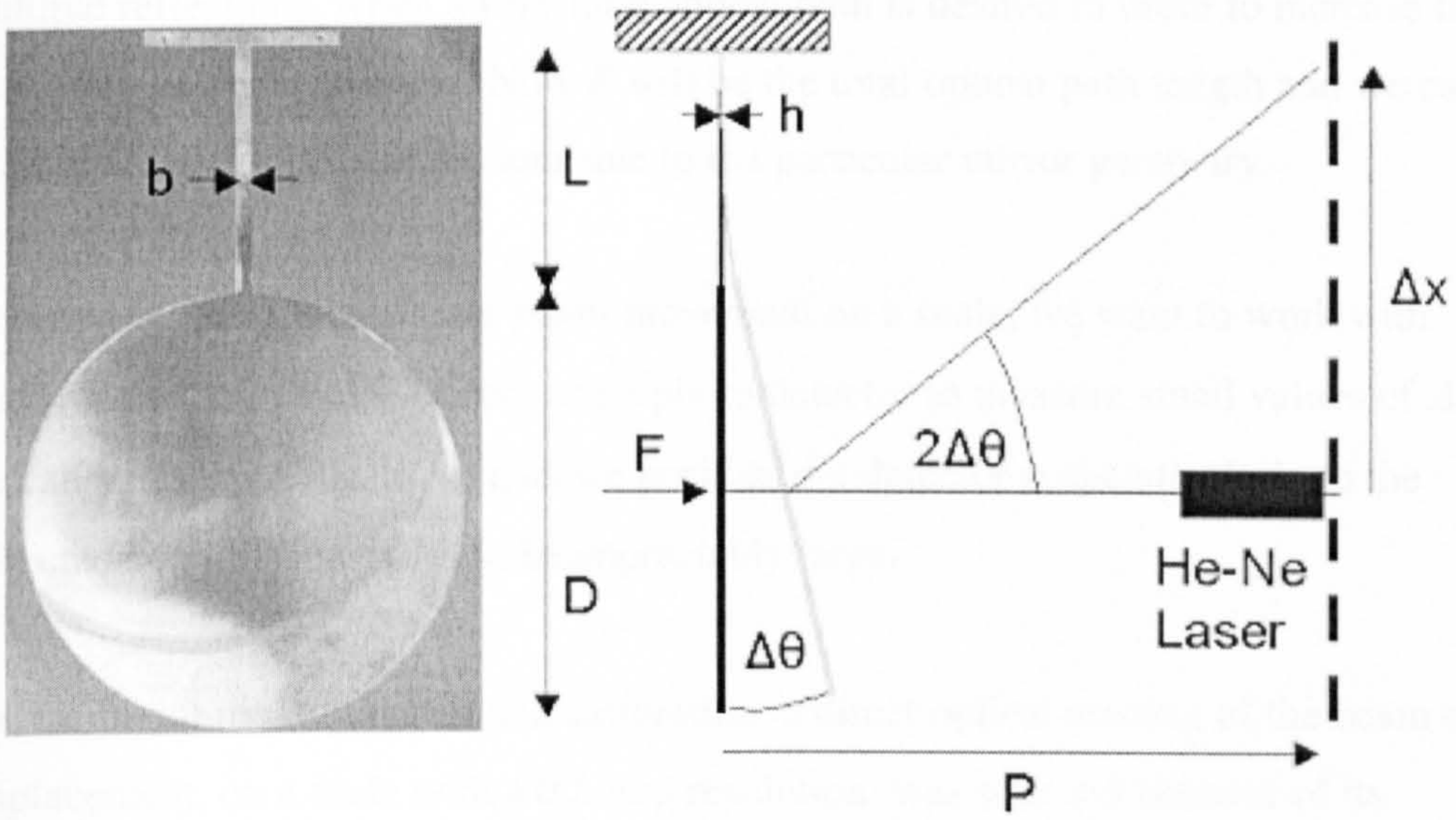

Figure 3.5 – Principle of operation of a LOL, together with a photo of the target (3GT) mounted horizontally, with force diagram.

For this simple case, which approximates well to the actual experimental conditions, the displacement of the laser beam end, Δx, is given by

$$\Delta x = 2P\Delta\theta \tag{3.8}$$

Provided that the angular deflection $\Delta\theta$ is small. In general, for $\theta \neq 0$, Δx can be written as

$$\Delta x = P[tan(\theta + 2\Delta\theta) - tan\,\theta] \tag{3.9}$$

which, if $\Delta\theta$ is much smaller than the initial angle θ, reduces, through a first-order Taylor series expansion and the use of trigonometric identities, to

$$\Delta x = 2P(1 + tan^2\,\theta)\Delta\theta \tag{3.10}$$

If, in turn, the angle θ is small as well, the above expression further reduces to (3.8).

For $\theta = 10°$, for example, the difference between the value of Δx calculated using (3.8) and (3.10) is only ~3%. Expression (3.8) also remains accurate in the case of multiple reflections, when a very long optical path is desired in order to increase the sensitivity of the instrument. Now P will be the total optical path length and we can, in general, neglect the corrections due to the particular mirror geometry.

If, instead of reading the laser beam movement on a scale, we want to work with small values of P, and therefore use a photo detector to measure small values of Δx, we can still use (3.10), as long as we position the detector perpendicularly to the reflected beam if θ happens to be appreciably large.

For the initial measurements and calibration, a direct optical reading of the beam end displacement, on a scale with a 0.5 mm resolution, was selected because of its simplicity. This required large values of Δx, and therefore the use of long optical paths, obtained through multiple reflections of the laser beam. In order to have a reasonably small light spot on the measuring scale, it was necessary to decrease the beam divergence. This was performed by expanding and collimating the beam with various optical arrangements, described in the following section.

3.3 – Initial Target Calibration and System Validation

3.3.0 – General Remarks

Our device approximates extremely well to a slender beam connected to a load (the square target, of much higher stiffness). Therefore, it was felt that the theoretical predictions regarding beam deflection would be verified to a high degree of accuracy. Nevertheless, a direct calibration of our system was performed, using the LOL to measure the angular deflection. This also allowed us to tackle the various practical problems concerning beam divergence and, in general, the optical set-up required. The LOL with direct optical reading on a scale does not need any calibration, just an accurate knowledge of the optical path geometry. Therefore, a good agreement between beam theory predictions and LOL measurements would be sufficient to corroborate both.

3.3.1 – Calibration Set-Up

For the calibration, the target, mounted on the stand that would be used in the actual measurement, was set up in a horizontal position, on an optical table (see Fig. 3.6).

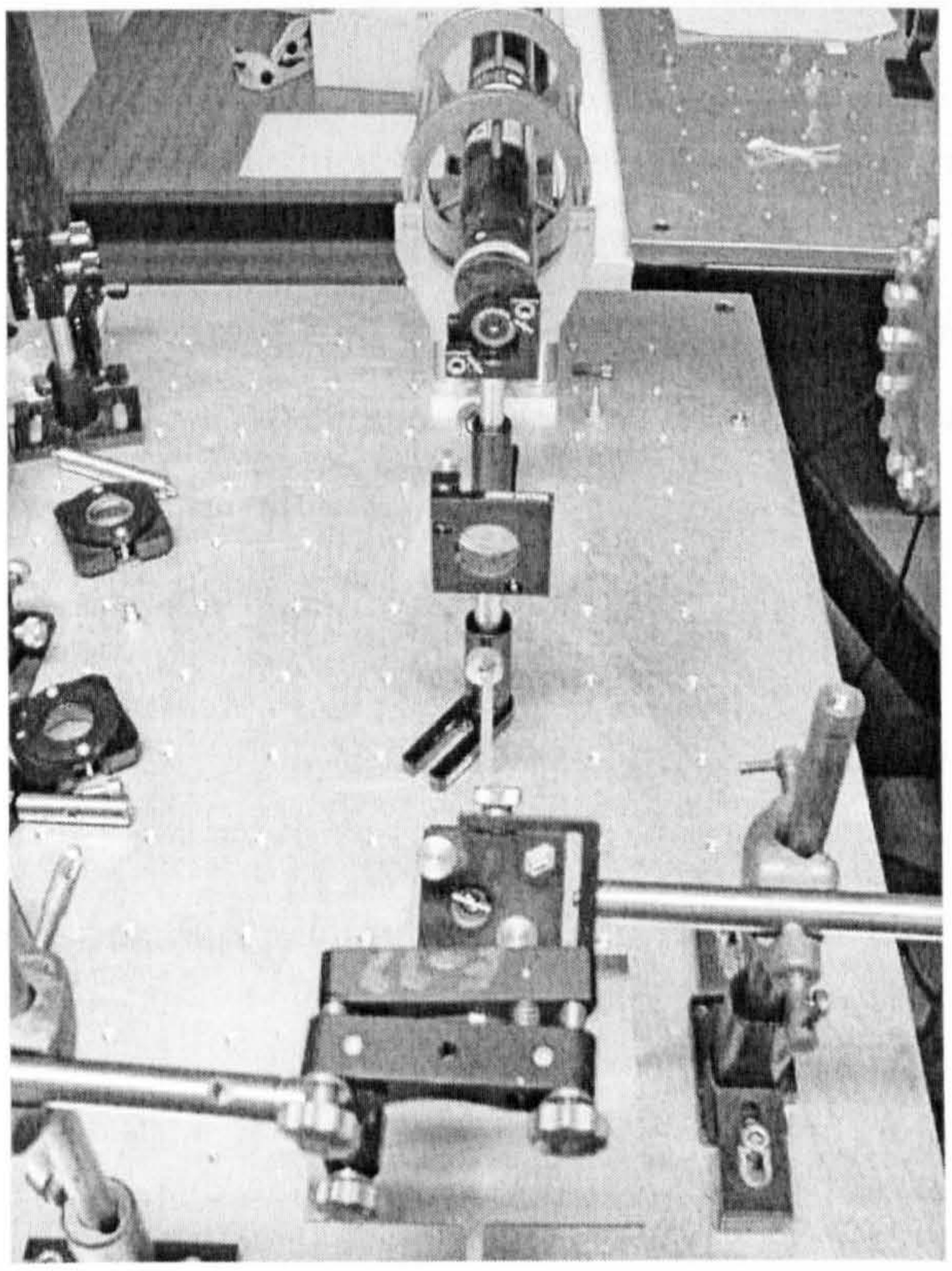

Figure 3.6 – The calibration set-up.

A mirror at ~ 45° with respect to the incident beam from a green (λ = 543.5 nm) He-Ne laser directs it onto a small mirror fixed to the target and the reflected beam then passes onto a system of mirrors. Through multiple reflections, optical path lengths of up to ~30 m have been easily achieved. At such lengths, though, vibrations caused by external disturbances render the reading of the beam's spot position on the scale extremely difficult.

One of the main problems while operating with a laser beam is that, in spite of its good collimation, it will spread considerably over long distances. Even if a Gaussian TEM_{00} laser beam wavefront is made perfectly flat at some plane, it will quickly acquire curvature and begin spreading in accordance with [140]

$$w(z) = w_0 \sqrt{1 + \left(\frac{\lambda z}{\pi w_0^2} \right)^2} \qquad \textbf{(3.11)}$$

Here z is the distance propagated from the plane where the wavefront is flat, λ is the wavelength and $w(z)$ is the beam radius after the wave has propagated a distance z.

The beam radius is commonly defined as the radius at which the irradiance (intensity) has fallen to $1/e^2$ (13.5 %) of its peak, or axial, value. At the plane where the wavefront is flat the laser beam is said to have a *waist*. The beam radius at this location ($z = 0$) is called the waist radius, $w(0) = w_0$. For large values of z, w(z) asymptotically approaches the value

$$w(z) \cong \frac{\lambda z}{\pi w_0} \qquad \textbf{(3.12)}$$

and the $1/e^2$ irradiance contours asymptotically approach a cone of semi-aperture

$$\theta_{FF} = \frac{w(z)}{z} = \frac{\lambda}{\pi w_0} \, . \qquad \textbf{(3.13)}$$

This value is the half-angle of divergence of the Gaussian TEM_{00} beam.

From (3.13) it is clear that, in applications where the optical path is of considerable length, it is advantageous to operate at shorter wavelengths. Also, most He-Ne lasers present an output beam with an extracavity waist, formed by a weak meniscus lens. The beam diameter commonly published in optical catalogues is twice this waist radius. Thus, for our application, a Melles Griot 05-LGP-151 green He-Ne laser, with $\lambda = 543.5$ nm and beam diameter = 0.77 mm was preferred over two red ($\lambda = 632.8$ nm) He-Ne lasers available, with beam diameters of 0.59 mm and 0.80 mm, as any reduction in divergence would be advantageous and quickly offset a smaller initial beam diameter in the far field. Also, green lasers have up to five times more visibility than red lasers with the same output power [141]. This facilitates aiming and pointing.

Even the selected laser, though, with a divergence $\theta_{FF} = 0.45$ mrad, would produce a spot of 9 mm diameter at a distance $z = 10$ m. It is therefore necessary to further reduce the divergence by expanding and refocusing the beam, in order to produce a waist of bigger radius. This can be simply achieved by using two confocal lenses, either both converging (Keplerian beam expander) or one converging and the other diverging (Galilean beam expander), as shown in Figure 3.7.

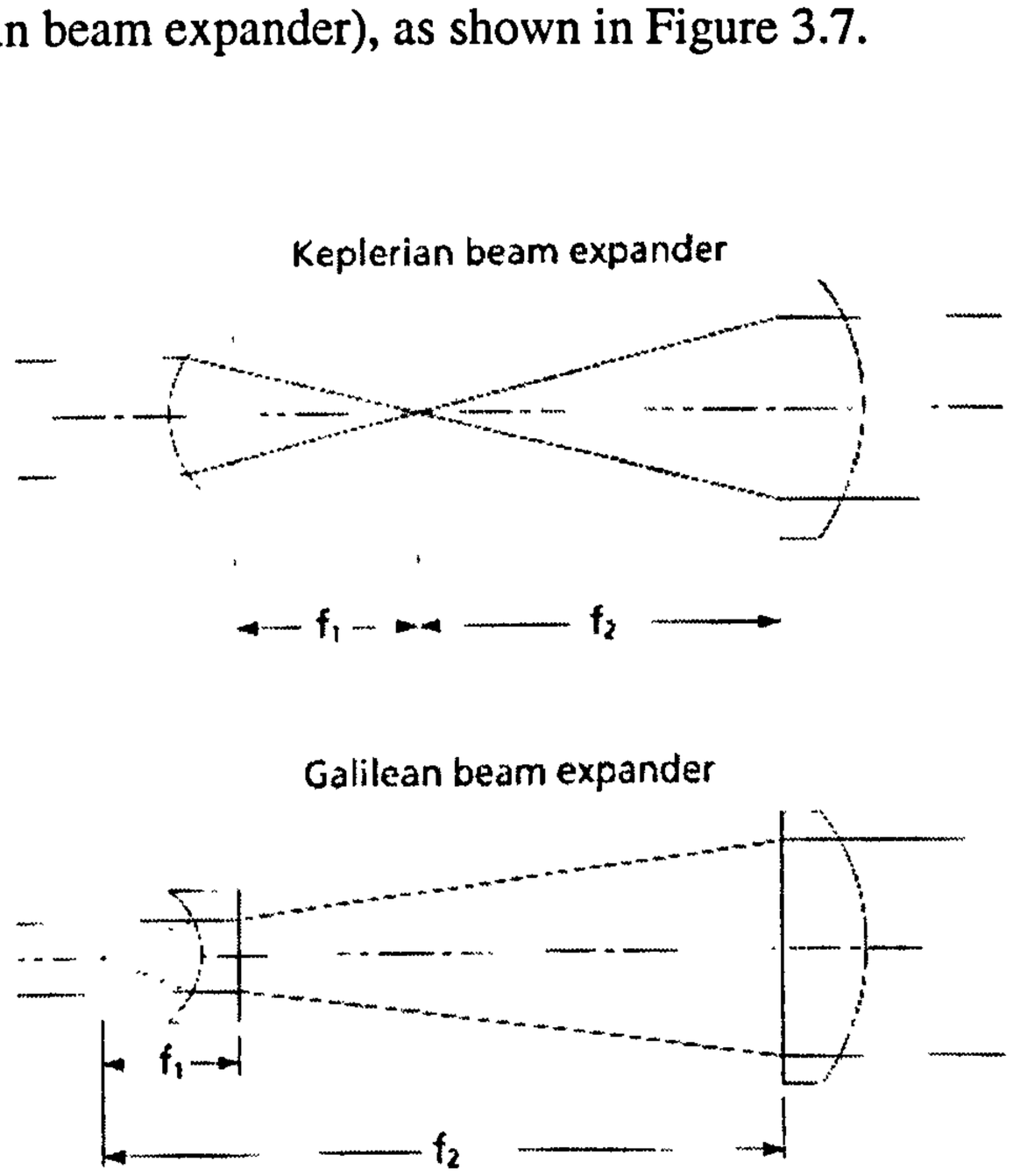

Figure 3.7 – The two types of beam expanders [140].

Using basic geometrical optics (see Figure 3.7), the overall length of the optical system OVL is

$$OVL = f_1 + f_2 \tag{3.14}$$

and the magnification MAG is

$$MAG = \frac{f_2}{f_1} \tag{3.15}$$

where f_1 and f_2 are the focal lengths of the two lenses.

Both types of beam expander were tried during the calibration, with various lenses of different focal lengths. The behaviour of a Gaussian beam can be significantly different from that which would be anticipated on the basis of simple geometrical optics, especially when, as in our case, a lens is placed in the near field of the incident beam. Throughout this work, the optimal set-ups were found by a combination of empirical adjustment and attention to the less familiar aspects of Gaussian beam optics [140, 142].

Good results have been obtained with a plano-convex lens with $f = 25.4$ mm (1") combined with other converging lenses of higher focal lengths. A neutral density filter (ND = 4) placed in front of the scale helps to reduce the size of the spot by cutting off the edges of the "spread" beam. This greatly facilitates the reading. Eventually a clear circular spot of ~ 3 mm diameter was obtained with a beam path of length $L = 18$ m.

3.3.2 – Results: Relative Calibration

Several targets were machined at the Engineering Design and Manufacturing Centre (EDMC) of the University of Southampton. Three of these, identical in shape but with different values of thickness h, were selected for our relative calibration. The thinnest one ($h = 0.8$ mm) was intended for the actual measurement in the vacuum chamber. The other two ($h = 1.5$ and 2.0 mm) were calibrated according to the method described in the previous section.

Our measurements, taken with different configurations of the LOL, extend into the sub-mN level, of interest here because the thrust obtainable from a T6 HC lies in such a range, as shown in Chapter 2 and in a previous paper [48]. Figure 3.8 shows the results for the targets with h = 1.5 and 2.0 mm, with their error bars and linear regressions and compares them with the predictions obtained from the theory of slender beams, also given with their uncertainty range (dashed lines). It can be seen that actual measurements and theoretical predictions show perfect agreement, well within errors and uncertainties.

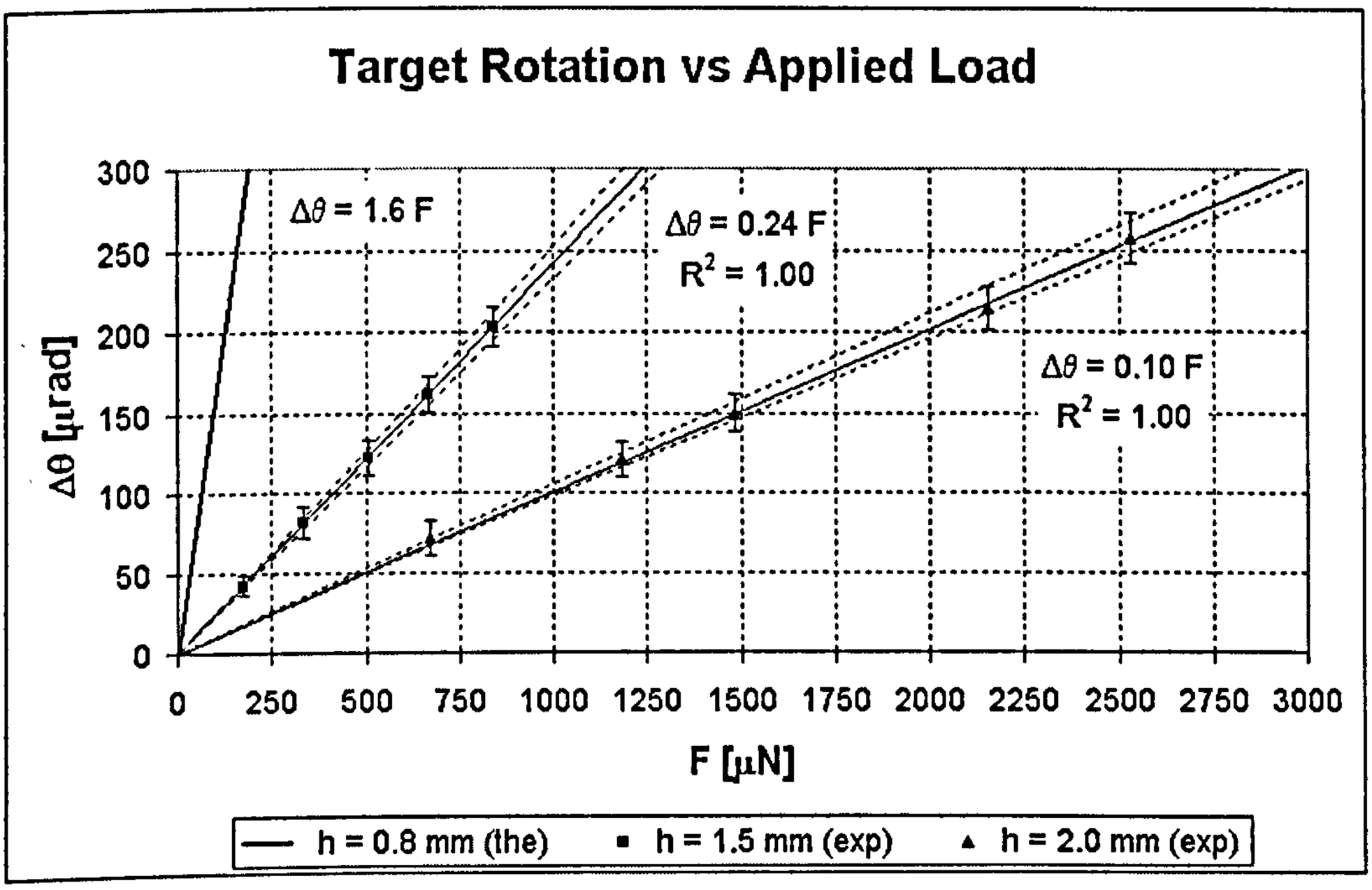

Figure 3.8 – Relative calibration results.

The error bars associated with the measurements were calculated from the errors in measuring the optical path length and the resolution to which the beam movement can be read on a scale with 0.5 mm divisions. The error in the theoretical predictions is given mainly by the precision of the mechanical machining, and therefore by the error in the geometrical dimensions of the cantilever beam target. The excellent agreement between theory and experiments confirms that the sensitivity scales like $1/h^3$ and allows us to confidently use Eq. (3.3) to calculate the sensitivity of the target with h = 0.8 mm, also shown in Figure 3.8 as a thicker line. It is not possible to calibrate the

thinner target with weights, because it would deflect excessively under its own weight. It is therefore necessary to resort to a relative calibration.

Using the CBT already available, with $h = 0.8$ mm ($\Delta\theta / F = 1.6$ μrad/μN) and a LOL arrangement with an optical path length $P = 30$ m, a thrust $F = 50$ μN would give a displacement of the laser beam end $\Delta x = 4.8$ mm. This could be read on an optical scale with 0.5 mm divisions, resulting in an estimated error of ~ ± 10%. Smaller thrusts can easily be measured by using thinner CBTs or different ways of measuring the beam displacement, such as photo detectors.

3.4 – Electrostatic Calibration

A different type of calibration was attempted with the 3GT, after implementing the PSD (Position Sensitive Detector, see Chapter 4). Instead of performing again a relative calibration, by having a target identical to the one that would be used for the actual thrust measurements, but thicker, in order not to undergo plastic deformation when mounted horizontally to receive the precision weights, it was decided to carry out a direct calibration with electrostatic forces. An identical target was mounted rigidly to a support next to the target cantilevered in the way that would be used in the thrust measurements. By grounding one and connecting the other to a power supply, a parallel-plate (disc) capacitor was formed [143]. The force between the plates could then be varied by simply varying the potential difference between them.

Unfortunately, it was only possible to obtain qualitative results, due to the difficulty of positioning the two plates with accuracy sufficient for a precise determination of the force exerted. However, even if a quantitative estimate of the target sensitivity was not obtained, the linear dependence of the target deflection on the voltage and therefore the force was verified to a great degree of accuracy. A typical result is shown in Fig. 3.9.

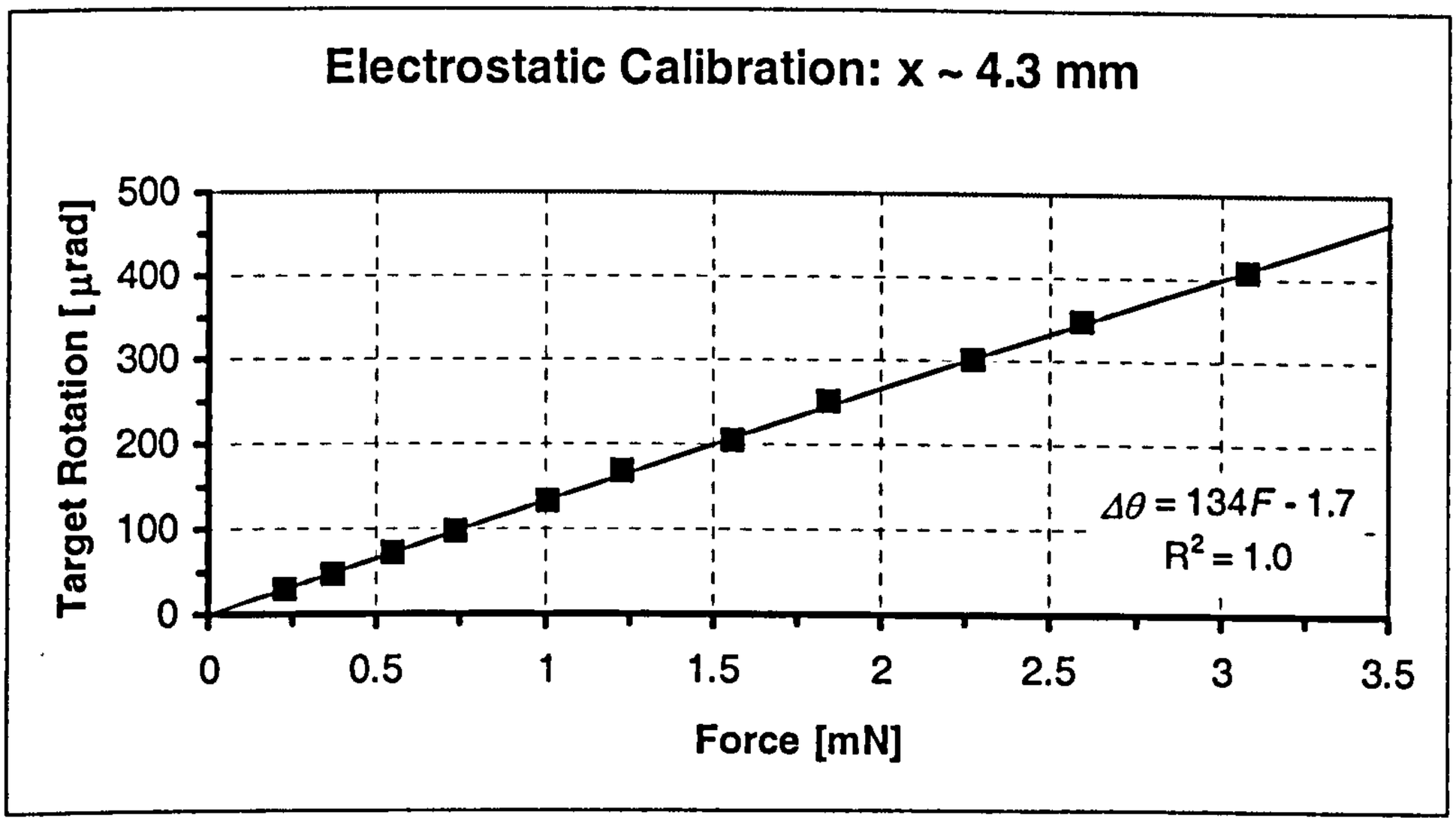

Figure 3.9 – Electrostatic calibration.

Chapter 4

Experimental Apparatus and Procedures

4.0 – Vacuum Rig

The vacuum rig used in the experimental campaign is, essentially, that constructed by Edwards [98] and modified by Milligan [144]. It is shown in Fig. 4.1. High vacuum ISO and CF flanges are used throughout the chamber. Pumping is achieved by the use of a rotary (Pfeiffer Balzers DUO 016B) and a turbo-molecular pump (Pfeiffer Balzers TPH 520 KTG) connected in series. In order to avoid oxygen poisoning of the HC, a background pressure in the 10^{-7} mbar range has to be reached prior to commencing an experimental run. Depending on the set-up, this may require running the pumping system overnight.

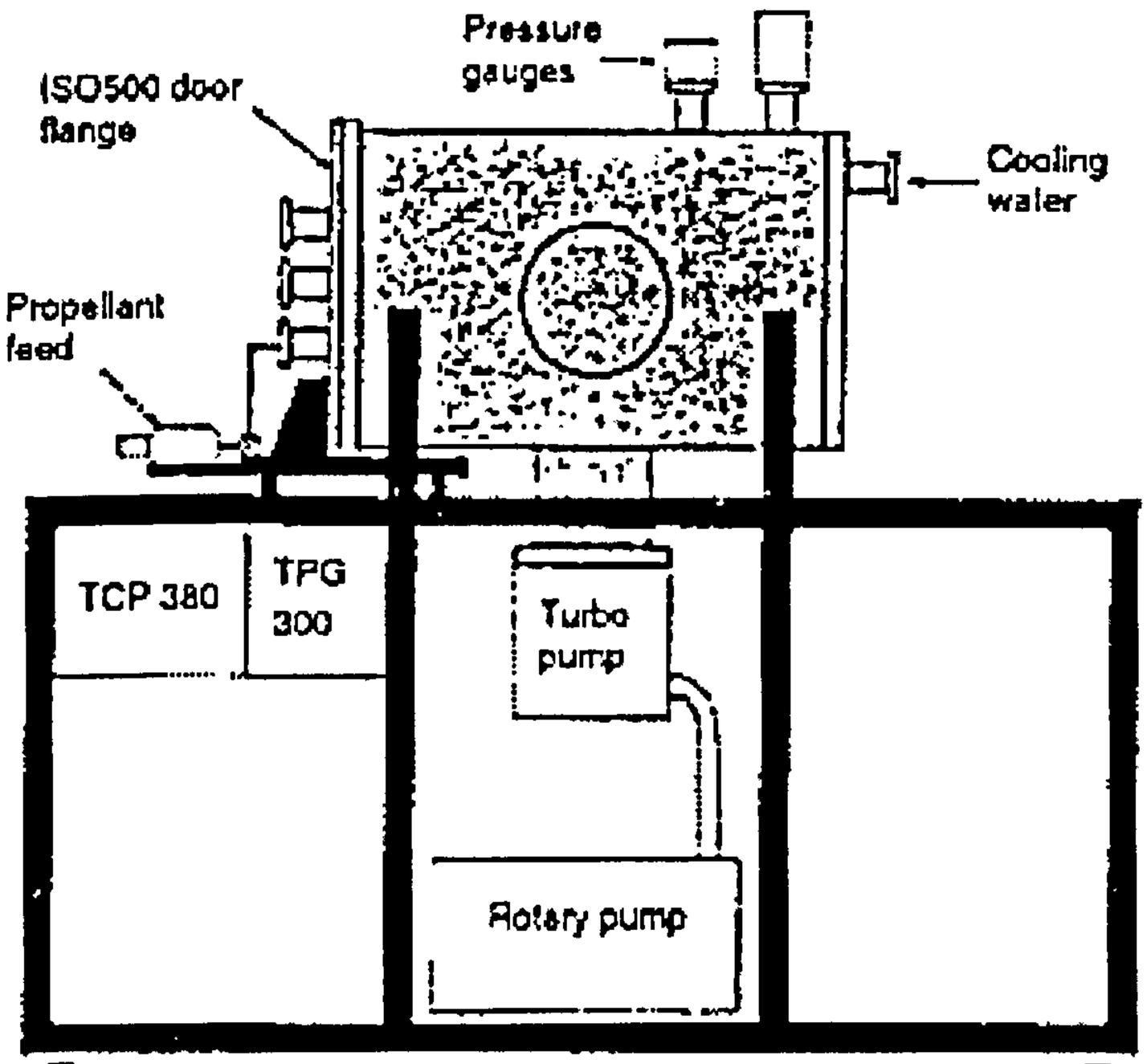

Figure 4.1 – The vacuum rig.

4.1 – Propellant Feed System

The propellant gas, generally high-purity argon or another noble gas, is fed into the HC from a pressurised bottle, through a pressure regulator and a needle valve. The latter allows the $\dot{m}$ to be set accordingly to the calibration described in the following section. The Negretti needle valve used in the experiments carried out with the 1GT and the 2GT, as well as in all the previous experiments by Edwards, Milligan and Rudwan, had to be replaced with an Edwards FCV10K extra fine control needle valve due to its failure.

To minimise the risk of oxygen poisoning of the HC, the high-purity argon is passed through an oxygen trap, mounted just prior to the needle valve. The original trap, first used by Edwards, was replaced, together with the needle valve, with two new ones: an indicating oxygen trap in series with a higher capacity one, both supplied by Agilent. This improves on the original design by Edwards by allowing monitoring of the trap status: when the indicating trap starts absorbing oxygen the high-capacity one, mounted upstream, needs to be replaced.

4.2 – The T6 Hollow Cathode / Anode Assembly

The HC investigated at the University of Southampton is the one designed for the T6 Kaufman-type ion thrusters [46, 47]. The basic features of this cathode have essentially remained unchanged since the start of the development programme and are described, together with the physics of HC operation, in numerous papers [33, 47, 48, 145]. The initial orifice diameter of this HC was 0.5 mm. This is a smaller value than those used in most measurements by other investigators, as the orifice diameter was one of the parameters the influence of which on the ion emission and the thrust we intended to explore. However, after the initial experimental runs described in Section 5.0.1, a certain amount of erosion was already visible. It has been observed in various experiments that, when operating a T6 HC at discharge currents above 10 A, a small orifice will quickly erode until it attains a diameter of about 0.7-0.8 mm [146]. In our case, the orifice diameter stayed at ~0.5 mm throughout our experiments, until it was drilled out to bring it to 1.0 mm, in spite of a substantial erosion of the HC tip face,

which caused a total, cumulative loss of ~20% of the initial orifice length. Due to a certain amount of material redeposition, actually, the orifice shape became irregular, with a diameter not exceeding ~0.45 mm, in some directions.

In all the experiments the HC was operated in an open-diode configuration, without using a keeper electrode. A circular anode, manufactured from a 100-mm diameter stainless steel disc, with a central orifice, was mounted in front of the HC tip, as shown in Figure 4.2.

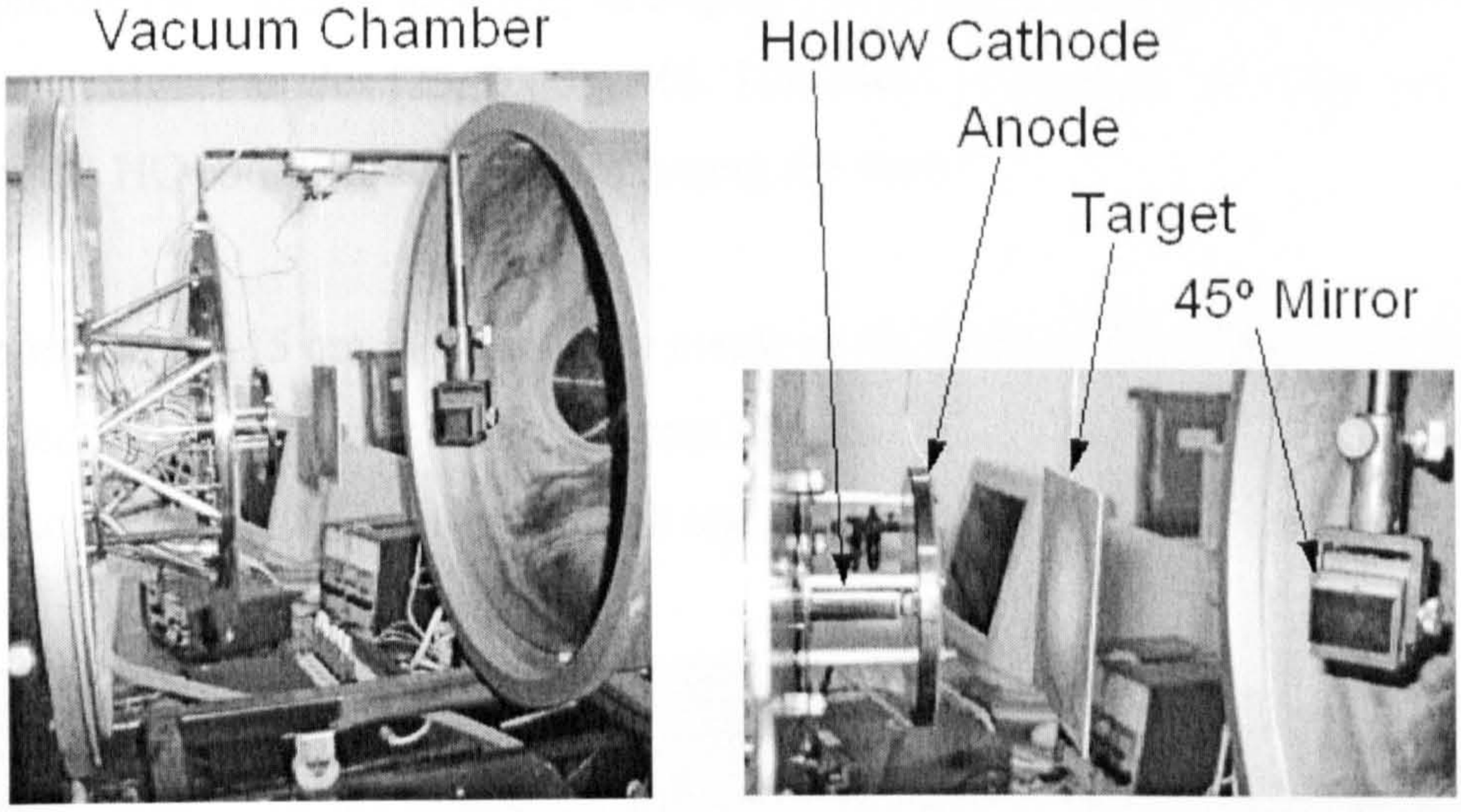

Figure 4.2 – The HC / anode and target (2GT, vertical mounting) assemblies in the vacuum chamber, with the internal mirror: detail on the right.

The initial value of the anode orifice diameter, 10 mm, was later increased to 20 mm and then to 40 mm. The HC-anode distance was 4.5 mm during the initial characterization described in Section 5.0.1. It was then reduced to 2.0-2.5 mm, effectively halving it, and kept at this value during all the thrust measurements. In all configurations, intense heating of the anode was observed, especially when operating in a plume mode. A visual examination of the anode face after many experimental runs revealed the presence of tantalum, sputtered from the HC tip. This was confirmed by an accurate Scanning Electron Microscope (SEM) analysis, the results of which are reported in Section 4.6.

4.3 – The Target Assembly

The CBT is mounted on an L-shaped support, connected to a UK-25 ion thruster back plate. It is positioned in front of the HC / anode assembly, with the centre of the target on the axis of radial symmetry, as shown in Fig. 4.2 (2GT). Through a micro-translation mechanism it is possible to finely adjust the target distance from the HC. The mechanism itself can be mounted at different positions on the support.
Measurements of the angular distribution of ion current show that most of the ions escape from the HC / keeper assembly at angles <30°, even if significant amounts are still present at higher angles [25, 26, 39, 40]. Therefore, positioning the target too far away from the HC could entail underestimating the thrust.

A 3GT, mounted at ~15 cm in front of the anode in the fashion described in Section 3.1, was used for all the thrust measurements reported in this thesis. Fig. 4.3 shows the differences between this set-up and the one used with the 2GT (see Fig. 4.2).

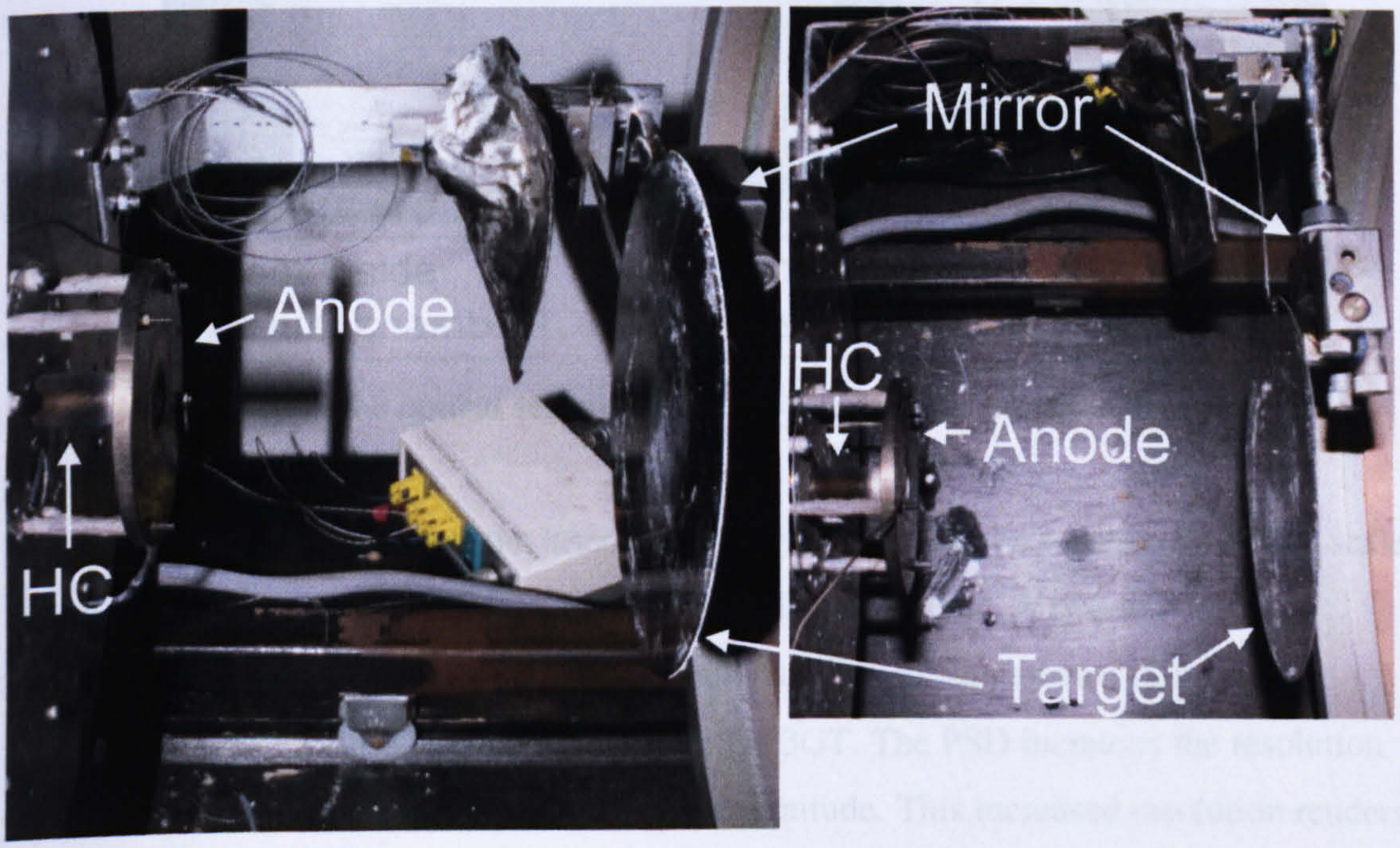

Figure 4.3 – The 3GT mounted in front of the HC/anode assembly: side view (left) and top view (right).

4.4 – The Optical Set-Up

A version of our LOL was set up with components both inside and outside the vacuum chamber, as shown in Figs. 4.4 (2GT experiments) and 4.5 (3GT experiments). It consisted of a green He-Ne laser mounted externally, two convex lenses forming a Keplerian beam expander (see Section 3.2) and four mirrors, one of which was the polished backside of the target, facing away from the HC. Two of the remaining mirrors are visible in Figs. 4.2, 4.4 and 4.5. These mirrors directed the laser beam onto the target inside the chamber and then the reflected beam outside, along an optical path with a length $P = 9.0$ m (1GT experiments), $P = 9.2$ m (2GT experiments) and P = 1.05 m (3GT experiments).

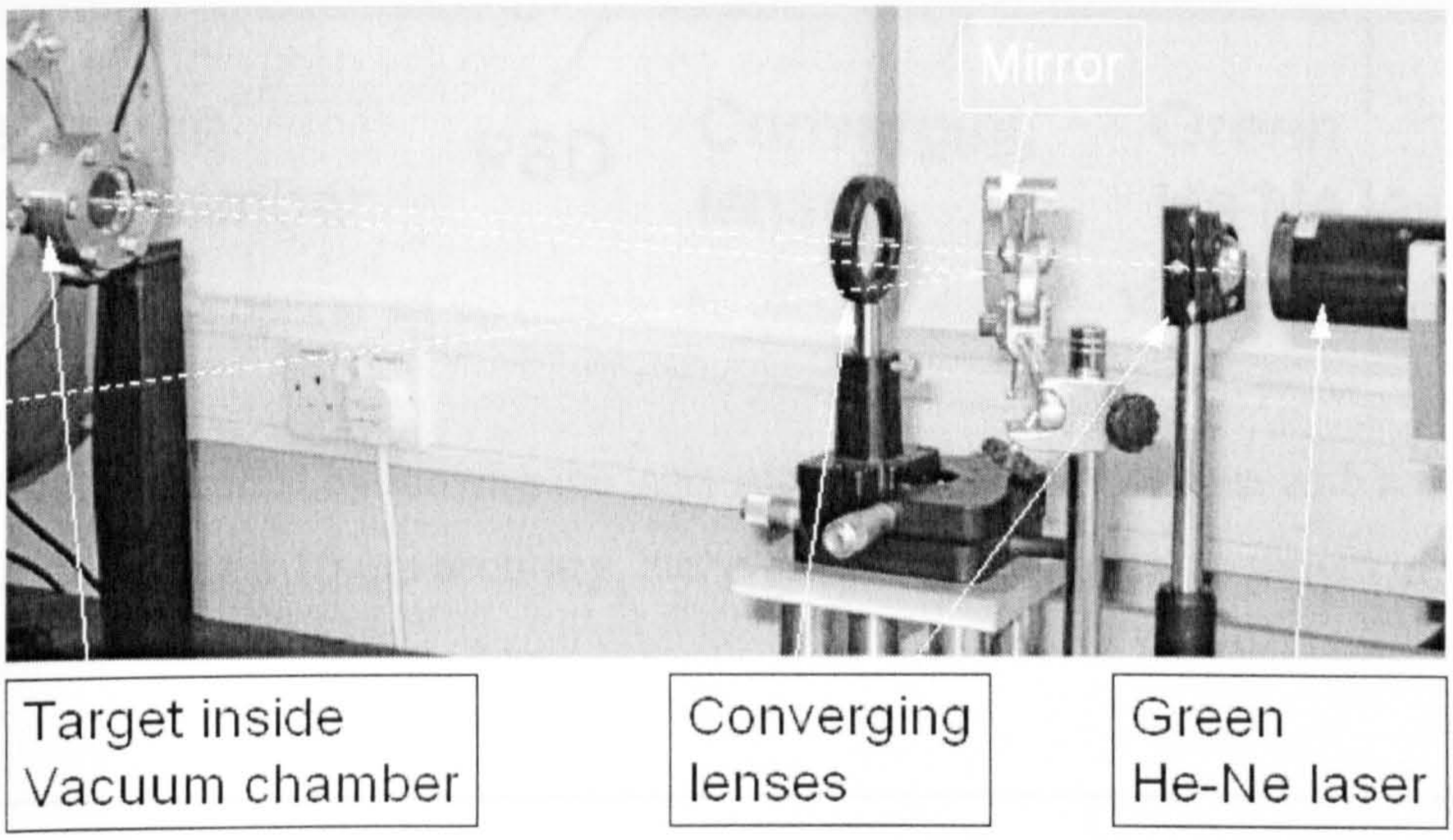

Figure 4.4 – The optical set-up outside the vacuum chamber, 2GT experiments.

The total displacement of the laser beam was read visually on a screen through a scale with a 0.5-mm resolution in the 1GT and 2GT experiments. A two-dimensional Position Sensitive Detector (PSD) was purchased from Hamamatsu [50] and implemented for use in experiments with the 3GT. The PSD increases the resolution of the displacement reading by orders of magnitude. This increased resolution renders the use of long optical paths to magnify the laser spot movement unnecessary. This in turn may eliminate the need for a beam expander to decrease the beam divergence and limit the size of the laser spot. Another great benefit is the possibility to follow and

record the time history of the laser beam movement with a visually unattainable accuracy, as the PSD time response is of the order of microseconds.

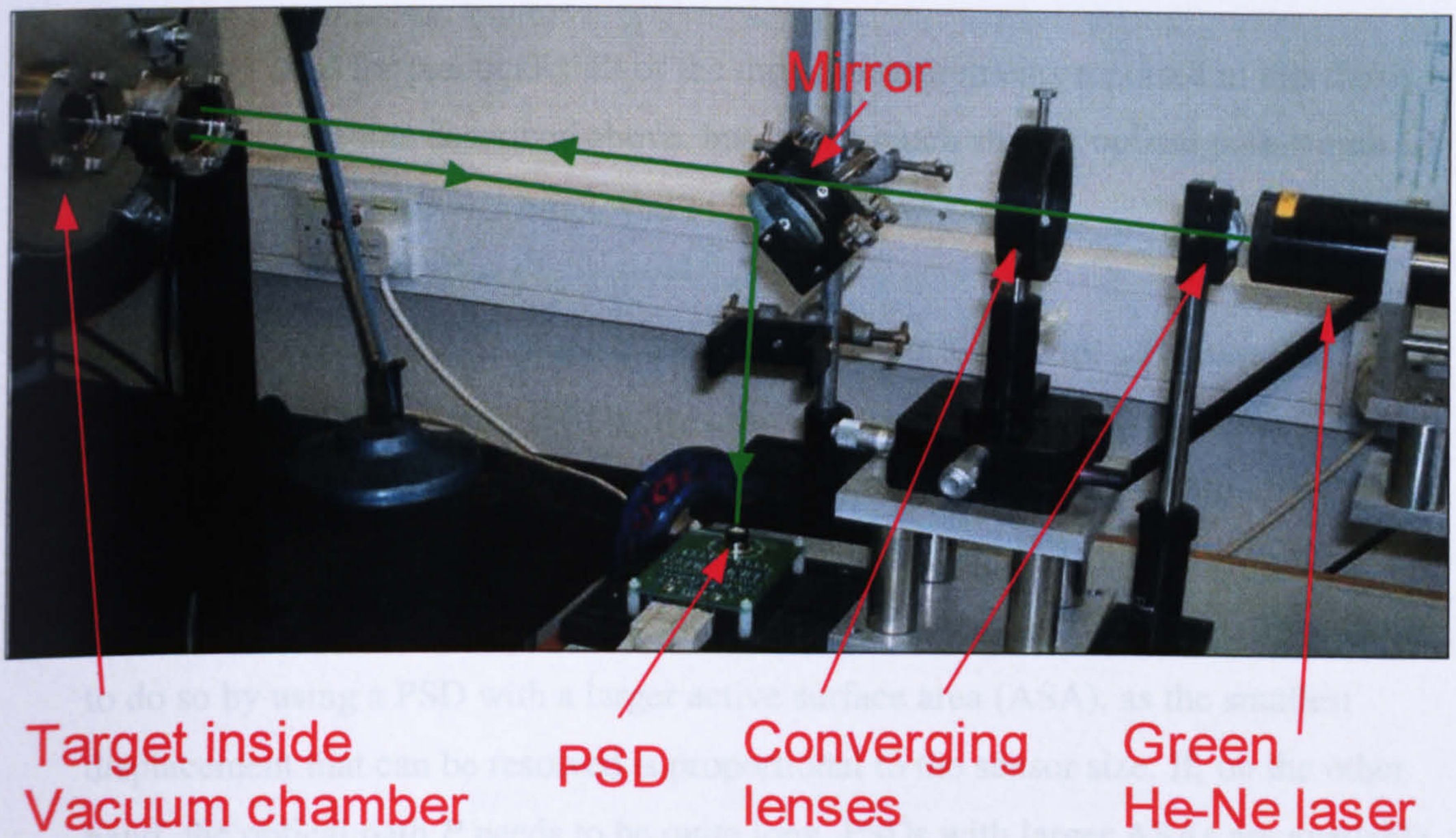

Figure 4.5 – The optical set-up outside the vacuum chamber, 3GT experiments.

A calibration, performed by moving the laser spot across the sensor area with a micro-translation stage with a 10-μm accuracy, has given excellent results, as shown in Figure 4.6.

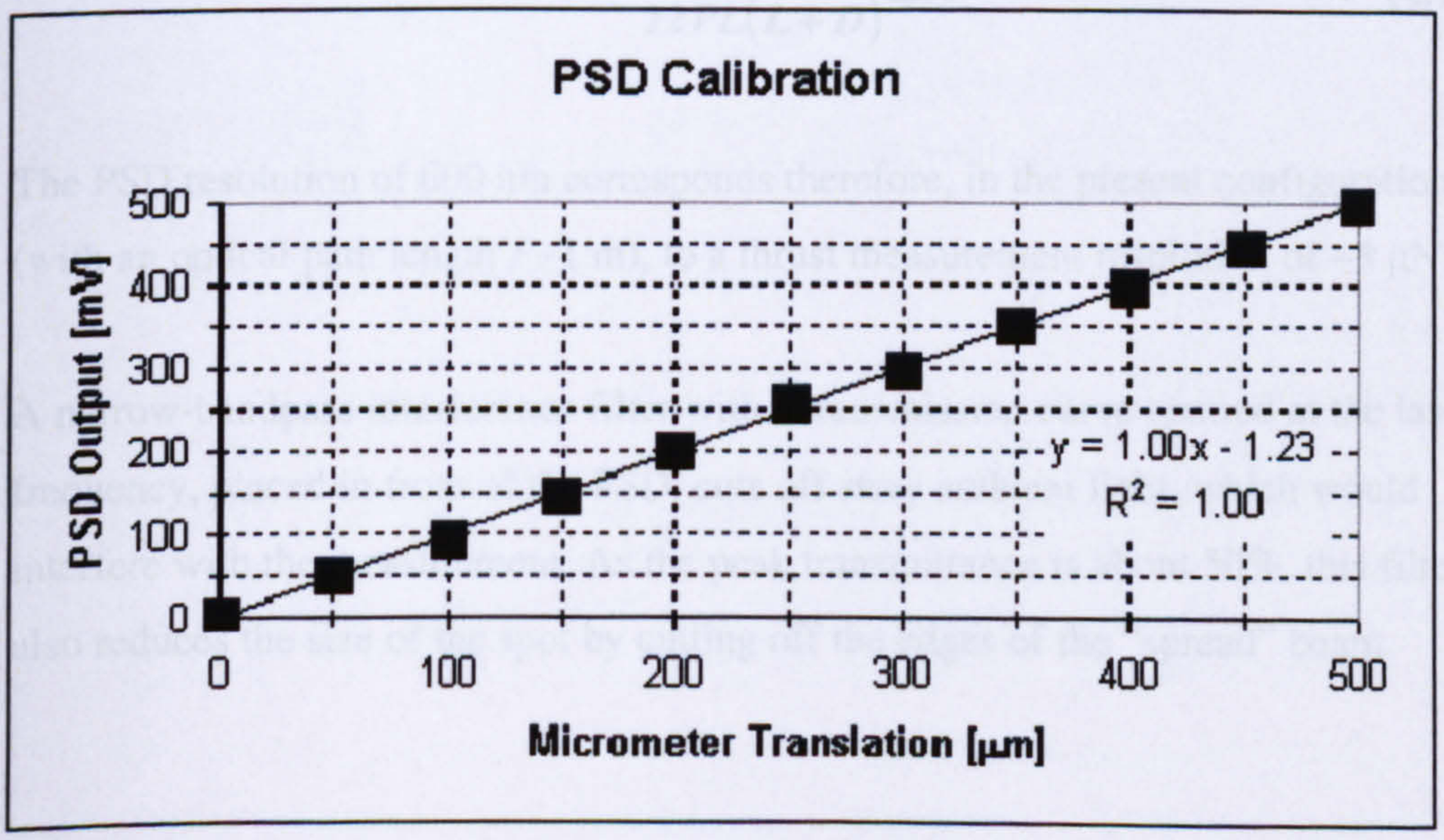

Figure 4.6 – Position Sensitive Detector (PSD) calibration results.

The discrepancies between the translation stage readings and the PSD output, in general below 2%, are to be attributed, in all likelihood, mostly to errors due to the manual operation of the stage and to slight misalignments.

The set-up used for practically all of the thrust measurements reported in this thesis is analogous to the one described above, but with a much shorter optical path length (P = 1.05 m), as the PSD was employed to detect Δx.

The total displacement Δx of the laser beam was measured with a Hamamatsu S2044 Position Sensitive Detector (PSD). This sensor allowed us to measure the displacement of the laser beam on its surface with a resolution of 600 nm [50]. The resolution could be improved, as shown by Eqs. (3.8) and (3.10), by increasing the optical path P and by using a different type of sensor. It would not be possible, in fact, to do so by using a PSD with a larger active surface area (ASA), as the smallest displacement that can be resolved is proportional to the sensor size. If, on the other hand, the optical path P needs to be quite long, PSDs with larger ASAs are available. The S1881 model, with an ASA of nearly 500 mm^2, over twenty times as large as the S2044 one, can measure values of Δx up to ~20 mm.

From Eqs. (3.3) and (3.8), the force is related to the laser spot displacement as:

$$F = \frac{Ebh^3}{12PL(L+D)}\Delta x\,. \tag{4.1}$$

The PSD resolution of 600 nm corresponds therefore, in the present configuration (with an optical path length P~1 m), to a thrust measurement resolution of ~3 μN.

A narrow-bandpass interference filter with a transmission curve centred at the laser frequency, placed in front of the PSD, cuts off stray ambient light, which would interfere with the measurement. As the peak transmittance is about 50%, this filter also reduces the size of the spot by cutting off the edges of the "spread" beam.

The basic principle of operation of the PSD is straightforward, as illustrated in Figs. 4.7 and 4.8 [50]. When the laser light spot strikes the detector, an electric charge proportional to the light intensity is generated at the incident position. As the active area is also a resistive layer, this electric charge is driven through it and collected by the output electrodes as photocurrents, while being divided in inverse proportion to the distance between the incident position and each electrode. The use of four electrodes, as shown in Fig. 4.8 for a pin-cushion (improved tetra-lateral) type PSD, allows a two-dimensional displacement measurement [50].

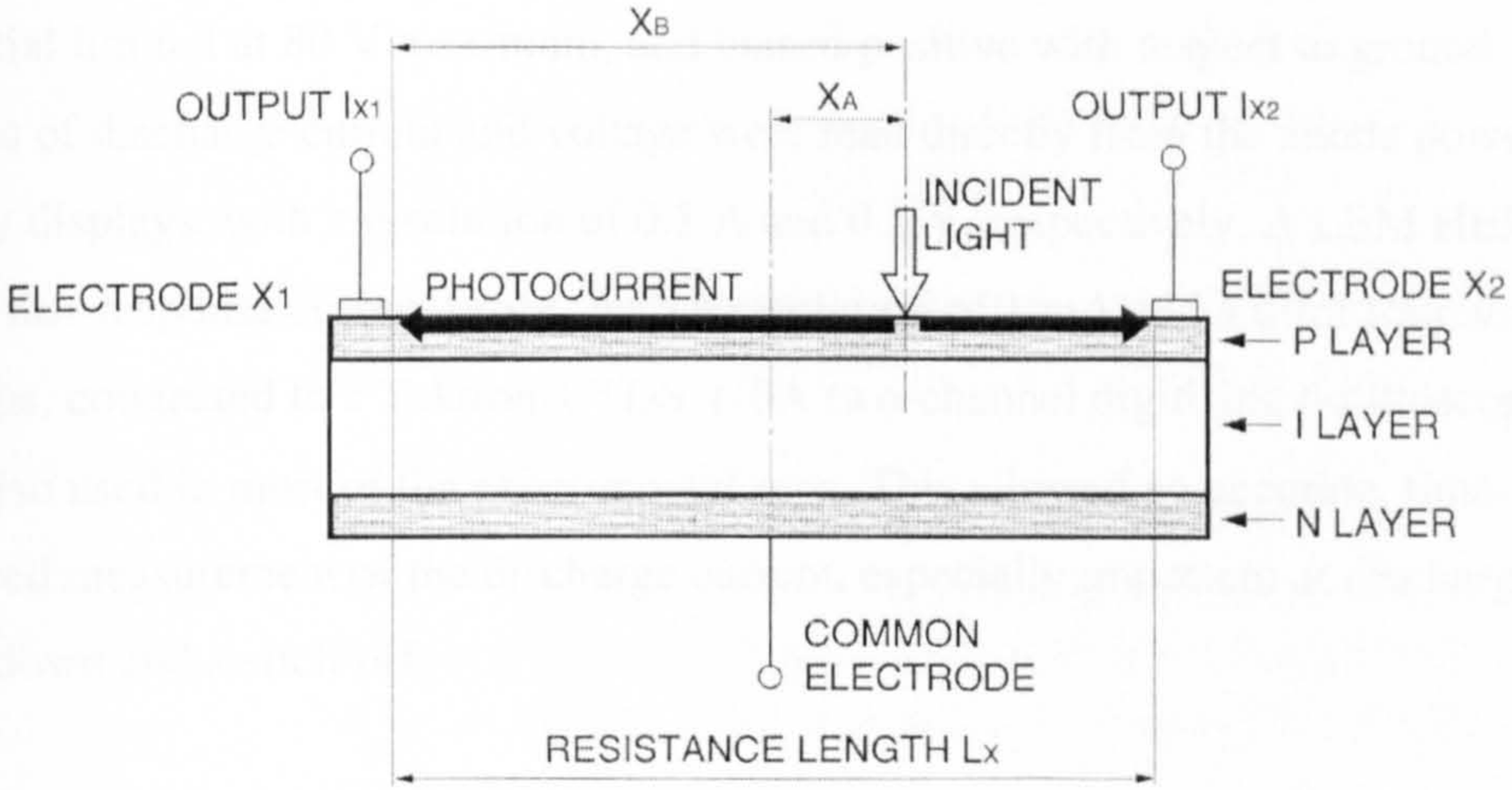

Figure 4.7 – PSD sectional view [Anonymous 2002].

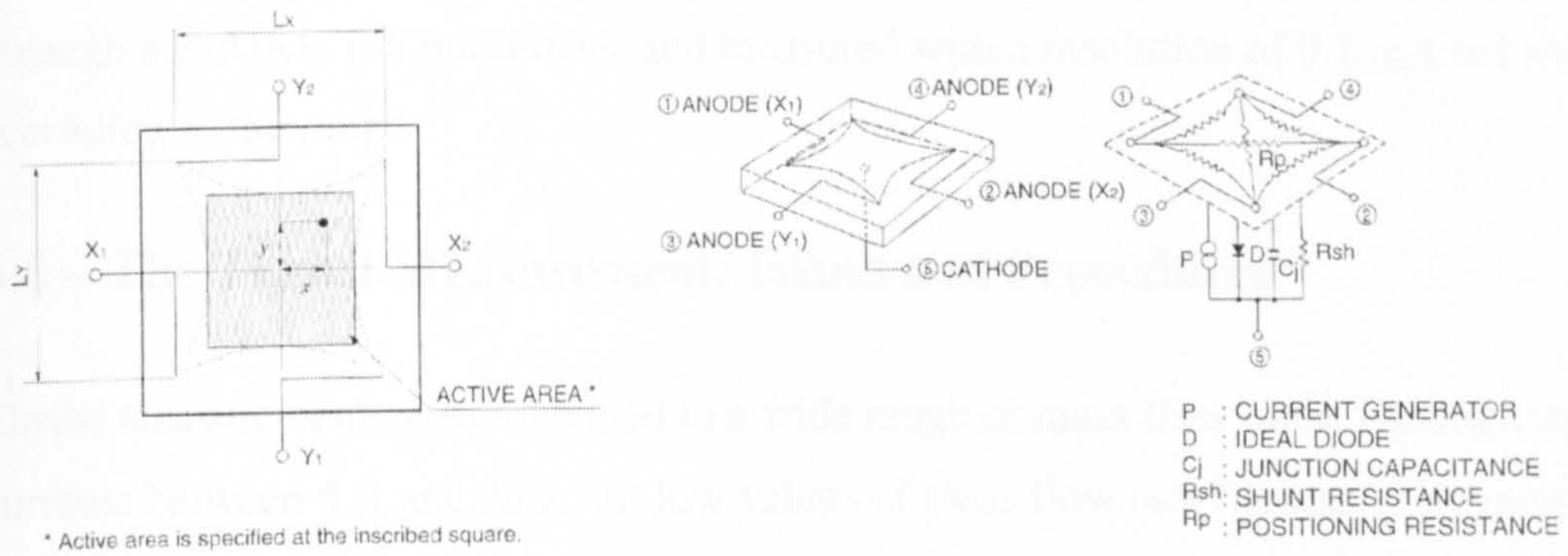

Figure 4.8 – Active area and structure chart, with equivalent circuit [50].

4.5 – The Electrical Set-Up

The rig electrical set-up, including various power supplies, is also the same as the one described by Edwards [98] and Milligan [144]. An important addition is the insertion of a high-power diode to isolate the low-voltage power supply from the high-voltage one, as now they are both connected to the anode.

During all the experimental runs described in this thesis, the HC was kept at ground potential. The anode was connected to a current-regulated power supply, with the potential limited at 80 V maximum, and biased positive with respect to ground. Values of discharge current and voltage were read directly from the anode power supply displays, with a resolution of 0.1 A and 0.1 V, respectively. A LEM HEME PR30 fast-response current probe, with a resolution of 1 mA and a dI/dt following of 20 A/μs, connected to a Tektronix TDS 410A two-channel digitising oscilloscope, was also used in most of the experimental runs. This allowed an accurate, time-resolved measurement of the discharge current, especially important at discharge breakdown and switch-off.

The target was biased with several power supplies, connected in series or in parallel, in order to allow current collection at different potentials, generally negative but also, in some cases, positive with respect to ground. The collected current was passed through a FLUKE 175 multimeter and measured with a resolution of 0.1 mA or1 mA, according to the range.

4.6 – The Thrust Measurement: Issues and Procedures

Thrust measurements were obtained in a wide range of mass flow rates, for discharge currents between 5 A and 25 A. At low values of mass flow rate (generally <1 mg/s) the discharge showed a tendency towards increasing instability and noise, with high voltage values that often led to power supply (limited at 80 V) switch off. At very high values of mass flow rate, above ~3 mg/s, the turbomolecular pump could not cope effectively with the gas input, and the pressure in the chamber went up to 10^{-2}-10^{-3} mbar. At these pressure values, the measured values of thrust exhibit large variations, depending on how much the chamber has been actually filled with gas,

tending to underestimate the thrust, with respect to the linear trends observed at lower mass flow rates. This is probably due to collisions between the plume particles and the ambient gas, scattering part of the plume momentum, which is not, therefore, transferred to the target. As an example, in the case of cold thrust, at a pressure of 10^{-3} mbar and a temperature of 20°C, the mean free path for neutral-neutral collisions is 6.22 cm for Ar, 4.78 cm for Kr and 3.45 cm for Xe [CRC]. These distances are smaller than the anode-target separation (~15 cm). Because of these reasons, data are presented for all propellant gases only for a range of mass flow rates between ~0.3 mg/s and ~3mg/s.

From a physical point of view, our target will tend to deform because the face receiving the heat flux from the HC will be at a higher temperature than the other one, radiating into a vacuum at room temperature. The thermal expansion will be therefore lower on the colder face. This will cause the CBT to bend and bring about an overestimate of the thrust deflection.

The sensitivity of our CBT is inversely proportional to E and that the laser spot displacement Δx is proportional to the angular deflection $\Delta\theta$. We can thus write, for the displacement we actually measure on the screen, Δx_m:

$$\Delta x_m = \frac{E_c}{E_h}\Delta x + \Delta x_{te}\,, \tag{4.2}$$

where E_c is the Young's modulus at room temperature and E_h its value after the temperature increase. Δx_{te} is the additional displacement that we will measure due to thermal deformation (differential expansion) of the target. In order to estimate the various terms in this equation, we need to assess the temperature increase of the target and relate it to the variation in E and the thermal deformation. The Young's modulus E, in general, decreases with increasing temperature. This produces an increase in the sensitivity of our CBT and could lead to overestimating the thrust. For aluminium, this effect is quite linear between room temperature and ~ 300°C, with E decreasing from ~ 70 GPa to ~ 60 GPa.

In order to relate this angular deflection to the energy flux into the target, a model of the heat transfer and induced strains and stresses is necessary. This is an essentially three-dimensional, time-dependent problem and, as such, an exact solution can only be obtained with numerical methods. However, an order-of-magnitude estimate can be reached analytically with a simple one-dimensional heat transfer model, involving elements of the elementary theory of beams and of strains and stresses induced by thermal gradients.

To go beyond a qualitative assessment, let us model our CBT as a cantilever beam subjected to a temperature gradient across its thickness h. The angular deflection $\Delta\theta$ can be related to a position l along the beam and the difference in temperature ΔT between the two faces by the relation [139, 147-149]

$$\Delta\theta = \frac{l}{h}\alpha\Delta T, \tag{4.3}$$

where α is the coefficient of linear reversible thermal expansion. ΔT can be estimated by modelling our CBT as a metal strip delimited by two parallel planes. In this case, analytical solutions can be obtained for various boundary conditions [150]. With a heat flux Q [Wm^{-2}] into one plane and radiation from the other plane into a background at the initial temperature, we have a transient heating to reach a steady-state temperature distribution which allows a drop ΔT across the thickness of the strip, due to the finite thermal conductivity K. Due to the high value of K for metals in general and aluminium in particular, ΔT is extremely small and is established very quickly, while the average temperature is still rising. Numerical calculations, performed with FEHT, a Finite Element Heat Transfer program, have allowed us to follow the transients to the steady states (reached after times $t \sim$ 15'-30') and to confirm that including radiation from the hotter face in our model would sensibly reduce ΔT. This is a non-linear phenomenon, very sensitive to variations in temperature, radiation being proportional to T^4. By neglecting it as a first approximation, we can write as an upper estimate of the temperature drop across the metal strip, at steady state [150]:

$$\Delta T = Q\frac{h}{K} \,. \tag{4.4}$$

Combining Eqs. 4.3 and 4.4 finally yields, for the CBT angular deflection:

$$\Delta\theta = Ql\frac{\alpha}{K} \,. \tag{4.5}$$

Equation 4.5 shows that, as a first approximation, the angular deflection does not depend on the beam thickness, as a thicker beam is more rigid but also allows a larger temperature drop across. As our CBT sensitivity is proportional to $1/h^3$, using a thin beam is advantageous anyway.

The heat flux into the target can be assessed as the sum of different contributions:

$$Q = \varepsilon_1\varepsilon_2 G\sigma T^4 + \frac{5}{2}kT\frac{\dot{m}}{m}\frac{1}{D^2} + \frac{I_i}{D^2}V_b \,. \tag{4.6}$$

Here ε is the emissivity, G a geometric coefficient, σ the Stefan-Boltzmann constant, k the Boltzmann constant, $\dot{m}$ the mass flow rate, I_i the ion current and V_b the target bias potential. The first term on the RHS of Eq. 4.6 is the radiation heat flux, the second one the energy transported by the heavy particles, assumed in equilibrium with the HC tip, the third one the energy transported by the ions accelerated by the target bias voltage. Once we have estimated Q with Eq. 4.6, we can calculate T analytically or numerically, the way we did using FEHT, and ΔT using Eq. 4.4. Using data in the literature we can estimate the variation in E, as we did above. Using Equations 4.3 and 3.8, we can calculate Δx_{te}. In this way, from Equation 4.2 we obtain the effective Δx and then the correct value for the thrust.

As pointed out above, the simple one-dimensional thermal model does not capture some important features of our problem, especially as far as the geometry is concerned. Our CBT is made up of a target connected to a much narrower beam. As the target is positioned with its centre on the axis of symmetry, it will receive most of the heat flux, which will then be conducted into the beam and then toward the insulating mount, as well as radiated away. These effects would have to be included in

order to have a more precise estimate of the thermal effects. This, though, would render the solution of the problem far less simple, even for steady state.

It soon became clear, in the course of our first measurements, that the various terms in Eq. 4.2 were comparable [52]. Therefore, in order to avoid the problems related to thermal warping, a measurement technique was adopted, which exploits the high time resolution in the laser spot determination made possible by the use of the PSD connected to the oscilloscope. Namely, data were taken at discharge switch-off, when the displacement plots show a clear and rapid step change. This allows us to separate the effects of the force due to the plume impingement being suddenly removed from the movements caused by the target deformation due to temperature variations as the heat flux changes, which have a longer timescale. Even after the curve smoothing, in fact, the step timescale is of the order of a second, which is also too short to significantly affect the HC temperature, as confirmed by a visual observation of the cathode tip radiance. We therefore assume that the thrust can be calculated as the sum of the negative step given by the switching off of the discharge and by a contribution due to the gas flowing through the hot HC, with no discharge, in a manner similar to that of the thrust measurements described in Section 5.0.3.1.

Even if a thermal modelling of the cathode-anode-target system accurate enough to give quantitative estimates would be a daunting task, mainly due to the uncertainty and non-repeatability of the inputs (energy fluxes due to anode temperatures and discharge conditions), inspection of hundreds of displacement time history plots shows that the errors due to thermal drifts are in most cases negligible in comparison to the uncertainty in our measurement, as long as we operate on the one-second timescale of the discharge switch-off. Changes in mass flow rate require several seconds from the needle valve setting variation. Even changing the discharge current, which could be done more quickly, often causes significant variations in anode voltage and, in general, discharge conditions, which take several seconds to stabilize. On these longer timescales, it becomes much harder to separate the effect of thrust variation from those of thermal drifts by inspecting the displacement time histories. To ensure consistency between data sets taken in different conditions and to minimize possible sources of error that are hard to quantify, all the measurements reported in this thesis were taken with the switch-off technique.

A few seconds of raw data (laser spot displacement Δx from PSD) are shown in Figs. 4.10 and 4.11. It is evident that the signal is not very "clean" and of immediate interpretation: high-amplitude oscillations at various frequencies are present, of which two appear to dominate. The lower one (~2.5 Hz) is close to the first natural frequency of the CBT, as confirmed by a finite-element simulation of the target performed with ANSYS® (see Fig. 4.9) and also by simple analytical calculations, and the higher one (~24 Hz) is forced by the rotary pump, operating at 50 Hz. In Figs. 4.10 and 4.11, the thin line is the raw signal, where a superposition of both frequencies is apparent, while the thick line, showing only the ~2.5 Hz oscillation, is obtained with a 250-point based moving average in Microsoft Excel. Filtering and smoothing of the signal was performed, at various stages during the research, also with routines written in MATLAB. The differences in the results obtained using different softwares and methods were, however, negligible.

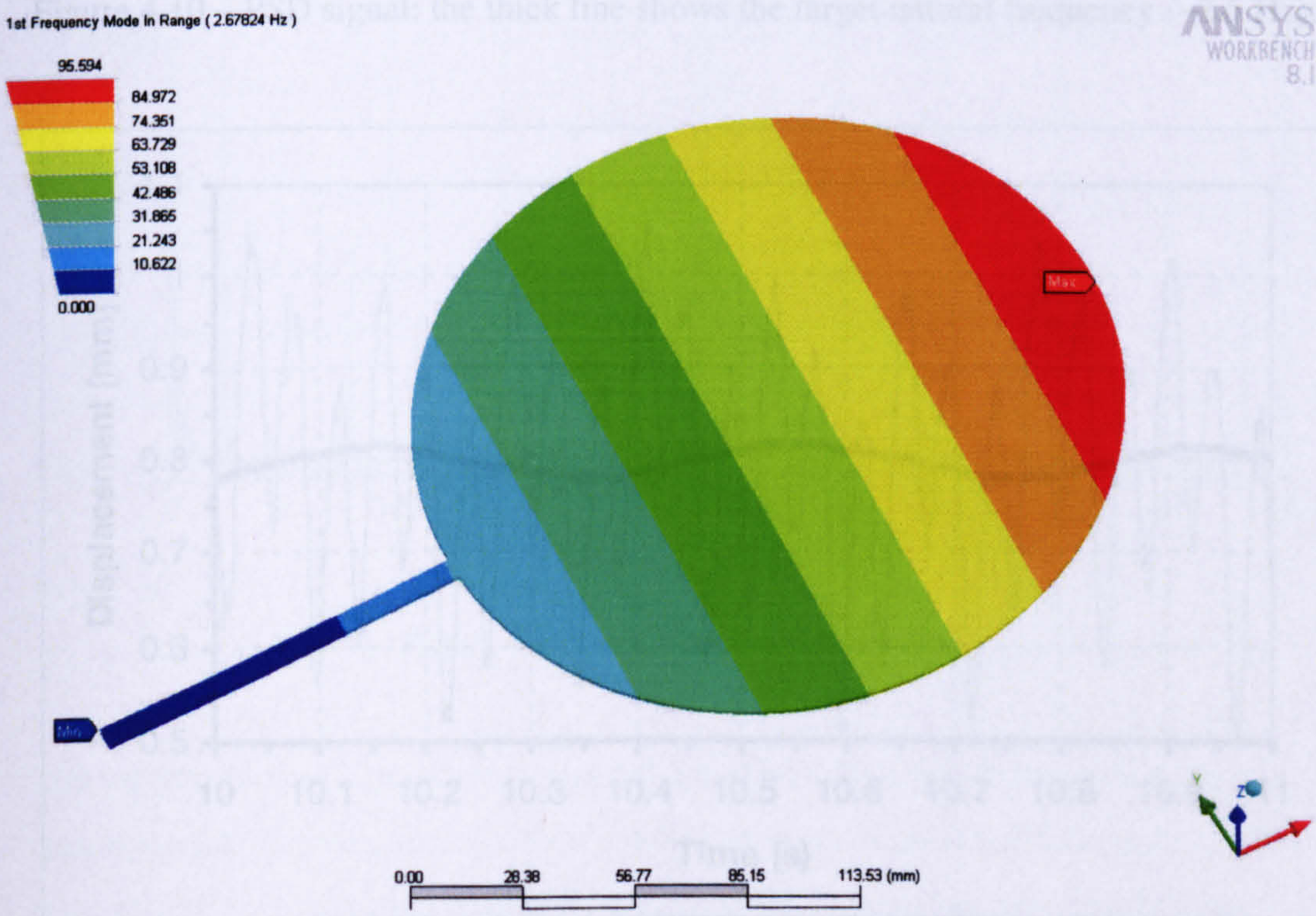

Figure 4.9 – 3GT first natural frequency

From Fig. 4.10, it is clear that, at switch-off, the step down corresponding to the sudden removal of the thrust is, even after smoothing of the signal curve, on a sub-second scale. As such, it is easily distinguished from the subsequent thermal

deformation due to variations in the heat flux and, therefore, in the temperature of the target, which is on a much longer time scale.

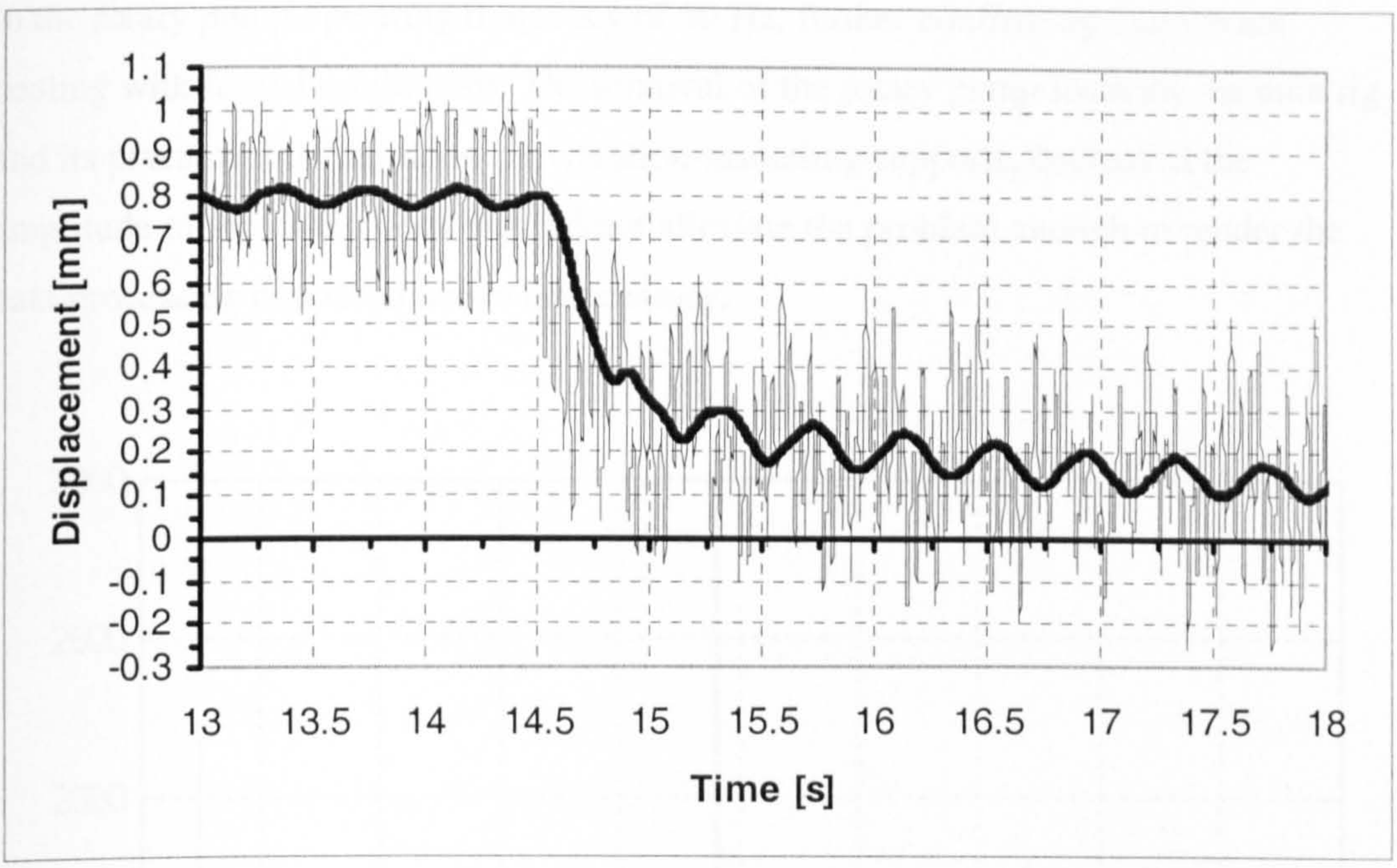

Figure 4.10 – PSD signal: the thick line shows the target natural frequency (~2.5 Hz).

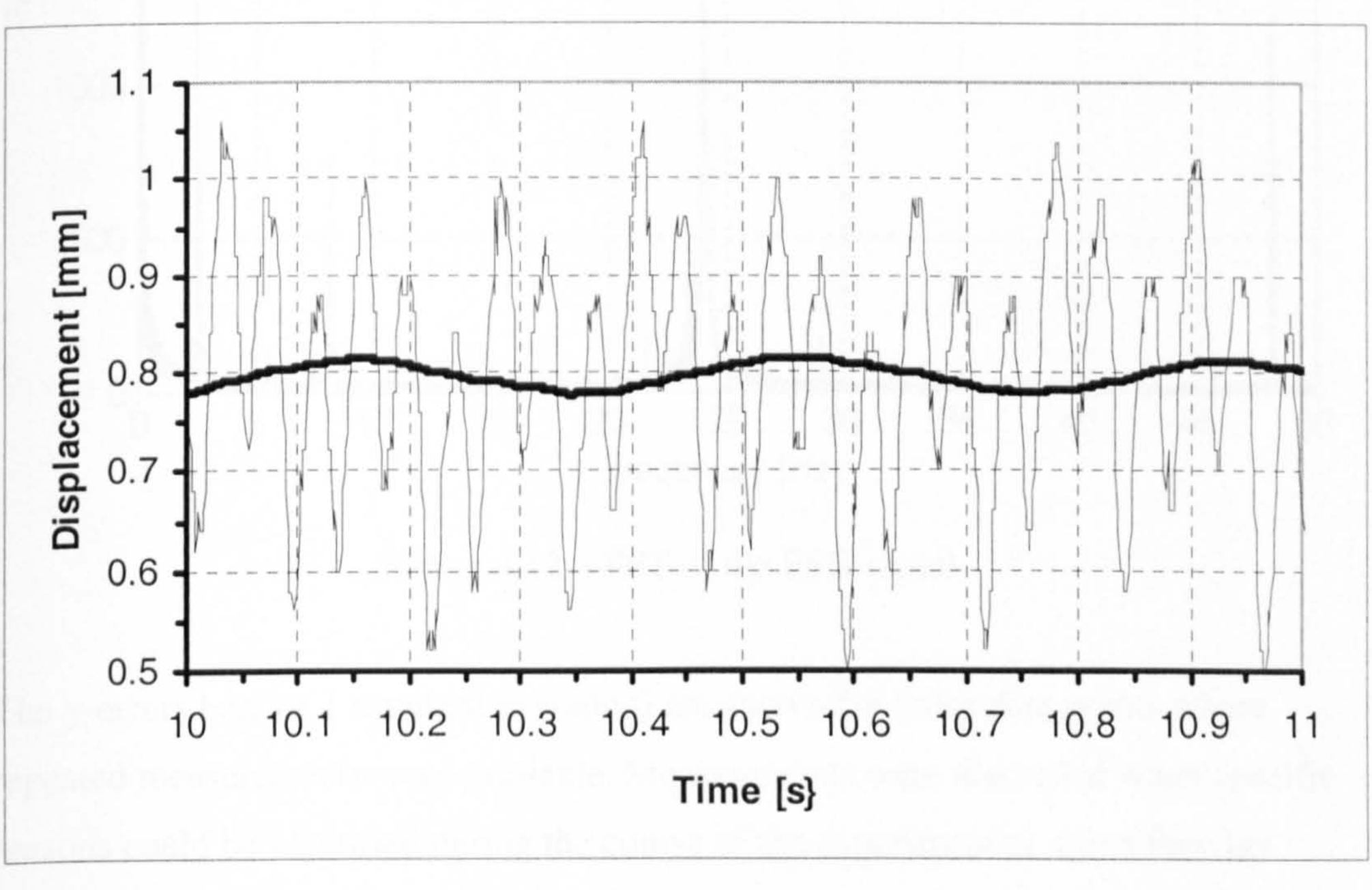

Figure 4.11 – Detail of Fig.4.10: the pump-induced ~24 Hz frequency is evident.

A Fast Fourier Transform (FFT) of the signal (see Fig. 4.12), obtained with MATLAB, reveals that other frequencies are present, like for instance a higher harmonic at twice the frequency (~48 Hz) of the dominating mode. This is very close to the rotary pump operating frequency of 50 Hz, further confirming that we are dealing with forced oscillations. The removal of the rotary pump from the vacuum rig and its placement on the floor, on vibration-insulating supports, decreased the amplitude of the oscillations, but did not alleviate the problem enough to render the data processing described above unnecessary.

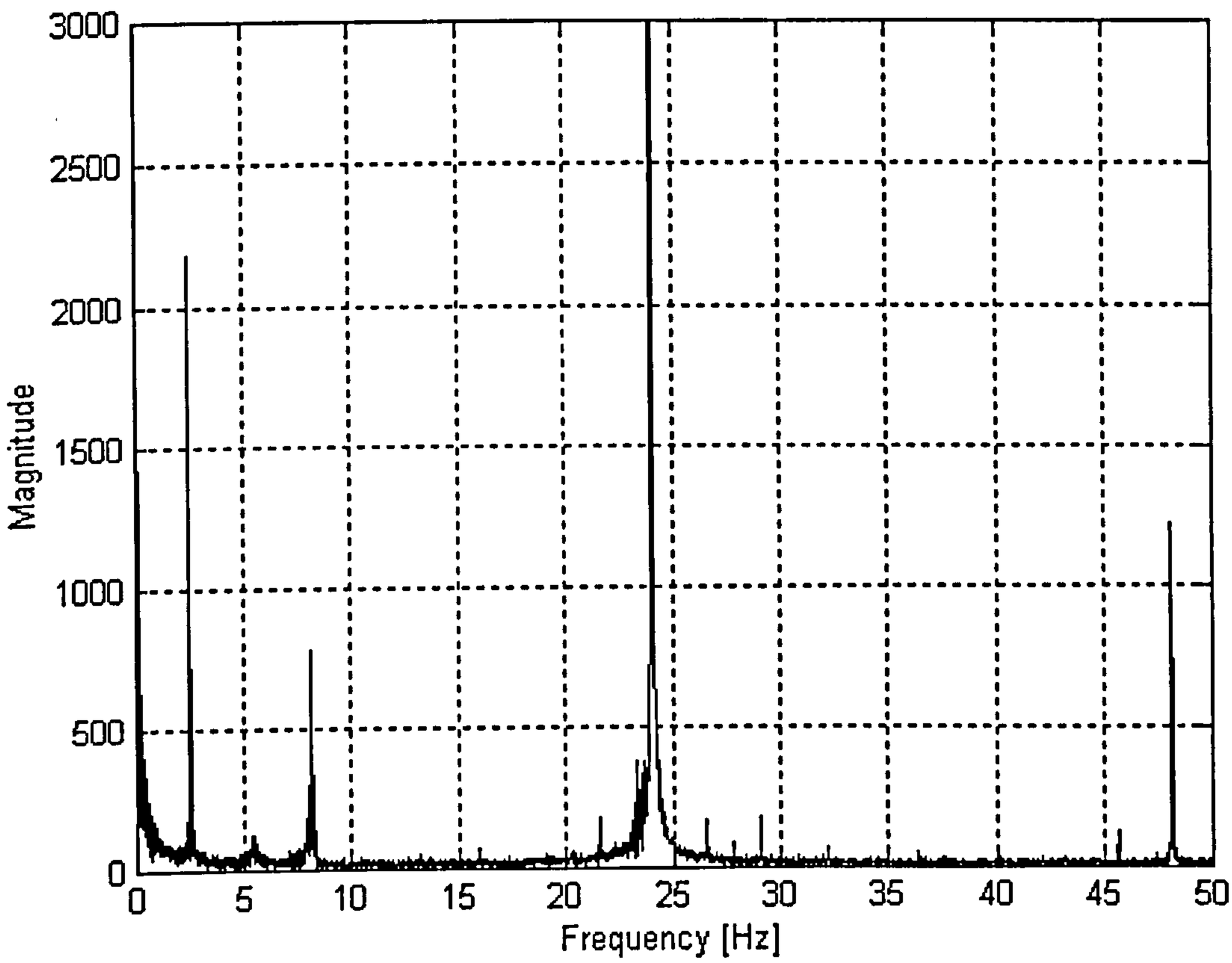

Figure 4.12 – FFT of the PSD signal.

The y-errors bars (± 1 standard deviation) are shown for those data points where repeated measurements were available. Measurements were discarded when specific reasons could be identified during the course of the experiment or when they lay outside a band of one and a half times the interquartile range, both sides of the median value. This latter criterion was applied only when a statistically significant set (more than five measurements per data point) was available. The error in the measured thrust

is generally below 10%, and can be as low as 5% and as high as 25% in the case of unstable discharge. The precision is mostly dominated by variability in the device operation, due for example to the hysteresis phenomenon described in Section 5.0.1 or by discharge oscillations, and not by the accuracy of the measurement system itself, hence the y-error bars. In other words, for the same mass flow rate and discharge current settings the device may operate in a substantially different fashion. This is especially true in those borderline regions between, for example, plume and spot mode operations, where a different temperature of the electrodes can cause variations in discharge voltage of more than 50%.

In the calculation of specific impulse, this error compounds with a $\pm 4\%$ accuracy in the mass flow rate settings, which also sets the x-error bars on many plots. The accuracy was estimated from the approximation of building calibration curves through polynomial interpolation of a finite number of data points taken at the beginning of each experimental run and from observed extreme cases of temperature variations from beginning to end of a run, which could last up to twelve hours. Such a value is in agreement with estimates by Edwards, the original designer of the vacuum rig and propellant feed system [98].

A visual inspection of the anode after several experimental runs revealed the presence of sputtered material, evident around the orifice in Figure 4.13, which shows the side facing towards the HC for the anode used initially, with a 10 mm orifice diameter. This was, most probably, caused by running the HC in plume mode at medium-to-high discharge currents.

The sputtering deposit was later confirmed, by an accurate SEM exam of the anode surface, to be made up of aluminium from the target and tantalum from the HC tip. Figure 4.14 shows a typical result from the side facing towards the HC, with the various elements present near the surface. We notice the Ta (80% in weight, 55% of atoms) from the HC tip and Fe and Cr from the anode, made of stainless steel.

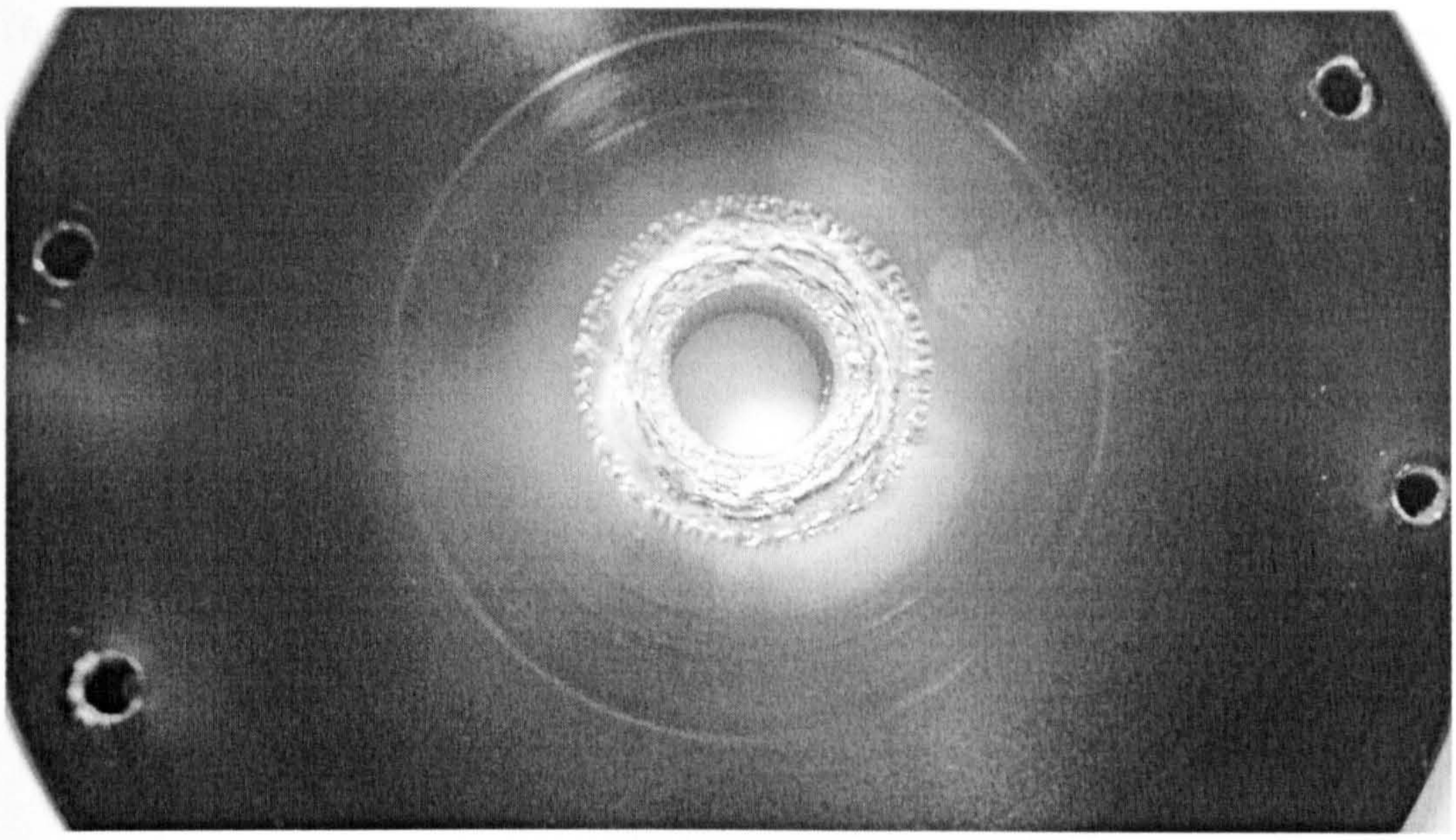

Figure 4.13 – Sputtered material on the anode side facing towards the HC.

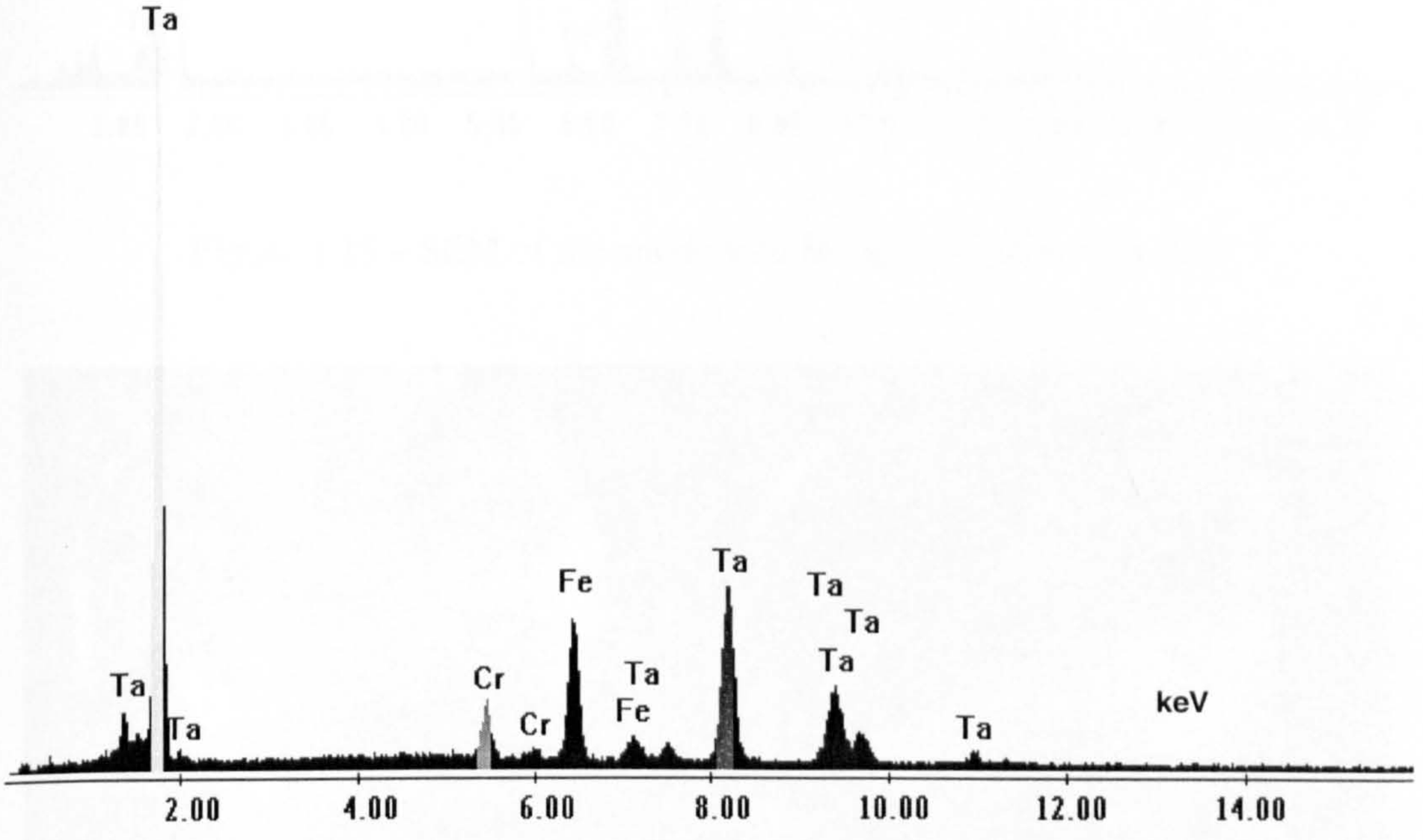

Figure 4.14 – SEM of the anode side facing towards the HC.

Figure 4.15, instead, shows SEM results from the anode side facing away from the HC, where Al from the target is present (40% in weight, 66% of atoms). This confirms the visual observation that the HC tantalum tip underwent severe erosion from the very first experiments. At a much later time, when the orifice was drilled out

(from 0.5 mm to 1.0 mm diameter, see Fig. 4.16), measurements taken with a vernier calliper showed that approximately 0.2 mm of orifice length had been lost because of tip erosion. At the same time, the orifice diameter had not increased.

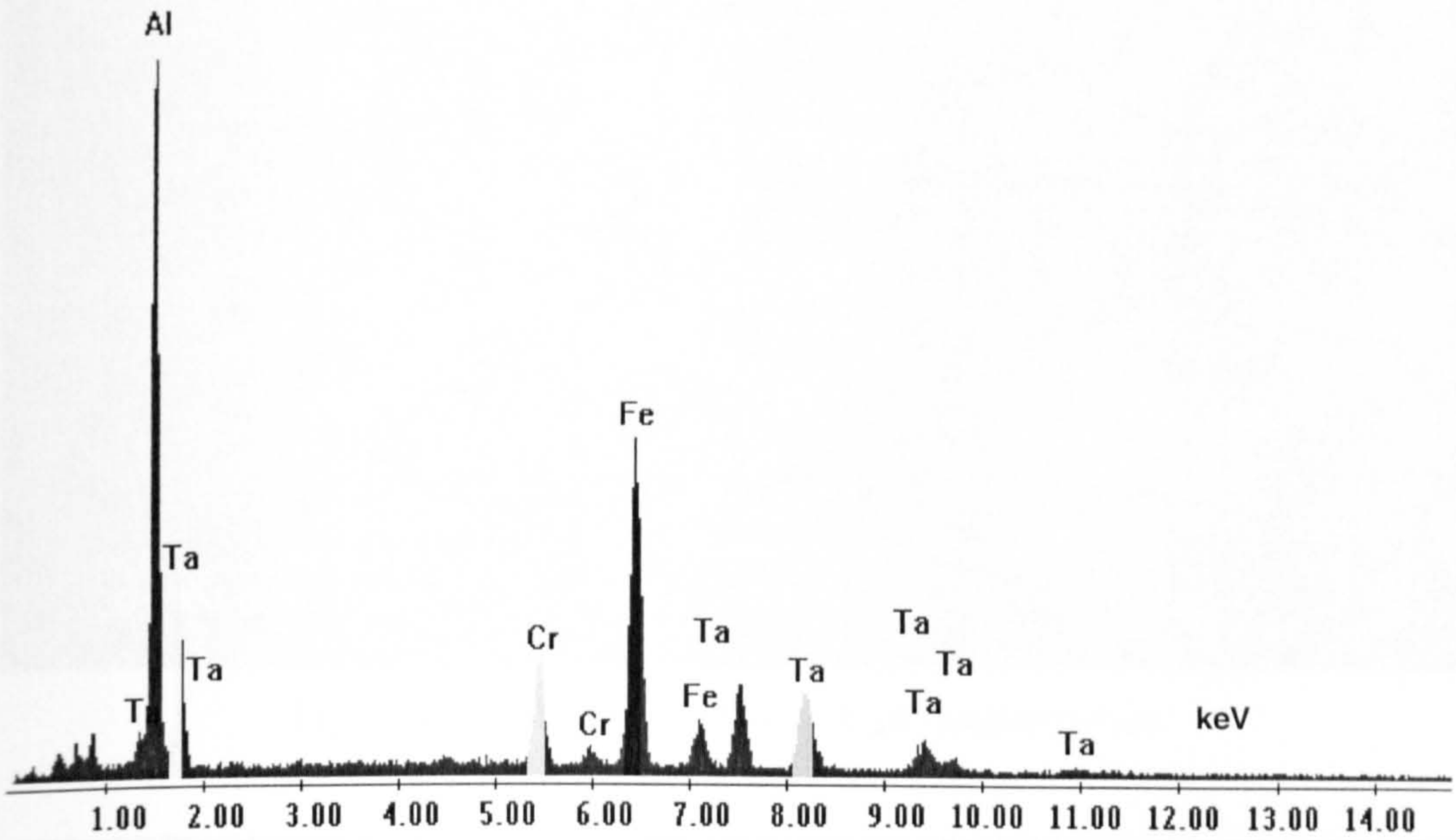

Figure 4.15 – SEM of the anode side facing away from the HC.

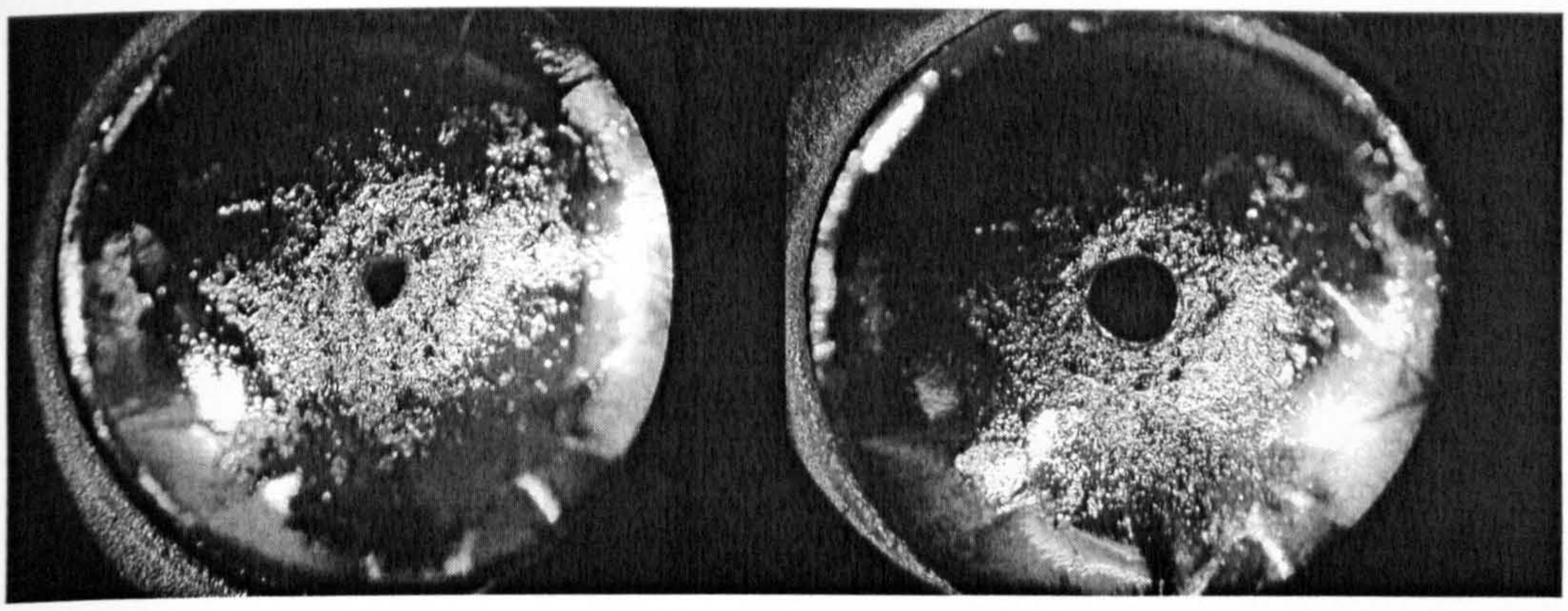

Figure 4.16 – The HC tip right before and after drilling out the orifice.

Actually, due to material redeposition, the orifice shape appeared irregular and a 0.45 mm precision drill bit could not be inserted. This changes in HC orifice shape and dimensions are confirmed by photos taken at different times, shown in Figs. 4.17 and 4.18.

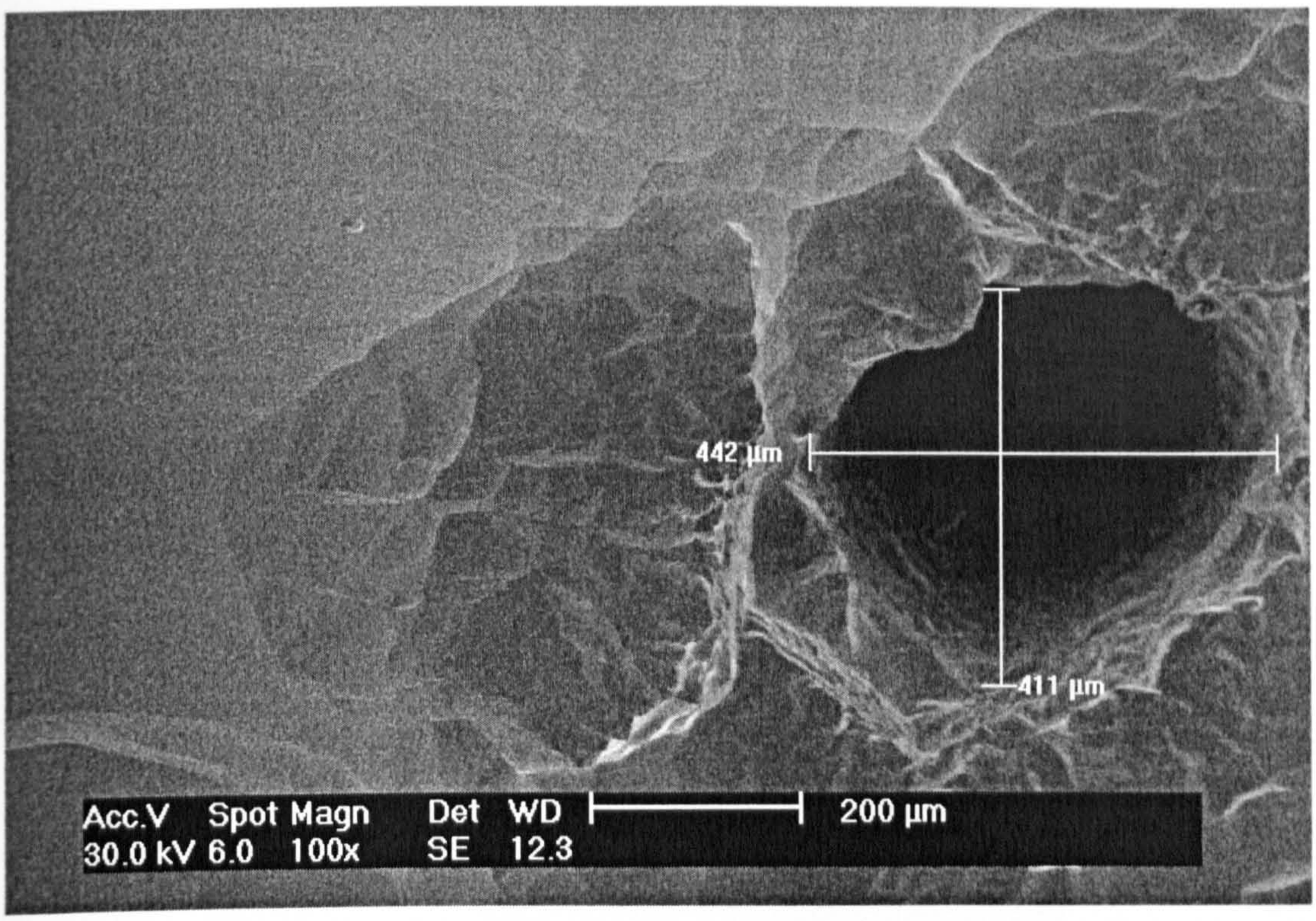

Figure 4.17 – The HC orifice at high magnification.

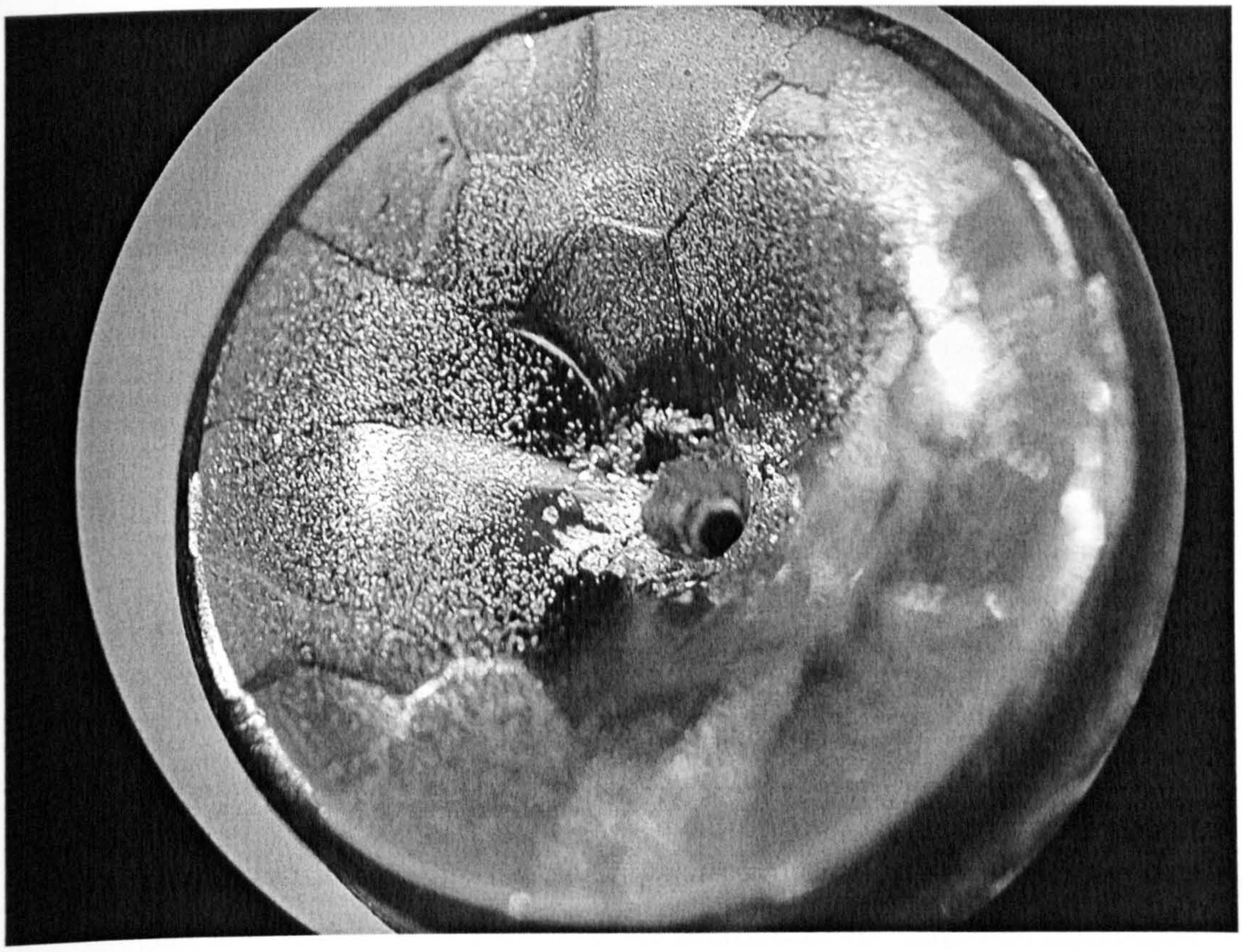

Figure 4.18 – The HC tip at medium magnification.

Both the target (2GT, see Figure 4.19) and, to some extent, the HC tip, showed clear traces of sputtering due to heavy-particle impacts. We know that rough surfaces can have emissivities, for the same material, even an order of magnitude higher than shiny ones. The surface finish of the target was clearly altered by exposure to the HC plume.

The surface conditions, like roughness and sputtering deposits, will also affect the interaction between impinging particles and target. This can be described in terms of the accommodation coefficients of various properties, in particular momentum and energy.

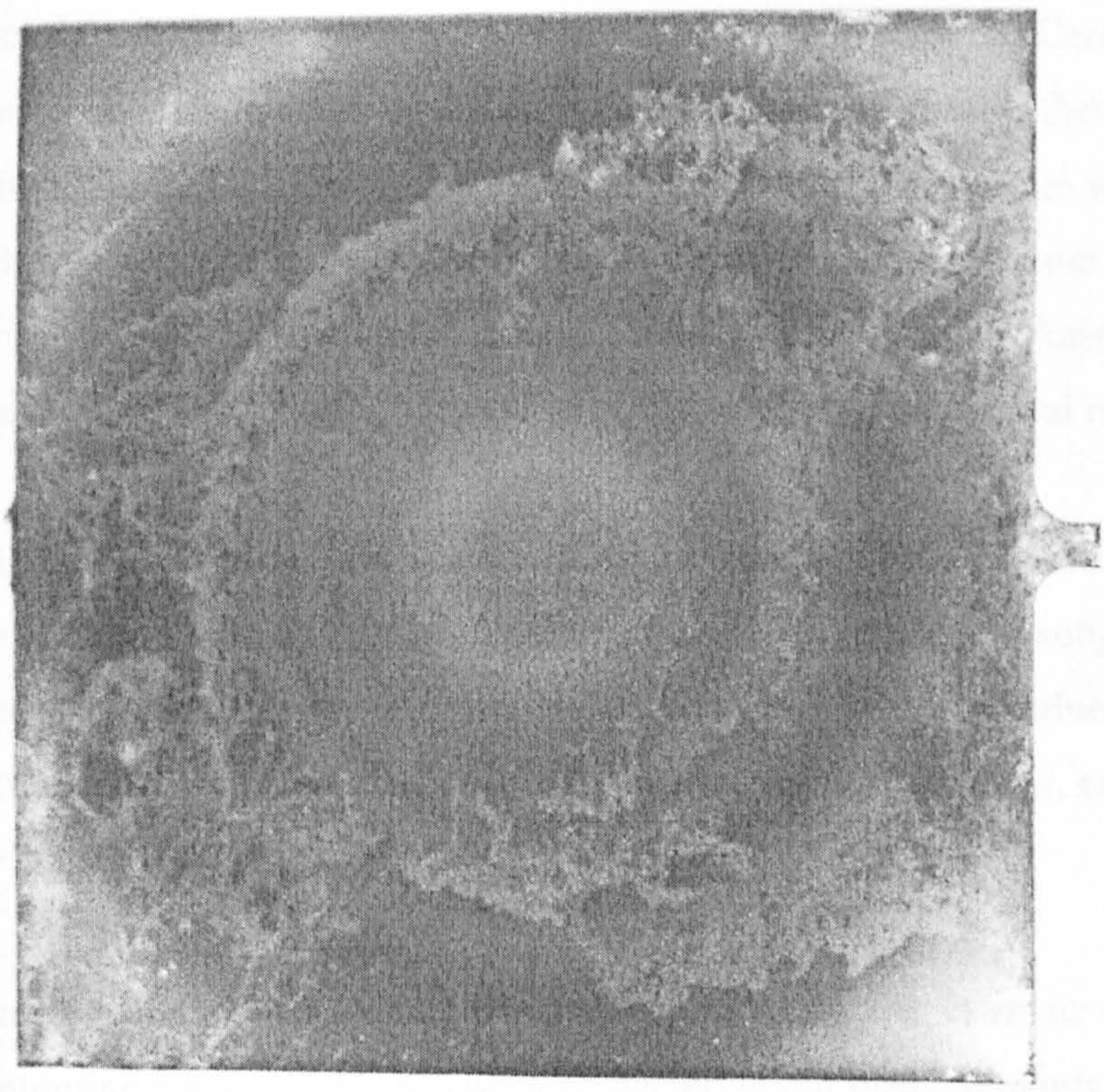

Figure 4.19 – The target after several runs, with traces of sputtering.

The concept of accommodation coefficient was introduced by Cercignani and Lampis [151]. Simply stated, it quantifies the extent to which a reflected property approximates diffuse reflection. Therefore, the coefficients for tangential momentum and the normal component of translational energy are both 1 or 0, respectively, for

completely diffuse or specular, perfectly elastic reflection, as described by the basic Maxwell model [152]. Equilibrium diffuse reflection requires that both the surface temperature and the temperature associated with the reflected gas Maxwellian distribution be equal to the incident gas temperature. This equilibrium between gas and surface is not always satisfied, which means that the thermal accommodation coefficient, indicating to what extent the reflected particles have their temperature adjusted toward that of the surface, will be less than unity. While the interaction between "engineering" surfaces and gases at normal temperature, in general, approximates diffuse reflection with complete thermal accommodation, there are cases when this assumption should be critically reviewed. These include smooth metal surfaces that have been outgassed, impacts of particles with molecular weight much smaller than that of the surface molecules or with translational energy, relative to the surface, larger than several electron volts [138]. Lord has extended the Cercignani-Lampis model to include the case of diffuse reflection with incomplete thermal accommodation, the most common and useful generalization [153]. From what stated above, this should approximate well the interaction between the HC plume and our target, especially as the side facing the cathode, already left at a rough finish, gets sputtered and contaminated during the course of the various experimental runs.

The interaction of heavy atoms and ions, with atomic weights between ~40 (Ar) and ~131 (Xe), with aluminium and molybdenum surfaces, unpolished and subjected to sputtering and "thermal roughening", should thus be characterized by values of the accommodation coefficients relatively close to, even if lower than, unity, especially for moderate impact energies and angles [154-159].

In view of the above and of the difficulties presented by a precise estimate of the effect of rebounding particles, this has been neglected in our measurements. The force producing the bending of the CBT, due to the momentum transfer from the HC plume, has therefore been assumed equal to the thrust. This will produce an overestimation of the actual thrust generated by the HC, as is always the case with target measurements system, unless one decides to adopt correction coefficients, as in [49]. By comparison with direct thrust measurements it has been shown that, with careful target designs, realising a nearly total transfer of the plume axial momentum to the target, these correction coefficients can be as high as 0.9, without any assumption about the exact

modalities of particle-surface interaction [160-162]. As we can confidently rule out the possibility of specular reflection, the thrust overestimation, in our case, while definitely not as small as the 10% in [162], will not be greater than the 50% in [49].

Chapter 5

Results and Discussion

5.0 - Results

5.0.1 – T6 HC Characterisation in Open-Diode Discharge Configuration

Prior to any other measurement, a brief characterization of the discharge behaviour of the T6 HC was undertaken. This was felt necessary due to the lack of data on this specific model of HC when operated with argon as a propellant in open-diode configuration. Rudwan has recently characterized a nearly identical device (a HET version of the T6 HC) but he used an enclosed keeper and, due to practical issues, his discharge current was limited to values between 0.5 A and 5 A [15]. The same investigator also elaborated a theory describing the dependence of the discharge behaviour on the electrode configuration, thus clearly pointing out that any experimental set-up markedly different from ones used previously has to be individually characterized [15]. Pottinger investigated the interior plasma of a T6 HC identical to the one described in this thesis, but a traditional diode configuration, with an open keeper [86], was used. In these experiments the T6 HC was operated in an open-diode configuration, with no keeper, using several noble gas as propellants and with current discharges as high as 25 A, as had never been done before. This initial characterization was performed with the 10 mm orifice diameter anode at 4.5 mm in front of the HC tip. The cathode orifice diameter was the initial 0.5 mm value.

Voltage readings were taken directly from the anode power supply, both with varying discharge current and constant $\dot{m}$ and with varying $\dot{m}$ and constant discharge current. In all cases, up to ~10 minutes were allowed for the discharge voltage to stabilize to within ±0.1 V. As such a time interval was not enough, in general, for the HC/anode system to reach a complete thermal equilibrium, a hysteresis effect was noticed, with voltage values being different, for example, at the same current values when increasing or decreasing discharge current. This phenomenon, as already noticed by Fearn and Patterson during experiments with the same type of HC [82], was greatly reduced by allowing more time (up to ~20 minutes) for the system to stabilize, reaching a more complete thermal equilibrium [163].

Voltage measurements were taken with varying $\dot{m}$ for several values of discharge current. Noise in the anode voltage and oscillations in the plume were noticed, from the power supply readings and by visual inspection of the discharge, especially close to mode transition (plume to spot and spot to plume) already noticed by Fearn and Patterson [82]. The transition from plume to spot mode with increasing $\dot{m}$ is clearly visible in Figure 5.1, where a $\dot{m}$ sweep from a typical run (12 A discharge current) is plotted.

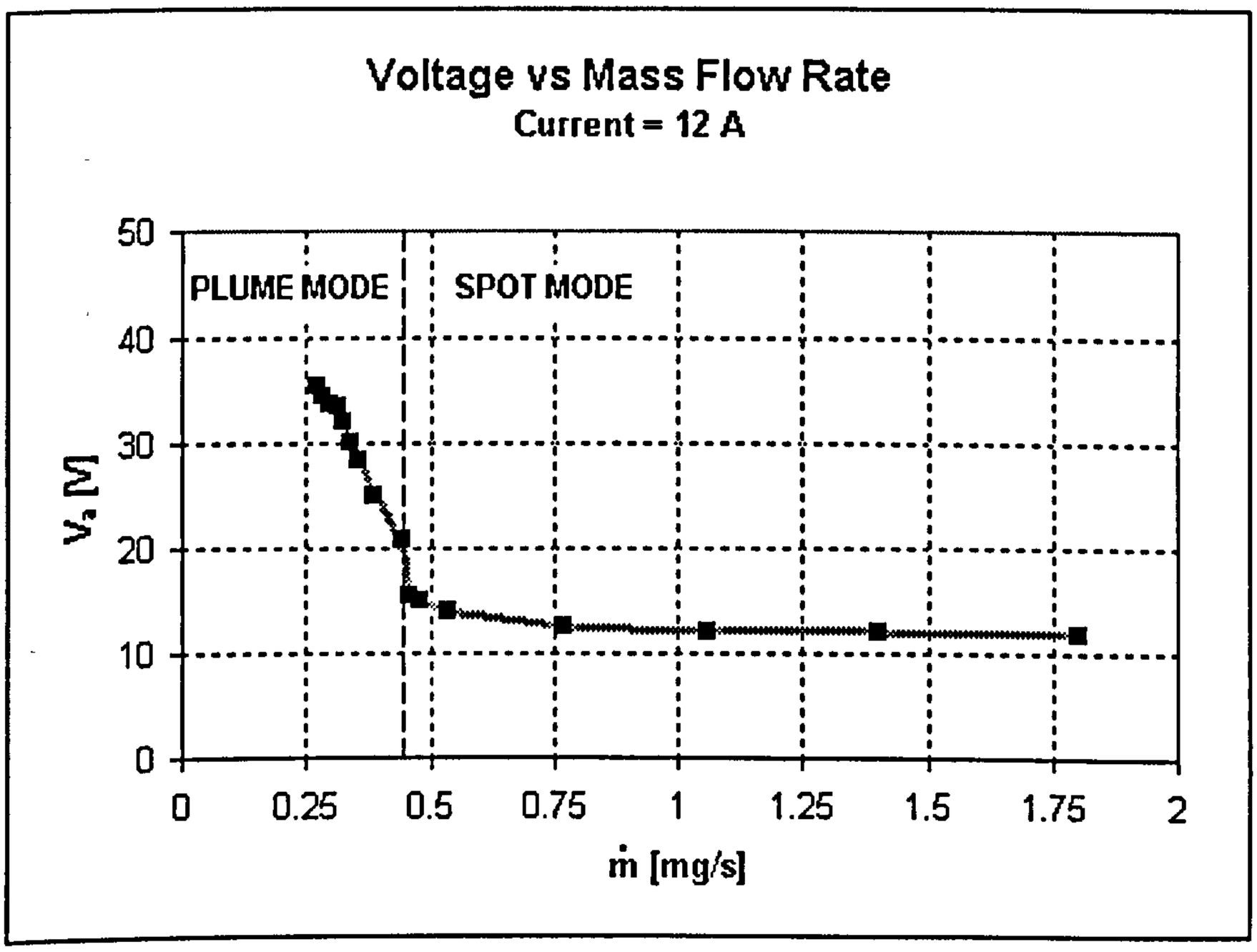

Figure 5.1 – Plume-to-spot transition, argon propellant.

As shown in Figure 5.2 (corresponding to a 10-A discharge), if not enough time is allowed for the system to reach a complete thermal equilibrium, the mode transition will be delayed, with higher anode voltages than before for the same values of $\dot{m}$, in a fashion similar to Fearn and Patterson's experiments [82]. The result is a clear hysteresis loop. As $\dot{m}$ is decreased, V_a increases and we have transition from spot to plume mode (curve A). When $\dot{m}$ is increased again, V_a decreases and the opposite transition, from plume to spot mode, takes place (curve B). Now the anode temperature is higher due to the higher power flowing through it. This is just a qualitative, visual observation, as no thermocouples were attached to the anode and no

pyrometer measurements were taken. An increase in temperature is visually evident, though, as the anode glows progressively red-hot, starting from around the orifice outwards.

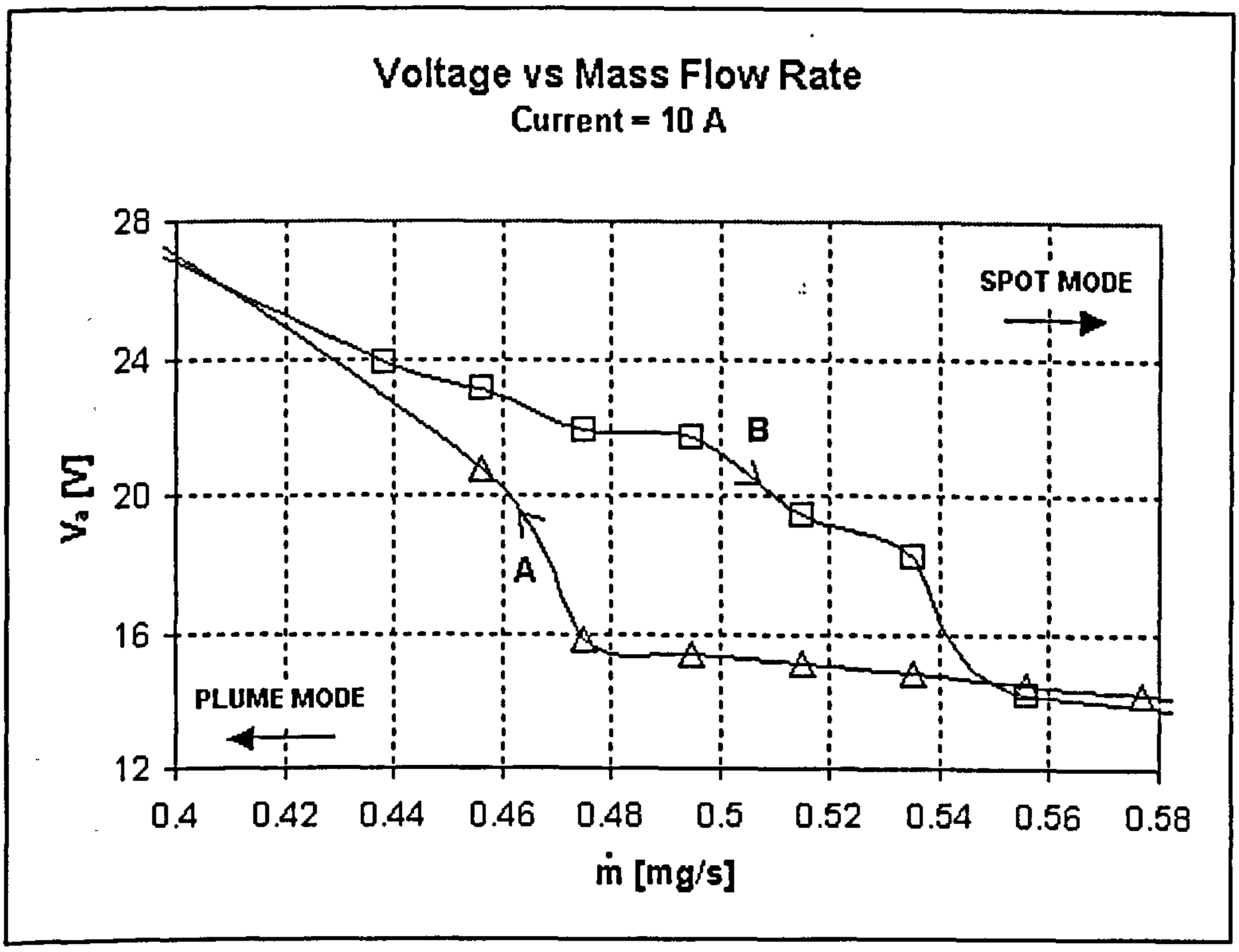

Figure 5.2 – Hysteresis loop during HC characterization.

If the HC is operated at high discharge power for several minutes, its temperature will increase and enhanced current emission, according to Equations 1.1 and 1.3, will make the discharge stable at lower values of $\dot{m}$, for which breakdown was not even possible at the beginning of the experimental run.

As the discharge current is decreased, the drop in V_a at the plume-to-spot transition seems to become less sharp. We notice from Figure 5.3 that in spot mode V_a stays nearly constant with varying $\dot{m}$ and is not very sensitive to current variations. In plume mode, instead, V_a exhibits large variations, increasing with decreasing $\dot{m}$ and, in general, tends to be lower for lower discharge currents, for the same values of $\dot{m}$. This is not the case, though, below certain levels of discharge current. Figure 5.3 shows, in the case of the 3-A experimental run, an increase in voltage with mass flow rate between the values of ~ 0.5 and ~ 1 mg/s, followed by a sharp drop at the plume-

to-spot mode transition. For currents up to 7 A, the hysteresis described in Fig. 5.2 is also evident, with two possible voltage values for the same values of current and mass flow rate. This phenomenon tends to disappear for higher currents, as the HC approaches thermal equilibrium more quickly with varying operating settings due to a higher power input and more stable discharge conditions.

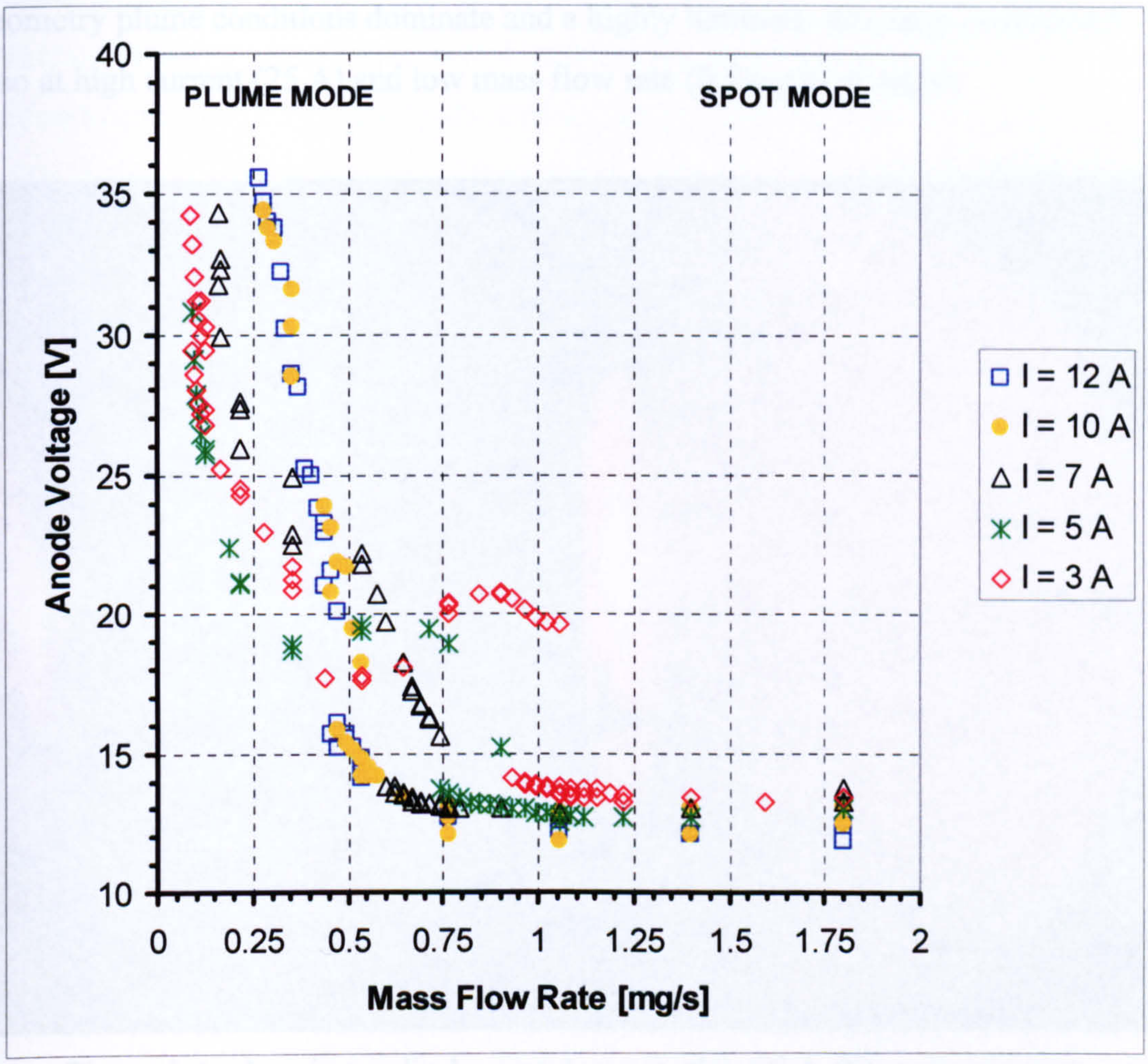

Figure 5.3 – Voltage dependence on argon mass flow rate for different currents.

The hysteresis phenomenon is of direct relevance to our study of the thrust generated by a HC, because it implies that, for the same values of current and mass flow rates, which can be considered as the inputs of our device, the outputs, that is, the anode voltage (the anode power supply is current-regulated) and the thrust generated, can be quite different. In some cases, the HC could be operating either at low voltage, with a quiet, low-power discharge (spot mode), or at high voltage, with a noisy, high-power discharge (plume mode).

At low values of discharge current and $\dot{m}$ the discharge appearance changes, sometimes radically, with an extremely bright plume. At these operating points the plasma luminosity fills the entire chamber. Fig. 5.4 shows visually similar discharge conditions obtained with a different anode (40 mm orifice diameter, insulated front face). Due to the much lower area available for the discharge attachment, with this geometry plume conditions dominate and a highly luminous discharge is obtained also at high current (25 A) and low mass flow rate (0.5 mg/s) of argon.

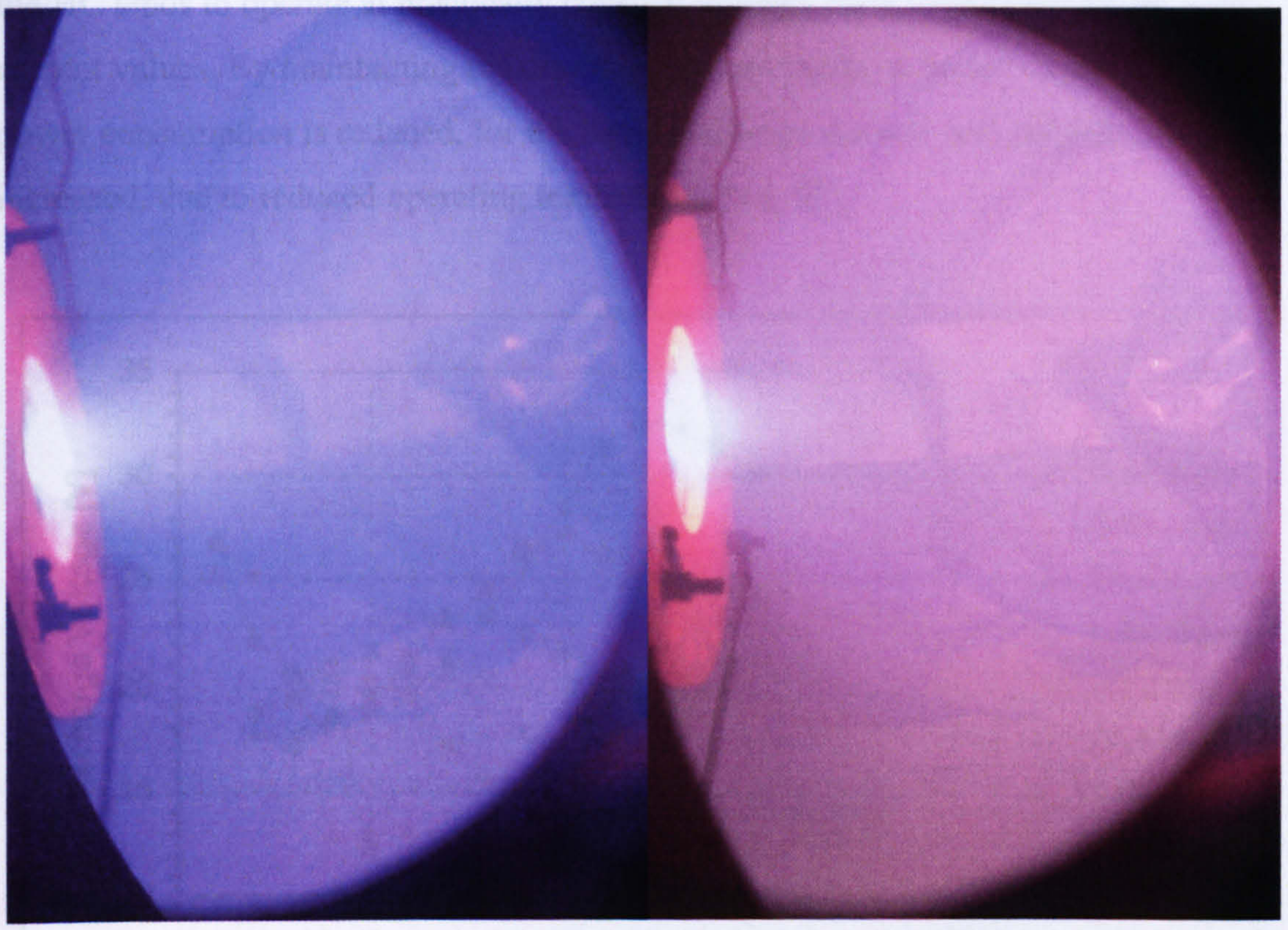

Figure 5.4 – Luminous discharge (plume mode): 25 A, 0.5 mg/s of argon.

The discharge in these conditions can be at times quite stable, albeit at voltages in excess of 50 V. Other times the noise is remarkable, with voltage peaks above 80 V, which cause the discharge to switch off, as the anode power supply is kept limited at 80 V. As these points correspond to extremely high anode heating and could not be consistently recorded, they are not plotted in Figure 5.3. They might correspond to the "neutralizer mode" and to one of the "forbidden regions" already described by Fearn and Patterson in a characterization of the T6 HC [82].

Numerous experimental runs were performed in order to obtain voltage-current characteristics of the T6 HC discharge at different values of $\dot{m}$. As the cathode was being operated with argon and in an open-diode configuration, we expected these curves to be qualitatively similar to previous results obtained with different discharge configurations and propellants, but quantitatively different, as was the case. A large number of results are summarized in the plots of Figure 5.5. It is evident that operation at higher values of $\dot{m}$ is less problematic, as the region of spot-mode operation extends then to lower values of discharge current. As $\dot{m}$ approaches 1 mg/s, the HC tends to operate at practically constant voltage, for a large range of discharge current values. By maintaining the discharge in spot mode, at lower values of V_a, power consumption is reduced, for the same discharge current, and cathode life is increased, due to reduced operating temperature [16, 82].

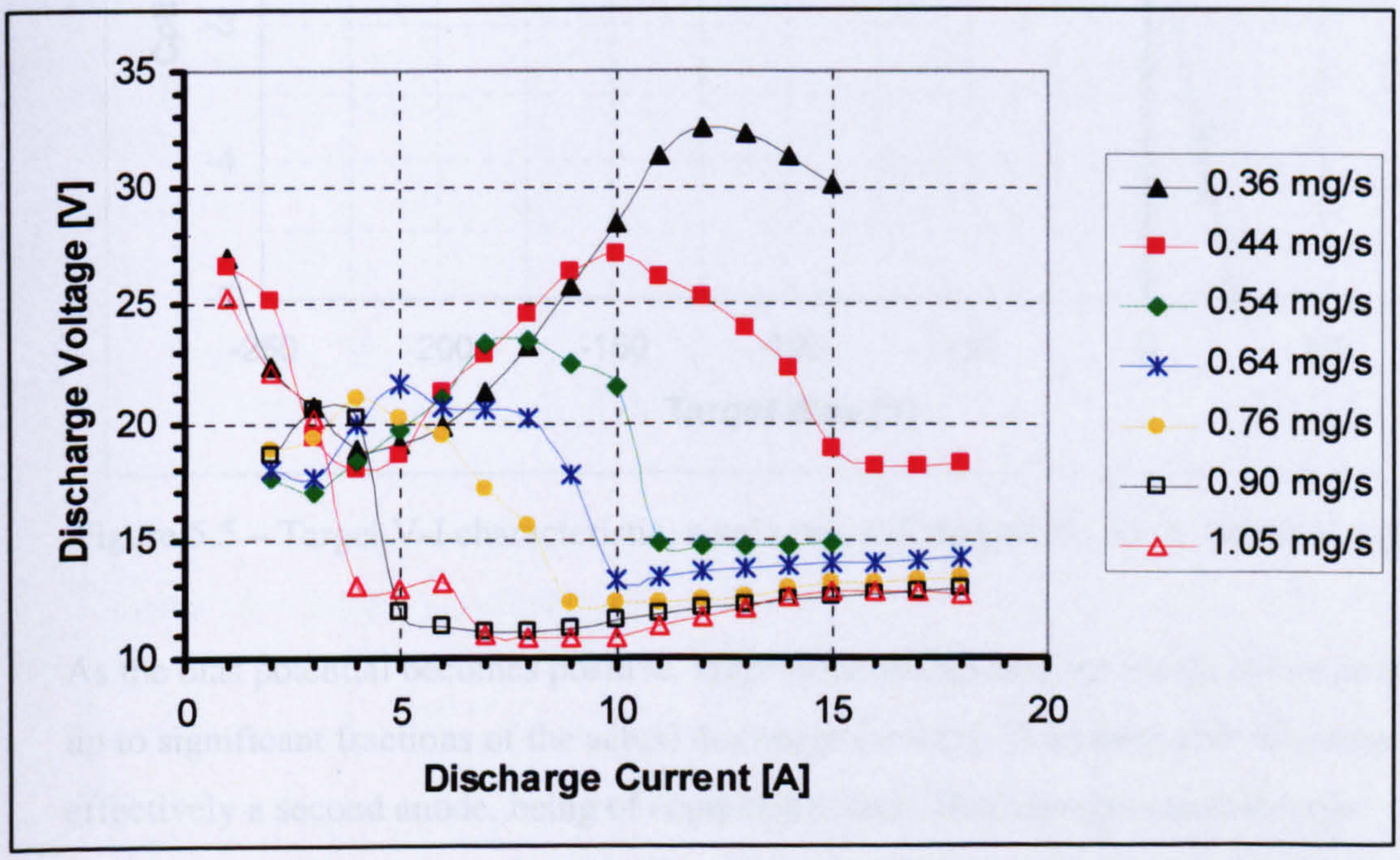

Figure 5.5 – Voltage-current characteristics with varying argon mass flow rate.

5.0.2 – Plume Current Measurements

The target was also used, at the beginning (1GT), as a Faraday plate, to collect the total current in the plume, using argon as propellant. The HC orifice diameter was the initial 0.5 mm value and the anode, with a 10 mm diameter orifice, was at 4.5 mm in front of the HC tip. By biasing the target at different potentials, electron and ion currents can be measured. Figures 5.5 and 5.6 show a typical voltage-current

characteristic of the target, obtained with data from a single experimental run and from several runs respectively. Here the target is acting, in effect, in a manner similar to that of a Langmuir probe, even if its dimensions are large (10 cm side, positioned 5 cm in front of the anode). For increasingly negative potentials, saturation of the collected ion current branch is quickly approached.

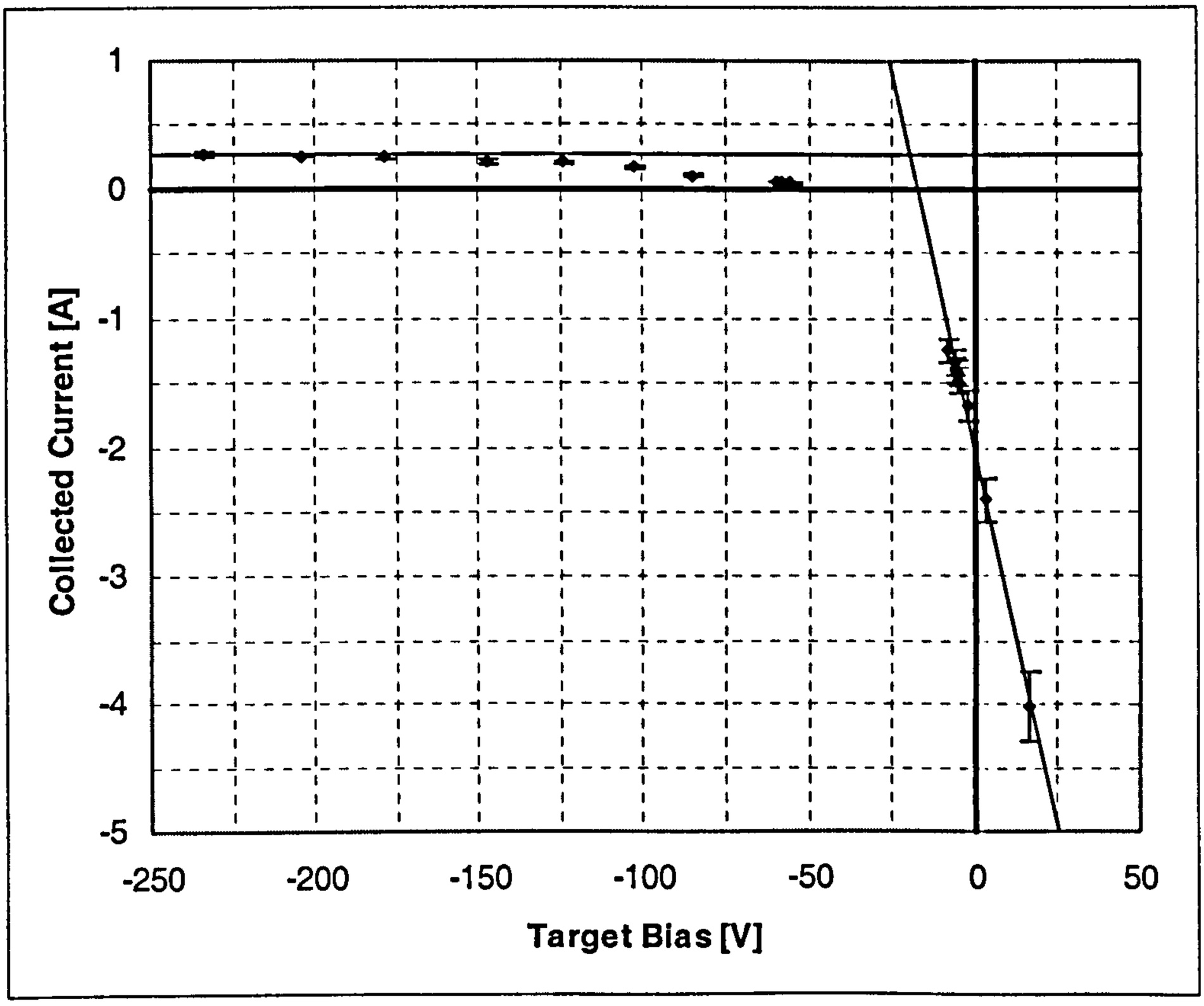

Figure 5.5 – Target V-I characteristic, single run, 0.5 Aeq of Ar, 15 A, 39-43 V [52].

As the bias potential becomes positive, large electron currents are drawn by the probe, up to significant fractions of the actual discharge currents. The target now becomes effectively a second anode, being of comparable size. This changes the discharge conditions, causing the anode voltage to vary. In addition to this, heating led to one of the 1GTs being seriously damaged. This accounts for the region of missing data in the curve in the electron-current saturation region. A positively biased target, therefore, alters the discharge considerably, while a negatively biased target, drawing a much smaller current, leaves it substantially unchanged. The anode voltage, for a target bias potential varying between -50 V and -230 V, shows a variation of only about ±5% for

a single experimental run (Figure 5.5) and ±18% if several runs are considered (Figure 5.6). The larger variation in anode voltage in the latter case is mostly due to differences in discharge conditions from one run to another, caused, for instance, by the hysteresis phenomenon described in Section 5.0.1. Such behaviour suggests that we can use a large negatively biased target, relatively close to the anode, to collect ion plume current measurements with just small alterations of the discharge parameters.

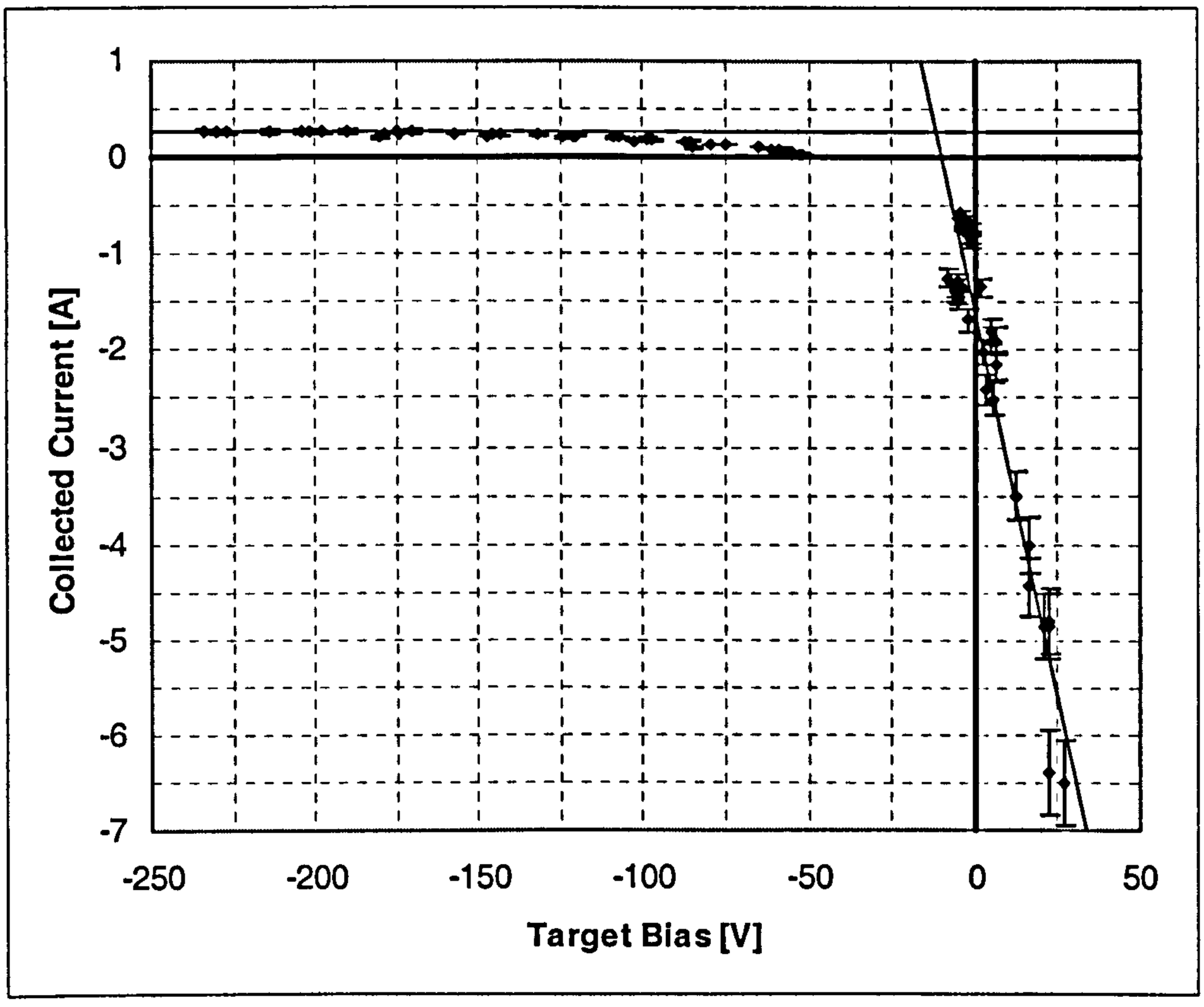

Figure 5.6 – Target V-I characteristic, several runs, 0.5 Aeq of Ar, 15 A, 35-50 V.

Due to limitations in the power supplies available, it was not possible to increase the target bias voltage beyond 230-240 V, so the saturation current values measured are only approximate and slightly lower than the real values. Figure 5.7 shows a detail of Figure 5.6 for the ion current collection region, with the target biased at negative potential with respect to ground. We see that taking the highest measured value of positive collected current as a value for the ion saturation current will produce an underestimation, although not a large one, as complete saturation is not actually

reached. We also see that the floating potential, at which the collected current is zero, is around 50 V negative with respect to the ground.

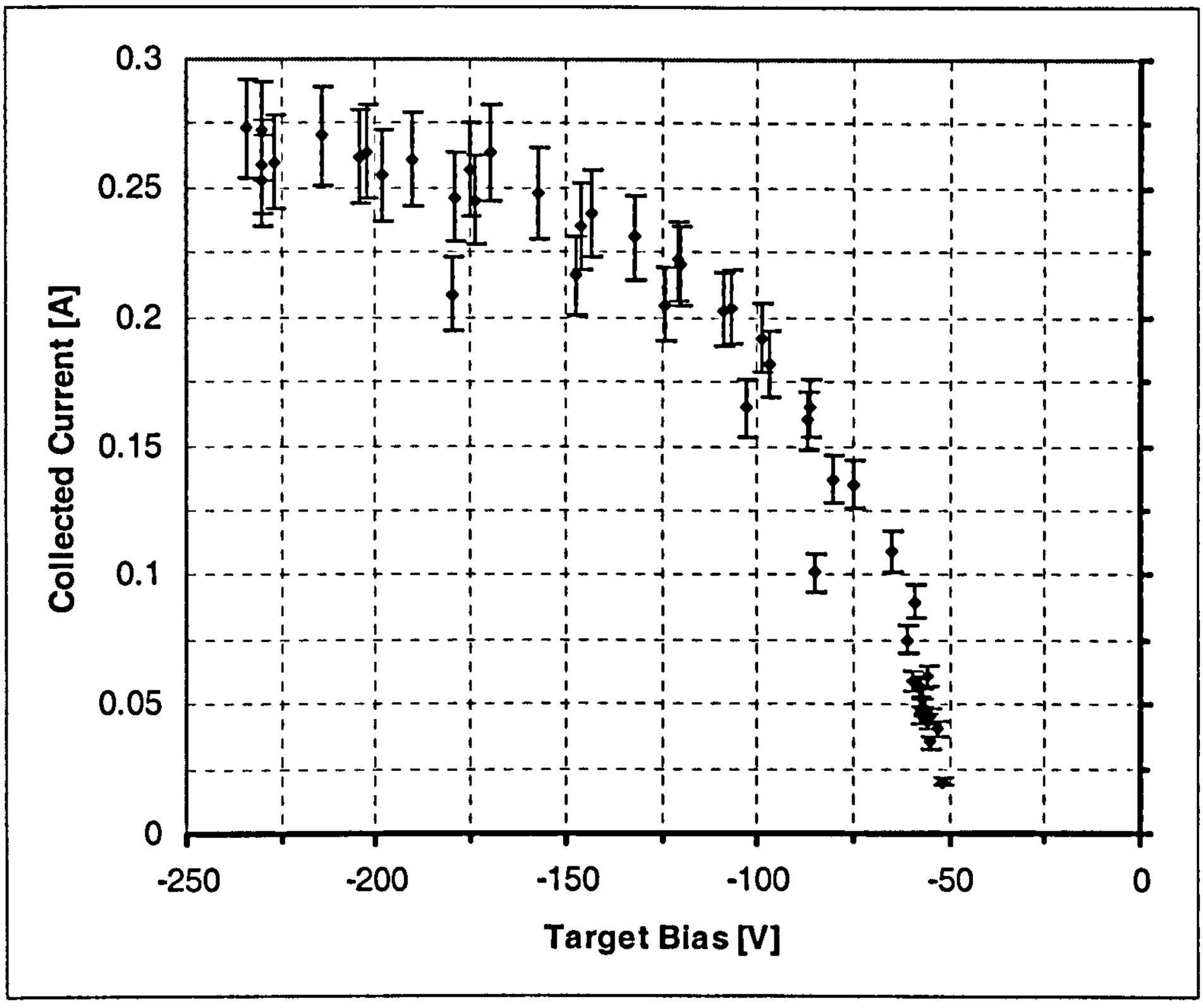

Figure 5.7 – Target V-I characteristic, ion current saturation branch (det. of Fig. 5.6).

The saturation ion current increases exponentially with increasing discharge current, as shown in Figure 5.8. For the same discharge current, increasing the mass flow rate results in a smaller value of collected ion current and therefore, assuming that Ar is singly ionized, ion flow rate. Figure 5.8 shows the values of collected current as fractions of the mass flow rate expressed as equivalent Amperes of singly, totally ionised propellant. We see that, at 0.5 Aeq, corresponding to ~0.2 mg/s of Ar, the ionisation fraction is already greater than 0.5 for a discharge current of 15 A. The extrapolated curves suggest that, for discharge currents of 20-25 A, full ionisation conditions should obtain even at higher mass flow rates (1.0 Aeq, ~0.4 mg/s of Ar). The lower values of collected current at higher mass flow rate could be explained by the fact that, at 10 A discharge current, anode voltages are ~ 40 V at 0.5 Aeq flow rate and only ~ 20 V at 1.0 Aeq. This means that the average power per heavy particle

available in the discharge decreases by a factor of four, namely from 400 W/0.5 Aeq = 800 W/Aeq to 200 W/1.0 Aeq = 200 W/Aeq.

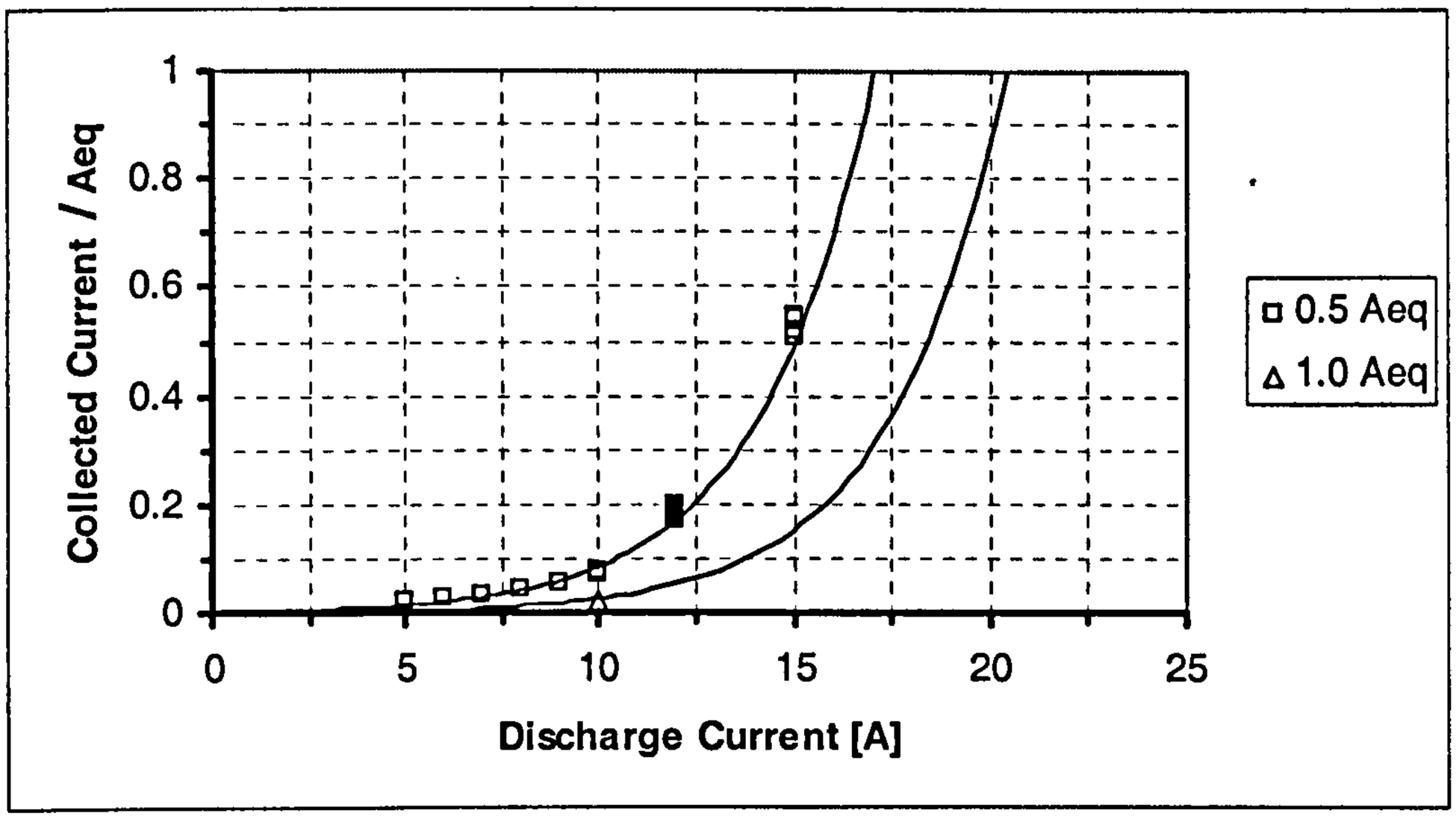

Figure 5.8 – Saturation collected ion current to mass flow rate [Aeq] ratio.

A correlation between increasing collected current and increasing thrust, at constant target bias potential, would suggest that the production of thrust is actually mainly due to ions. An increase in collected current as we increase the target bias potential, on the other hand, may suggest that, as its sheath expands, more low-energy ions are extracted from the plasma and collected. This would increase the current measured, while the thrust, due mainly to hot neutrals, MHD mechanisms and a small amount of high-energy ions, would be substantially unaffected [52]. Large amounts of high-energy ions already present in the plume would reach the target anyway, unless they were repelled by highly positive potentials. Only negative bias potentials strong enough to extract and accelerate positive ions to substantially higher energies would produce a significant increase in the thrust together with the current measured.

Unfortunately, due to the lack of data on ion energies, it is not possible to correlate the measured ion current with thrust generation. Also, at the time these measurements were performed, a PSD had not been set up and a satisfactory measurement procedure for the thrust generated by the HC discharge had not been developed yet. Tentative thrust measurements were abandoned as giving unsatisfactory results. Thus, it was not

possible to relate bias potential to thrust generated, but only bias potential to current collected. As a result, it was not possible to establish any correlation between plume current and thrust. A comparison of results obtained with different gases and widely varying first ionisation potentials (21.56 eV for Ne, 12.13 eV for Xe) would also have been instructive.

A likely source of error in the collected current measurement is secondary electron emission. This can be caused by the impingement of metastable atoms, photons, electrons and ions. For a platinum electrical probe in an argon discharge photoelectric emission may contribute, in some cases, up to 10% of the observed saturation ion current [164]. We need to remember, though, that our target is fundamentally different from traditional electrical probes, in that its size is comparable to the dimensions of the plasma, which will thus be perturbed by the presence of the probe. The problem will be made worse by the presence of impinging energetic ions, especially when the target is kept at a strong negative potential bias.

Even allowing for all these limitations, our measurements of collected current still retain a certain significance, as they suggest that high ionisation fractions might actually be attained, at least at high currents and low mass flow rates (see Fig. 5.8). Therefore, for these discharge regimes thrust production mechanisms such as MHD plasma acceleration or ion acceleration by a potential hump cannot be ruled out, even if their significance remains yet to be demonstrated.

5.0.3 – Thrust Measurements

The thrust produced by a T6 HC was measured with different noble gas propellants (Ar, Kr, Xe) and various discharge configurations. Operation with neon proved problematic, because of issues related to the actual discharge and to the pumping speed of the vacuum system. As often the case with low-atomic mass gases [16], the pumping speed was inadequate at most of the mass flow rates involved, with pressure in the vacuum chamber rapidly increasing and the turbomolecular pump slowing down. Breakdown was actually achieved in a more limited number of cases and the discharge was often unstable, with a tendency to shut down sometimes as conditions were varied. Therefore, thrust measurements with neon as a propellant were performed in a narrower range of mass flow rates and for fewer values of discharge

current. As they are not enough to show significant trends, they are not presented in this thesis. Thrust with no discharge and with a cold or heated cathode, however, was measured with Ne, Ar, Kr and Xe.

5.0.3.1 – Cold and Heater Thrust (Discharge Off)

As a way of both validating our thrust measurement system and also providing a baseline for our thrust measurements, as described in Section 4, numerous measurements have been taken of the thrust generated by a gas flow through the HC with the discharge off. This was done with the heater on, at different power settings, and also with the heater off. Several noble gases were used as propellants, namely Ne, Ar and Xe, with the 1.0 mm orifice diameter HC, Ar and Kr with the 0.5 mm one.

Raw data (values of displacement, Δx) are shown in Figs. 5.7 and 5.8 for typical experimental runs of "heater" thrust measured with the 0.5 mm orifice diameter HC. The gas flow is varied by quickly turning the needle valve, then the system is then left for a few minutes to stabilize, in order to be able to subtract thermal drifts and other disturbances. In Fig. 5.7 the mass flow rate of argon is increased from 0 to 1.5 mg/s in steps of 0.5 mg/s at 4-minute intervals (dashed lines). The heater power is ~80 W. In Fig. 5.8 the mass flow rate of krypton is increased from 0 to 1.0 mg/s in steps of 0.5 mg/s at 4-minute intervals (dashed lines). The heater power is ~60 W.

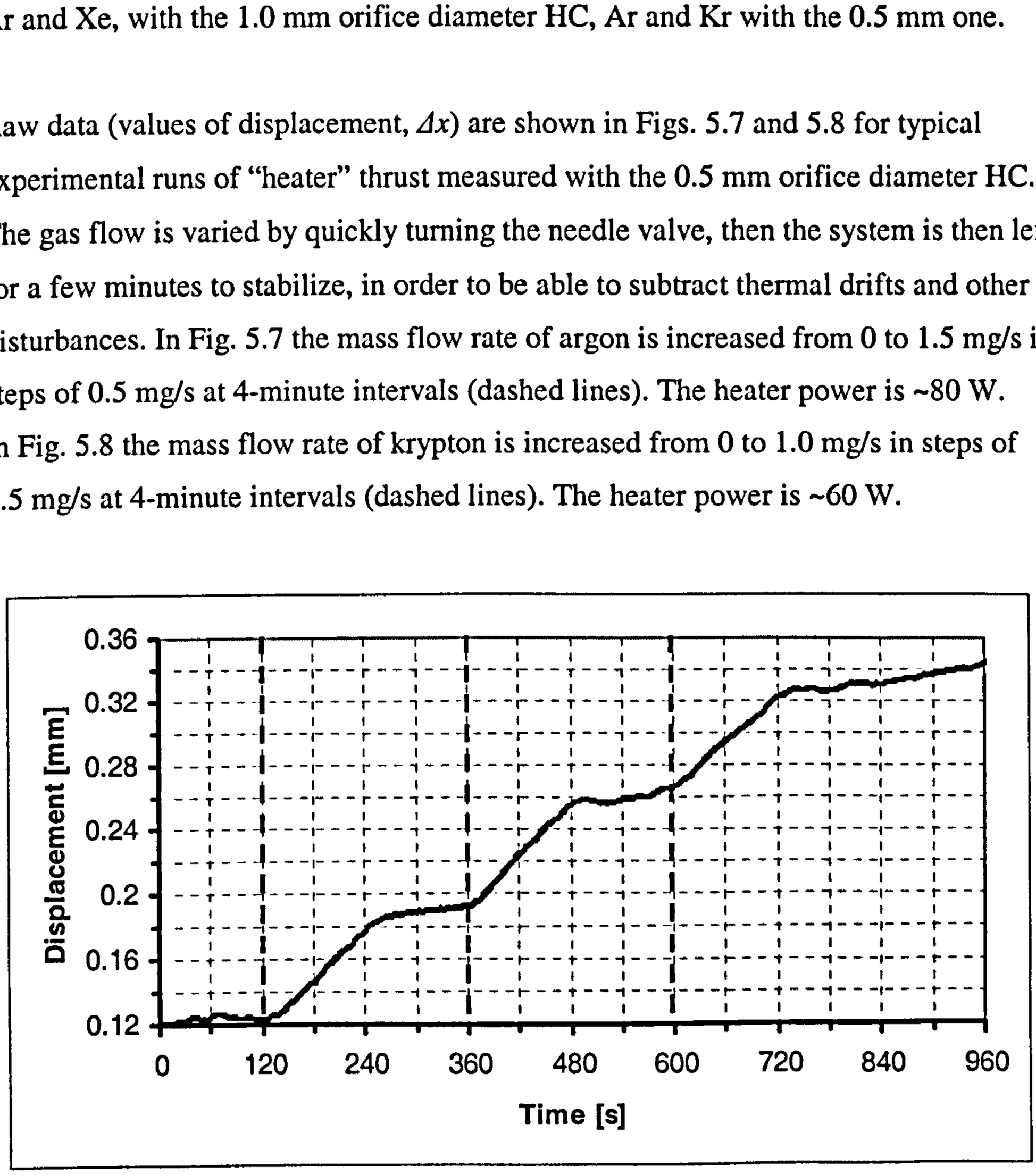

Figure 5.7 – "Heater" thrust run with Ar, 0.5 mm HC orifice diameter.

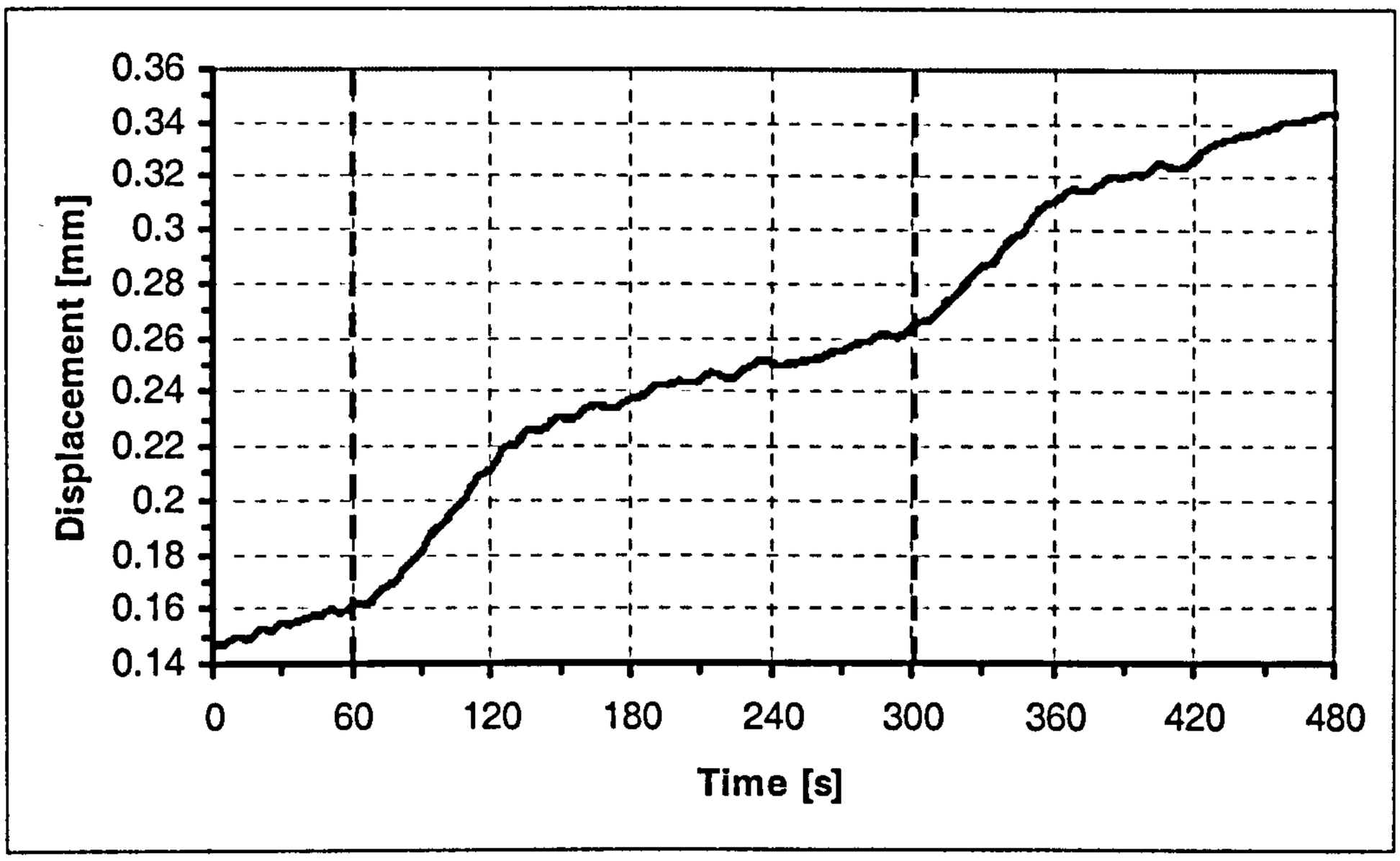

Figure 5.8 – "Heater" thrust run with Kr, 0.5 mm HC orifice diameter.

The data plotted in Figs. 5.7 and 5.8 are straight PSD reading, only averaged to filter out oscillations, as described in Chapter 4. It is to be noticed that such averaging of the curves, while smoothing down the oscillations, introduces also a phase shift. Thus, the mass flow rate increase at each step, much sharper in reality, in the plots appears "spread out" over more than one minute. These are just two examples of many different data sets taken in very different conditions over a long period of time. Measurements from all these data sets were averaged to account for the influence of slightly different conditions and of the chamber background pressure (as described in Chapter 4) on thrust at levels much smaller than those encountered during discharge operation. By using data obtained at mass flow rates below ~1 mg/s results, shown in Table 5.1 and Fig. 5.10, were obtained in excellent agreement with the theoretical predictions outlined in Section 2.0, as far as the square-root dependence of Isp on temperature is concerned. Cold and "heater" thrust measurements are assumed to have a precision of ±20%, estimated from the standard deviation of the cases involving the highest variability between different measurements. This translates into a ±20% precision in the specific impulse estimates given in Table 5.1 and Fig. 5.10, which agrees with the precision given in Section 2.0 for the theoretical I_{sp} estimate of Eq. (2.10). Varying the heater power level between ~40 W and ~80 W did not have a

clear effect on the thrust, which was much higher than that measured with a cold HC. Also, the different anode configurations tested did not affect the thrust with no discharge, apart from early data collected with the 10 mm orifice diameter anode at 4.5 mm from the HC tip (see Fig. 5.9), which yield an average specific impulse of ~48 s ±20%. This is definitely lower than measured in the other anode configurations, but still the error bars overlap.

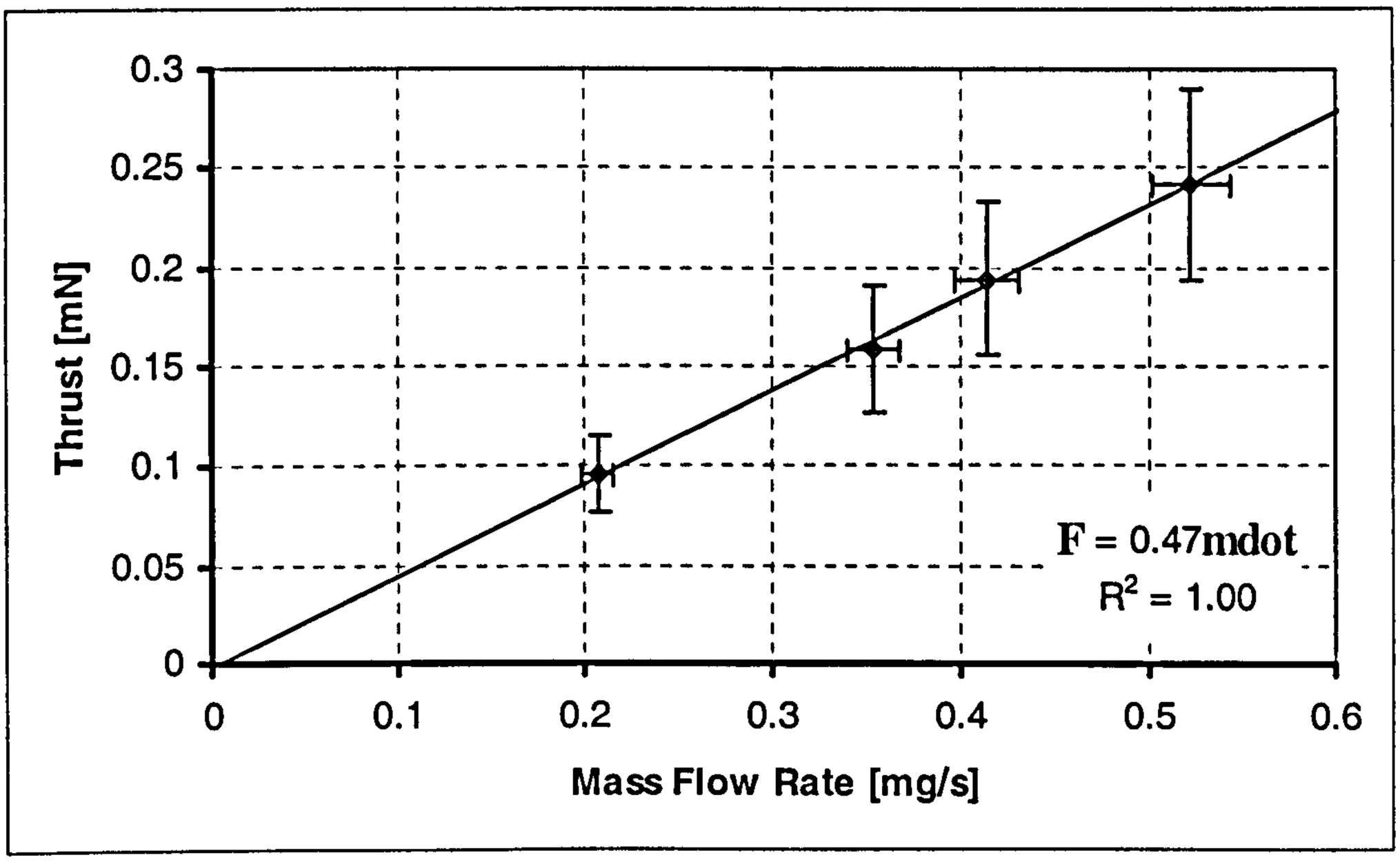

Figure 5.9 – Cold thrust with Ar, HC orifice diam. = 0.5 mm, anode diam. = 10 mm.

It is to be noted that the measurements shown in Fig 5.9 were taken prior to the implementation of the PSD, with the 2GT, when the laser spot displacement was still read visually on a 0.5 mm precision scale, with much lower accuracy, which could account for the differences. Such a method, while completely inappropriate for measurements with electric discharge, as illustrated in Chapter 4, was still deemed adequate for cold thrust, where no concern about thermal deformations (even those caused by the HC heater alone) was involved. This allowed us to wait for the laser spot to stabilize, facilitating the visual reading. A slight drop in specific impulse could also be attributed to plume impingement on the anode. For the 10 mm orifice, in fact, the "open" half angle available for plume expansion was only ~22° while, for the other anode configurations, it was always greater than 45°. While the maximum turning angle for the Prandtl-Meyer expansion of the ideal flow of a monoatomic gas

from a sonic orifice into a tank at negligible pressure is 90° , viscous effects at the orifice exit and the continuum flow assumption breaking down already a few diameters downstream of the orifice substantially change the picture. As shown by simulations and measurements , the plume divergence half-angle is always much lower than 90°. This could make the diameter of the anode orifice and its distance from the HC tip very important. The fact that measurements, taken with widely different anode and target (2GT and 3GT) configurations, actually give results that are quite consistent, is confirmation of the reliability and robustness of our measurement system.

Increasing the orifice diameter from 0.5 mm to 1.0 mm caused the thrust per unit mass flow rate to decrease by 50%. The results for all the various combinations of parameters are presented in Table 5.1, in the form of average specific impulse estimates.

	Cold HC	**Heated HC**
0.5 mm orifice diameter	Ar: I_{sp} = 27 s	Ar: I_{sp} = 65 s Kr: I_{sp} = 46 s
1.0 mm orifice diameter	Ar: I_{sp} = 13 s	Ne: I_{sp} = 44 s Ar: I_{sp} = 32 s Xe: I_{sp} = 18 s

Table 5.1- Cold and heated HC specific impulse values.

As expected from the theory in Section 2.0, the specific impulse for all propellants is, to a very good approximation, inversely proportional to the square root of the atomic weight (20 for Ne, 40 for Ar, 84 for Kr, 131 for Xe). This is shown in Fig. 5.10 for the heated cathode case: the deviation from a square-root dependence is ~5%.

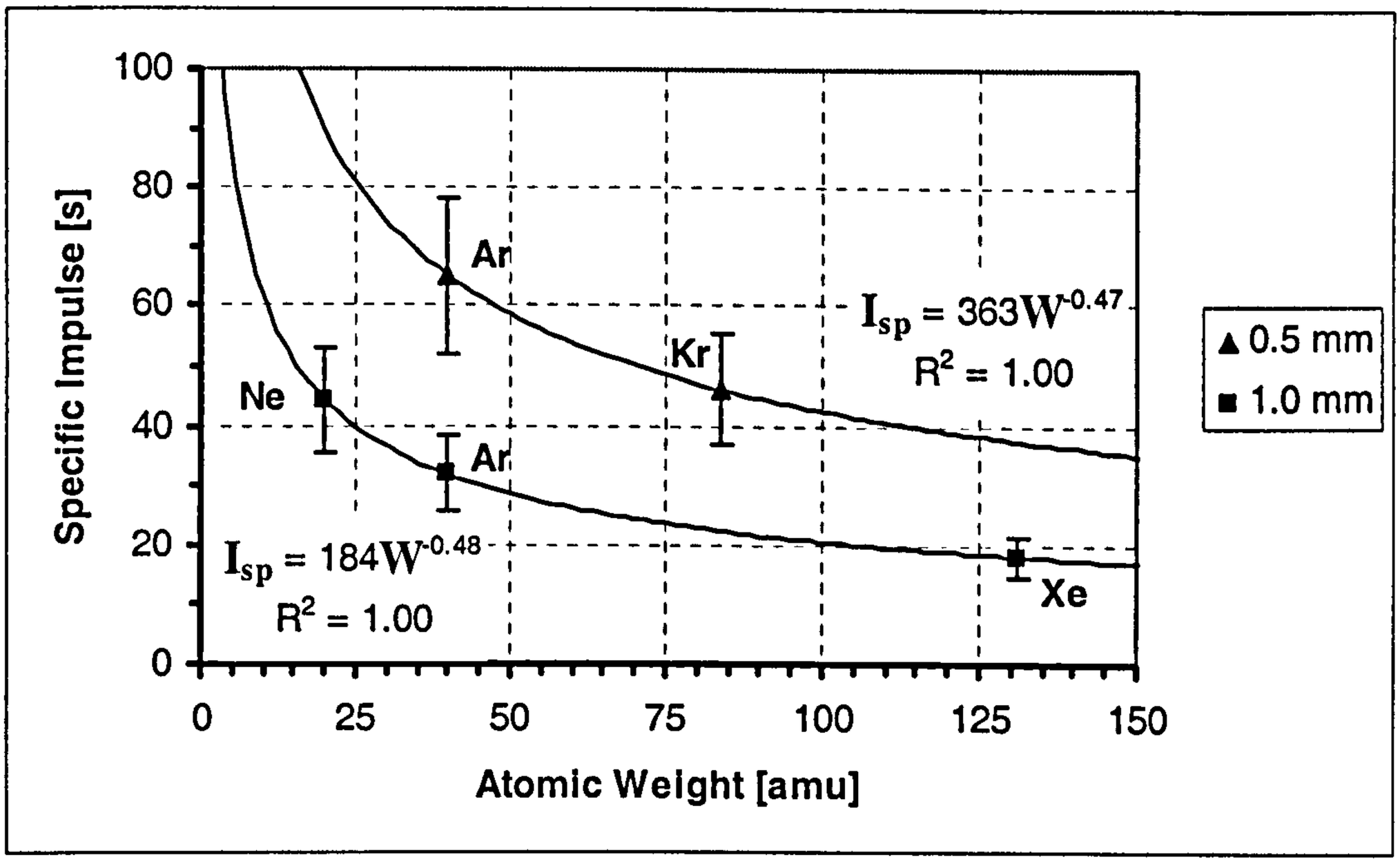

Figure 5.10 – Heated HC specific impulse as a function of propellant atomic weight.

Assuming a dependence of the thrust on the square root of temperature (see Section 2.0), and the gas atoms to be in equilibrium with the HC insert wall, the ratio of specific impulses for the heated cathode and the cold one, at room temperature (~300 K), allows us to estimate the insert temperature, when heated, at 1700-1800 K, with an increase of ~5.5-6 times. This compares very well with optical measurements of the HC interior conditions obtained by Pottinger [57, 86, 96]. The HC tip face temperature measured with ~80 W heater power (~ 1600 K) is close to the upper end of a range of values measured with varying discharge current and mass flow rate of argon. Measurements were taken at the HC tip face and at the orifice (0.5 mm in diameter). Only the measurements taken at 1.5 mg/s mass flow rate are shown in Fig. 5.11, as those at 1.0 mg/s are thought to be affected by error caused by the HC not reaching complete thermal equilibrium. Such a variation in mass flow rate, however, did not appear to greatly affect the temperature values.

All these temperature measurements were taken with a disappearing filament optical pyrometer and are not corrected for emissivity or transmittance effects. They are, therefore, probably underestimating the real temperature values, as the emissivity will be smaller than unity and the radiation is not perfectly transmitted or reflected, with

losses at the various optical surfaces. They are, nonetheless, valuable in a relative sense, allowing us to compare different discharge conditions [53]. As the plasma in a T6 HC discharge is, in general, optically thin in the visible and near infrared for gases of interest [15, 86], the temperature measurements taken at the orifice also retain a definite significance. It is interesting to note the good agreement, in magnitude and trends, with the temperature measurements made by Monterde in a UK-25 HC [165] and by Patterson in a T6 HC [85] operating on xenon in a diode configuration .

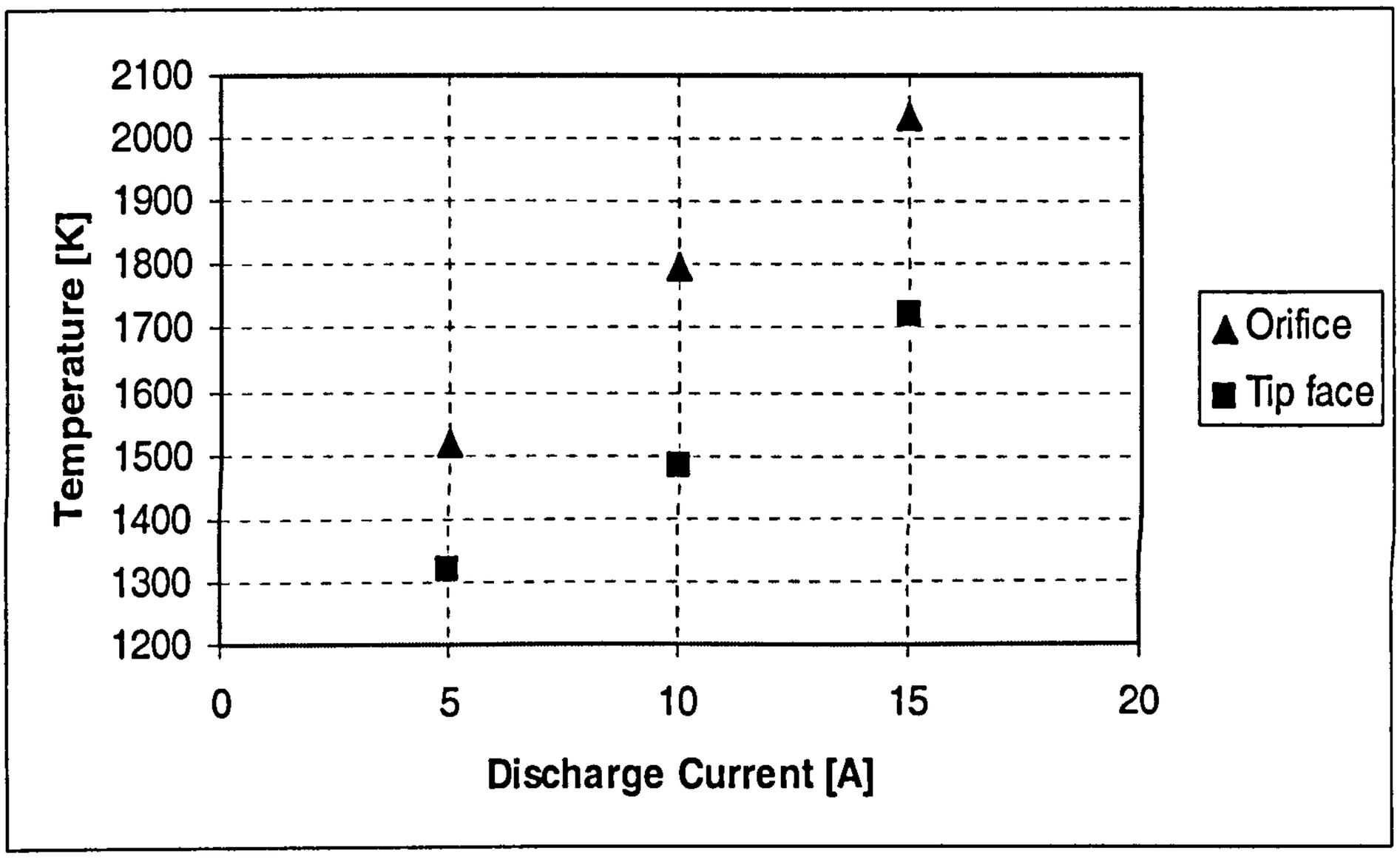

Figure 5.11 – HC tip face and orifice temperature at 1.5 mg/s of argon.

5.0.3.2 – Electric Thrust (Discharge On)

Thrust measurements are presented for all propellants, except neon, for a range of mass flow rates between ~0.3 mg/s and ~3mg/s and a range of discharge currents between 5 A and 25 A, for the reasons described in Chapter 4.

All measurements shown in figs. 5.13-5.17 were taken with a 20 mm orifice anode positioned at 2.0-2.5 mm in front of the HC tip. The reasons behind the choice of this discharge configuration are detailed in Chapter 3. Figs. 5.13, 5.14 and 5.15 are, respectively, for argon, krypton and xenon and a 0.5 mm HC orifice diameter. Figs.

5.16 and 5.17 show measurements taken with argon and xenon and a 1.0 mm HC orifice diameter.

Fig. 5.12 shows comparison between the first data taken with the PSD system, with the 20 mm orifice anode placed at D ~ 4 mm in front of the HC tip, and data taken later, with the same anode placed closer, at D ~ 2 mm. We notice that, for constant mass flow rate of argon, the thrust increases linearly with increasing current. It is interesting to note that, while at 1.0 mg/s there is practically no difference in performance between the two configurations, at 1.5 mg/s the thrust produced with the anode farther away from the HC tip is lower. This could be ascribed, at least in part, to a higher divergence of the jet as we increase the mass flow rate. The open half-angle available to plume expansion, in fact, is lower with the anode farther away from the HC tip (44° instead of 51°).

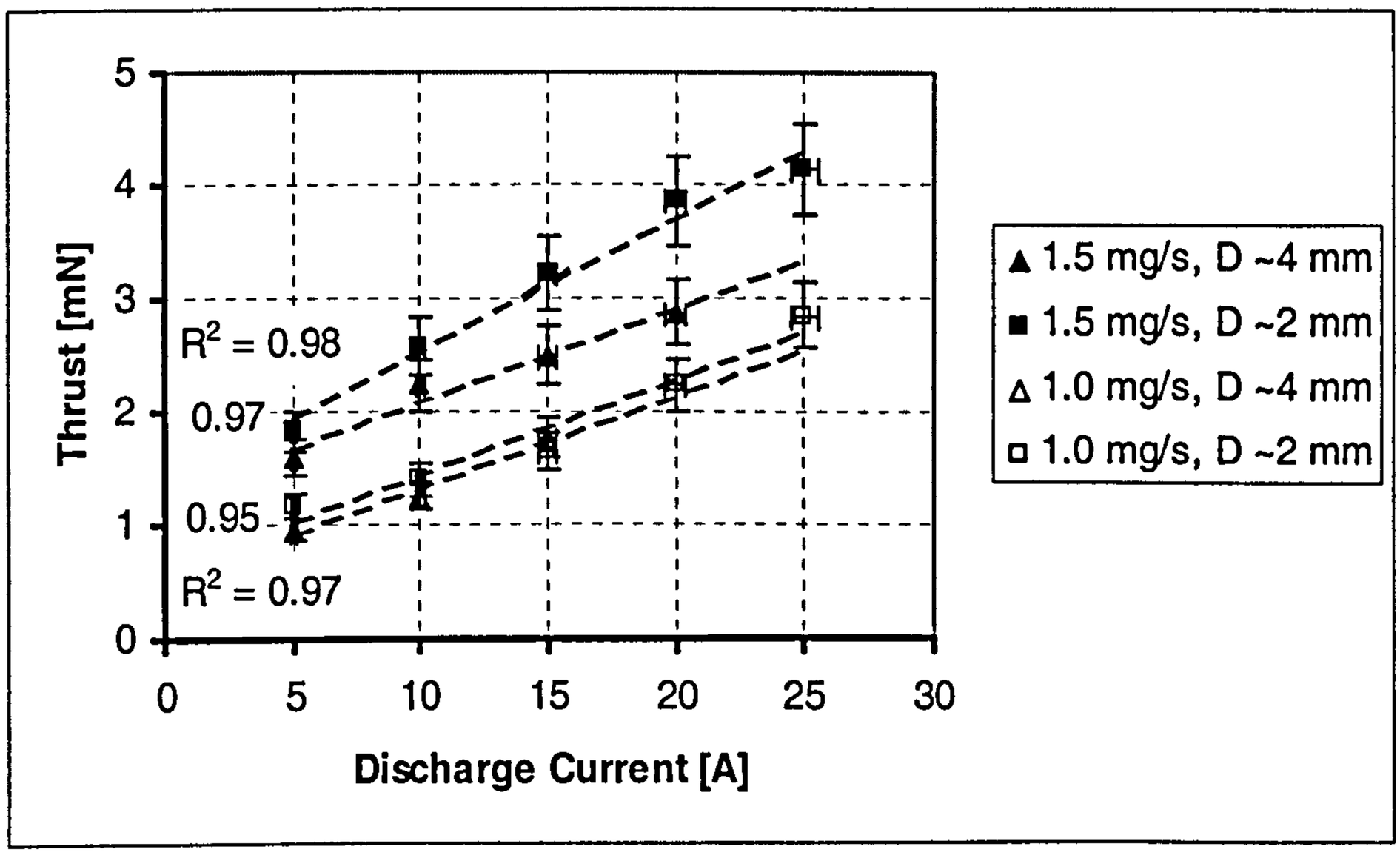

Figure 5.12 – Performance comparison between different values of the HC-anode distance D, 0.5 mm HC orifice diameter, argon propellant.

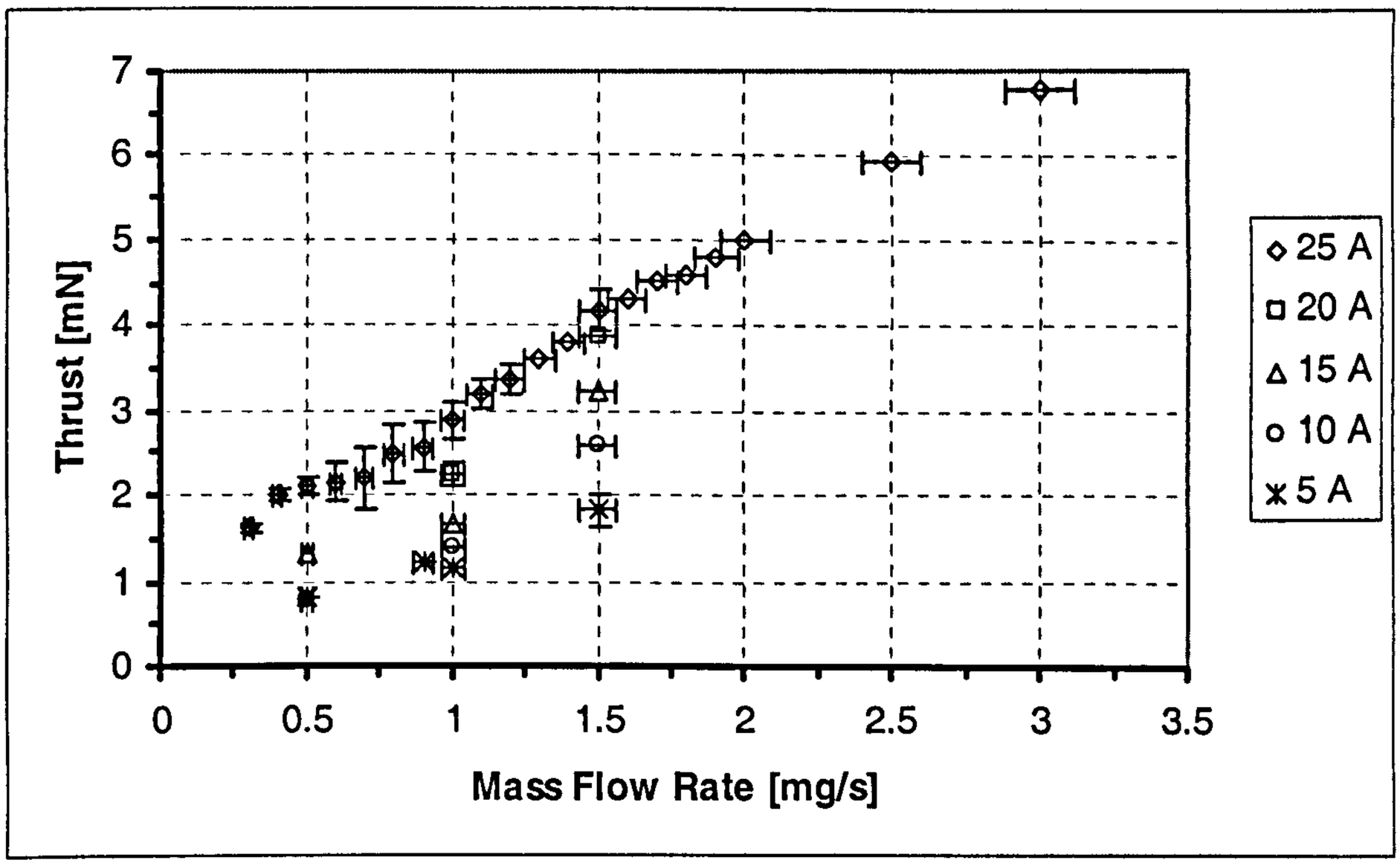

Figure 5.13 – Thrust vs. mass flow rate for argon, 0.5 mm HC orifice diameter.

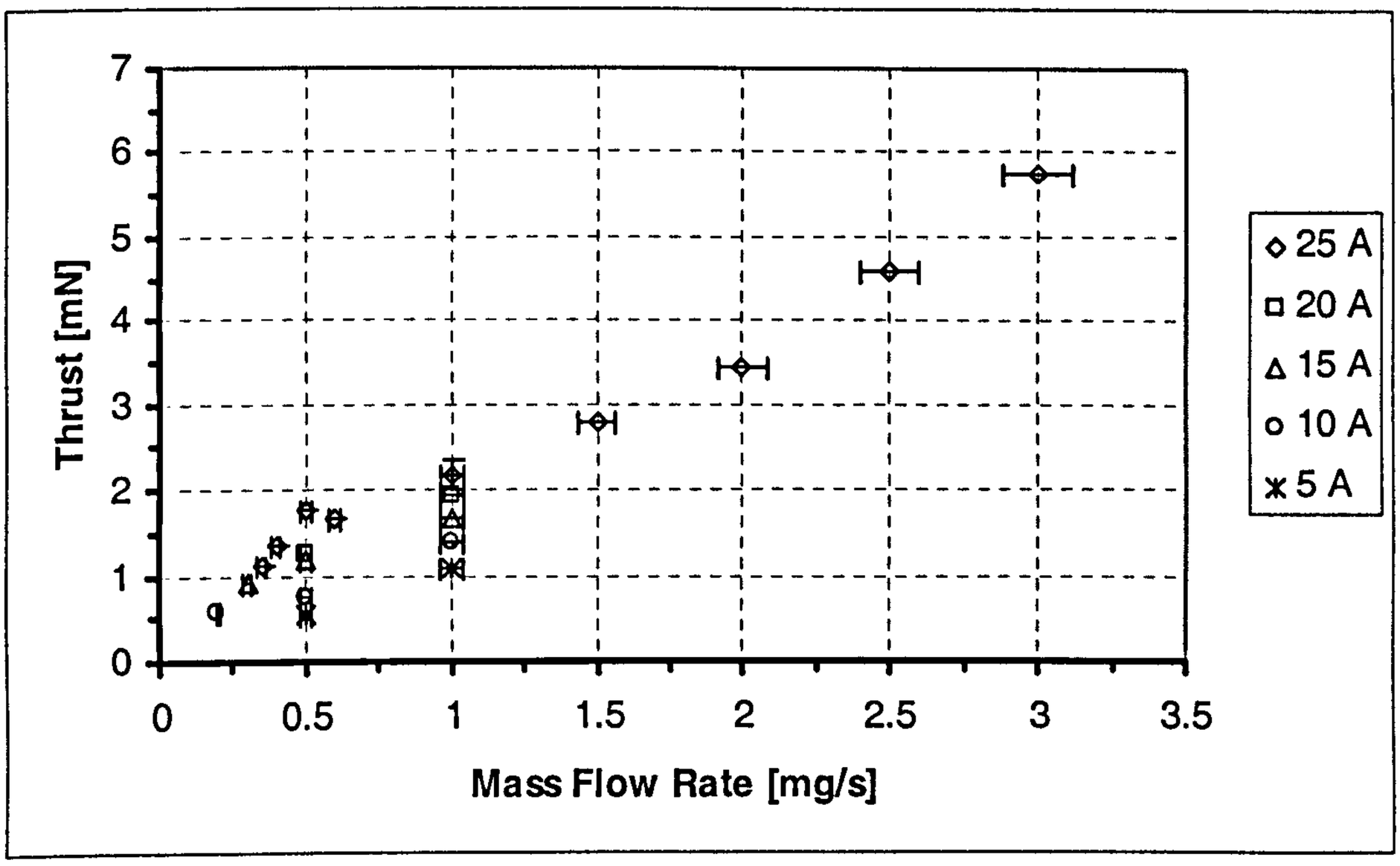

Figure 5.14 – Thrust vs. mass flow rate for krypton, 0.5 mm HC orifice diameter.

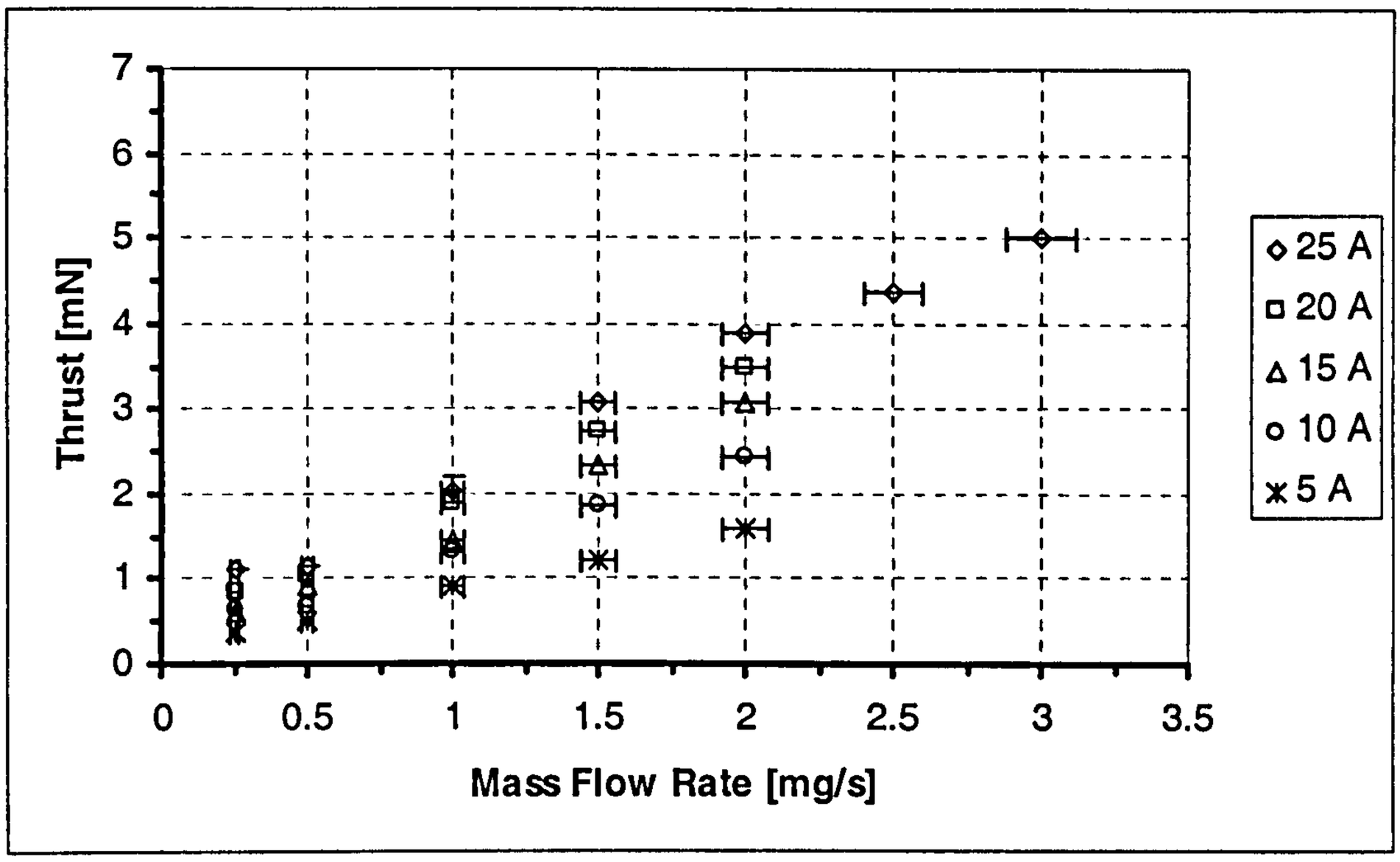

Figure 5.15 – Thrust vs. mass flow rate for xenon, 0.5 mm HC orifice diameter.

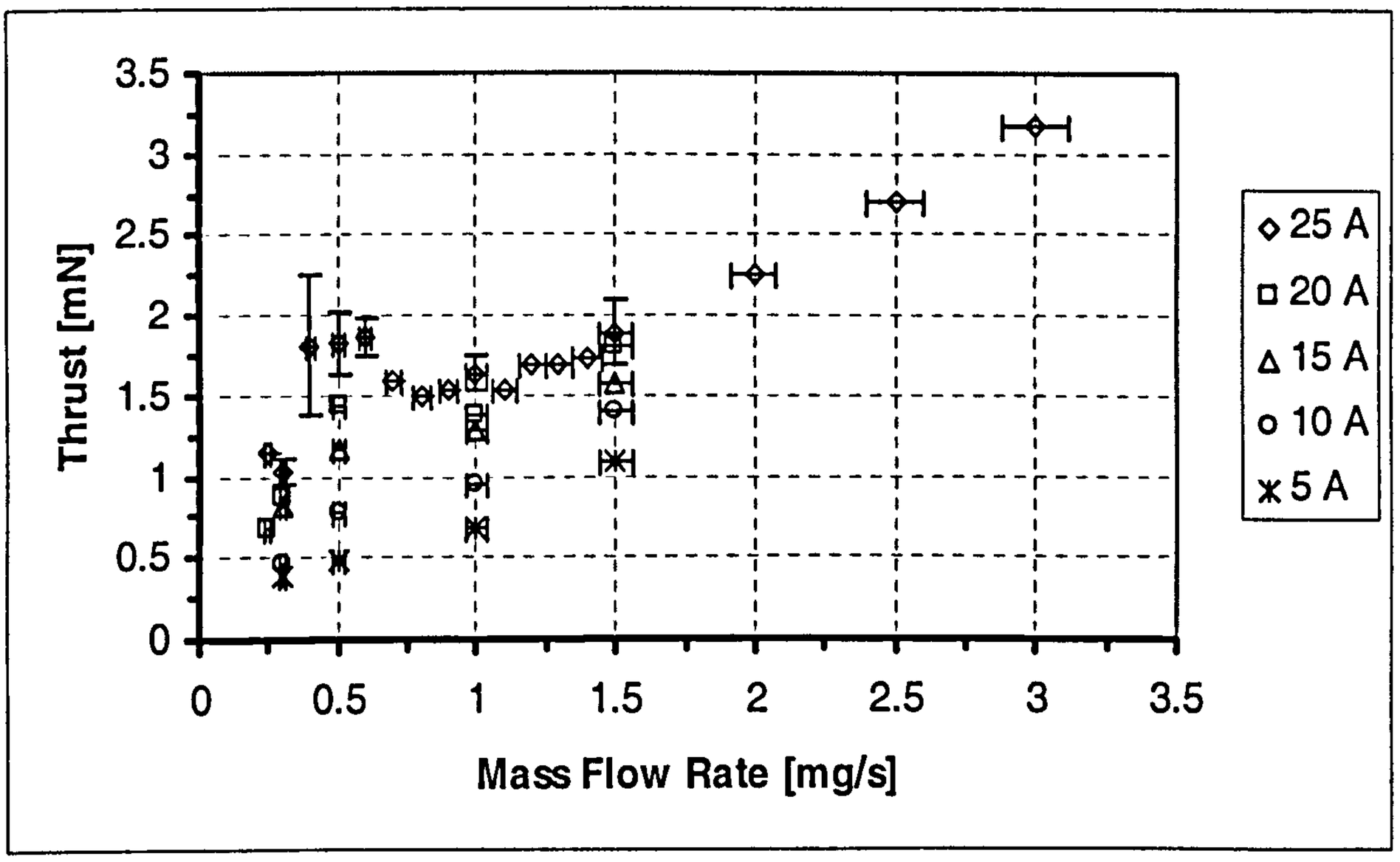

Figure 5.16 – Thrust vs. mass flow rate for argon, 1.0 mm HC orifice diameter.

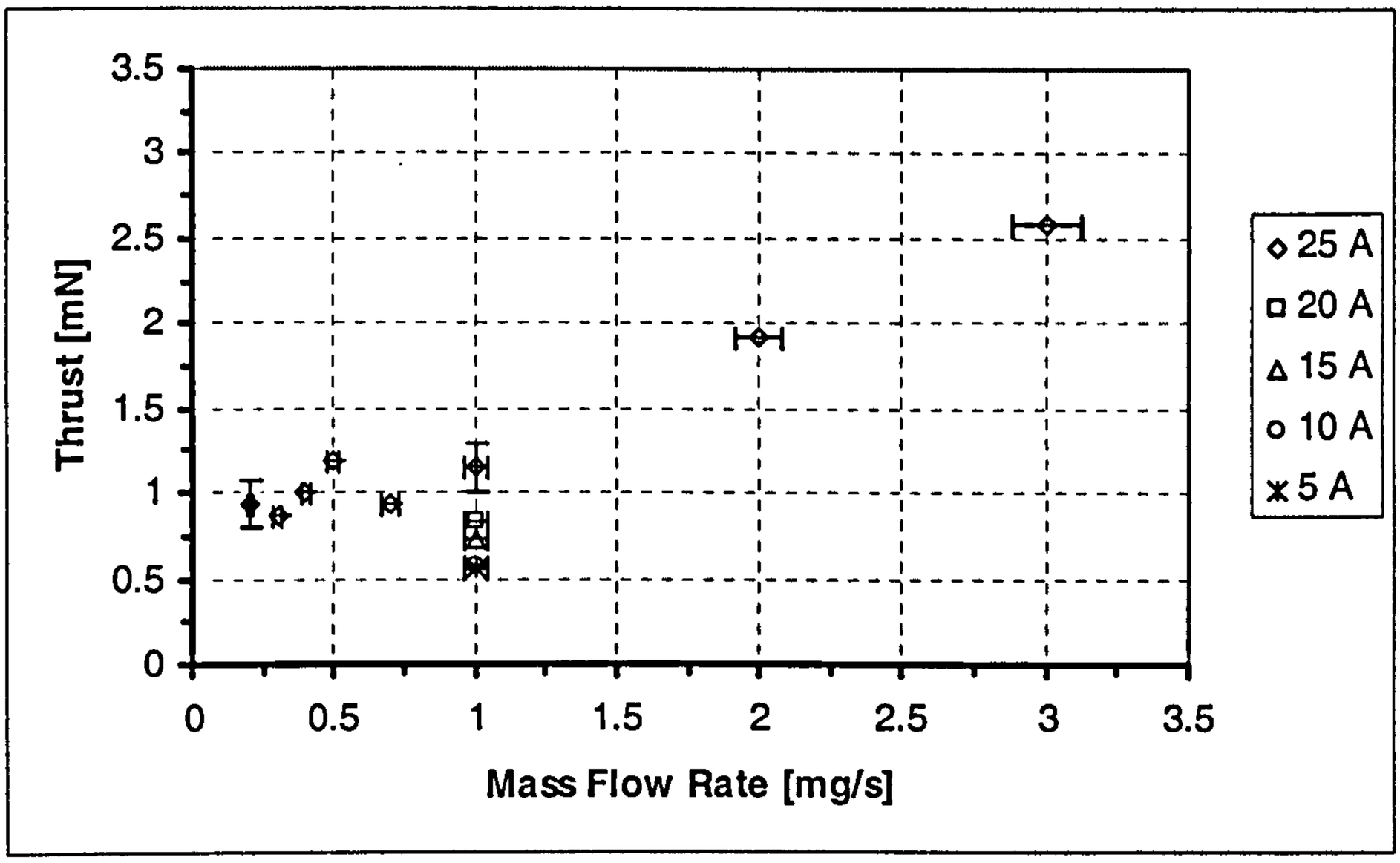

Figure 5.17 – Thrust vs. mass flow rate for xenon, 1.0 mm HC orifice diameter.

General trends are clear and show consistently for all propellant gases and geometries. As expected, at constant discharge current the thrust increases with increasing mass flow rate and, at constant mass flow rate, the thrust increases with increasing current, as more energy is deposited into the flow. For values of mass flow rate higher than ~1 mg/s the thrust shows a linear dependence on mass flow rate, for constant discharge current. As these conditions correspond in general to spot mode operation , at a discharge voltage constant to within ±5%, this corresponds also to operation at constant power. For a given mass flow rate, the thrust for a 1.0 mm diameter orifice is approximately half of that for a 0.5 mm diameter, consistent with the results obtained for the "cold" and "heater" thrust, with no discharge (see Section 5.0.3.1). For values of mass flow rate lower than ~1 mg/s we notice a departure from this linear behaviour, with the thrust presenting a local plateau and, in the 1.0 mm orifice diameter case, even a relative maximum around 0.5 mg/s.

All of the above is further clarified by plotting the values of the specific impulse, which is just thrust per unit flow rate in weight. Figs. 5.18-5.22 show data taken at maximum discharge current (25 A, 20-25 A for mass flow rates below ~0.5 mg/s). The discharge voltage is roughly constant (10-13 V) for mass flow rates higher than ~1 mg/s, corresponding to stable spot mode. For mass flow rates lower than ~1 mg/s,

corresponding to noisy, unstable plume mode, the discharge voltage increases rapidly, in some cases above 50 V. The specific impulse I_{sp} is, in general, higher for lighter gases, as shown in Figs. 5.20-5.22. I_{sp} shows a large increase with decreasing mass flow rate, corresponding to increasing discharge power to mass flow rate ratio, as discussed in Section 5.1.

Figs. 5.18 and 5.19 compare the specific impulse obtained with a 0.5 mm and a 1.0 mm orifice diameter HC with argon and xenon respectively. Doubling the orifice diameter nearly exactly halves the specific impulse at high mass flow rates, consistent with our measurements of "heater" thrust (see Section 5.0.3.1), which showed a 50% drop in I_{sp} with the 1.0 mm diameter orifice. It is quite clear that a larger orifice causes a general degradation in performance, with lower values of specific impulse for the same discharge conditions even at lower mass flow rates. At mass flow rates below ~1 mg/s, however, we notice a rapid recovery, until the I_{sp} values for both orifice diameters essentially coincide, within the error bars, for mass flow rates below ~0.5 mg/s.

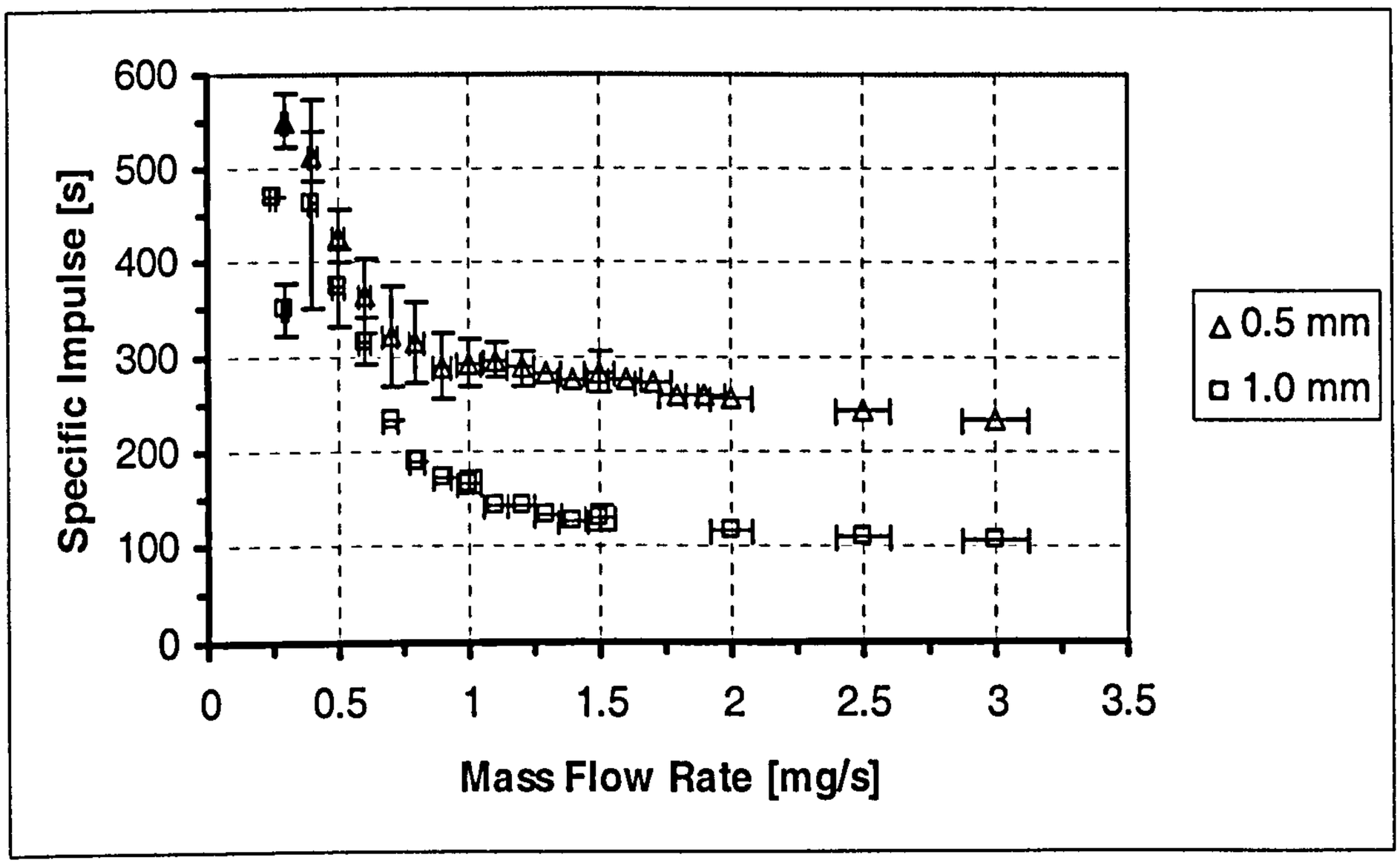

Figure 5.18 – Argon operation at two different HC orifice diameters.

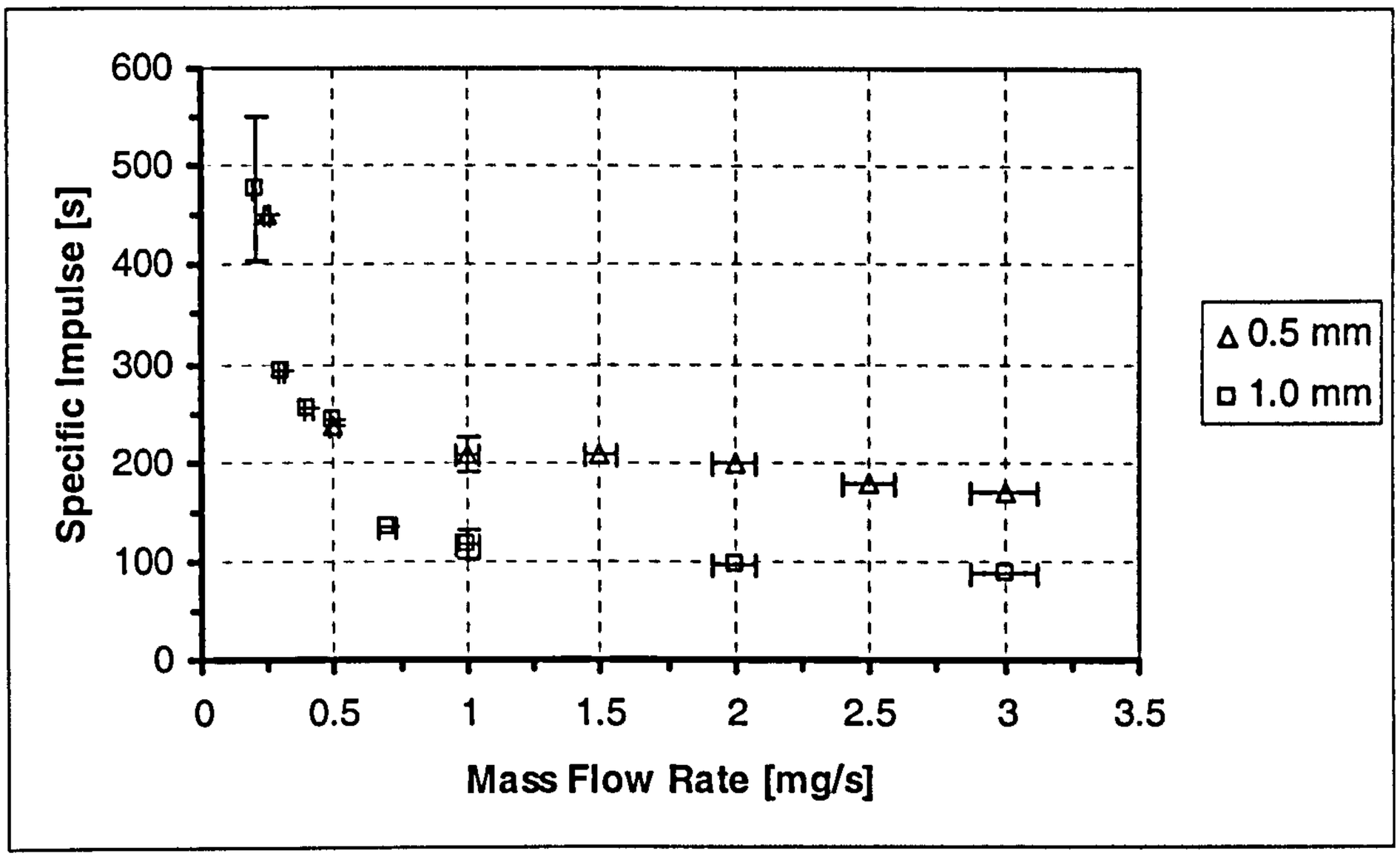

Figure 5.19 – Xenon operation at two different HC orifice diameters.

Figs. 5.20 and 5.21 compare the specific impulse obtained with different propellant gases for 0.5 mm and 1.0 mm HC orifice diameter, respectively. In both cases, higher values of specific impulse are obtained using propellants with lower atomic mass. Krypton presents a somehow more irregular behaviour, which disappears at high mass flow rates, where the values show approximately the relative magnitudes expected from theory in Chapter 2 and verified in the "heater" thrust measurements, even if they are closer to each other than would be dictated by a scaling with the inverse of the atomic mass square root.

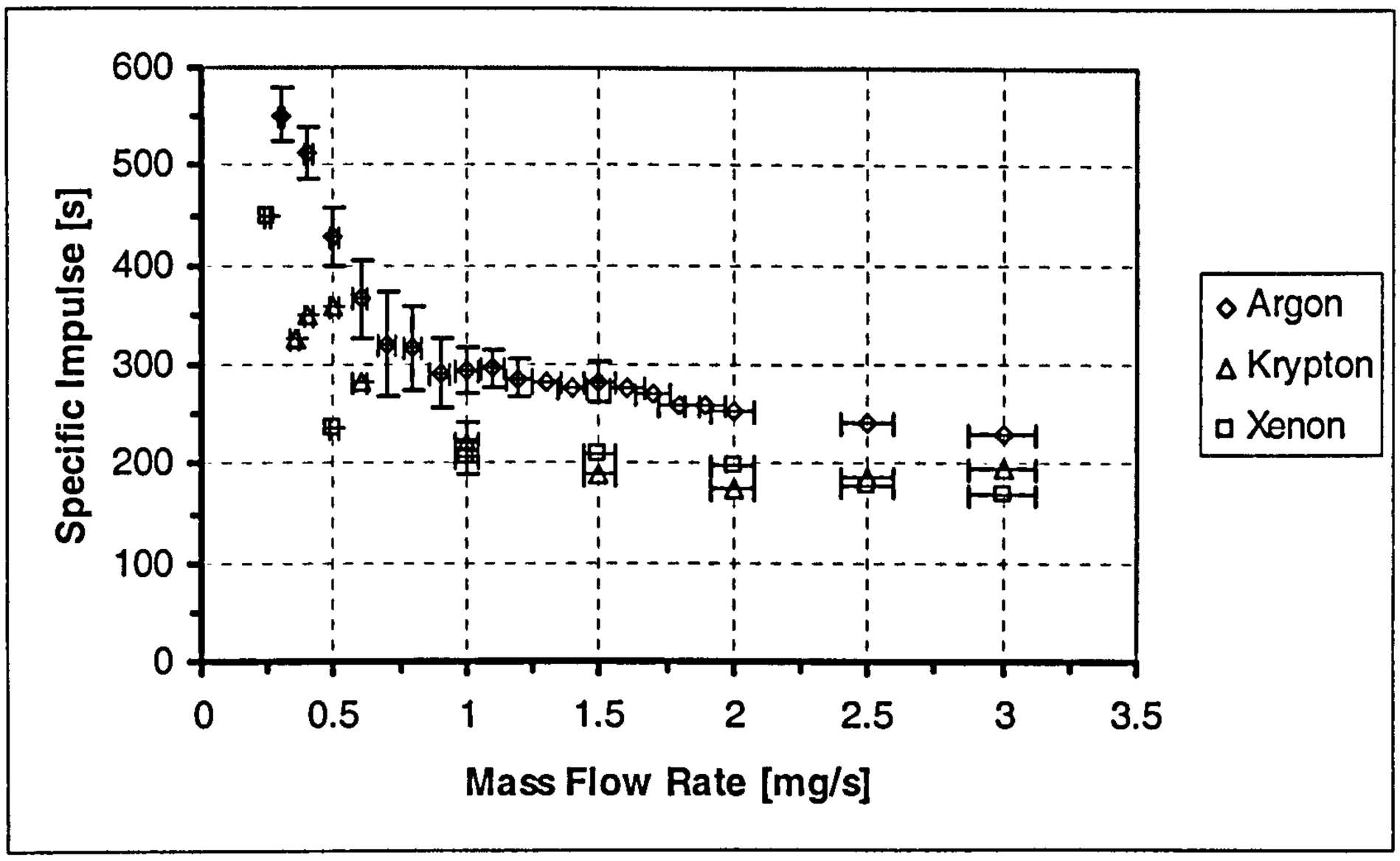

Figure 5.20 – Operation with different propellants for 0.5 mm HC orifice diameter.

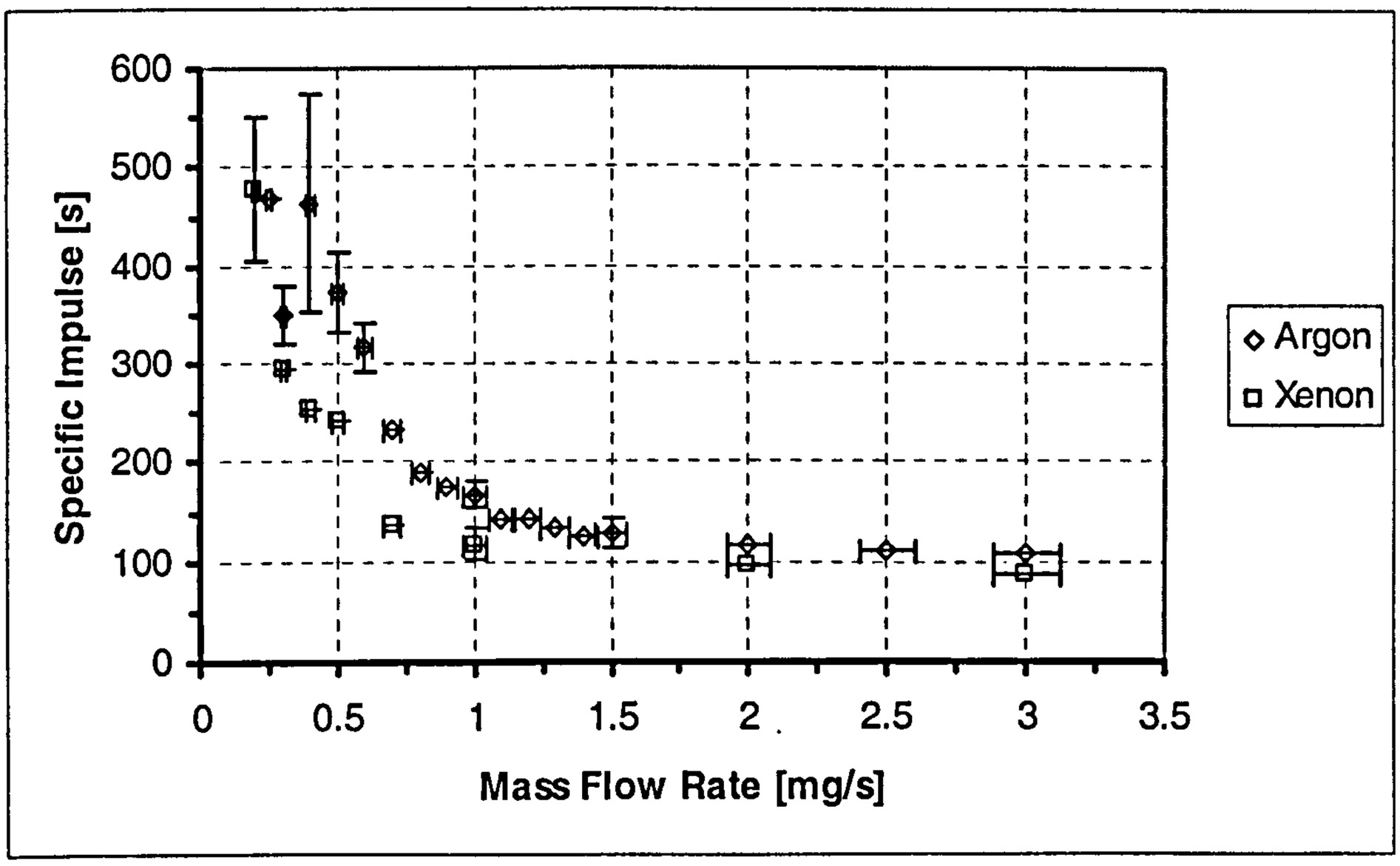

Figure 5.21 – Operation with different propellants for 1.0 mm HC orifice diameter.

Measurements for argon and xenon propellant and both values of HC orifice diameter are plotted in Fig. 5.22. It is evident that, while for both propellants the difference in performance between the two orifices is about 50% at high mass flow rates, for the larger orifice the difference in I_{sp} between argon and xenon is much less pronounced.

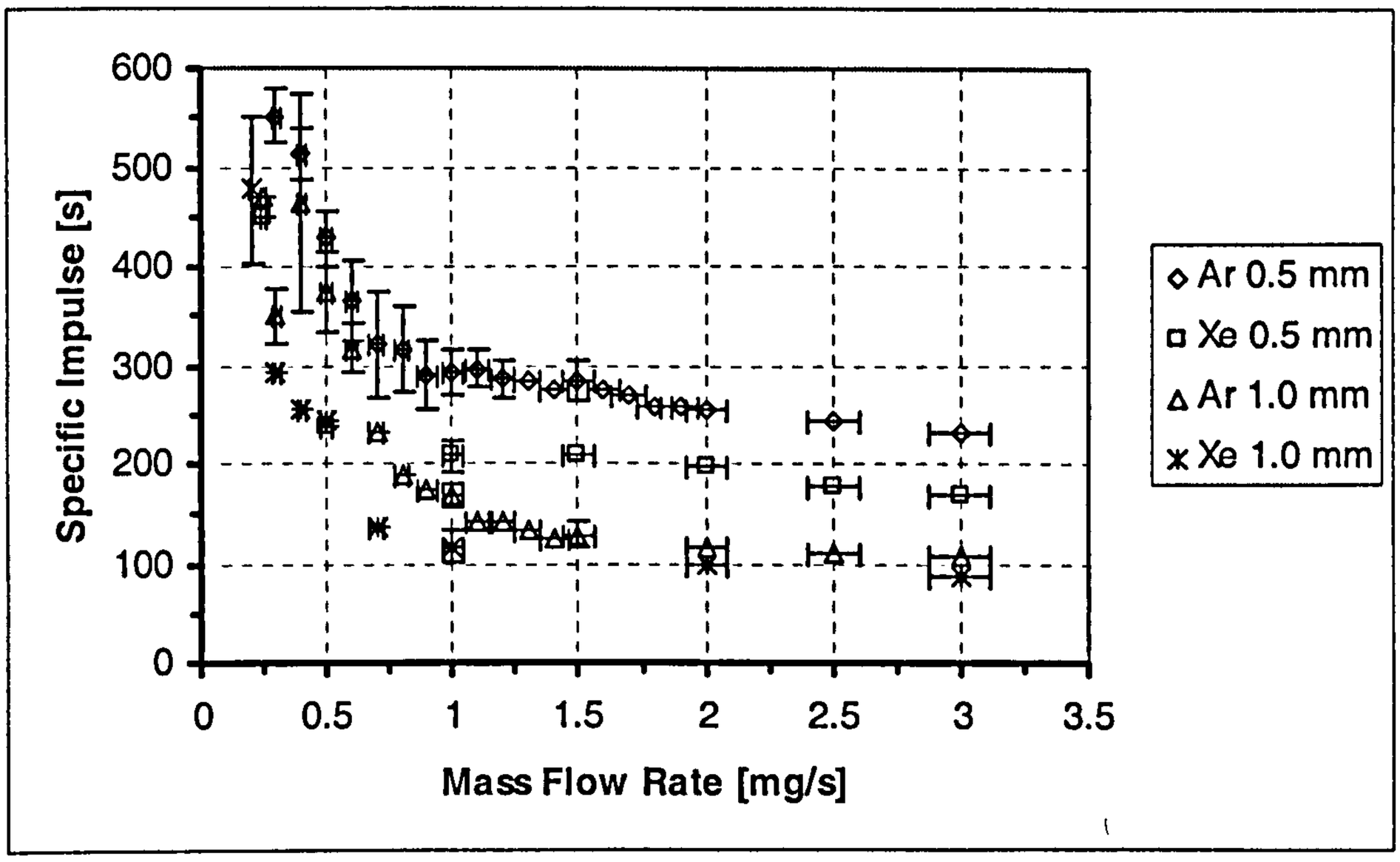

Figure 5.22 – Operation with Ar and Xe for different HC orifice diameters.

In order to investigate the influence of anode geometry on the production of thrust, measurements were taken with the 1.0 mm diameter HC operating with argon and an anode with a 40 mm diameter orifice, otherwise identical to the 20 mm orifice one. A version of the 40 mm anode with the face towards the HC insulated with a layer of MACOR® (machinable mass ceramic) was also tested, in order to evaluate the influence of discharge attachment patterns. Operation with this latter geometry proved particularly troublesome, with difficulties starting the discharge and very unstable conditions, including large oscillations and high discharge voltages (~40-50 V), at mass flow rates below 1 mg/s, where it was not easy to obtain data. Figs. 5.23 and 5.24 show the thrust measurements obtained with the standard and the insulated 40 mm orifice anode, respectively. The same trends as in the 20 mm anode can be observed in Fig. 5.23. Namely, thrust increases with increasing current at constant mass flow rate and, for constant current, we see a linear increase of thrust with mass flow rate for values greater than 1 mg/s. For lower values, the thrust is essentially constant, within the error bars, actually showing a slight increase with decreasing mass flow rate. These same trends can be clearly observed in Fig. 5.24, even if the low mass flow rate region is unfortunately represented only by one data point.

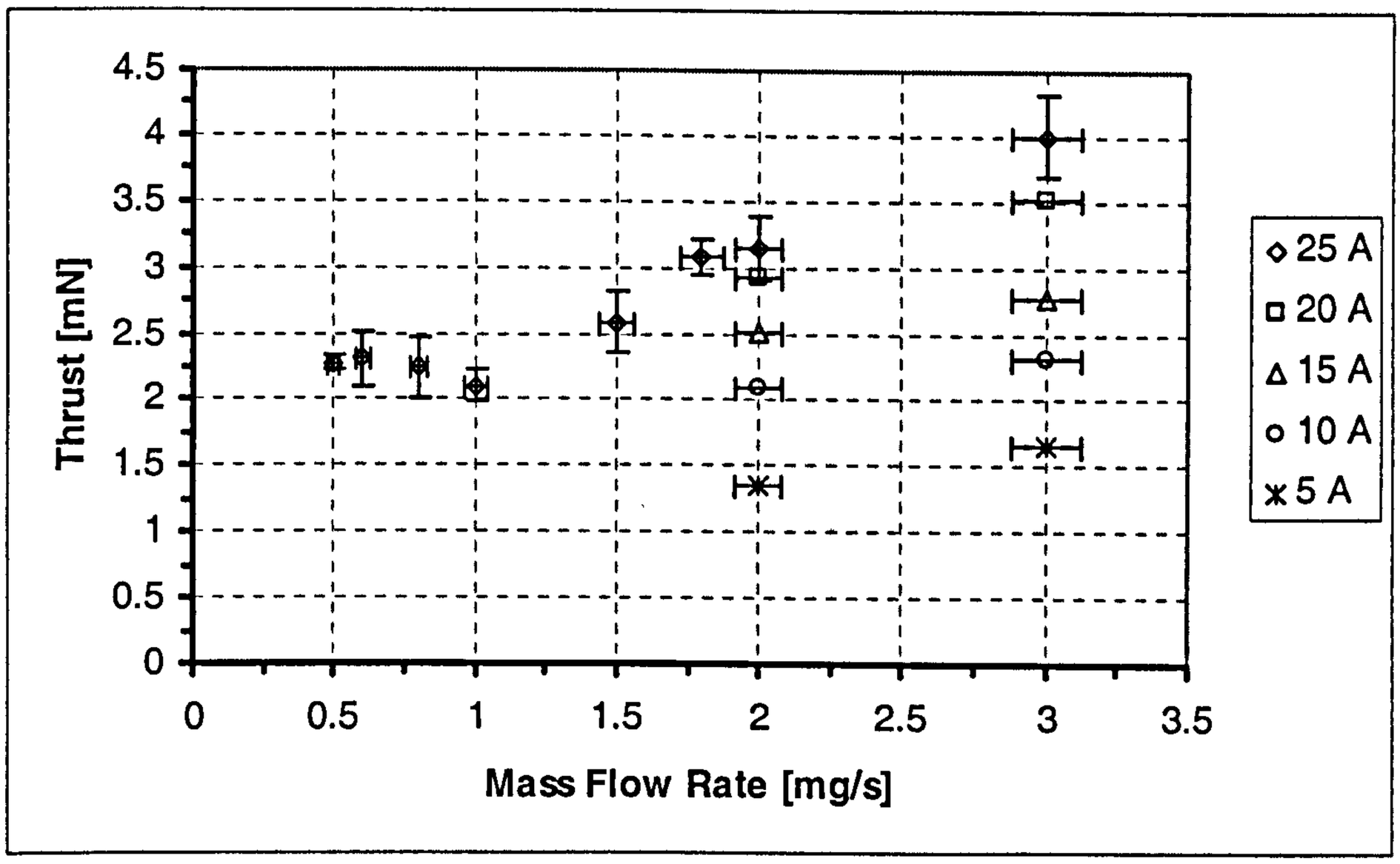

Figure 5.23 – Thrust vs. mass flow rate for argon, 1.0 mm HC orifice, 40 mm anode orifice diameter.

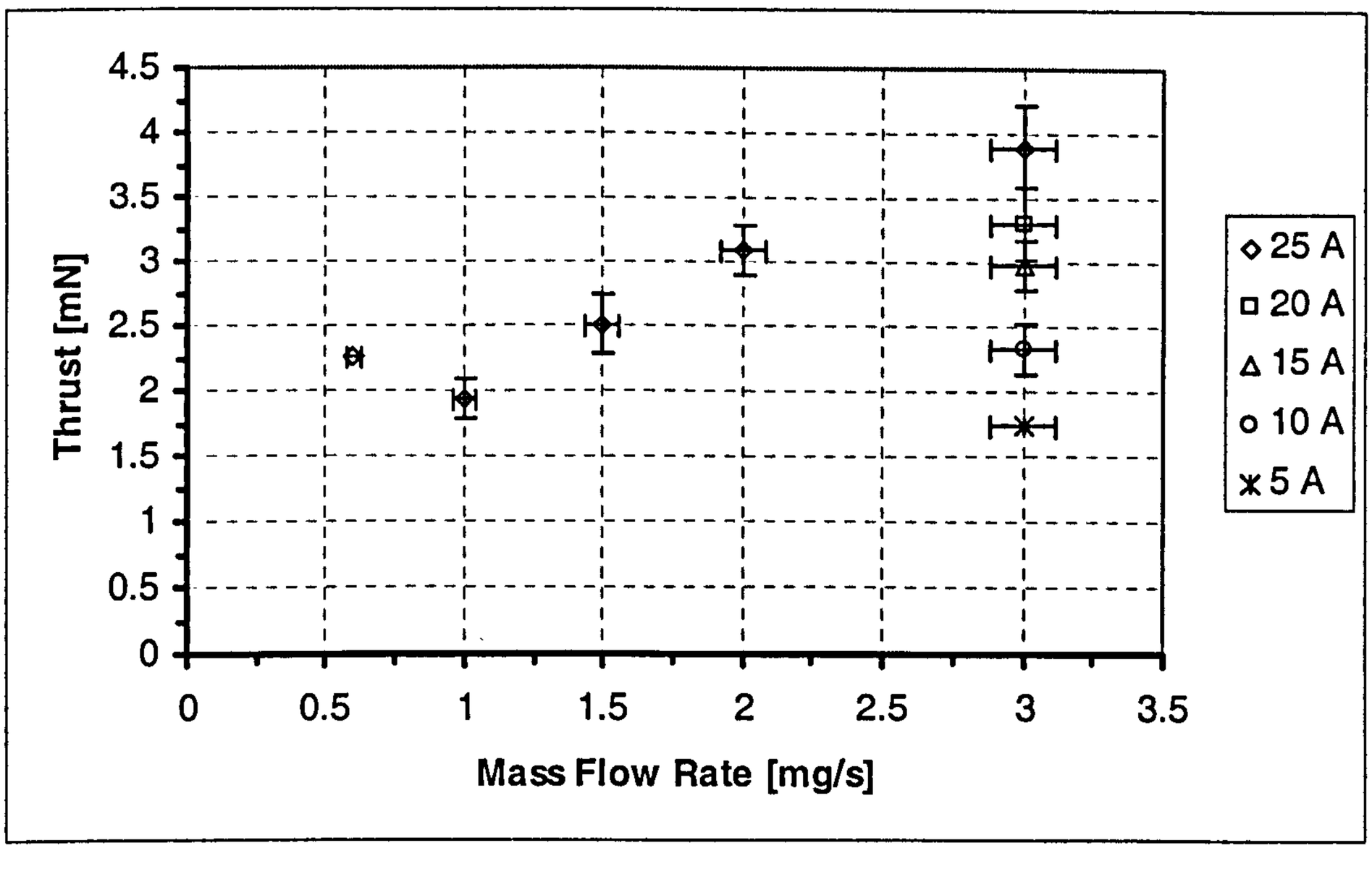

Figure 5.24 – Thrust vs. mass flow rate for argon, 1.0 mm HC orifice, 40 mm orifice diameter insulated anode.

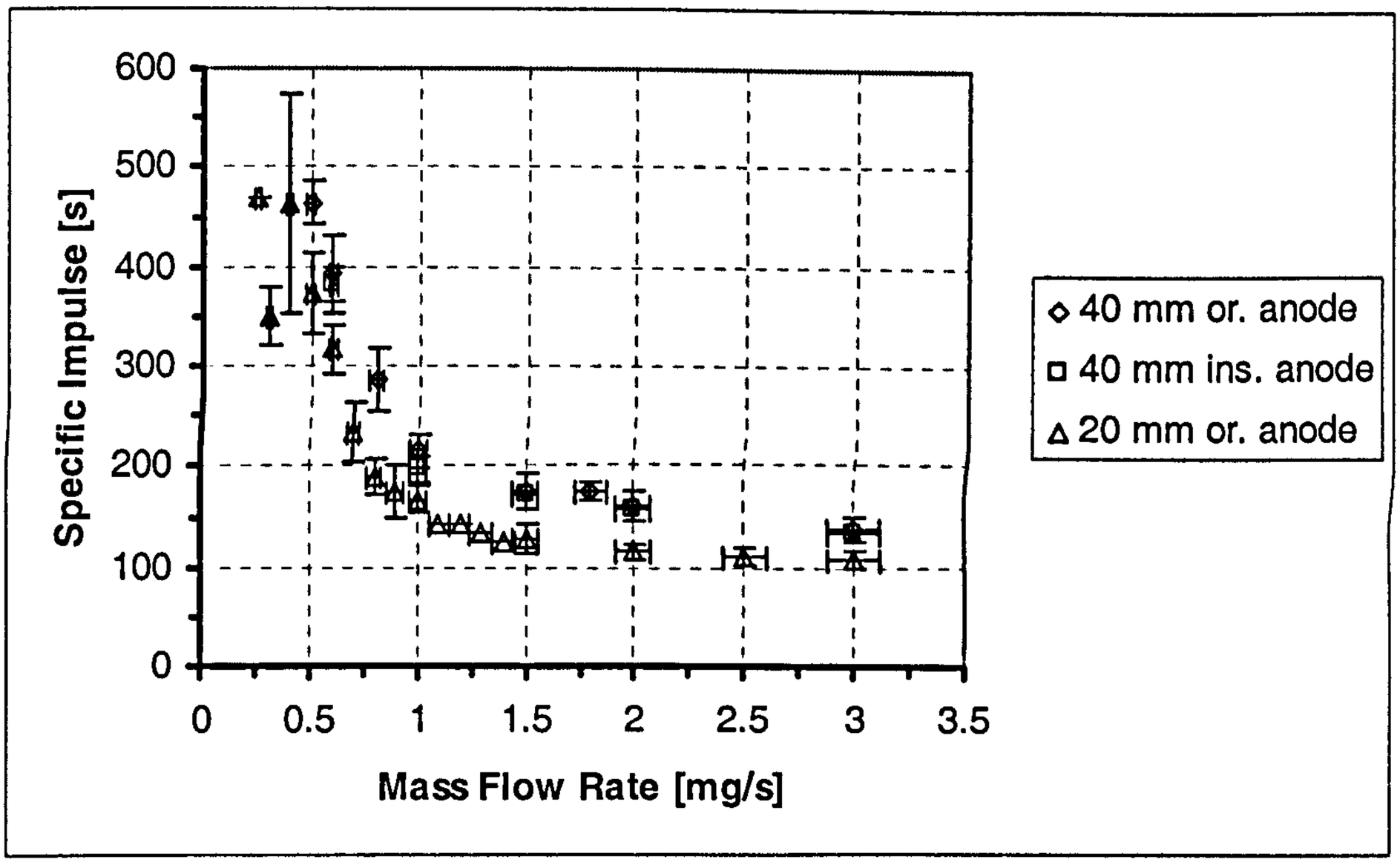

Figure 5.25 – Argon operation with three different anodes, 1.0 mm HC orifice.

Also with the 40 mm orifice diameter anode, the specific impulse shows a large increase with decreasing mass flow rate, corresponding to increasing discharge power to mass flow rate ratio, as discussed in Section 5.1. A comparison of the I_{sp} values obtained at maximum discharge current with the 20 mm, 40 mm and insulated 40 mm orifice anodes is especially interesting (see Fig 5.25). The specific impulse obtained with the 40 mm orifice anode is substantially (~30-40%) higher than the one obtained with the 20 mm orifice anode. Insulating the anode face towards the anode produced no appreciable changes: the I_{sp} values for both cases are within each other's error bars.

Fig 5.26 shows the variation of thrust with current at constant mass flow rate, with argon as a propellant, for the insulated and the non-insulated 40 mm orifice diameter anode. It is clear that insulating the face of the anode toward the HC has negligible influence on thrust generation, at least as far as the dependence on current is concerned. The same data are plotted in Fig 5.27 with no distinction between the insulated and the non-insulated anode for the 3 mg/s case. In Figs. 5.26 and 5.27 curve-fitting shows that the thrust dependence on current is actually, to a very good approximation, linear. This is in agreement with what already shown for the 20 mm orifice diameter anode (see Fig. 5.12), confirming the general validity of this result.

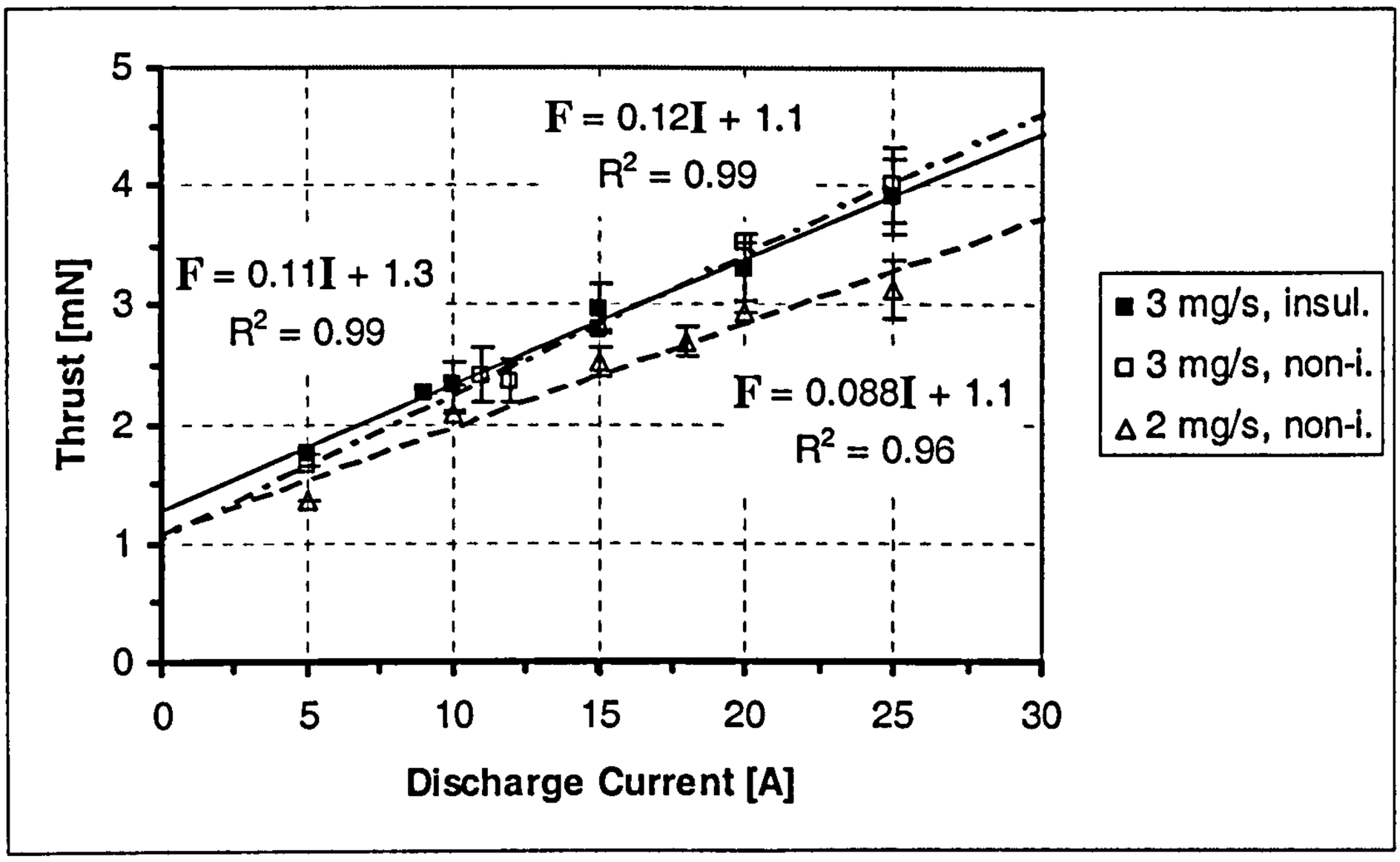

Figure 5.26 – Thrust vs. current with 40 mm orifice diameter anode, argon propellant.

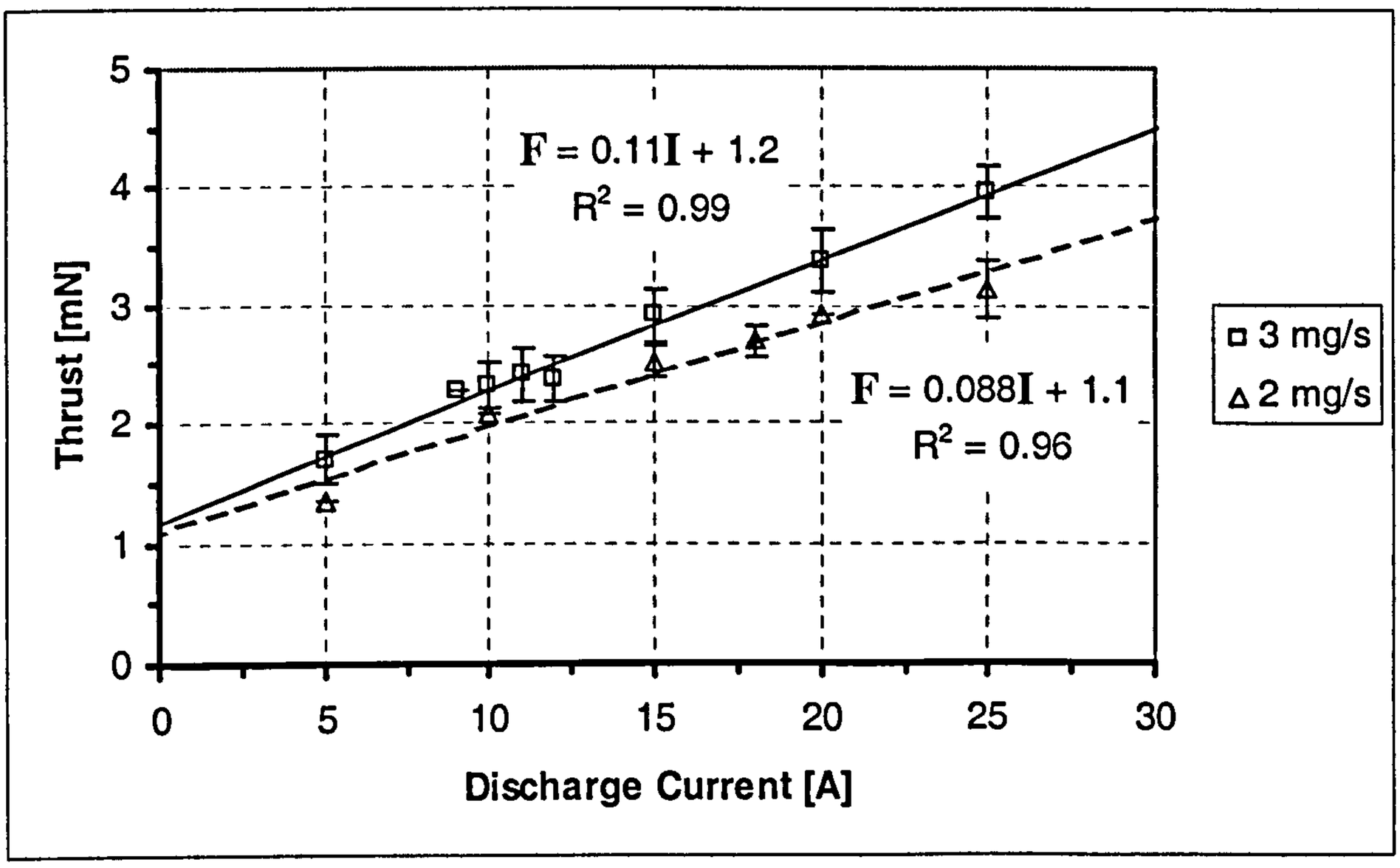

Figure 5.27 – Same as in Fig. 5.26: no distinction bet. insulation and no insulation.

5.1 – Discussion

The experiments performed allow us to formulate some hypotheses about the acceleration mechanisms involved in thrust generation. It is useful to plot some of our

data in different ways, in order to throw light on the influence of various parameters, like for instance discharge power.

It is particularly instructive to consider the 40 mm orifice anode, as the main effect of insulating the face of the anode towards the HC was to increase, in general, the discharge voltage, widening the range of conditions for which the cathode operated in plume mode. This means that similar values of thrust were obtained at higher power levels, for the same currents and mass flow rates, thus decreasing the efficiency of our device, as shown in Figs. 5.28-5.31.

Figs. 5.28 shows that, in spot mode, a linear dependence of thrust on discharge current, for a given mass flow rate, implies a linear dependence on power as well, the discharge voltage being nearly constant. In plume mode, instead, the thrust first shows a general increase, and then seems to become nearly constant with increasing discharge power W, although with a large data scatter, for W greater than ~500 W, as shown in Fig. 5.29. A similar behaviour, but with a smaller data scatter, is shown if the thrust is plotted against specific power W_s (discharge power per unit mass flow rate), with thrust becoming nearly constant for W_s greater than ~1000 J/mg, as shown in Fig. 5.30.

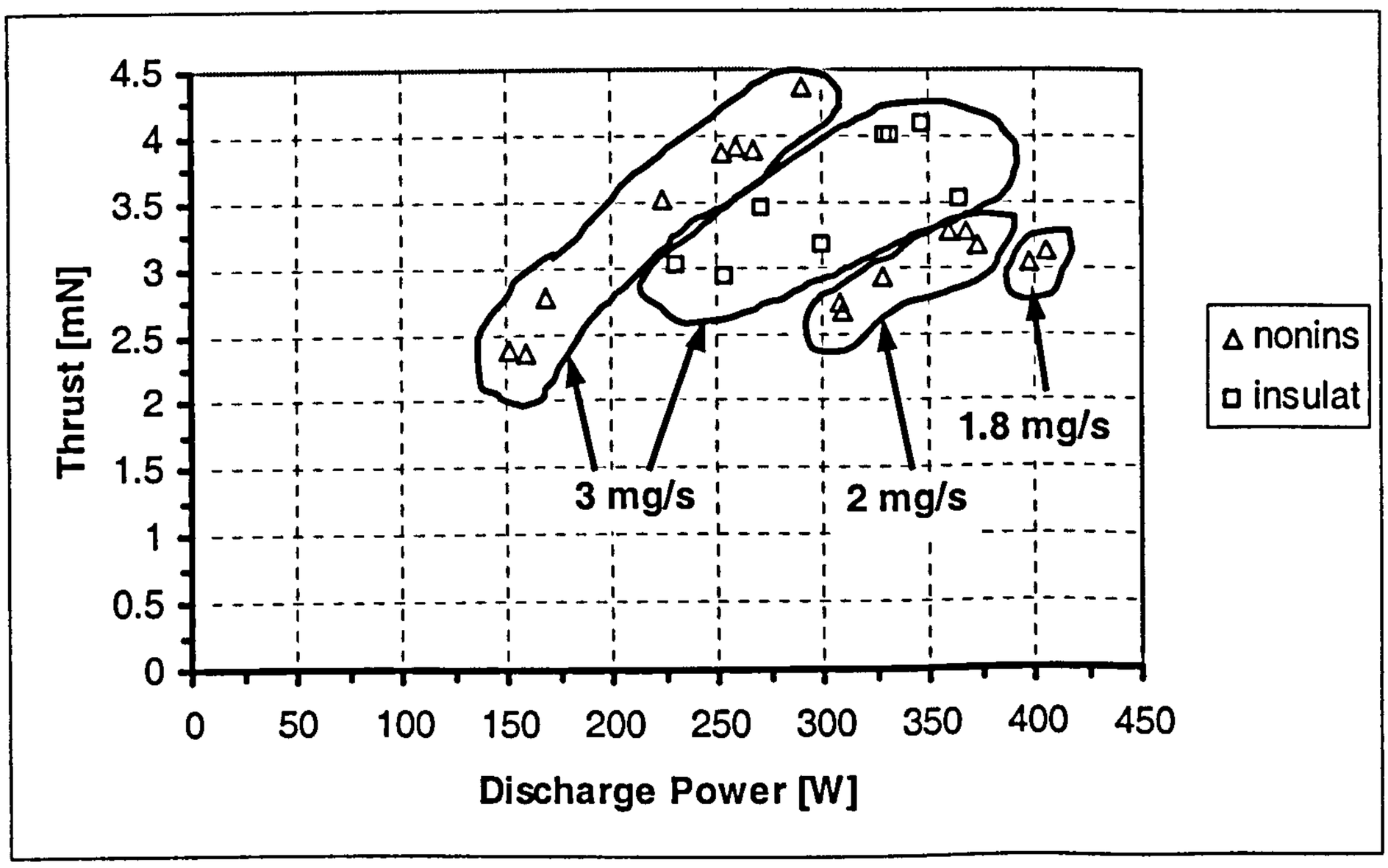

Figure 5.28 – Thrust vs. discharge power, 40 mm orifice anode, spot mode.

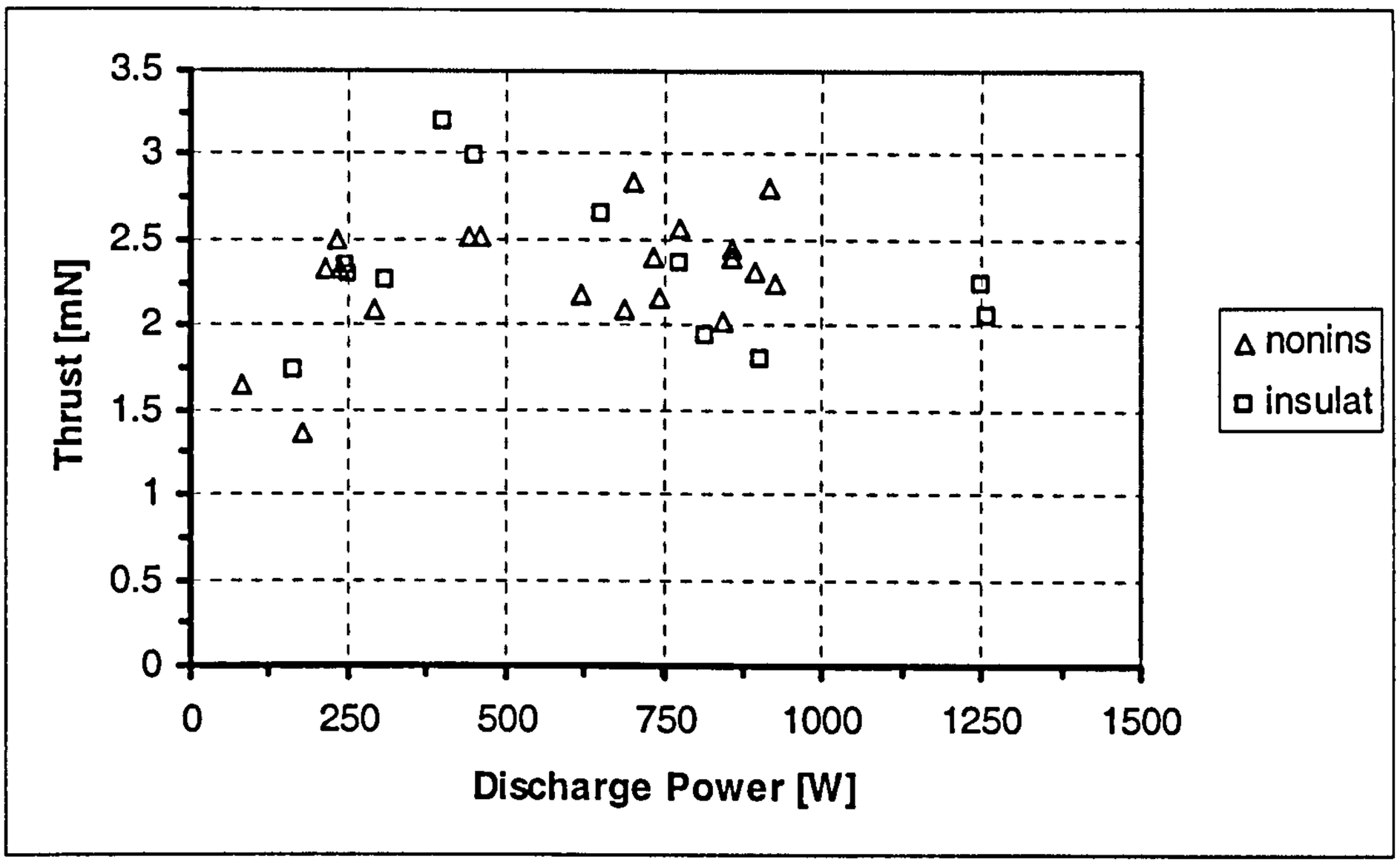

Figure 5.29 – Thrust vs. discharge power, 40 mm orifice anode, plume mode, argon.

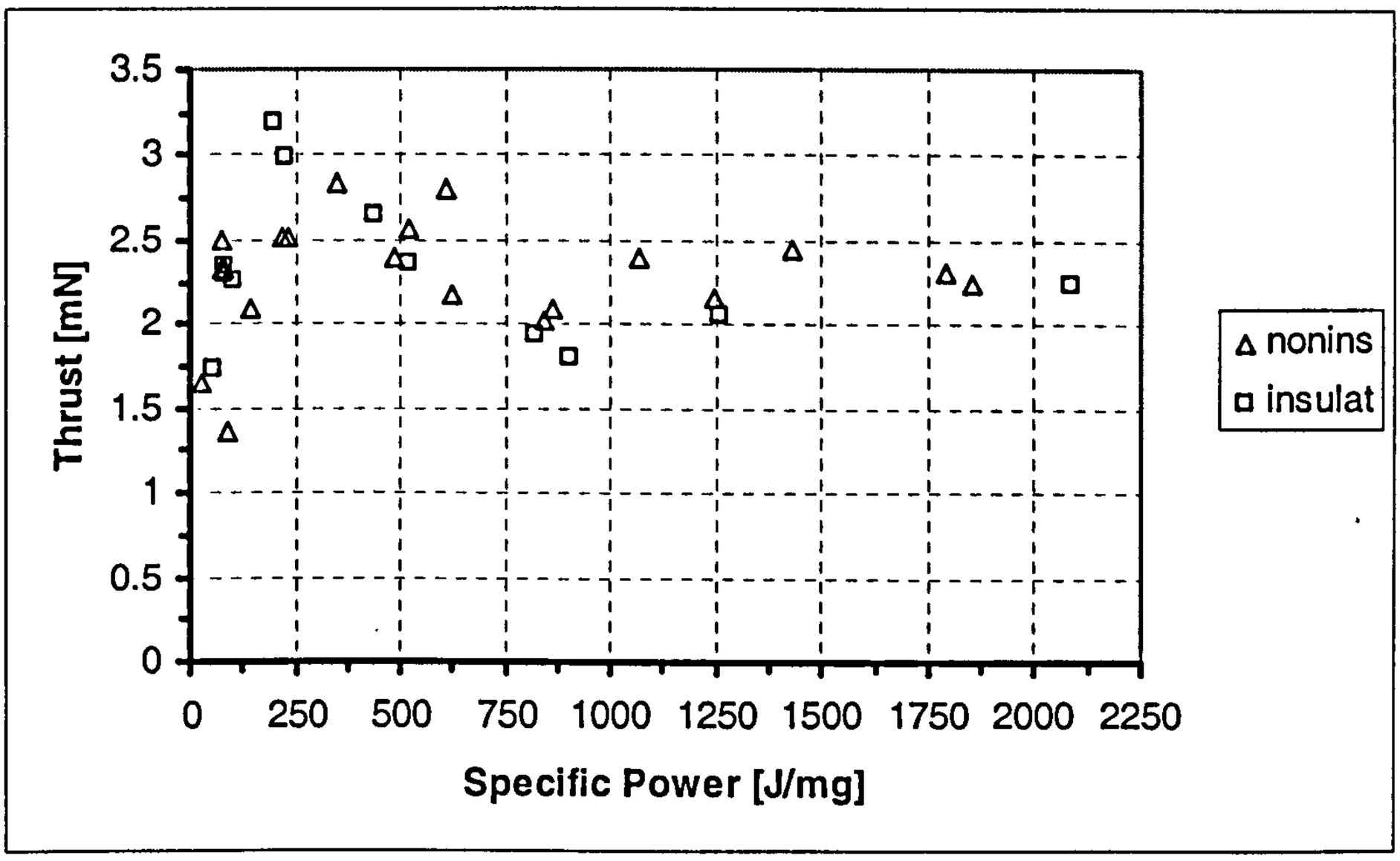

Figure 5.30 – Thrust vs. specific power, 40 mm orifice anode, plume mode, argon.

In Figs. 5.31-5.34 the measurements are plotted as specific impulse (thrust per unit mass flow rate in weight) versus discharge power W, for spot-mode operating points (Figs. 5.31-5.32) and for both modes together for the non-insulated anode (Fig. 5.33), and versus specific power W_s, for plume-mode operating points (Fig. 5.34). A linear

dependence of the thrust on current, at constant mass flow rate, translates, for spot mode operation, where the discharge voltage is nearly constant, in a linear dependence of thrust on power. Hence the linear dependence of specific impulse (thrust over mass flow rate in weight) on discharge power, a result already published by the author [55-57]. Also reported in the same papers [55-57] is the high data scatter observed in plume mode. Here the results correlate much better when plotted versus W_s instead of W, as shown by the linear trend in Fig. 5.34 (I_{sp} versus W_s) compared to the trend in Fig. 5.33 (I_{sp} versus W), where the linear correlation of all data points for the non-insulated anode is much worse. It is interesting to note, in Figs. 5.32 and 5.33, that the trend gives, for W=0, a value of I_{sp} coincident, within the error bars, with that measured for with the heater on and no discharge. This is good confirmation of the accuracy of our method for determining the thrust, described in detail in Chapter 4, which sums the discharge contribution, measured at switch-off, with the baseline thrust from the heated cathode flow.

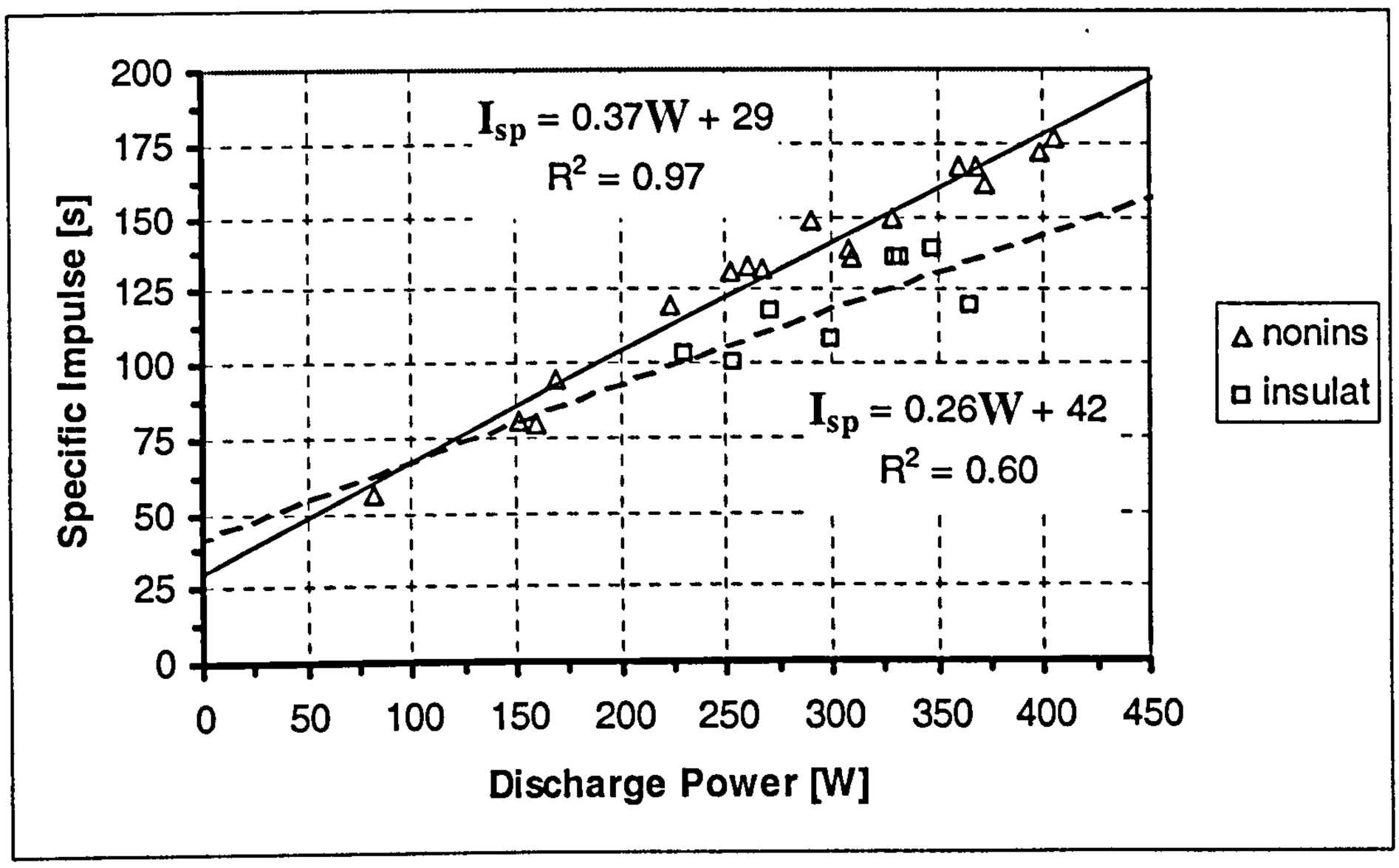

Figure 5.31 – Specific impulse vs. discharge power, 40 mm orifice anode, spot mode, argon propellant.

Apart from under-performing with respect to its non-insulated counterpart, the insulated anode caused the discharge to be extremely noise and unstable, with high,

oscillating voltages. This is reflected in the much higher data scatter visible in Figs. 5.28 and 5.31, where the linear correlation is much worse for the insulated anode data.

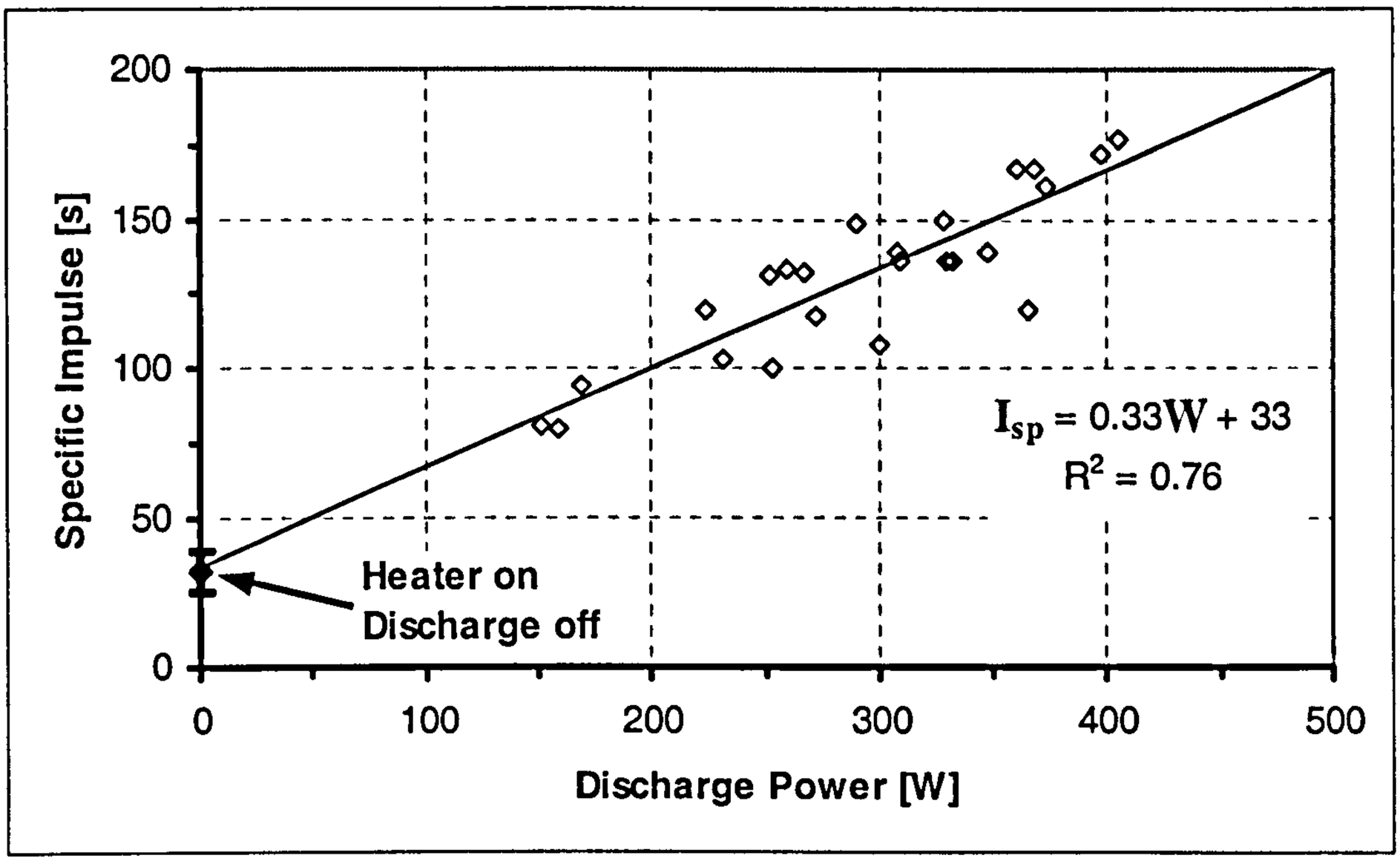

Figure 5.32 – Same as Fig. 5.31, both anode data together with heater measurements.

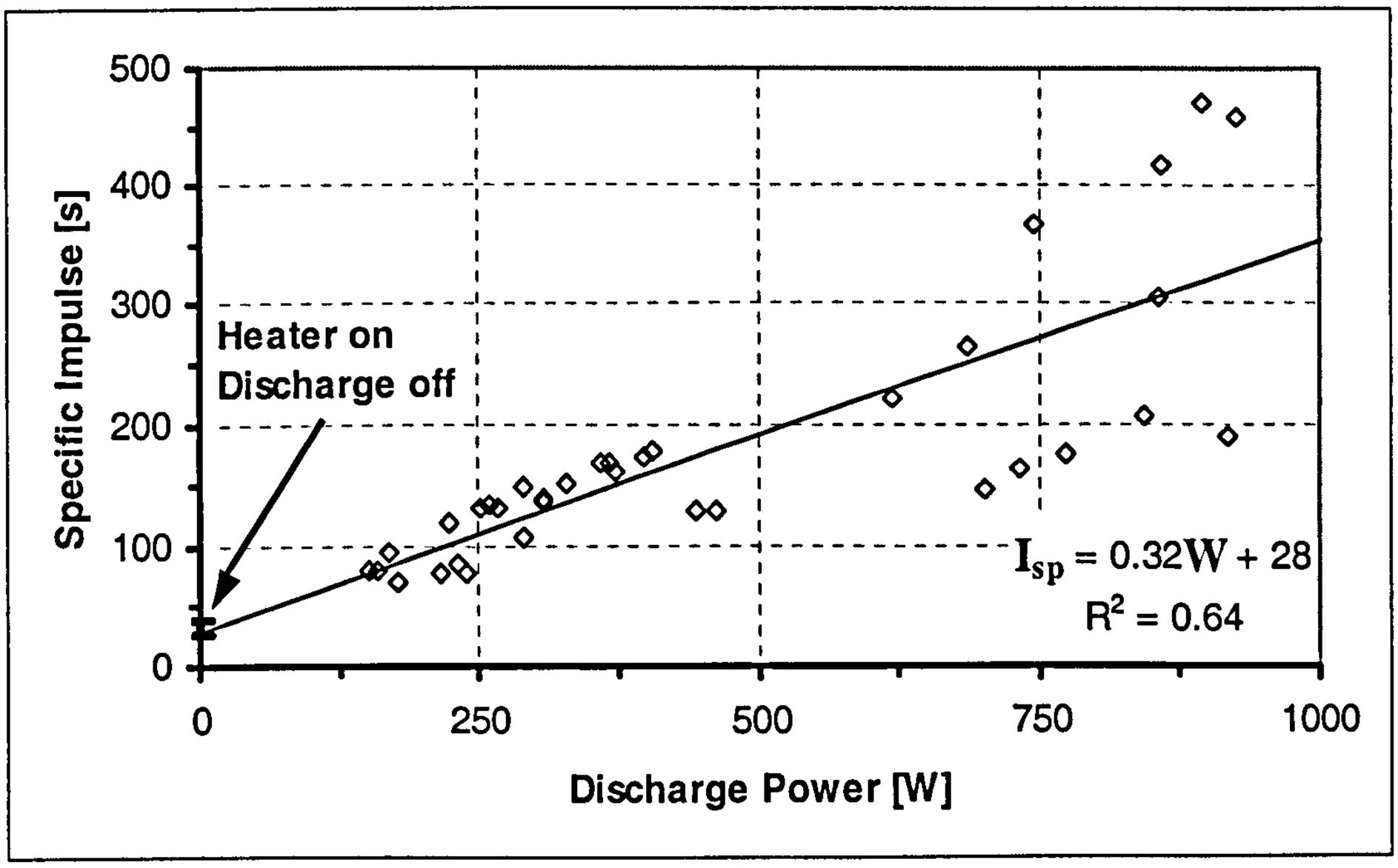

Figure 5.33 – Specific impulse vs. discharge power, 40 mm diameter non-insulated anode, argon propellant, together with heater measurements.

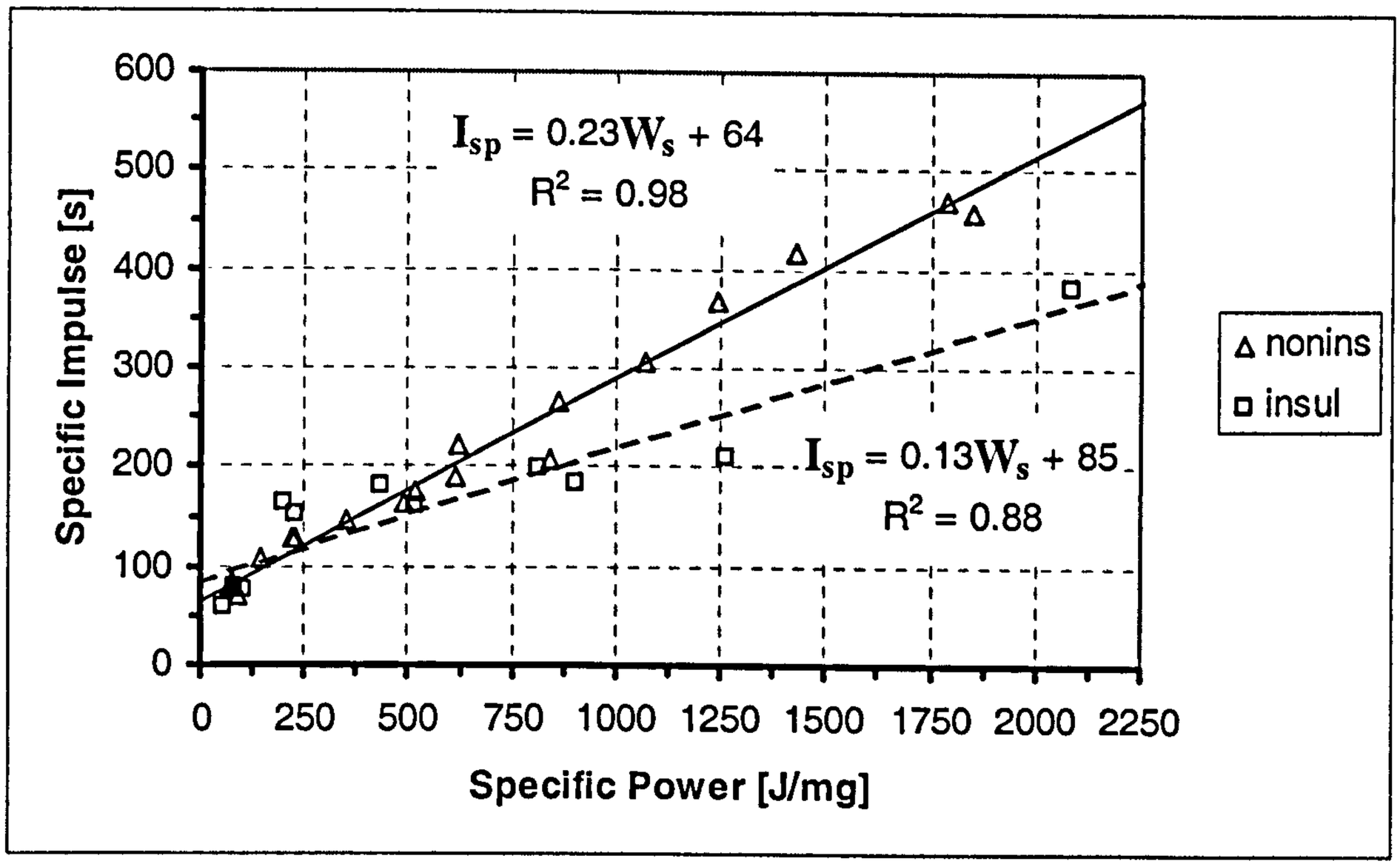

Figure 5.34 – Specific impulse vs. specific power, 40 mm orifice anode, plume mode, argon propellant.

The linear dependence of thrust on discharge power, in spot mode, implies that the thrust-to-power ratio remains sensibly constant with varying power, for a given value of mass flow rate, as shown in Fig. 5.35. The same behaviour is evident in Fig. 5.36, where the measurements are plotted against specific power. It is to be noted that the data points for the insulated anode actually show a slightly decreasing trend, while *F/W* is more rigorously constant for the non-insulated anode.

In plume mode, the thrust-to-power ratio is, to a good approximation, inversely proportional to discharge power, as shown in Fig. 5.37. The same data, when plotted against specific power, show an approximate inverse-square-root proportionality (see Fig. 5.38).

The behaviour suggested by Fig. 5.37, thrust becoming constant with increasing power, seems to agree with what shown in Fig. 5.29, but we conclude that this type of scaling is not correct, let alone useful. The plots that actually illuminate the correct behaviour of our device are Figs. 5.28 and Figs. 5.31-5.35. They clearly show that the thust is proportional to discharge power, at constant mass flow rate and, moreover, that the specific impulse, which is thrust per unit mass flow reate in weight, is

proportional to discharge power. This relation holds both in spot and in plume mode, even if in the latter a large data scatter is observed. It seems to be a more fundamental relation than the proportionality of thrust to discharge current, allowing us to correlate measurements at very low mass flow rates and very high discharge voltages.

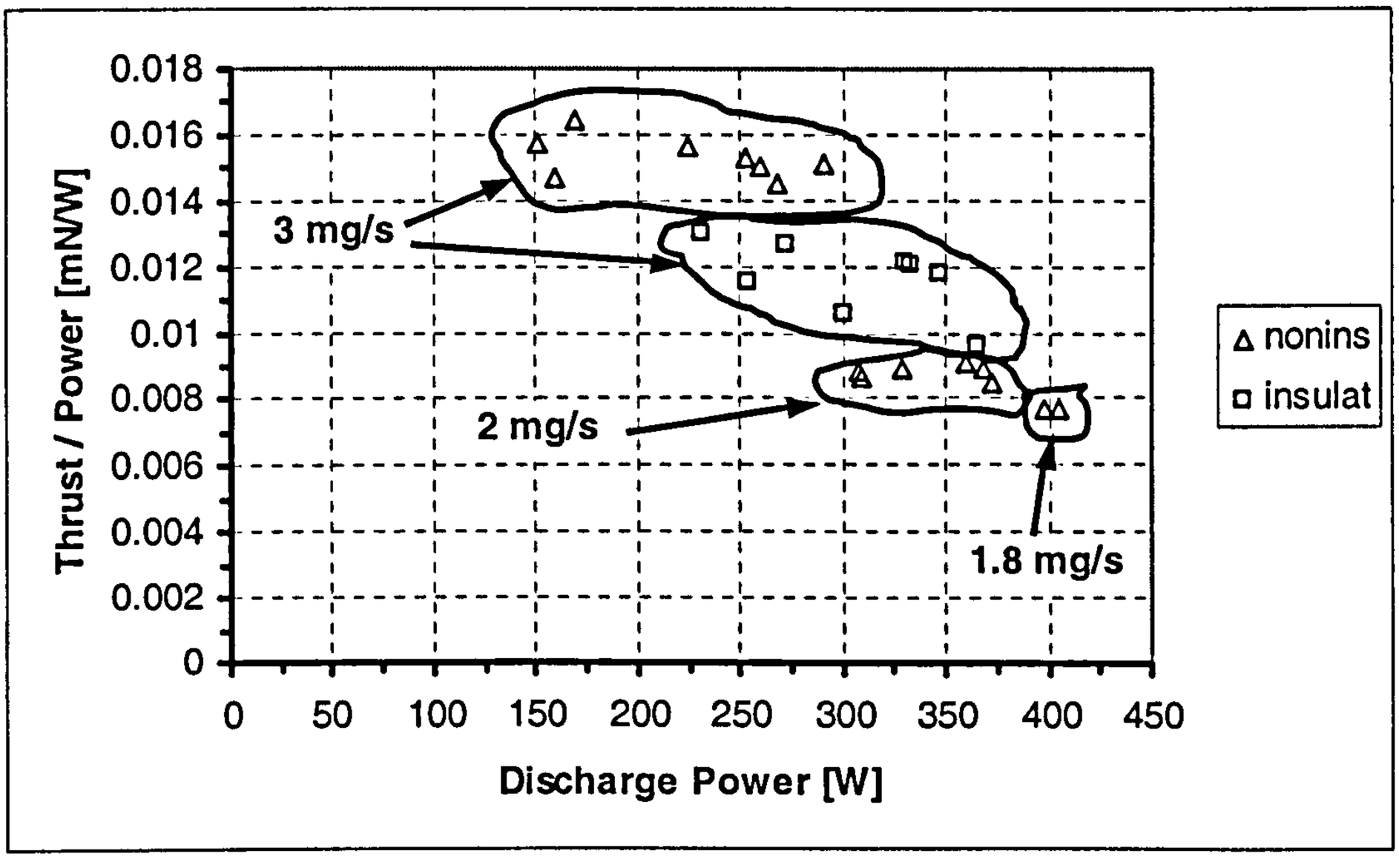

Figure 5.35 – Thrust-to-power ratio vs. power, 40 mm anode, spot mode, argon.

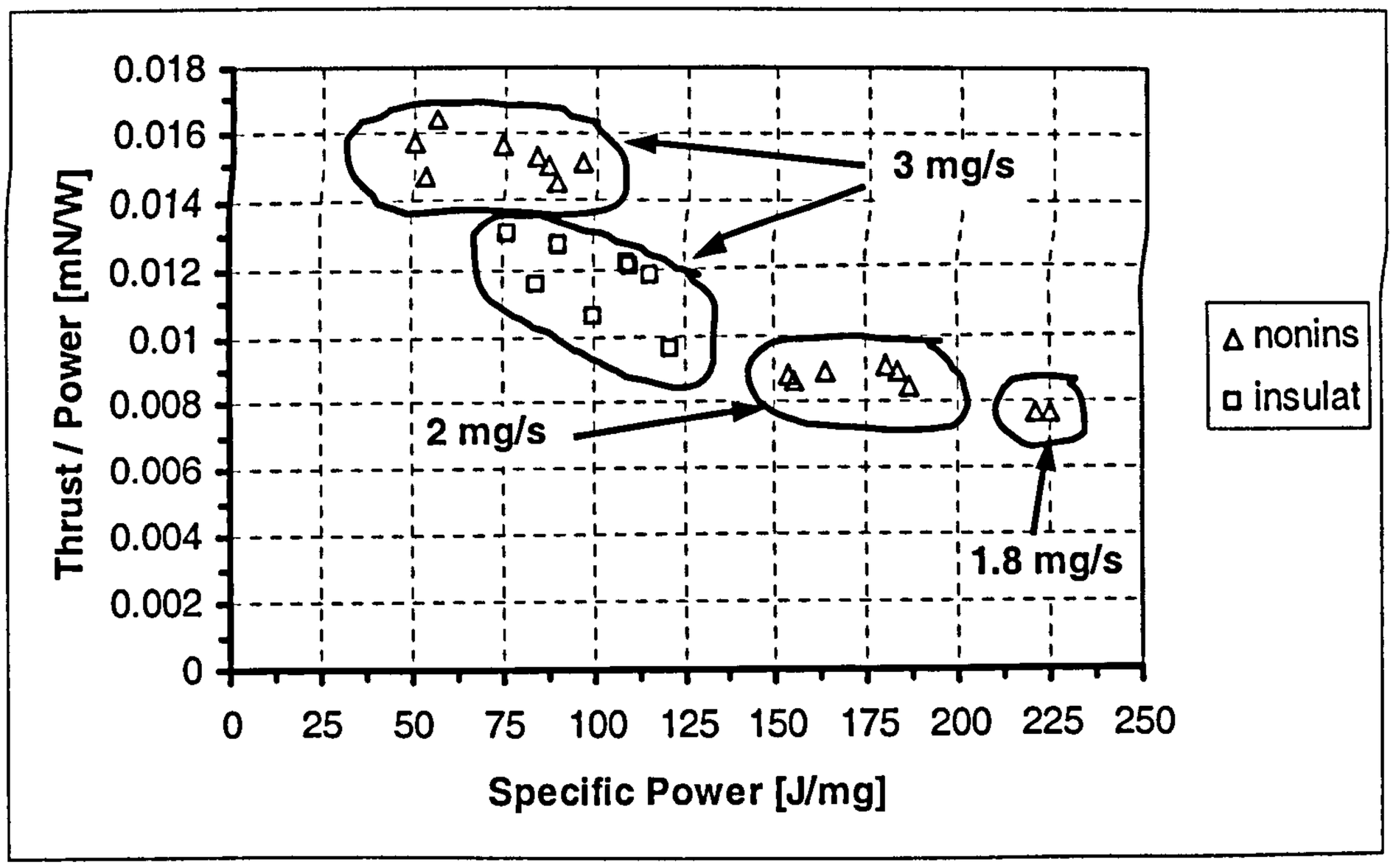

Figure 5.36 – Thrust-to-power ratio vs. spec. power, 40 mm anode, spot mode, argon.

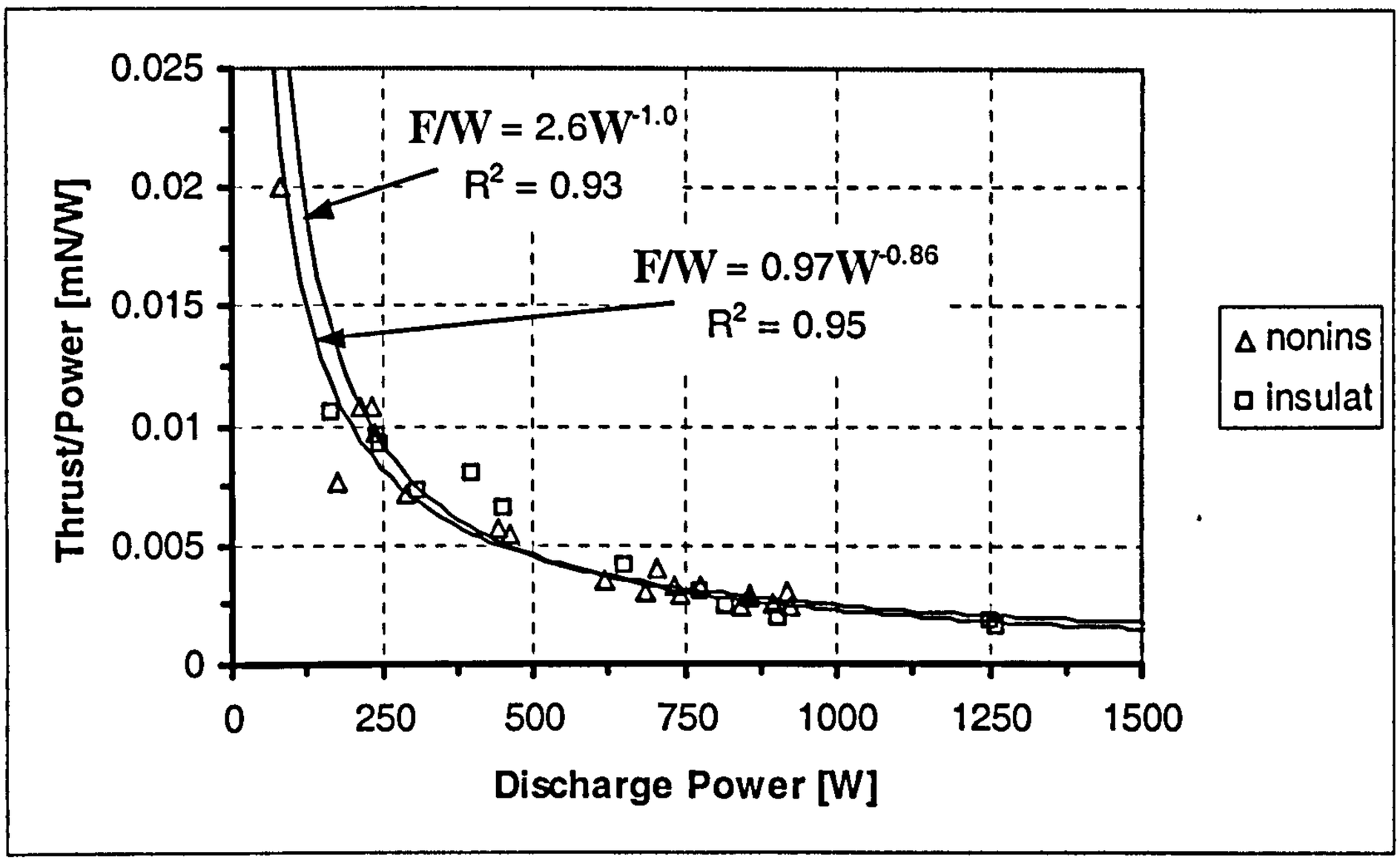

Figure 5.37 – Thrust-to-power ratio vs. discharge power, 40 mm anode, plume mode.

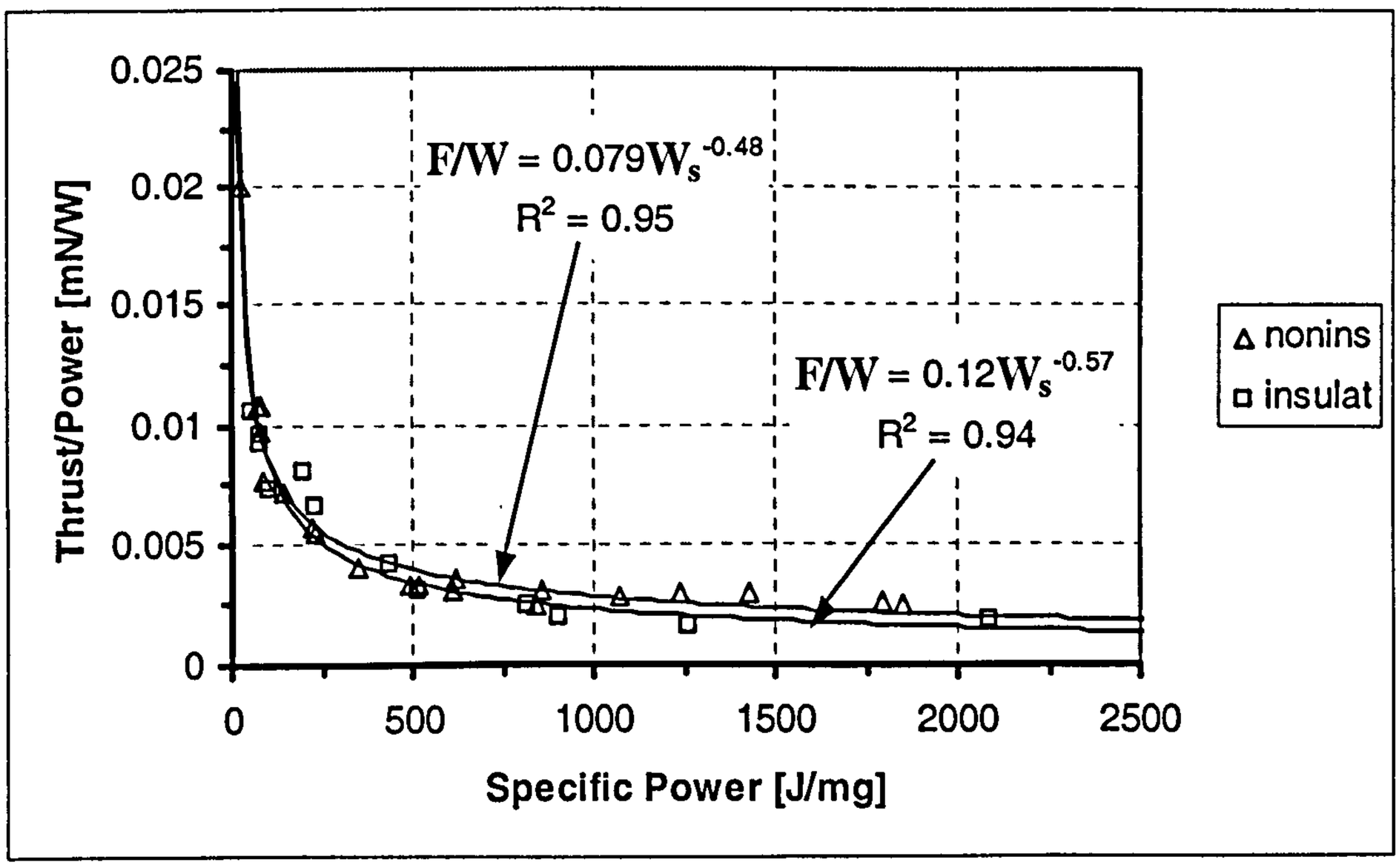

Figure 5.38 – Thrust-to-power ratio vs. specific power, 40 mm anode, plume mode.

A parameter that has been considered important in the scaling of HCs and that was also used in this thesis to compare results from different devices is the ratio of discharge current to mass flow rate in Ampere equivalent, which can be interpreted as

the ratio of electron current to positive ion current, assuming the propellant to be fully and singly ionised. Fig. 5.39 shows a plot of the specific impulse against this non-dimensional parameter *I/Aeq*. The data points seem to correlate pretty well, with I_{sp} increasing with increasing *I/Aeq*. For values of *I/Aeq* greater than ~10 the specific impulse shows a linear increase, with a slope value slightly higher than the one showed for *I/Aeq* smaller than ~5. For 5<*I/Aeq*<10 a transition zone seems to exist.

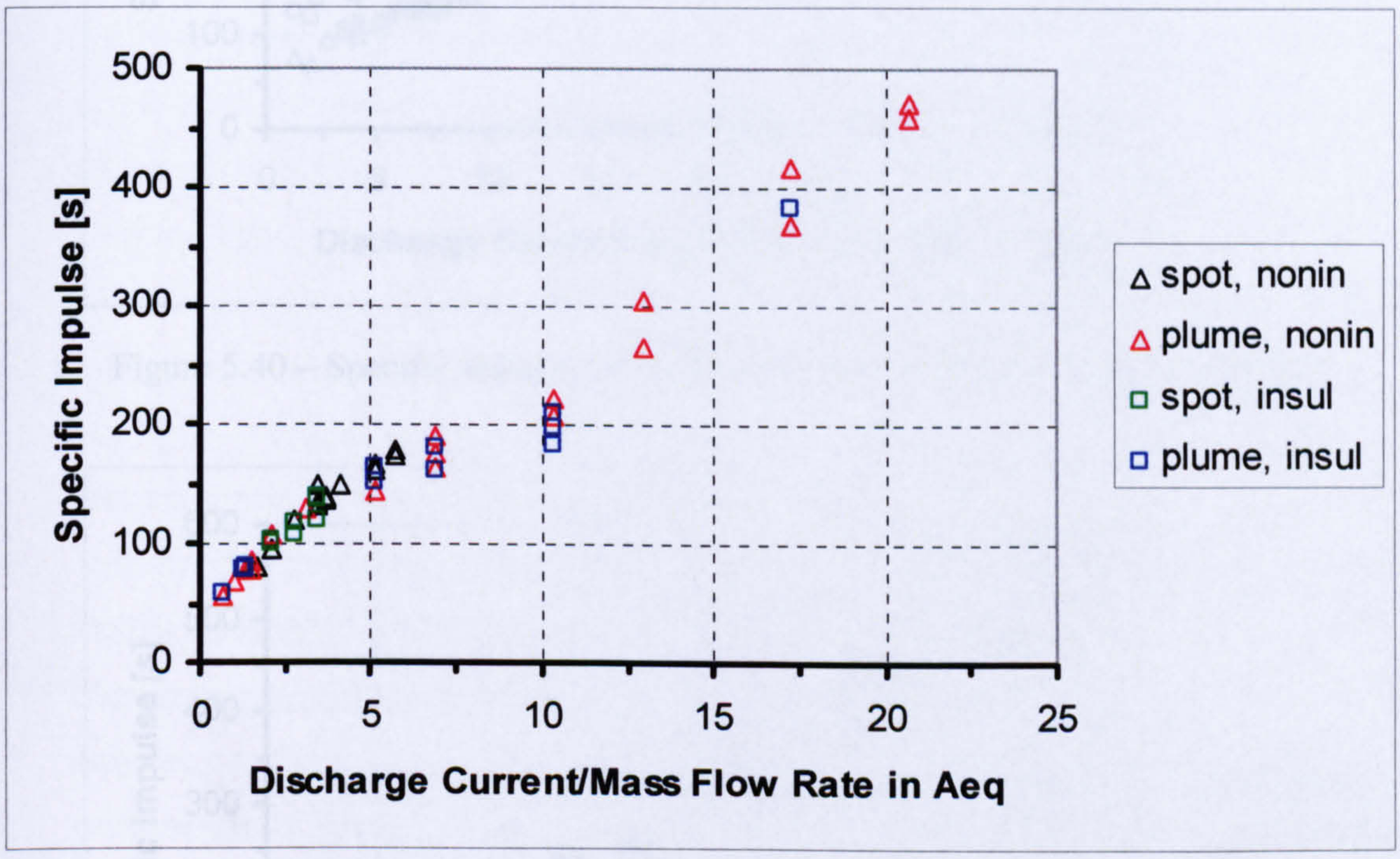

Figure 5.39 – Specific impulse vs. *I/Aeq*, 40 mm orifice anode, argon propellant.

As no measurement was taken at exactly the same power, all data points are plotted in Figs. 5.28-5.39, without any averaging. The y-error bars are therefore replaced by the actual data scatter, while the x-error bars, given by the uncertainties in the electric parameters and mass flow rates, are not shown in the plots either in order to avoid crowding them excessively.

Figs. 5.40 and 5.41 are analogous to Fig. 5.39, showing data for the 20 mm orifice anode with argon and xenon as propellants, respectively, and for both values of the HC orifice diameter. I_{sp} is higher for argon and for the smaller HC orifice diameter, as already shown above. The same qualitative behaviour as in Fig. 5.39 is evident, with the I_{sp} dependence on *I/Aeq* becoming linear for *I/Aeq* greater than a certain value.

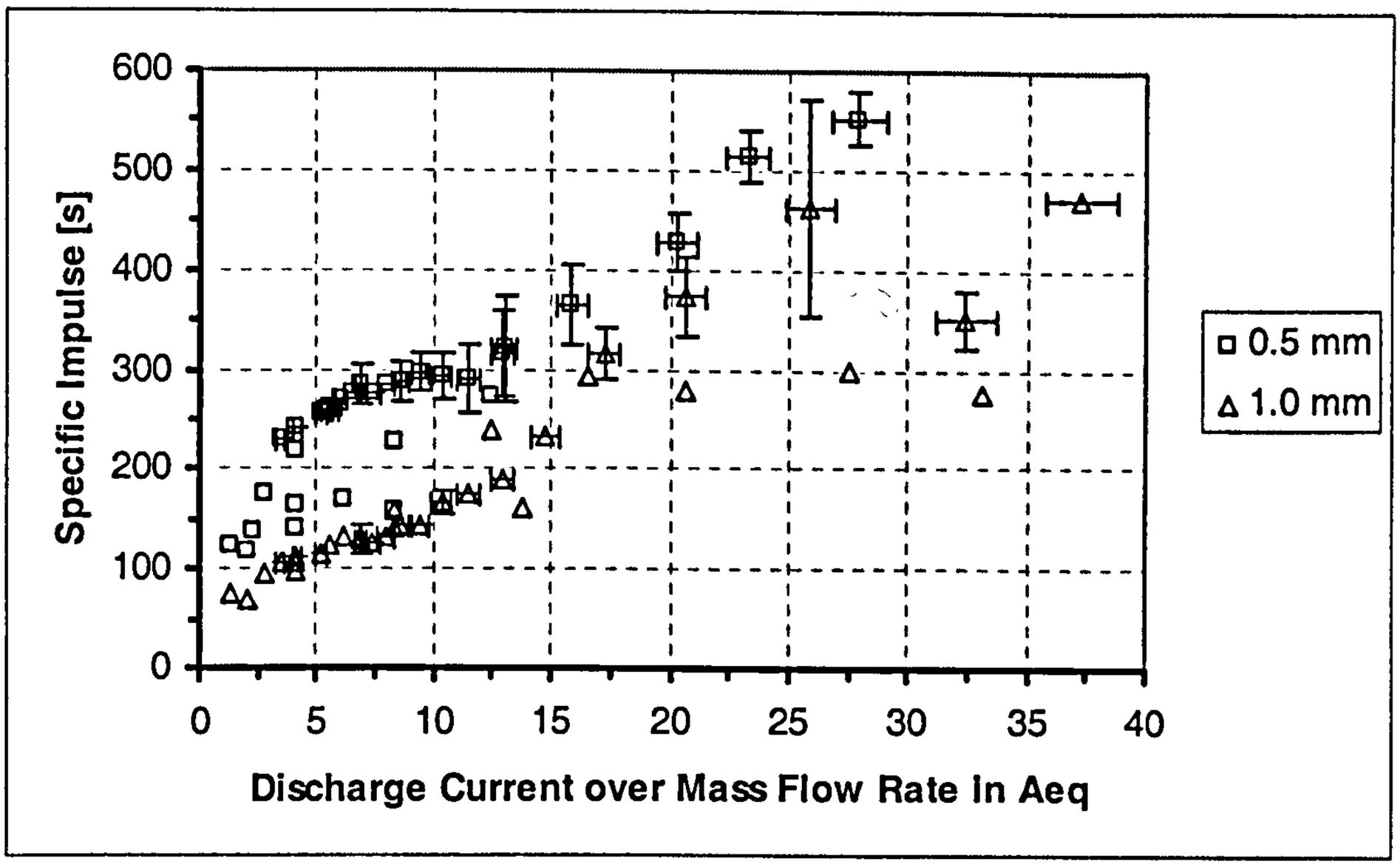

Figure 5.40 – Specific impulse vs. *I/Aeq*, 20 mm orifice anode, argon propellant.

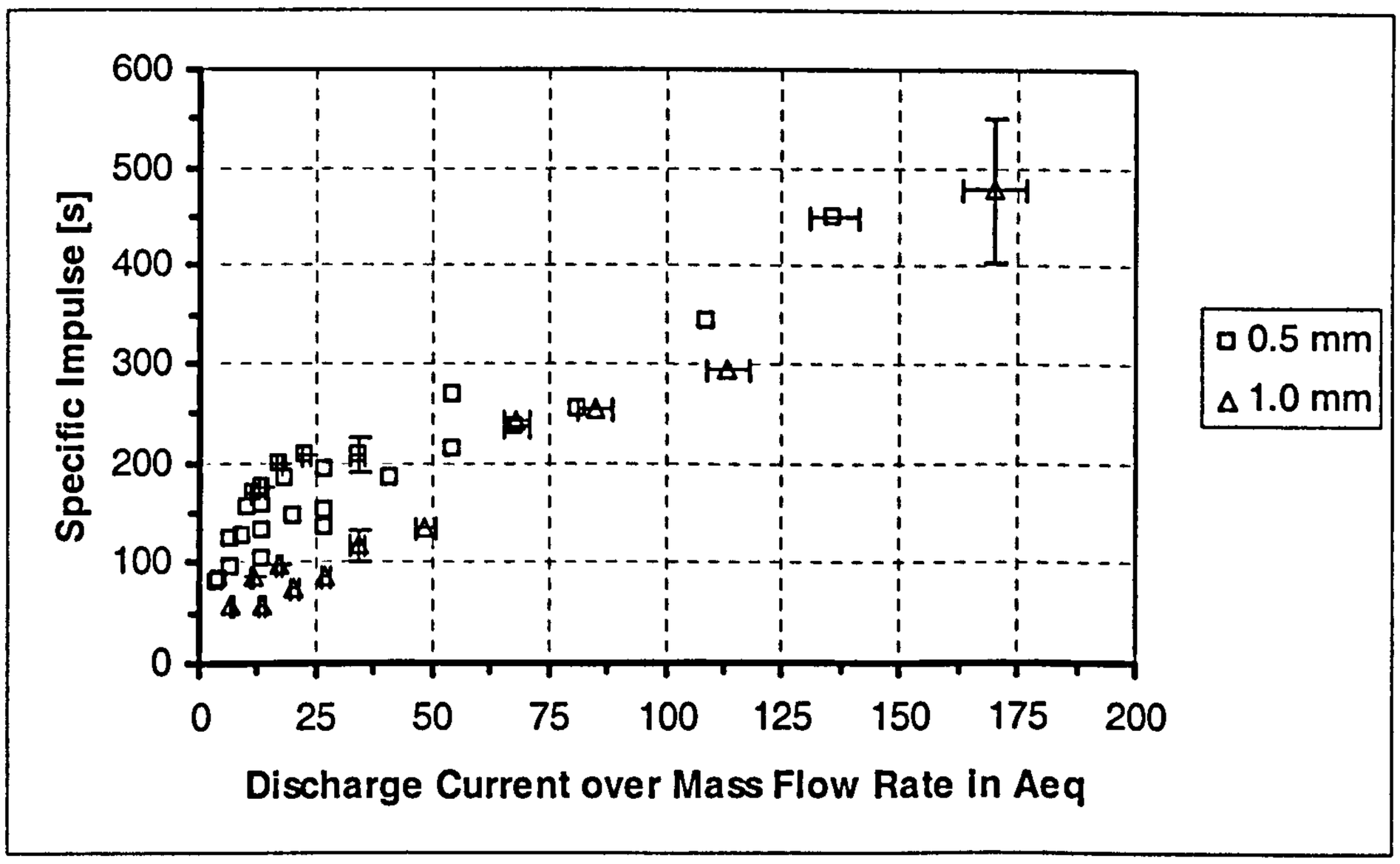

Figure 5.41 – Specific impulse vs. *I/Aeq*, 20 mm orifice anode, xenon propellant.

The data points in Figs. 5.40 and 5.41 are obtained by averaging measurements taken at the same current and mass flow rate, with error bars calculated according to the procedure described in Chapter 4.

The pressure in the vacuum chamber is always much lower than the pressure at the HC exhaust section. Even at very high operating mass flow rates chamber pressures do not rise above ~10^{-2} mbar, whereas the propellant lines are fed at ~1.5 bar from the pressure regulator. We can therefore assume that the flow at the exhaust section stays choked. If the velocity at the orifice exit is sonic, a decrease in thrust of ~ 50% for the same mass flow rate, regulated by background pressure and needle valve setting, would indicate that the flow temperature there has effectively decreased by 75%, according to the square-root dependence of I_{sp} on temperature described in Chapter 2. As the decrease in HC temperature with increasing orifice diameter is too modest to justify such a drastic drop in flow temperature, both when heating and when operating the HC, [16, 85], we can surmise that the interior flow conditions (pressure, density, velocity) change in such a way as to prevent the gas from reaching full equilibrium with the walls in the former case and to reduce the power deposition into the plasma in the latter, therefore reducing the flow temperature at the exhaust section.

It is interesting to note that HCs of different design have shown opposite behaviour. Namely, a slight decrease in operating temperature (~50 K) with a 25% decrease in orifice diameter [166]. As resistive dissipation in the orifice scales quadratically with current density, orifice heating increases dramatically with decreasing diameter. This may have a strong affect on the axial temperature gradient, between the insert and the orifice regions. While in the T6 HC, due to its one-piece construction, these two regions are very effectively coupled, in cathodes of different design the thermal coupling may not be that good. Thus, the orifice plate temperature may not always be a reliable indicator of insert temperature, as is often assumed [166].

With no discharge and the HC at room temperature (~300K), or heated by running an electric current through the heater coil, the thrust generated is compatible with theoretical predictions for heating a gas by conduction/convection through a solid wall, in a fashion similar to what happens in a resistojet. The differences in thrust between cold and hot HC suggest a temperature increase of ~5.5-6 times, from 300 K to 1700-1800 K. This is somewhat high, but still quite close to measurements and estimates of the HC temperature. The differences between various propellants confirm, to a very good degree, a proportionality to the square root of the atomic mass, in agreement with the theory in Chapter 2. Increasing the orifice diameter from

0.5 to 1.0 mm, therefore the orifice area by a factor of four, practically halves the specific impulse. This is probably due to less efficient thermal conduction. A wider orifice will allow a larger ΔT across it, with hotter gas close to the walls and a colder core flow towards the axis. This will decrease the average temperature, and hence the specific impulse, with respect to a smaller orifice, where the temperature radial profile will be much more uniform and close to the wall temperature.

The characteristics observed with a heated cathode are actually replicated with a discharge running, especially as a trend at the highest mass flow rates. This is to be expected, because we can suppose that in those conditions the power per unit mass flow rates is only enough to basically heat the gas. The mechanism will be different, though, as the plasma is now heated through an electric discharge, after a fashion similar to that of an arcjet. In fact, even if the trends are the same, and doubling the orifice diameter still halves the specific impulse, the actual values of I_{sp} are higher than those observed without discharge, suggesting plasma temperatures still higher than the heater-generated ones at ~3 mg/s.

This drop in specific impulse may be due to lower current densities and to smaller ohmic dissipation in the orifice, because a larger area will cause a lower resistance, as a first approximation. Smaller power deposition into the plasma means lower heavy-particle average temperature, hence the drop in I_{sp}. The expected rough inverse proportionality to the square root of the atomic mass, in agreement with the theory of Chapter 2 and the measurements taken with no discharge, may be somehow mitigated, with discharge on, by a penalty due to the higher ionization potential of lighter atoms and other factors, like differences in electrical resistivity and thermal conductivity. For argon, at 3 mg/s mass flow rate the values of specific impulse are greater by a factor of ~3.6 with respect to those obtained by simply heating the HC. Assuming the acceleration, in this regime, to be essentially thermal, of a gasdynamic type, this yields an effective, average plasma temperature higher by a factor of ~1.9, proportional to the square root of the temperature, in agreement with the theory of Chapter 2. This means that, in the interior of our HC, strong radial gradients of temperatures must exist, supporting a relatively hot flow core. From a wall value of ~1500-2000 K, the temperature increases towards the axis of symmetry, so that the average value is ~3000-3500 K. The HC flow model described in Chapter 2, where

the orifice is treated like a homogeneous plasma cylinder, could allow us to confirm that the average heavy-particle temperature in the orifice rises above the wall temperature, but would obviously be unable to shed any light on its radial variation, which can only be inferred.

It is quite clear that a larger orifice causes a general degradation in performance, with lower values of specific impulse for the same discharge conditions even at lower mass flow rates, where the behaviour shows, however, different features. The thrust ceases to be proportional to the mass flow rate, becoming, within the error bars, independent of it, at least between ~0.5 mg/s and 1.0 mg/s, and then starts dropping again for even lower values of the mass flow rate, when the discharge becomes, in general, extremely unstable. As this corresponds to plume mode operation , with voltages rapidly increasing with decreasing mass flow rates, at constant current, such increase in thrust corresponds to an increase in discharge power, and is probably related to a higher power available per unit mass flow rate. Therefore, the discharge power to mass flow rate ratio increases rapidly with decreasing mass flow rate. This may be the cause of the corresponding increase in specific impulse in this region, already reported by the author [54], as suggested by the linear correlation shown in Fig. 5.31.

I_{sp} increases rapidly with decreasing mass flow rate and, interestingly, shows values closer to each other for the various propellants. The inverse proportionality of I_{sp} to the square root of the atomic weight, verified to an excellent agreement for the heated cathode and, to a lesser extent, for the discharge cathode at high mass flow rates, where it may be mitigated by the higher ionisation potential of the lighter atoms, becomes less valid for mass flow rates below ~1 mg/s. This suggests that while the main acceleration mechanism is still of the thermal type, with a hotter core, arcjet-like operation, other mechanisms may come into play. An increased power deposition into the flow, in fact, could justify an increase in specific impulse, but it should still accelerate to higher velocities propellants of lower atomic mass. This is still the case, except for some points at the lowest mass flow rates, where the sharply rising I_{sp} trend appears to be interrupted. For those conditions, though, the discharge was extremely unstable, with very high voltages and large oscillations, and the maximum current dropped from 25 A to ~20 A.

Acceleration of positive ions to high energies by a potential hill was suggested in the past as a manner in which it could be possible to build an efficient microthruster from a HC [25, 26, 48]. In order for this to happen, a large enough fraction of the flow to significantly increase the specific impulse should be accelerated in this way. A potential hill of a given height would impart the same amount of kinetic energy to ions with the same charge. Thus, their velocities would still scale in inverse proportion to their atomic weight square roots. Relying solely on thrust measurements, without knowledge of the abundance and of the energies of such ions, therefore, it would be extremely difficult to separate the effects of this mechanism from the electrothermal, arcjet-like one.

The measurements reported in Section 5.0.2 strongly suggest that a significant fraction of the mass flow rate is actually ionised. As the values of specific impulse observed at the lower mass flow rates are compatible with the fraction of the propellant ionised being accelerated by a potential hill of the order of the anode voltage, while the rest is exhausted at thermal speeds, this possible contribution to thrust generation cannot indeed be ruled out.

A calculation of the possible contribution to specific impulse from high energy ions can be performed using data by Crofton and Boyd [40]. These were obtained using a T6 HC with an enclosed keeper and an orifice diameter of 0.9 mm, operated with xenon. By inspection of Figs. 1.3-1.9 [40], by choosing an operating point at 10 A discharge current and 0.5 mg/s mass flow rate, we can estimate an average energy for the ions of 25-30 V, a peak value, on the axis, of 8μA/cm^2 and a linear angular distribution for the collected current density, from the peak value to zero for ±90°. By integrating over a hemisphere, we obtain a total emitted ion current of 64 mA, corresponding to ~18% of the mass flow rate (0.5 mg/s = 0.367 Aeq of Xe). If we assume that the rest of the gas is exhausted as neutrals with a velocity calculated with Eq. (2.7) (hybrid model) and T = 1500-2000 K, we have 18% of the mass flow rate exhausted at ~650 s and 82% at ~50 s. This would give a total I_{sp} of ~160 s. Our measurements (see Section 5.0.3) give values for the specific impulse of 136 s and 236 s, respectively, for a T6 HC with 0.5 mm orifice diameter and 0.5 mg/s of Xe at 10 A and 25 A discharge current. Data for 1.0 mm HC orifice diameter are only available at 0.5 mg/s of Xe and 25 A current, giving a value of I_{sp} = 242 s. We can

therefore estimate a value of I_{sp} ~140 s at 0.5 mg/s of Xe, 10 A current and orifice diameter between 0.5 and 1.0 mm. This is only ~15% lower than the value calculated using the data from [40]. This difference could be attributed to the differences in the experimental configurations, and in particular to the enclosed keeper, which could enhance ion production.

Magnetohydrodynamic (MHD) effects have also been invoked [28, 33] as possible acceleration mechanisms. According to the classic Maecker's formula, the specific impulse I_{sp} produced by a magnetoplasmadynamic (MPD) arcjet is, to a good approximation [1],

$$I_{sp} = \frac{F}{\dot{m}g} = \frac{\mu}{4\pi g}\left(ln\frac{r_a}{r_c} + C\right)\frac{I^2}{\dot{m}} = \frac{\mu}{4\pi g} b \frac{I^2}{\dot{m}} \quad , \tag{5.5}$$

where μ is the magnetic permeability, I is the discharge current, r_a and r_c are, respectively, anode and cathode radii and C is a constant, depending on the actual current density distribution over the cathode end surface. This thrust generation mechanism would be independent of propellant atomic weight and mass flow rate, dependent only on total current and discharge geometry. This latter dependence is contained in the coefficient b. The contribution of this mechanism to the overall specific impulse would thus become particularly important at low mass flow rates, and could in part explain the differences in behaviour that we pointed out above. A plot of specific impulse against the Maecker's formula parameters (see Fig. 5.42) shows the correct qualitative behaviour (linear dependence) for low mass flow rates. However, this would give, for the coefficient b, an unrealistically high value of ~40. We can therefore conclude that, even if it the estimation of the coefficient b for an open-diode HC discharge is not immediate, MPD-type acceleration mechanisms are most likely not important in this operating regime.

It may be interesting to remember that HCs have actually been used in MPD thrusters with good results [10]. The values of thrust produced were in agreement with those predicted by the classic formulation, as in Eq. (5.5) [1, 10].

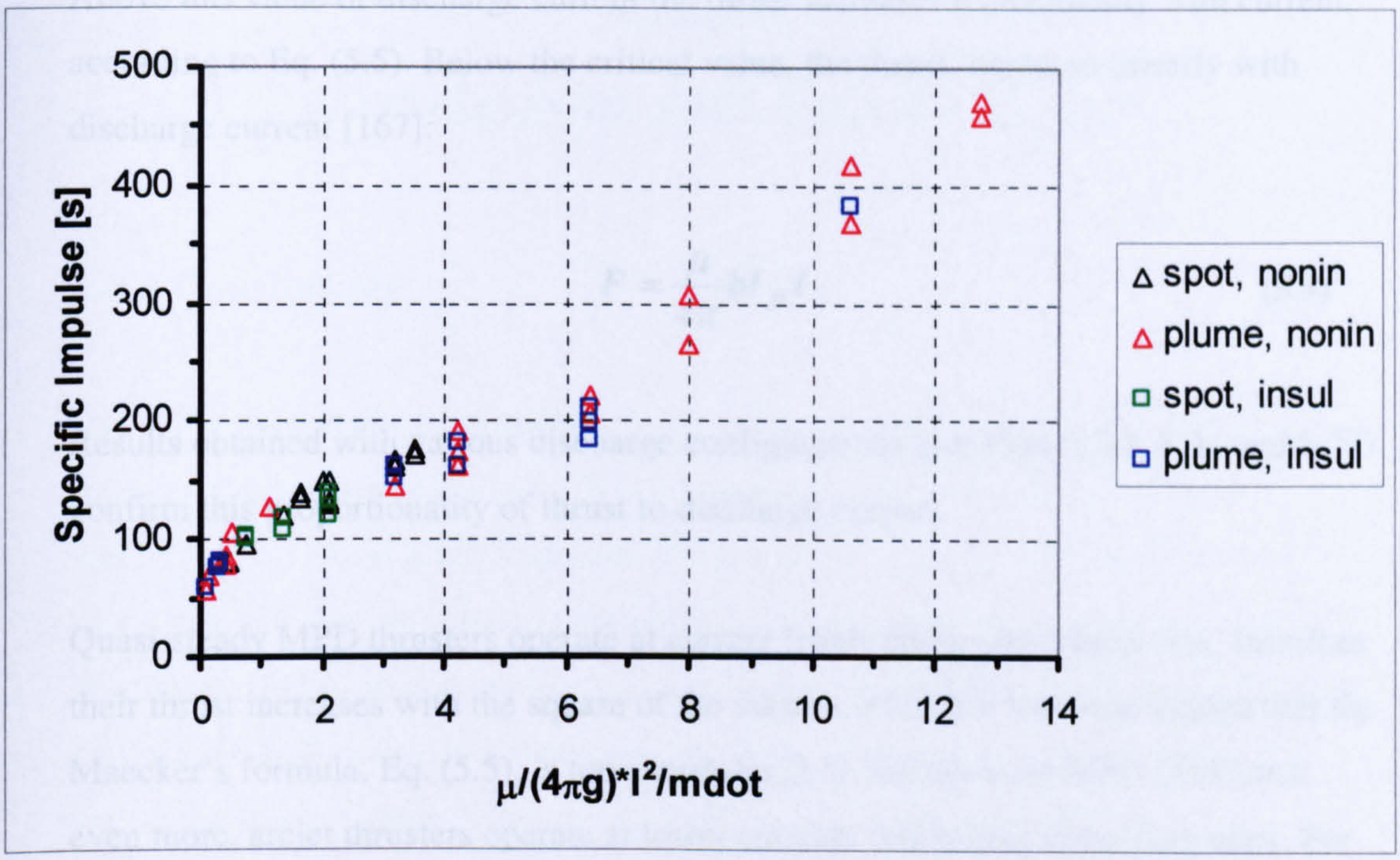

Figure 5.42 – Specific impulse vs. Maecker's formula parameters, 40 mm anode.

It is also possible to say that, for the propellants and mass flow rates investigated in this thesis, our device operates at discharge *currents well below the* critical or full ionisation current I_{fi}, at which all propellant is exhausted at the Alfven velocity

$$u_{Alf} = \sqrt{\frac{2E_i}{m}}, \tag{5.6}$$

where E_i is the first ionisation energy and m the atomic mass of the propellant, yielding for the thrust:

$$F = \dot{m}u_{Alf} = \frac{\mu}{4\pi} bI_{fi}^2, \tag{5.7}$$

And therefore

$$I_{fi} = \sqrt{\frac{4\pi\dot{m}u_{Alf}}{\mu b}}. \tag{5.8}$$

Above this value of discharge current the thrust increases quadratically with current, according to Eq. (5.5). Below the critical value, the thrust increases linearly with discharge current [167]:

$$F = \frac{\mu}{4\pi} b I_{fi} I \,. \tag{5.9}$$

Results obtained with various discharge configurations (see Figs. 5.12, 5.26 and 5.27) confirm this proportionality of thrust to discharge current.

Quasi-steady MPD thrusters operate at current levels above the critical one, therefore their thrust increases with the square of the current, even if it has been argued that the Maecker's formula, Eq. (5.5), is too simplistic [11]. Steady-state MPD [168] and, even more, arcjet thrusters operate at lower currents and higher mass flow rates. For these latter devices, scaling of thrust with power and of specific impulse with specific power have been proposed [169, 170].

Chapter 6

Conclusions and Future Work

6.0 – Conclusions

The HC operation mechanisms are, to date, still imperfectly understood and modelled. Actual measurement of the thrust was deemed necessary in order to assess the viability of the HC as a microthruster. To this end, a thrust measurement system, consisting of a cantilever beam target (CBT) and a laser optical lever (LOL), was developed, calibrated and tested with cold and heater thrust measurements (discharge off) of a T6 hollow cathode. Extensive hot thrust measurements, with discharge on, were subsequently taken, using argon, krypton and xenon as propellants.

The cold and heater thrust measurements are in good agreement with fluid dynamics theory, showing a square root dependence on the flow temperature and the inverse of the propellant atomic weight. In this mode of operation, our HC behaves like a cold gas or a resistojet thruster, with the flow heated through exchange with the walls. Continuum flow in the HC interior and sonic conditions at the orifice exit obtain for a wide range of operating parameters.

Measurements of the hot thrust have produced interesting results. The trends seen with discharge off are still observed with discharge on at high mass flow rates and, to a lesser extent, at low mass flow rates, where the specific impulse increases greatly. This can be ascribed to the increase of discharge power per unit mass flow rate. Power dissipated through ohmic heating, especially in the orifice region, is deposited into the flow, raising the average temperature to values much higher than those expected from a flow in equilibrium with the walls. For this to happen, large radial temperature gradients in the plasma must exist, with a core much hotter than the flow close to the walls. This is somewhat similar to the operation of an arcjet thruster and quite different from the behaviour with no discharge. The heavy particles will therefore have an average temperature higher than the wall value and lower than that of the electrons, far less massive. Sonic conditions still obtain, in general, at the orifice exit,

but now the heavy particle velocities, related to the square root of their local temperature, will be much higher. Hence, the specific impulse, proportional to the square root of the average heavy-particle temperature, will increase.

Acceleration of positive ions to high energies by a potential hill outside the HC and a $\vec{j} \times \vec{B}$, MPD-like contribution are also mechanisms that could enhance thrust generation, especially at low values of mass flow rate. It is extremely difficult to evaluate the magnitude of the former contribution without actually measuring the ion emission characteristics, but the mechanism is still compatible with the values of Specific impulse measured and with ion energy distribution data in the literature. The latter is bound to be marginal at the values of discharge current and mass flow rate that we have investigated. Our thruster could, from this point of view, also be considered similar to an MPD thruster operating at discharge current values well below the full ionisation one. As the current decreases, for a certain mass flow rate, the thermal acceleration mechanisms become preponderant over the electromagnetic ones, as in an arcjet thruster.

Values of specific impulse in excess of 500 s were obtained. Unfortunately, this happened at low mass flow rate and high current, with the HC operating in what is commonly referred to as plume mode, with high discharge voltages. In these conditions, power consumption is higher than in the so-called spot mode. Also, the electrodes reach higher temperatures, decreasing the lifetime of the device.

Even in spot mode, though, values of I_{sp} around 300 s can be obtained, generating several mN of thrust at about 300 W discharge power, with mass flow rates of a few mg/s of argon. It is clear that a small HC orifice diameter is beneficial, with I_{sp} inversely proportional to orifice diameter, even if experiments were performed only with two different orifice diameters. It also appears that increasing the anode orifice diameter, and therefore the effective anode to cathode radius ratio, has the effect of increasing I_{sp}.

Such values of I_{sp} are at least partially competitive with other types of microthruster, and were obtained using a device that is flight-qualified and has a long proven

lifetime, with very little attempt at optimisation. Therefore, a whole host of potential applications may be envisioned. In a satellite, for instance, the use of a HC thruster for attitude control could be convenient, even at modest values of I_{sp}, in conjunction with an ion engine for drag compensation and maybe orbit raising, as these two devices could share the same propellant and power conditioning subsystems. This would avoid the need for a separate chemical propulsion system. Such an "all-electric spacecraft" would be considerably lighter and simpler, due to a reduced number of subsystems and to the propellant mass savings made possible through the higher specific impulse.

In order to ensure that the specific impulse is actually higher, and not just comparable to that of chemical thrusters, it will be necessary to operate at low mass flow rates. This runs counter, though, to the need for improving the thrust-to-power ratio, as operation at low mass flow rates is associated with higher discharge voltages. As an alternative, or in conjunction with low mass flow rate operation, the increase in specific impulse obtained with decreasing atomic mass suggests that operation with lighter propellants would be beneficial.

6.1 – Future Work

Even if the initial results are encouraging, further work is necessary to fully understand the thrust production mechanisms and to improve the performance of our HC microthruster.

The increase in specific impulse obtained with decreasing atomic mass suggests that operation with lighter propellants should be explored. Operation with propellants other than noble gases, for example hydrogen or methane, though, raises issues concerning possible chemical interactions with the insert of this particular type of HC.

The use of an enclosed keeper should be investigated, as it would allow operation at low mass flow rates without the HC switching to plume mode operation, with high voltages, detrimental both for the power consumption and for the electrode lifetime. In this way, high values of specific impulse could probably be obtained in conjunction with values of thrust to power ratio competitive with other thrusters. As the use of

lower atomic mass propellants is related, in general, to higher discharge voltages and a larger range of parameters leading to plume mode operation, the use of an enclosed keeper could allow spot mode operation with propellants like neon, for instance, which in the experiments described in this thesis was always associated to noisy, unstable plume mode.

The effect of varying the orifice diameter needs further testing, in order to confirm the inverse proportionality trend showed by the specific impulse. Also, more drastic changes in anode configuration could to be explored, to fully understand the potential benefits already shown by a simple anode change. Large inter-electrode gaps will probably require the addition of a keeper electrode in order to facilitate breakdown. This could affect plume geometry, through impingement, and therefore thrust production.

Measurement of the emitted ion currents and energy distributions for different discharge conditions could allow us to estimate how much of this thrust is due to electromagnetically accelerated ions, to neutrals heated up by the discharge and to energetic ions accelerated by a potential hump. If considerable ionisation fractions in the orifice and the plume are achieved, as seems likely, then the use of an extracting/accelerating electrode should further improve the thruster performance. In this way, a proper HC-based ion microthruster could be developed.

References

[1] R. G. Jahn, *Physics of Electric Propulsion*: McGraw-Hill, Inc., 1968.

[2] P. G. Hill and C. R. Peterson, *Mechanics and Thermodynamics of Propulsion*: Addison-Wesley Publishing Company, 1965.

[3] G. A. Csiky, "Investigation of a Hollow Cathode Discharge Plasma," AIAA-69-258, presented at the AIAA 7th Electric Propulsion Conference, 1969.

[4] C. M. Philip, "A Study of Hollow Cathode Discharge Characteristics," *AIAA Journal*, Vol. 9, pp. 2191-2196, 1971.

[5] A. Lorente-Arcas, "A Model for the Hollow Cathode Discharge," *Plasma Physics*, Vol. 14, pp. 651-659, 1972.

[6] D. G. Fearn and C. M. Philip, "An Investigation of Physical Processes in a Hollow Cathode Discharge," *AIAA Journal*, Vol. 11, pp. 131-132, 1973.

[7] J.-L. Delcroix and A. R. Trindade, "Hollow Cathode Arcs," *Advances in Electronics and Electron Physics*, Vol. 35, pp. 87-190, 1974.

[8] M. Krishnan, R. G. Jahn, W. F. von Jaskowsky and K. E. Clark, "Physical Processes in Hollow Cathodes," *AIAA Journal*, Vol. 15, pp. 1217-1223, 1977; also, AIAA-76-984.

[9] C. M. Ferreira and J.-L. Delcroix, "Theory of the Hollow Cathode Arc," *Journal of Applied Physics*, Vol. 49, pp. 2380-2395, 1978.

[10] K. Toki, "Quasisteady MPD Arcjet with Hollow Cathode," *Journal of Propulsion and Power*, Vol. 2, pp. 402-407, 1986.

[11] E. Y. Choueiri, "Scaling of Thrust in Self-Field Magnetoplasmadynamic Thrusters," *Journal of Propulsion and Power*, Vol. 14, pp. 744-753, 1998.

[12] T. M. Jack, S. W. Patterson and D. G. Fearn, "The Effect of the Keeper Electrode on Hollow Cathode Characteristics," AIAA-2000-3533, presented at the 36th AIAA/ASME/SAE/ASEE Joint Propulsion Conference and Exhibit, 2000.

[13] W. R. Hudson and B. A. Banks, "An 8-cm Electron Bombardment Thruster for Auxiliary Propulsion," AIAA-73-1131, presented at the AIAA 10th Electric Propulsion Conference, 1973.

[14] D. G. Fearn, "The UK-10 Ion Propulsion System - a Technology for Improving the Cost-Effectiveness of Communications Spacecraft," IEPC-91-009, presented at the AIDAA/AIAA/DGLR/JSASS 22nd International Electric Propulsion Conference, 1991.

[15] I. M. A. Rudwan, "Physics of Hollow Cathode Breakdown and Steady-State Operation with Several Inert Gas Propellants," PhD Thesis, University of Southampton, 2003.

[16] D. G. Fearn, A. Singfield, N. C. Wallace, S. A. Gair and P. T. Harris, "The Operation of Ion Thruster Hollow Cathodes using Rare Gas Propellants," AIAA-90-2584, presented at the AIAA/DGLR/JSASS 21st International Electric Propulsion Conference as AIAA-90-2584, 1990.

[17] M. P. Monterde, A. E. Dangor, M. G. Haines, A. K. Malik and D. G. Fearn, "Spectroscopic Measurements of the Plasma Within a Hollow Cathode," AIAA-95-2383, presented at the AIAA/ASME/SAE/ASEE 31st Joint Propulsion Conference and Exhibit, 1995.

[18] A. K. Malik, M. P. Monterde and M. G. Haines, "Spectroscopic Measurements on Xenon Plasma in a Hollow Cathode," *Journal of Physics D: Applied Physics*, Vol. 33, pp. 2037-2048, 2000.

[19] J. D. Cobine, *Gaseous Conductors*: Dover Publications, Inc., 1958.

[20] D. G. Fearn, "Mission Analysis, Spacecraft Concept and Ion-Thruster Design for a Low-Cost Rendezvous with an Asteroid," IEPC-05-226, presented at the 29th International Electric Propulsion Conference, 2005.

[21] J. Lyman Spitzer, *Physics of Fully Ionized Gases*, Second Revised Ed.: Interscience Publishers, John Wiley & Sons, 1962.

[22] A. D. Ketsdever and J. Mueller, "System Considerations and Design Options for Microspacecraft Propulsion Systems," AIAA-99-2723, presented at the AIAA/ASME/SAE/ASEE 35th Joint Propulsion Conference and Exhibit, 1999.

[23] G. Yashko, G. Giffin and D. Hastings, "Design Considerations for Ion Microthrusters," IEPC-97-072, presented at the 25th International Electric Propulsion Conference, 1997.

[24] M. Young, E. P. Muntz, A. D. Ketsdever and D. C. Wadsworth, "Unique Hollow Cathode as a Code Validation Experiment and Candidate Non-Magnetic Ion Micro-Thruster," AIAA-99-2854, presented at the 35th AIAA/ASME/SAE/ASEE Joint Propulsion Conference and Exhibit, 1999.

[25] M. W. Crofton, "The Feasibility of Hollow Cathode Ion Thrusters: A Preliminary Characterization," AIAA-2000-5354, presented at the 36th AIAA/ASME/SAE/ASEE Joint Propulsion Conference and Exhibit, 2000.

[26] M. W. Crofton and I. D. Boyd, "Plume Measurement and Modeling Results for a Hollow Cathode Micro-Thruster," AIAA-2001-3795, presented at the 37th AIAA/ASME/SAE/ASEE Joint Propulsion Conference and Exhibit, 2001.

[27] M. J. Patterson and J. E. Foster, "Hollow Cathode Micro-Thruster Performance," IEPC-01-226, presented at the 27th International Electric Propulsion Conference, 2001.

[28] P. M. Latham, A. J. Pearce and R. A. Bond, "Erosion Processes in the UK-25 Ion Thruster," IEPC-91-096, presented at the AIDAA/AIAA/DGLR/JSASS 22nd International Electric Propulsion Conference, 1991.

[29] V. J. Friedly and P. J. Wilbur, "High Current Hollow Cathode Phenomena," *Journal of Propulsion and Power*, Vol. 8, pp. 635-643, 1992; also, AIAA-90-2587.

[30] I. Kameyama and P. J. Wilbur, "Characteristics of Ions Emitted from High-Current Hollow Cathodes," IEPC-93-023, presented at the AIAA/AIDAA/DGLR/JSASS 23rd International Electric Propulsion Conference, 1993.

[31] M. W. Crofton, "A Small Diagnostics Facility for Electric Propulsion Issues: Initial Hollow Cathode Results," AIAA-99-0454, presented at the 37th AIAA Aerospace Sciences Meeting and Exhibit, 1999.

[32] G. J. Williams, T. B. Smith, M. T. Domonkos, K. J. Shand, A. D. Gallimore and R. P. Drake, "Laser Induced Fluorescence Characterization of Ions Emitted from Hollow Cathode," AIAA-99-2862, presented at the 35th AIAA/ASME/SAE/ASEE Joint Propulsion Conference and Exhibit, 1999.

[33] S. W. Patterson and D. G. Fearn, "The Generation of High Energy Ions in Hollow Cathode Discharges," IEPC-99-125, presented at the 26th International Electric Propulsion Conference, 1999.

[34] M. W. Crofton, "Preliminary Mass Spectrometry of a Xenon Hollow Cathode," *Journal of Propulsion and Power*, Vol. 16, pp. 157-159, 2000; also, AIAA-99-0454.

[35] G. J. Williams, T. B. Smith, M. T. Domonkos, A. D. Gallimore and R. P. Drake, "Laser-Induced Fluorescence Characterization of Ions Emitted from Hollow Cathodes," *IEEE Transactions on Plasma Science*, Vol. 28, pp. 1664-1675, 2000.

[36] I. Kameyama and P. J. Wilbur, "Measurements of Ions from High-Current Hollow Cathodes Using Electrostatic Energy Analyzer," *Journal of Propulsion and Power*, Vol. 16, pp. 529-535, 2000.

[37] G. J. Williams and S. D. Kovaleski, "Near-Field Plasma Characterization of a 15 A Hollow Cathode via Laser Diagnostics," AIAA-2002-2192, presented at the 33rd AIAA Plasmadynamics and Lasers Conference, 2002.

[38] J. E. Foster and M. J. Patterson, "Plasma Emission Characteristics form a High Current Hollow Cathode in an Ion Thruster," AIAA-2002-4102, presented at

the AIAA/ASME/SAE/ASEE 38th Joint Propulsion Conference and Exhibit, 2002.

[39] M. W. Crofton and I. D. Boyd, "Plume Measurement and Modeling Results for a Xenon Hollow Cathode," AIAA-2002-4103, presented at the 38th AIAA/ASME/SAE/ASEE Joint Propulsion Conference and Exhibit, 2002.

[40] M. W. Crofton and I. D. Boyd, "The T6 Hollow Cathode: Measurements and Modeling," AIAA-2003-4171, presented at the 34th AIAA Plasmadynamics and Lasers Conference, 2003.

[41] J. E. Foster and M. J. Patterson, "Characterization of Downstream Ion Energy Distributions from a High Current Hollow Cathode in a Ring Cusp Discharge Chamber," AIAA-2003-4865, presented at the 39th AIAA/ASME/SAE/ASEE Joint Propulsion Conference and Exhibit, 2003.

[42] C. C. Farnell, J. D. Williams and P. J. Wilbur, "Characteristics of Energetic Ions Emitted from Hollow Cathodes," IEPC-03-072, presented at the 28th International Electric Propulsion Conference, 2003.

[43] T. R. Sarver-Verhey, "28,000 Hour Xenon Hollow Cathode Life Test Results," IEPC-97-168, presented at the 25th International Electric Propulsion Conference, 1997.

[44] D. G. Fearn, "An Assessment of the Durability of the UK-25 Ion Thruster," RAE SP(89)WP23, 1989.

[45] D. G. Fearn and M. J. Patterson, "The Compatibility of Hollow Cathode Characteristics with a Variety of Ion Thruster Designs," IEPC-99-133, presented at the 26th International Electric Propulsion Conference, 1999.

[46] N. C. Wallace and D. G. Fearn, "The Design and Performance of the T6 Ion Thruster," AIAA-98-3342, presented at the AIAA/ASME/SAE/ASEE 34th Joint Propulsion Conference and Exhibit, 1998.

[47] N. C. Wallace, D. H. Mundy and D. G. Fearn, "A Review of the Development of the T6 Ion Thruster System," IAF-99-S.4.08, presented at the 50th International Astronautical Congress, 1999.

[48] P. Gessini, S. B. Gabriel and D. G. Fearn, "The Hollow Cathode as a Micro-Ion Thruster," IEPC-01-233, presented at the 27th International Electric Propulsion Conference, 2001.

[49] A. Snyder and B. A. Banks, "Thrust Measurements of a Hollow-Cathode Discharge," NASA TN D-6705, 1972.

[50] Anonymous, in *Hamamatsu Cat. No. KPSD0001E01*, 2002.

[51] P. Gessini, S. B. Gabriel and D. G. Fearn, "Hollow Cathode Thrust Measurement Using a Target: System Development and Calibration," AIAA-

2002-4104, presented at the AIAA/ASME/SAE/ASEE 38th Joint Propulsion Conference and Exhibit, 2002.

[52] P. Gessini, S. B. Gabriel and D. G. Fearn, "Hollow Cathode Thrust Measurements Using a Target: Initial Results and Some Issues," IEPC-03-253, presented at the 28th International Electric Propulsion Conference, 2003.

[53] P. Gessini, S. B. Gabriel and D. G. Fearn, "Hollow Cathode Thrust Measurements Using a Target," ISPC-04-230, presented at the 4th International Spacecraft Propulsion Conference, 2004.

[54] P. Gessini, S. B. Gabriel and D. G. Fearn, "Thrust Characterization of a T6 Hollow Cathode," IEPC-05-257, presented at the 29th International Electric Propulsion Conference, 2005.

[55] P. Gessini, S. B. Gabriel and D. G. Fearn, "The T6 Hollow Cathode as a Microthruster," AIAA-2005-4078, presented at the AIAA/ASME/SAE/ASEE 41st Joint Propulsion Conference and Exhibit, 2005.

[56] P. Gessini, R. Intini Marques, S. B. Gabriel and S. M. Veres, "Propulsion System Optimisation for Satellite Formation Flying," presented at the 4th International Workshop on Satellite Constellations and Formation Flying, 2005.

[57] S. J. Pottinger, P. Gessini, D. Webb, R. Intini Marques and S. B. Gabriel, "Electric Propulsion Research at the University of Southampton," *Journal of the British Interplanetary Society*, Vol. 59, pp., 2006.

[58] R. V. Kennedy, "Theory of the Arc Hollow Cathode," *Journal of Physics D: Applied Physics*, Vol. 34, pp. 787-793, 2001.

[59] D. E. Siegfried and P. J. Wilbur, "Studies on an Experimental Quartz Tube Hollow Cathode," AIAA-79-2056, presented at the Princeton University/AIAA/DGLR 14th International Electric Propulsion Conference, 1979.

[60] D. E. Siegfried and P. J. Wilbur, "An Investigation of Mercury Hollow Cathode Phenomena," AIAA-78-705, presented at the AIAA/DGLR 13th International Electric Propulsion Conference, 1978.

[61] L. Rehn and H. R. Kaufman, "Correlation of Inert Gas Hollow Cathode Performance," AIAA-78-707, presented at the AIAA/DGLR 13th International Electric Propulsion Conference, 1978.

[62] D. E. Siegfried and P. J. Wilbur, "A Model for Mercury Orificed Hollow Cathodes: Theory and Experiment," AIAA-82-1889, presented at the AIAA/JSASS/DGLR 16th International Electric Propulsion Conference, 1982.

[63] D. E. Siegfried and P. J. Wilbur, "Phenomenological Model Describing Orificed, Hollow Cathode Operation," *AIAA Journal*, Vol. 21, pp. 5,6, 1983; also, AIAA-81-0746.

[64] D. E. Siegfried and P. J. Wilbur, "A Model for Mercury Orificed Hollow Cathodes: Theory and Experiment," *AIAA Journal*, Vol. 22, pp. 1405-1412, 1984.

[65] A. Salhi and P. J. Turchi, "A First-Principles Model for Orificed Hollow Cathode Operation," AIAA-92-3742, presented at the AIAA/SAE/ASME/ASEE 28th Joint Propulsion Conference and Exhibit, 1992.

[66] A. Salhi and P. J. Turchi, "Theoretical Modeling of Orificed, Hollow Cathode Discharges," IEPC-93-024, presented at the AIAA/AIDAA/DGLR/JSASS 23rd International Electric Propulsion Conference, 1993.

[67] I. Katz, V. A. Davis, M. J. Mandell and M. J. Patterson, "Hollow Cathode Micro Thruster," AIAA-2000-3267, presented at the AIAA/ASME/SAE/ASEE 36th Joint Propulsion Conference and Exhibit, 2000.

[68] I. Katz, B. M. Gardner, M. J. Mandell, G. A. Jongenward, M. J. Patterson and R. M. Myers, "Model of Plasma Contactor Performance," *Journal of Spacecraft and Rockets*, Vol. 34, pp. 824-828, 1997.

[69] V. A. Davis, I. Katz, M. J. Mandell and D. E. Parks, "Model of Electron Collecting Plasma Contactors," *Journal of Spacecraft and Rockets*, Vol. 28, pp. 292-298, 1991.

[70] M. Domonkos, "A Particle and Energy Balance Model of the Orificed Hollow Cathode," AIAA 2002-4240, presented at the AIAA/ASME/SAE/ASEE 38th Joint Propulsion Conference and Exhibit, 2002.

[71] M. Jugroot and J. K. Harvey, "Particle Simulation of the Main Chamber of a Kaufman-Type Ion Thruster," ESA SP-465, presented at the 3rd International Conference on Spacecraft Propulsion, 2000.

[72] M. J. Mandell and I. Katz, "Theory of Hollow Cathode Operation in Spot and Plume Modes," AIAA-94-3134, presented at the AIAA/ASME/SAE/ASEE 30th Joint Propulsion Conference, 1994.

[73] D. M. Murray, O. R. Tutty and S. B. Gabriel, "Numerical Modelling of Ion Thruster Hollow Cathode Interior Flow," AIAA-97-0793, presented at the AIAA 35th Aerospace Sciences Meeting & Exhibit, 1997.

[74] P. Rossetti, F. Paganucci and M. Andrenucci, "A Hollow Cathode Model for Application to the Electric Propulsion," AIAA-2002-4239, presented at the AIAA/ASME/SAE/ASEE 38th Joint Propulsion Conference and Exhibit, 2002.

[75] E. P. Vaulin, M. V. Kiryushkina, V. A. Obukhov and F. Scortecci, "Mathematical Modelling of Arc Hollow Cathodes," AIAA-96-3184, presented at the AIAA/ASME/SAE/ASEE 32nd Joint Propulsion Conference, 1996.

[76] F. T. A. Crawford and S. B. Gabriel, "Modelling Small Hollow Cathode Discharges for Ion Microthrusters," AIAA 2002-2101, presented at the AIAA 33rd Plasmadynamics and Lasers Conference, 2002.

[77] F. T. A. Crawford and S. B. Gabriel, "Numerical Simulation of the Hollow Cathode Plasma Using a PIC-DSMC Code," IEPC-03-027, presented at the 28th International Electric Propulsion Conference, 2003.

[78] I. Katz, J. R. Anderson, J. E. Polk and J. R. Brophy, "A Model of Hollow Cathode Plasma Chemistry," AIAA 2002-4241, presented at the AIAA/ASME/SAE/ASEE 38th Joint Propulsion Conference and Exhibit, 2002.

[79] I. Katz, J. R. Anderson, J. E. Polk and D. M. Goebel, "Model of Hollow Cathode Operation and Life Limiting Mechanism," IEPC-03-243, presented at the 28th International Electric Propulsion Conference, 2003.

[80] G. A. Csiky, "Measurements of Some Properties of a Discharge from a Hollow Cathode," NASA TN D-4966, 1969.

[81] G. A. Csiky, "Lamgmuir Probe Measurements in a Discharge from a Hollow Cathode," *Journal of Spacecraft and Rockets*, Vol. 7, pp. 474-475, 1970.

[82] D. G. Fearn and S. W. Patterson, "Characterisation of the High Current Hollow Cathode for the T6 Ion Thruster," AIAA-98-3346, presented at the AIAA/ASME/SAE/ASEE 34th Joint Propulsion Conference and Exhibit, 1998.

[83] D. G. Fearn and S. W. Patterson, "The Hollow Cathode - a Versatile Component of Electric Thrusters," ESA SP-465, presented at the ESA/CNES International Conference on Spacecraft Propulsion, 2000.

[84] S. W. Patterson, A. K. Malik and D. G. Fearn, "Noise and Oscillatory Disturbances in the T6 Ion Thruster Hollow Cathode," AIAA-99-2577, presented at the AIAA/ASME/SAE/ASEE 35th Joint Propulsion Conference and Exhibit, 1999.

[85] S. W. Patterson, "Discharge Physics and Associated Phenomena in an Ion Thruster Type Hollow Cathode," PhD Thesis, Imperial College, 2003.

[86] S. J. Pottinger, "Investigation of Steady State Characteristics of Hollow Cathode Internal Plasmas Using Optical Emission Spectroscopy," PhD Thesis, University of Southampton, 2005.

[87] I. Kameyama and P. J. Wilbur, "Effects of External Flow near High-Current Hollow Cathodes on Ion-Energy Distributions," IEPC-97-173, presented at the 25th International Electric Propulsion Conference, 1997.

[88] J. D. Williams and P. J. Wilbur, "Electron Emission from a Hollow Cathode-Based Plasma Contactor," *Journal of Spacecraft and Rockets*, Vol. 29, pp. 820-829, 1992.

[89] V. N. Korovkin, L. A. Latyshev, V. A. Obukhov and V. G. Grigoryan, "Research of Ion Thrusters in the USSR," IEPC-91-081, presented at the AIDAA/AIAA/DGLR/JSASS 22nd International Electric Propulsion Conference, 1991.

[90] J. D. Williams and P. J. Wilbur, "Experimental Study of Plasma Contactor Phenomena," *Journal of Spacecraft and Rockets*, Vol. 27, pp. 634-641, 1990.

[91] G. Aston and P. J. Wilbur, "Ion Extraction from a Plasma," *Journal of Applied Physics*, Vol. 52, pp. 2614-2626, 1981.

[92] J. Kutzner and H. C. Miller, "Ion Flux from the Cathode Region of a Vacuum Arc," *IEEE Transactions on Plasma Science*, Vol. 17, pp. 688-694, 1989.

[93] G. Y. Yushkov, A. Anders, E. M. Oks and I. G. Brown, "Ion Velocities in Vacuum Arc Plasmas," *Journal of Applied Physics*, Vol. 88, pp. 5618-5622, 2000.

[94] K. Tsuruta, K. Sekiya and G. Watanabe, "Velocities of Copper and Silver Ions Generated from an Impulse Vacuum Arc," *IEEE Transactions on Plasma Science*, Vol. 25, pp. 603-608, 1997.

[95] J. Scott Miller, S. H. Pullins, D. J. Levandier, Y.-h. Chiu and R. A. Dressler, "Xenon Charge Exchange Cross Sections for Electrostatic Thruster Models," *Journal of Applied Physics*, Vol. 91, pp. 984-991, 2002.

[96] S. J. Pottinger and S. B. Gabriel, "Optical Probe Measurements on the Internal Plasma of a T6 Type Hollow Cathode," IEPC-03-219, presented at the 28th International Electric Propulsion Conference, 2003.

[97] C. H. Edwards and S. B. Gabriel, "The Effect of Propellant Selection on Mission Cost for the UK-25 Inert Gas Ion Thruster," IEPC-93-239, presented at the AIAA/AIDAA/DGLR/JSASS 23rd International Electric Propulsion Conference, 1993.

[98] C. H. Edwards, "Discharge Characteristics and Instabilities in the UK-25 Ion Thruster Operating on Inert Gas Propellants," PhD Thesis, University of Southampton, 1997.

[99] M. P. Monterde, M. G. Haines, A. E. Dangor, A. K. Malik and D. G. Fearn, "Kaufman-Type Xenon Ion Thruster Coupling Plasma: Langmuir Probe

Measurements," *Journal of Physics D: Applied Physics*, Vol. 30, pp. 842-855, 1997.

[100] S. J. Pottinger, personal communication, 2003.

[101] V. K. Rawlin, "Internal Erosion Rates of a 10-kW Xenon Ion Thruster," AIAA-88-2912, presented at the AIAA/ASME/SAE/ASEE 24th Joint Propulsion Conference and Exhibit, 1988.

[102] A. P. Semenov and B.-S. C. Batuev, "On the Extraction of Ions from a Hollow-Cathode Discharge with a Penetrating Plasma," *Soviet Physics - Technical Physics*, Vol. 36, pp. 570-572, 1991.

[103] M. J. Patterson and M. T. Domonkos, "Recent Development Activities in Hollow Cathode Technology," IEPC-01-270, presented at the 27th International Electric Propulsion Conference, 2001.

[104] M. Domonkos, A. D. Gallimore and G. J. Williams, "Low Current Hollow Cathode Evaluation," AIAA 99-2575, presented at the AIAA/ASME/SAE/ASEE 35th Joint Propulsion Conference and Exhibit, 1999.

[105] G. J. Williams, T. B. Smith and A. D. Gallimore, "30 cm Ion Thruster Discharge Cathode Erosion," IEPC-01-306, presented at the 27th International Electric Propulsion Conference, 2001.

[106] G. J. Williams, M. T. Domonkos and J. M. Chavez, "Measurement of Doubly Charged Ions in Ion Thruster Plumes," IEPC-01-310, presented at the 27th International Electric Propulsion Conference, 2001.

[107] F. G. Baksht and A. B. Rybakov, "Fully Ionized Dense Plasma in a Hollow-Cathode Arc," *Soviet Physics - Technical Physics*, Vol. 23, pp. 141-146, 1978.

[108] M. W. Crofton, "Evaluation of the United Kingdom Ion Thruster," *Journal of Spacecraft and Rockets*, Vol. 33, pp. 739-747, 1996.

[109] L. B. King and A. D. Gallimore, "Propellant Ionization and Mass Spectral Measurements in the Plume of an SPT-100," AIAA-98-3657, presented at the AIAA/ASME/SAE/ASEE 34th Joint Propulsion Conference and Exhibit, 1998.

[110] L. B. King and A. D. Gallimore, "Ion Energy Diagnostics in the Plume of an SPT-100 from Thrust Axis to Backflow Region," AIAA-98-3641, presented at the AIAA/ASME/SAE/ASEE 34th Joint Propulsion Conference and Exhibit, 1998.

[111] L. B. King and A. D. Gallimore, "Ion-Energy Diagnostics in the Plasma Exhaust of a Hall Thruster," *Journal of Propulsion and Power*, Vol. 16, pp. 50, 51, 2000.

[112] L. B. King and A. D. Gallimore, "Mass Spectral Measurements in the Plume of an SPT-100 Hall Thruster," *Journal of Propulsion and Power*, Vol. 16, pp. 157-159, 2000.

[113] F. S. Gulczinski and A. D. Gallimore, "Near-Field Ion Energy and Species Measurements of a 5-kW Hall Thruster," *Journal of Propulsion and Power*, Vol. 17, pp. 418-427, 2001; also, AIAA-99-2430.

[114] A. K. Malik and D. G. Fearn, "The Study of the Physics of Hollow Cathode Discharges," IEPC-93-026, presented at the AIAA/AIDAA/DGLR/JSASS 23rd International Electric Propulsion Conference, 1993.

[115] P. M. Latham, "The UK-25 Ion Thruster," AEA InTec 1384, 1993.

[116] I. Katz, personal communication, 2003.

[117] J. R. Anderson, personal communication, 2003.

[118] I. Katz, M. J. Mandell, M. J. Patterson and M. Domonkos, "Sensitivity of Hollow Cathode Performance to Design and Operating Parameters," AIAA-99-2576, presented at the AIAA/ASME/SAE/ASEE 35th Joint Propulsion Conference and Exhibit, 1999.

[119] P. J. Turchi and A. Salhi, "Low Power Plasma Thruster Based on Hollow Cathode Discharge," AIAA-94-3126, presented at the AIAA/ASME/SAE/ASEE 30th Joint Propulsion Conference, 1994.

[120] F. T. A. Crawford, "A Numerical Model of the Ion Thruster Hollow Cathode Plasma," PhD Thesis, University of Southampton, 2004.

[121] "Sonic Flow Through Orifices, Nozzles and Venturis," Optimal Systems Limited, http://www.optimal-systems.demon.co.uk/flow-orifice.htm, 1999.

[122] P. J. Turchi, *Molecular Theory of Gas Flow*. Lecture Notes: The Ohio State University, 1996-97.

[123] A. H. Shapiro, *The Dynamics and Thermodynamics of Compressible Fluid Flow*: The Ronald Press Company, 1953.

[124] C. L. Tien and J. H. Lienhard, *Statistical Thermodynamics*: Hemisphere Publishing Corporation, 1979.

[125] W. G. Vincenti and C. H. Kruger, *Introduction to Physical Gas Dynamics*: John Wiley & Sons, Inc., 1965.

[126] A. Salhi, R. M. Myers and P. J. Turchi, "Experimental Investigation of a Hollow Cathode Discharge," IEPC-93-025, presented at the AIAA/AIDAA/DGLR/JSASS 23rd International Electric Propulsion Conference, 1993.

[127] D. Kannappan and T. K. Bose, "Transport Properties of a Two-Temperature Argon Plasma," *The Physics of Fluids*, Vol. 20, pp. 1668-1673, 1977.

[128] X. Chen and P. Han, "On the Thermodynamic Derivation of the Saha Equation Modified to a Two-Temperature Plasma," *Journal of Physics D: Applied Physics*, Vol. 32, pp. 1711-1718, 1999.

[129] M. Hayashi, "Determination of Electron-Xenon Total Excitation Cross-Sections, from Threshold to 100 eV, from Experimental Values of Townsend's α," *Journal of Physics D: Applied Physics*, Vol. 16, pp. 581-589, 1983.

[130] P. L. Bartlett and A. T. Stelbovics, "Calculation of Electron-Impact Total-Ionization Cross Sections," *Physical Review A*, Vol. 66, pp. 1-10, 2002.

[131] W. L. Owens, "A Noble Gas Ion Propulsion System," AIAA-73-1114, presented at the AIAA 10th Electric Propulsion Conference, 1973.

[132] T. F. Yang, P. Liu, F. R. Chang-Diaz, H. Lander, R. A. Childs, H. D. Becker and S. A. Fairfax, "A Double Pendulum Plasma Thrust Balance and Thrust Measurement at a Tandem Mirror Exhaust," *Review of Scientific Instruments*, Vol. 66, pp. 4637-4643, 1995.

[133] G. Paccani and R. Ravignani, "Sulla Misura Indiretta della Spinta di Propulsori Elettrici," *Aerotecnica Missili e Spazio*, Vol. 74, pp. 103-110, 1995.

[134] D. G. Chavers, F. R. Chang-Diaz, C. Irvine and J. P. Squire, "Momentum and Heat Flux Measurements in the Exhaust of VASIMR Using Helium Propellant," IEPC-03-028, presented at the 28th International Electric Propulsion Conference, 2003.

[135] N. Matsunami, Y. Yamamura, N. Itoh, H. Tawara and T. Kawamura, "Energy Dependence of Ion-Induced Sputtering Yields of Monoatomic Solids in the Low Energy Region," Nagoya Institute of Plasma Physics IPPJ-AM-52, 1987.

[136] Y. Yamamura and H. Tawara, "Energy Dependence of Ion-Induced Sputtering Yields from Monoatomic Solids at Normal Incidence," *Atomic Data and Nuclear Data Tables*, Vol. 62, pp. 149-253, 1996.

[137] J. R. Gruber, "Low-Energy Sputter Erosion of Various Materials in a T5 Ion Thruster," IEPC-01-307, presented at the 27th International Electric Propulsion Conference, 2001.

[138] G. A. Bird, *Molecular Gas Dynamics and the Direct Simulation of Gas Flows*: Oxford University Press, 1994.

[139] A. Morley, *Strength of Materials*: Longmans, Green and Co. Ltd., 1946.

[140] Anonymous, "Gaussian Beam Optics," in *Melles Griot Catalogue*, 1997-98.

[141] Anonymous, "Helium Neon Lasers," in *Melles Griot Catalogue*, 1997-98.

[142] S. A. Self, "Focusing of Spherical Gaussian Beams," *Applied Optics*, Vol. 22, pp. 658-661, 1983.

[143] L. D. Landau, E. M. Lifshitz and L. P. Pitaevskii, *Electrodynamics of Continuous Media*, Second Revised and Enlarged Ed.: Pergamon Press Ltd., 1984.

[144] D. J. Milligan, "The Baffle Aperture Region of an Ion Thruster," PhD Thesis, University of Southampton, 2001.

[145] S. W. Patterson, M. Jugroot and D. G. Fearn, "Discharge Initiation in the T6 Thruster Hollow Cathode," AIAA 2000-3532, presented at the AIAA/ASME/SAE/ASEE 36th Joint Propulsion Conference and Exhibit, 2000.

[146] D. G. Fearn, personal communication, 2002a.

[147] W. McGuire, R. H. Gallagher and R. D. Ziemian, *Matrix Structural Analysis*: John Wiley & Sons, 2000.

[148] C. B. White, personal communication, 2003.

[149] C. Schwingshackl, personal communication, 2003.

[150] H. S. Carslaw and J. C. Jaeger, *Conduction of Heat in Solids*, Second Ed.: Oxford University Press, 1959.

[151] C. Cercignani and M. Lampis, "Free Molecular Flow Past a Flat Plate in the Presence of a Nontrivial Gas-Surface Interaction," *Journal of Applied Mathematics and Physics*, Vol. 23, pp. 713-728, 1972.

[152] M. S. Woronowicz and D. F. G. Rault, "Cercignani-Lampis-Lord Gas-Surface Interaction Model: Comparisons Between Theory and Simulation," *Journal of Spacecraft and Rockets*, Vol. 31, pp. 532-534, 1994.

[153] R. G. Lord, "Some Extensions to the Cercignani-Lampis Scattering Kernel," *Physics of Fluids A: Fluid Dynamics*, Vol. 3, pp. 706-710, 1991.

[154] K. T. Compton and E. S. Lamar, "A Test of the Classical "Momentum Transfer" Theory of Accommodation Coefficients of Ions at Cathodes," *Physical Review*, Vol. 44, pp. 338-344, 1933.

[155] F. G. Collins and E. C. Knox, "Parameters of Nocilla Gas/Surface Interaction Model from Measured Accommodation Coefficients," *AIAA Journal*, Vol. 32, pp. 765-773, 1994.

[156] S. R. Cook and M. A. Hoffbauer, "Absolute Momentum Transfer in Gas-Surface Scattering," *Physical Review E*, Vol. 55, pp. 3828-3831, 1997.

[157] S. R. Cook and M. A. Hoffbauer, "Analyzing Gas-Surface Interactions Using the Reduced Force Coefficients," *Physical Review E*, Vol. 58, pp. 504-511, 1998.

[158] C. C. Van Voorhis and K. T. Compton, "Accommodation Coefficients of Positive Ions of Argon, Neon and Helium," *Physical Review*, Vol. 37, pp. 1596-1610, 1931.

[159] R. G. Lord, "Application of the Two-Temperature Maxwellian Model to Describe Re-Emission of Gas Molecules from Surfaces," *Journal of Physics D: Applied Physics*, Vol. 25, pp. 327-330, 1992.

[160] R. Yanagi and I. Kimura, "A New Type Target for the Measurement of Impulse Bits of Pulsed Plasma Thrusters," AIAA-81-0712, presented at the 15th International Electric Propulsion Conference, 1981.

[161] I. Kimura, R. Yanagi and S. Inoue, "Preliminary Experiments on Pulsed Plasma Thrusters with Applied Magnetic Fields," AIAA-78-655, presented at the AIAA/DGLR 13th International Electric Propulsion Conference, 1978.

[162] M. Kameoka, H. Takegahara, Y. Shimizu and K. Toki, "Single Impulse Measurement of a Coaxial Pulsed Plasma Thruster," IEPC-03-093, presented at the 28th International Electric Propulsion Conference, 2003.

[163] D. G. Fearn, personal communication, 2002b.

[164] J. D. Swift and M. J. R. Schwar, *Electrical Probes for Plasma Diagnostics*: Iliffe Books Ltd., 1970.

[165] M. P. Monterde, "Physiscs of the Hollow Cathode in a Kaufman Type Electrostatic Ion Thruster," PhD Thesis, Imperial College, 1996.

[166] J. E. Polk, A. Grubisic, N. Taheri, D. M. Goebel, R. Downey and S. Hornbeck, "Emitter Temperature Distributions in the NSTAR Discharge Hollow Cathode," AIAA-2005-4398, presented at the AIAA/ASME/SAE/ASEE 41st Joint Propulsion Conference and Exhibit, 2005.

[167] V. B. Tikhonov, N. N. Antropov, G. A. Dyakonov, V. A. Obukhov, F. Paganucci, P. Rossetti and M. Andrenucci, "Investigation of a New Type of MPD Thruster," ECA Vol. 24B (2000) 81-84, presented at the 27th EPS conference on Controlled Fusion and Plasma Physics, 2000.

[168] M. Winter, M. Auweter-Kurtz, J. Heiermann and W. T., "Experimental and Numerical Comparison of High Power Steady State MPD-Thrusters with Radiation-and Water-Cooled Anodes," IEPC-03-207, presented at the 28th International Electric Propulsion Conference, 2003.

[169] M. Auweter-Kurtz, B. Glocker, T. Golz, H. L. Kurtz, E. W. Messerschmid, M. Riehle and D. M. Zube, "Arcjet Thruster Development," *Journal of Propulsion and Power*, Vol. 12, pp. 1077-1083, 1996.

[170] D. Bock, M. Auweter-Kurtz and H. L. Kurtz, "1 kW Ammonia Arcjet System Development for a Science Mission to the Moon," IEPC-2005-075, presented at the 29th International Electric Propulsion Conference, 2005.